CMB as a Probe of New Physics and Old Times

Thesis by

Vera Gluščević

In Partial Fulfillment of the Requirements

for the Degree of

Doctor of Philosophy

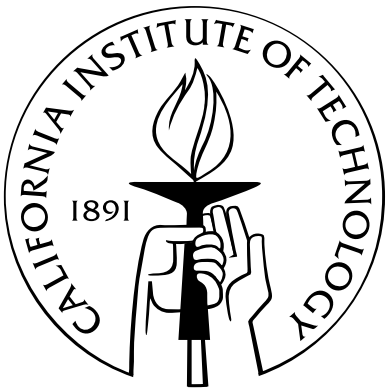

California Institute of Technology

Pasadena, California

2013

(Submitted February 28, 2013)

To Tim, the love of my life, and to Babyo,
for the best-ever kicks of support that enabled the completion of this thesis.

"The vastness of the heavens stretches my imagination—stuck on this carousel my little eye can catch one-million-year-old light. A vast pattern—of which I am a part... What is the pattern or the meaning or the why? It does not do harm to the mystery to know a little more about it. For far more marvelous is the truth than any artists of the past imagined it..."

— *Footnote*,
Richard Feynman

"I come in search of the truth."

— *The Star Trek series: Where Silence Has Lease*,
Q

Acknowledgements

"It is the act of understanding this beautiful Universe that bids our minds run so wild—perhaps one of the highest pleasures of life... but Love is the giver of life and meaning, and stands marvelous at the source of it all..."

The Universe is beautiful. My road from Serbia, around the world, and to the United States has taught me that very few people are in a position to earn a living on a passion of understanding beauty. The incredibly lucky situation I am in as a cosmologist I owe to those in this country who recognize and generously support the value of scientific research, to the existence of the extraordinary place that is Caltech, and to the decisions of the admissions committee and my adviser Marc Kamionkowski to support me as a graduate student. I am particularly indebted to Marc for allowing me to benefit from his ability to provide excellent guidance and insight in matters of research and academic navigation, completely devoid of judgment and personal bias, and especially to give time for a student to learn at her own pace and in her own manner, while staying readily available to offer advice at all times. His capacity to abstract the most relevant, to see the solution long before beginning the "hard work," and his intuition for where the interesting questions lie, remain an inspiration and a goal of my own professional future.

I also had the good fortune to be co-advised by Chris Hirata in the last two years. Chris is a rare individual whose astonishing breadth and depth of understanding all things physics, and readiness to make as much time as one can desire for infinitely patient explanations, is perhaps only surpassed by his unassuming humility and his kindness to those around him. I am truly privileged and humbled to be among the people who have a chance to work with him. In addition, I would like to express gratitude to Annika Peter for leading me into the world of dark-matter research and being the saving voice of encouragement and support at times when I most needed it. I wouldn't have made it through my last few years at Caltech had it not been for this voice.

I am very grateful to my collaborators, Robert Caldwell, Asantha Cooray, and Rennan Barkana, for sharing the excitement of research with me, expanding my experience into their areas of expertise, and providing advice and support along the way. I am especially lucky to have had a chance to work closely with Duncan Hanson and experience his committed tutoring on data analysis and

Python, which now constitute life ingredients for my research, and also thankful for many fun and intellectually challenging conversations we had in the past year. Finally, many thanks to Sean Carroll for enlightening conversations on cosmic birefringence!

My enjoyment of learning was abundantly rewarded at Caltech by a number of lecturers in the Physics Department whom I wish to thank for their devotion and excellence in teaching. Also, had it not been for the many Caltech staff who are able and willing to sweep away all sorts of problems efficiently as if they never existed, life in graduate school would not have been half the sheltered fun that it was.

Many other people have sustained me, academically and in life, throughout my years at Caltech, or otherwise have contributed to laying out the road that led me to complete my doctoral work. Some of those whose influence was most striking I mention here.

Thinking back to the fun times at Caltech, several groups of dear, dear people immeditately come to mind. My classmates: Gwen, Drew, Tucker, Sam, Mike, Tim, Krzysztof, and Elisabeth—guys, thanks so much for pushing together through the challenges of the first year; it's no exaggeration to say I wouldn't have made it (many times over) without you. "The Physicists": Evan, Itamar, Ron, Kevin, Brian, Paula, Laura, M'hair, Jasper, Milivoje, Dan, and others—you are the smartest and funnest (and funniest!) group of troopers I mingled with; it was a great joy being around you, from our late-night problem-solving sessions at the SFL, all the way through all those games, nerdy discussions, and trips we did together. I now somehow need to deal with the hole that's left in my life since we all started graduating. For mentoring, presenting me with role models to look up to, and giving golden advice at crucial times, several senior grad students are especially responsible: Adrienne, Dan, Yacine, and Tristan. Also, thanks to all fellow TAPIRs for sharing Thursday "lunch and enlightenment" and pride in being a theorist! Finally, the St. James' family, in particular Rev. Anne Tumilty, Rev. Jon Dephouse, the Choir, and the 20s–30s crowd, whose loving support has carried me through both happy and challenging times—many thanks for the overflow of grace from you folks.

Crucial additions to my education were the summer schools, conferences, and workshops I attended—I am very much in debt to the organizers of these events as well as to the participants (many of whom became dear friends), for the life-changing experiences they brought. Especially dear to my heart was the STScI Summer Program of 2006, where my adventure in US-based astronomy began. Dave Soderbloom, Daniela Calzetti, and Mario Livio—you have quite literally altered the course of my career and life.

There are two people to whom I owe much for being my unofficial advisers at various stages in my career: Milan Ćirković, during my very first scientific beginnings in Belgrade's X High School, and Dragan Huterer, whose dear friendship and continuous support were a boost all along this road. Many teachers throughout my life inspired sparks of the passion for knowledge, but especially

Prof. Dostanić who introduced me to the impeccable elegance of proof-based mathematics, and my Serbian teacher Milica Opačić, who taught me how logical thinking enbodied and adorned in words can make for a thrilling kind of beauty.

Folks at the Public Observatory and Planetarium in Belgrade, Goran, Mića, Otaš, Bane, and others, opened wide the doors of astronomy for me during my high-school years by teaching courses for the public and by letting us get a closer peek into the night sky. I was hooked to astrophysics ever since. Otaše: even after having heard many of the best lecturers this world has to offer, I still think you belong on the list. Warm thanks also to my friends, the many pearls scattered around the world. Kvokane: I cherish the memory of being in your company while getting the hard work done for school. And Zverko: thanks for making me jealous enough to gather courage and take the Test to become a collaborator at the Belgrade Observatory—step one on this journey. Also, in principle, thanks for growing up with me and sharing my Beograd—such wonderous place to be free and dream a dream.

Many roads start from home; mine too started with my family. I owe them my life and who I am today. My aunt Mirjana, who deserves a medal for the fiercest cheerer-on for all my successes. My dad who did a great job with igniting curiosity at a very early age when he showed me a flagellum through a microscope—the fire burned ever since. My grandmas and my grandpa, for the purest loving kindness since day zero (Eko: volela bih da si sad tu da bratski podelimo slavljeničku čokoladu dok mi se smeješ što sam ti postala "Doktor Filozofije"!). The Mortons, John, Dan, Roberta, Deborah, Rebecca, Bela: thanks, guys, for the many ways you supported me since you first met me; it truly is an honor to take up your name. Ron and Itamar: your friendship and unconditional love made Pasadena a home away from blood-family. And again, Itamar: I can never say all the thanks that would match what you did when you pushed me into the "easy-and-correct" physics way while I was still pondering if I'm cut out for this research thing, nor what you still do whenever I need some light along the way.

And the very special thanks I keep for the end...

To Mama, for shaping who I am, for supporting with every fiber of her being (and beyond) all my causes, and for selflessly and lovingly directing her many qualities I can only hope to acquire some day to the well-being of her child.

To my husband Tim—my light, my strength, my team, my completion—for the Love such as I never dreamed existed, surpassing all words and worlds. Thanks, Bubs.

Abstract

Cosmic birefringence (CB)—a rotation of photon-polarization plane in vacuum—is a generic signature of new scalar fields that could provide dark energy. Previously, WMAP observations excluded a uniform CB-rotation angle larger than a degree.

In this thesis, we develop a minimum-variance–estimator formalism for reconstructing direction-dependent rotation from full-sky CMB maps, and forecast more than an order-of-magnitude improvement in sensitivity with incoming Planck data and future satellite missions. Next, we perform the first analysis of WMAP-7 data to look for rotation-angle anisotropies and report null detection of the rotation-angle power-spectrum multipoles below L=512, constraining quadrupole amplitude of a scale-invariant power to less than one degree. We further explore the use of a cross-correlation between CMB temperature and the rotation for detecting the CB signal, for different quintessence models. We find that it may improve sensitivity in case of marginal detection, and provide an empirical handle for distinguishing details of new physics indicated by CB.

We then consider other parity-violating physics beyond standard models—in particular, a chiral inflationary-gravitational-wave background. We show that WMAP has no constraining power, while a cosmic-variance–limited experiment would be capable of detecting only a large parity violation. In case of a strong detection of EB/TB correlations, CB can be readily distinguished from chiral gravity waves.

We next adopt our CB analysis to investigate patchy screening of the CMB, driven by inhomogeneities during the Epoch of Reionization (EoR). We constrain a toy model of reionization with WMAP-7 data, and show that data from Planck should start approaching interesting portions of the EoR parameter space and can be used to exclude reionization tomographies with large ionized bubbles.

In light of the upcoming data from low-frequency radio observations of the redshifted 21-cm line from the EoR, we examine probability-distribution functions (PDFs) and difference PDFs of the simulated 21-cm brightness temperature, and discuss the information that can be recovered using these statistics. We find that PDFs are insensitive to details of small-scale physics, but highly sensitive to the properties of the ionizing sources and the size of ionized bubbles.

Finally, we discuss prospects for related future investigations.

Contents

List of Figures

List of Tables

Part I

General Introduction

Few questions ever spoken so perpetually excite the human mind as those inquiring about the origins and fabric of the entire observable Cosmos. Several decades after cosmology assumed its place on the pedestal of modern science, they are beginning to be answered.

The science of cosmology now rests upon several major pillars: the Big Bang paradigm about a hot, explosive birth of our Universe followed by the everlasting expansion and cool-down we witness today; inflationary theory, assigning quantum origins to the seeds of structure and explaining the flatness and homogeneity of spacetime; and the gravitational-collapse scenario for growth of non-linearities in matter that gave rise to nearly everything in the realm of astrophysics. These pillars stand upon percent-level measurements of the age, geometry, and energy content of the Universe, reinforced by many observations of experimental particle physics and astrophysics.

In spite of a number of fascinating breakthroughs in the last few decades, a long road is still ahead: to pick out details of the Universe's infancy; to unravel the "mysterious" nature of its two major components: *dark matter* and *dark energy*, and tame them into the frameworks of particle physics and General Relativity; to catch glimpses from the true cosmic dawn, when the first stars ended *the dark ages* during *cosmic reionization*, and to understand these distant beginnings of the astrophysical Universe—this is just an incomplete sketch of a modern cosmologists' "to-do list" for the 21st century.

The goal of the research presented in this doctoral thesis is to address some of these big questions, through novel theoretical approaches designed to extract information about new fundamental physics and very early cosmic times from current state-of-the-art observations of the cosmic microwave background (CMB) radiation. The plan of the rest of this thesis is as follows.

Part II (based on Refs. [1–3]) gives a brief overview of the physics, observations, and formalism used to describe the CMB; most of the subsequent text relies on the definitions and concepts presented therein. Part III (based on Ref. [4–7]) presents CMB tests of new fundamental physics. In particular, we focus on *anisotropic cosmic birefringence* and similar exotic mechanisms, discussing theoretical underpinnings, developing optimized analysis formalisms, obtaining the first constraints from WMAP data[1] [8], proposing new statistical avenues to be applied to future data sets, and forecasting sensitivities of upcoming and next-generation CMB experiments[2]. Part IV (based on Refs. [12, 13]) studies very early (astrophysical) times through two complementary investigations of the epoch of cosmic reionization. We first adopt the formalism from Part III to constrain key reionization parameters with WMAP data, and interpret our results in the context of a simple analytic reionization model. Next, we diverge from the CMB-themed discussions in the rest of the

[1] In various parts of this work, we use WMAP 5-, 7-, and 9-year data release, depending on what was available at the time relevant part of the work was completed. However, we do not expect that updating all the results to account for the latest and final (9-year) data release would change our conclusions in any significant way.

[2] We considered various stages of the WMAP mission, as a current CMB experiment, *Planck*'s [9] and SPIDER's [10] upcoming data releases, and also the proposed CMBPol-EPIC mission [11], as a next-generation (futuristic) experiment. We did not consider any ground-based experiments, but we note that they might be highly relevant for the work done or proposed in this thesis.

presented work and use simulations of the redshifted 21-cm signal from the epoch of reionization in order to develop and test new statistical tools, designed to analyze future data from low-frequency radio arrays currently under construction. We make concluding remarks in Part V. Appendix A provides some useful formulas involving Wigner-3j symbols, and Appendix B presents a derivation of Maxwell's equations in the presence of an electromagnetic Chern-Simons term. The bulk of Parts III, and IV has been adapted from previously published material of which I was an author and is reproduced here with permission.

Part II

CMB as a Precision Tool: A Brief Overview

Cosmic microwave background radiation, coming isotropically from all directions as almost perfect black-body radiation at about 2.73K (corresponding to a mean energy density of about 0.26eV cm^{-3}), consists of photons that last scattered more than 13 billion years ago. It therefore paints a picture of an infant Universe on the sky, first observed in 1965 [14]. Maps of the miniscule directional fluctuations of its temperature and polarization, now routinely acquired by space-based, balloon-borne, and ground-based telescopes, bear an astonishing amount of information, enabling the CMB to become a power tool that boosted cosmology from a speculative discipline to a precision science. Today, it continues to inform research in the areas of astrophysics and fundamental physics, probing distances and energy regimes inaccessible by any imaginable human-built laboratory.

The CMB constitutes a special data set for several reasons. As the oldest (primordial) signal we observe today, it provides insight into the physics of very early times and very high energies. Since it travelled through all later epochs of cosmic evolution, it also probes large distances, bearing signatures from a wide range of processes that took place along the way, such as cosmic reionization, structure formation and evolution of gravitational potentials, late-time cosmic acceleration (driven by dark energy), etc. Finally, and most importantly, this plethora of signatures can be disentangled owing to the fact that the CMB was created when the Universe was a linear system, the physics of which is well understood. The purpose of this part of the thesis is to provide a concise review of the physics, observations, and formalisms used nowdays to describe statistical properties of the CMB temperature and polarization fields. The work presented in this thesis heavily relies on the concepts presented in this part, since the main subject we deal with is extraction and interpretation of a variety of secondary signatures that the new undiscovered physics and early astrophysical epochs might have left in the CMB.

Chapter 1

Story of the CMB

Instead of reviewing calculational details, we devote this chapter to a heuristic storyline, intended to capture the essence of the physics that gave rise to the CMB anisotropies, linking it to the main traits of the observed CMB sky. For a more technical resource, see, e.g., Refs. [1, 15]

In the beginning, there was *inflation*—an epoch of accelerated (faster-than-light) expansion of the observable Universe that ended in the first 10^{-35} seconds of time. The speed of this expansion allowed for the (ever-present and extremely short-lived) "quantum flutterings" of the metric field to become classical fluctuations, sowing seeds of structure which gradually grew into bound astrophysical objects—stars, galaxies, clusters, etc.—through the process of gravitational collapse. In addition, inflation ironed out any prior amount of curvature, making our Universe spatially flat. Finally, by blowing up small causal patches by (at least) 60 $e-$folds, it made the entire content of our present-day cosmological horizon homogeneous in temperature, down to 1 part in 100 000. Even though details of these very early times are still speculative, the inflation was probably driven by a slowly evolving scalar field—the *inflaton*—whose potential dominated the energy budget of the Universe, until its decay (the process of *reheating*) ended inflation[1].

Soon after, the Universe was populated with baryonic matter[2], dark matter, and radiation: a mesh of particles in thermal equilibrium whose abundances can be calculated knowing their interactions, and using the *Boltzmann equations*. As the expansion and cool-down continued, different species "froze" when reactions controlling their abundance lost the race with cosmic expansion. When the Universe was about 3 minutes old, *Big-Bang nucleosynthesis* took place, setting primordial abundances of chemical elements, whereby roughly 3/4 of the baryonic mass stayed in the form of single protons (hydrogen nuclei). The radiation component dominated the energy density of the Universe in these very early times, and the expansion rate maintained the pace sufficient for the Fourier modes of primordial density fluctuations to continue exiting the causal horizon. Past redshift

[1] Modeling reheating is an active area of research, and a quite challenging one; to figure out *what* inflaton decayed into during reheating requires detailed knowledge of the Standard Model, as well as assumptions about new physics that might arise at these high energies.

[2] In this context, "baryonic matter" stands for all Standard Model particles, including leptons and force carriers.

of $z \approx 3000$, matter took over (with only about 1/5 in baryons, and the rest in the dark matter component), and at that time, fluctuation modes started re-entering the horizon and falling under the influence of causal physics—i.e., they started *growing*.

Another important transition happened when temperatures approached the hydrogen ionization energy: the Universe transformed from the state of plasma to a neutral state, in a brisk process of *recombination*. It is the physics of this primordial plasma just before recombination (380 000 years after the Big Bang) that shaped the CMB anisotropies we observe today.

Prior to recombination, photons were tightly coupled to baryons, through Thomson scattering off free electrons. The evolution of this *photon-baryon fluid* was controlled by two major forces: gravity of the overdensities (imprints of density fluctuations inherited from inflationary times), and pressure from relativistic photons. The perturbations in the fluid behaved like simple acoustic oscillations, driven by the balance of these two forces and damped by the expansion of the Universe. Perturbation modes of shorter wavelengths entered the horizon earlier and went through a number of oscillation periods, while some of the largest ones just got through a fraction of the first oscillation period (1/4 for those corresponding to the size of horizon at recombination). When the Universe recombined, photons were released, free-streamed, and redshifted ever since, forming the CMB radiation we see coming from all directions in the sky, as a cold "echo" of these early times. The apparent source of the radiation is a sphere of radius $z \approx 1100$ in redshift space, called the *last-scattering surface*. CMB anisotropies represent a "snapshot" of these primordial sound waves frozen at different oscillation phases and projected onto the celestial sphere. Finally, the CMB is polarized at a few-percent level, owing to the existence of quadrupolar anisotropy in the radiation field at the last-scattering surface (see Figure 1.1 for illustration).

Due to the quantum origins of the temperature fluctuations in the CMB, modes at a given angular scale represent, to a very good approximation, a random Gaussian field, uncorrelated with modes at other scales. A two-point correlation function, i.e., their variance, therefore describes the statistics of the CMB sky. Its analogue in spherical-harmonic space is the *power spectrum* C_ℓ (see Chapter 3), where multipole ℓ roughly corresponds to a particular angular scale in the sky θ,

$$\theta[\mathrm{rad}] \approx \pi/\ell. \tag{1.1}$$

Most of the current CMB experiments take measurements of the difference in signal in two directions in the sky, and are thus insensitive to the monopole ($\ell = 0$), and the mean CMB temperature. The dipole ($\ell = 1$) is the largest anisotropy (with the amplitude of about 3.4 mK), but it presumably mostly comes from the Earth's motion with respect to the CMB rest frame (with velocity of about 370 km/sec), and is thus typically discarded from the analysis of anisotropies[3]. Higher multipoles

[3]This is why the sums in the calculation of the temperature power spectra, such as those in Eq. (3.1) start from the quadrupole, $\ell = 2$; in the case of polarization, however, the first non-zero multipole is the quadrupole.

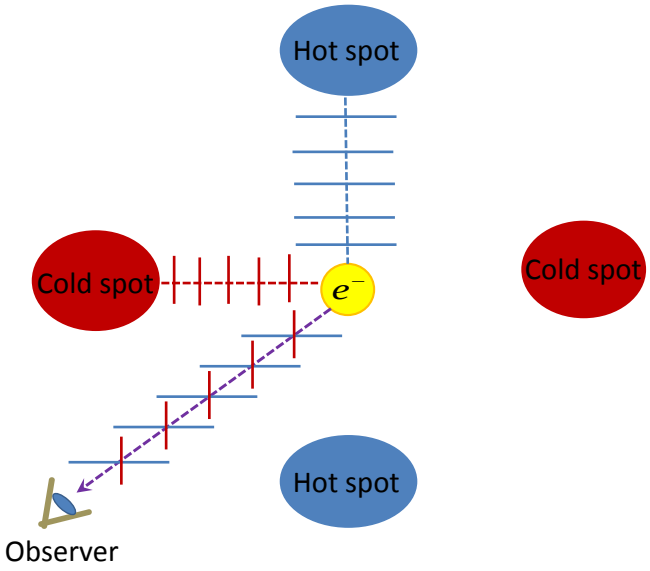

Figure 1.1: Quadrupolar anisotropy is illustrated, where the hot and cold spots lie at the surface of last scatter (plane of the drawing), and the observer's line of sight is perpendicular to it. The short lines represent the direction of polarization of light incident on the electron at the last-scattering surface; their length signifies the intensity of incident radiation, corresponding to the same polarization component in the light scattered toward the observer. Note that there are also polarization components parallel to the observer's line of sight, but they do not contribute to the polarization of scattered light. As a result of such scattering process, the light coming to the observer has a net polarization in the direction connecting cold spots.

carry abundance of information about the initial conditions, inflation, and secondary effects.

We can distinguish three angular regimes for the anisotropies in the sky, according to the dominant physical processes that shaped them. On sub-degree scales, the fluctuations in the CMB temperature are governed by the acoustic oscillations described above. The variance of the fluctuations peaks at about a degree scale, corresponding to the angular size of the (sound) horizon at recombination seen from a distance of $z \approx 1100$. At smaller angular scales, the power of the oscillations progressively drops; at about a few arcminutes, the so-called *(Silk) damping tail* appears in the power spectrum, as a result of photon-diffusion suppression of the small-wavelength fluctuations. At scales above a degree or so, the power of the fluctuations was not changed much by causal physics, and most pristinely reflects the initial conditions. The corresponding low$-\ell$ region of the temperature power spectrum is called the *Sachs-Wolfe plateau* (visible in Figure 3.4). Furthermore, a slight rise in power at the lowest ℓ's appears due to the *integrated Sachs-Wolfe effect*—time evolution of gravitational potentials of large-scale structure, that the CMB photons traversed on their way to the observer (also visible in Figure 3.4).

Aside from the anisotropies imprinted at the last-scattering surface, secondary anisotropies are also induced by various late-time astrophysical processes on various angular scales. Two most distinct and well-studied examples are: additional power added at large scales in the CMB polar-

ization ($\ell \lesssim 10$), during the epoch of cosmic reionization, and *weak gravitational lensing*, where the large-scale structure gravitationally deflected photon paths, changing the statistical description of anisotropies below arcminute scales. All these secondary anisotropies, if disentangled from primordial signatures, provide plenty of information about later times—either by themselves or, especially, in cross-correlation with other astrophysical data sets.

As pointed out before, the primordial perturbations that gave rise to the CMB temperature and polarization anisotropies were in the linear regime, and thus computationally tractable and well understood. Efficient Boltzmann codes for calculating CMB-anisotropy power spectra are now publicly available (e.g., CMBFAST [16] and CAMB [17]) and accurate to $\sim 1\%$ level; we make use of these codes a number of times in the work presented in this thesis.

Chapter 2

Current Observations

Ever since the faint radio glow was first discovered coming from all directions in the sky—a remnant from the Big Bang—hundreds of experiments were built to observe and characterize this cosmic microwave background radiation. Here, we briefly describe just a few current experiments, with special focus on the Willkinson Microwave Anisotropy Probe (WMAP) [18], whose data we use later in this work.

CMB observations are conducted from space, high-altitude balloons, or very dry ground-based sites, because the peak of its spectrum (at 160.2 GHz) corresponds to a frequency range which is heavily absorbed by water vapor in Earth's atmosphere. Full-sky coverage is only possible from space, while the ground-based experiments typically conduct deep surveys of small patches of the sky. Combination of the two modes of observation enables mapping of anisotropies at different angular scales, driving complementary science goals. Most of the work in this thesis has focused on the science enabled by all-sky surveys. However, several ground-based surveys currently underway will have a large impact on CMB science in the near future, and might be optimal for future directions of study that stem from the research presented here (see Conclusions of Parts III and IV for more details on this). Here, in addition to reviewing the basic description of the two preeminent satellite missions, we also briefly turn to these ground-based experiments.

The first measurement of the acoustic peaks that allowed for a percent-level determination of key cosmological parameters was derived from all-sky maps (in both temperature and polarization; see Figures 2.1 and 2.2) acquired by NASA's WMAP satellite mission, launched in 2001. WMAP's final 9-year data release came out in December 2012. The instrument on board the spacecraft is a radio telescope with two primary reflecting mirrors—a pair of Gregorian dishes facing opposite directions in the sky. The receivers are polarization-sensitive differential radiometers, which measure the difference in the sky signal between two telescope beams, separated by a 141° angle. WMAP has multi-frequency coverage, with five frequency bands, ranging from 23 GHz to 94 GHz. The spacecraft's location is at the Sun-Earth's second Lagrange point (L2, which is 1.5 million kilometers from Earth), which minimizes the amount of contamination from solar, terrestrial, and lunar emissions,

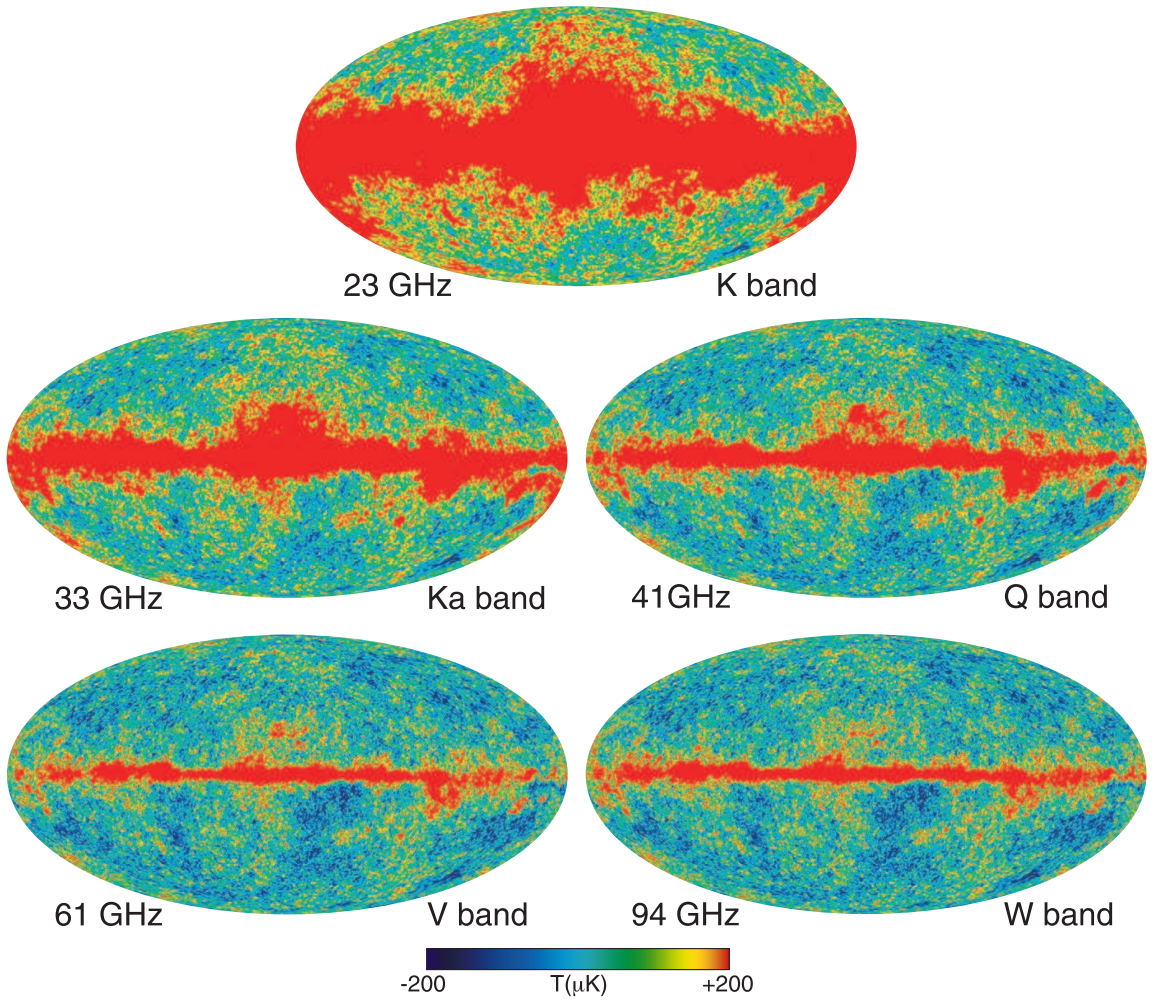

Figure 2.1: Temperature sky maps in Galactic coordinates (smoothed) from WMAP-9 (Figure from Ref. [19]).

and allows for thermal stability. WMAP traces an orbit around L2 with a 6-month period, acquiring a complete sky coverage each time. The telescope's scan strategy also includes a short-period rotation and precession.

The next-generation CMB space mission, the *Planck* satellite [9], was launched in 2009 by the European Space Agency. First release of the CMB data from *Planck* is expected in early 2013. The major difference in detector technology that enabled lower instrumental noise and better angular resolution in comparison to WMAP is the use of bolometers coupled to the telescope through cold optics. *Planck* carries two instruments, both of which are able to measure the total intensity and polarization of photons, and together cover a frequency range of 30 to 857 GHz, in 9 frequency bands. Both instruments use high electron mobility transistors, and are cryogenically cooled (with

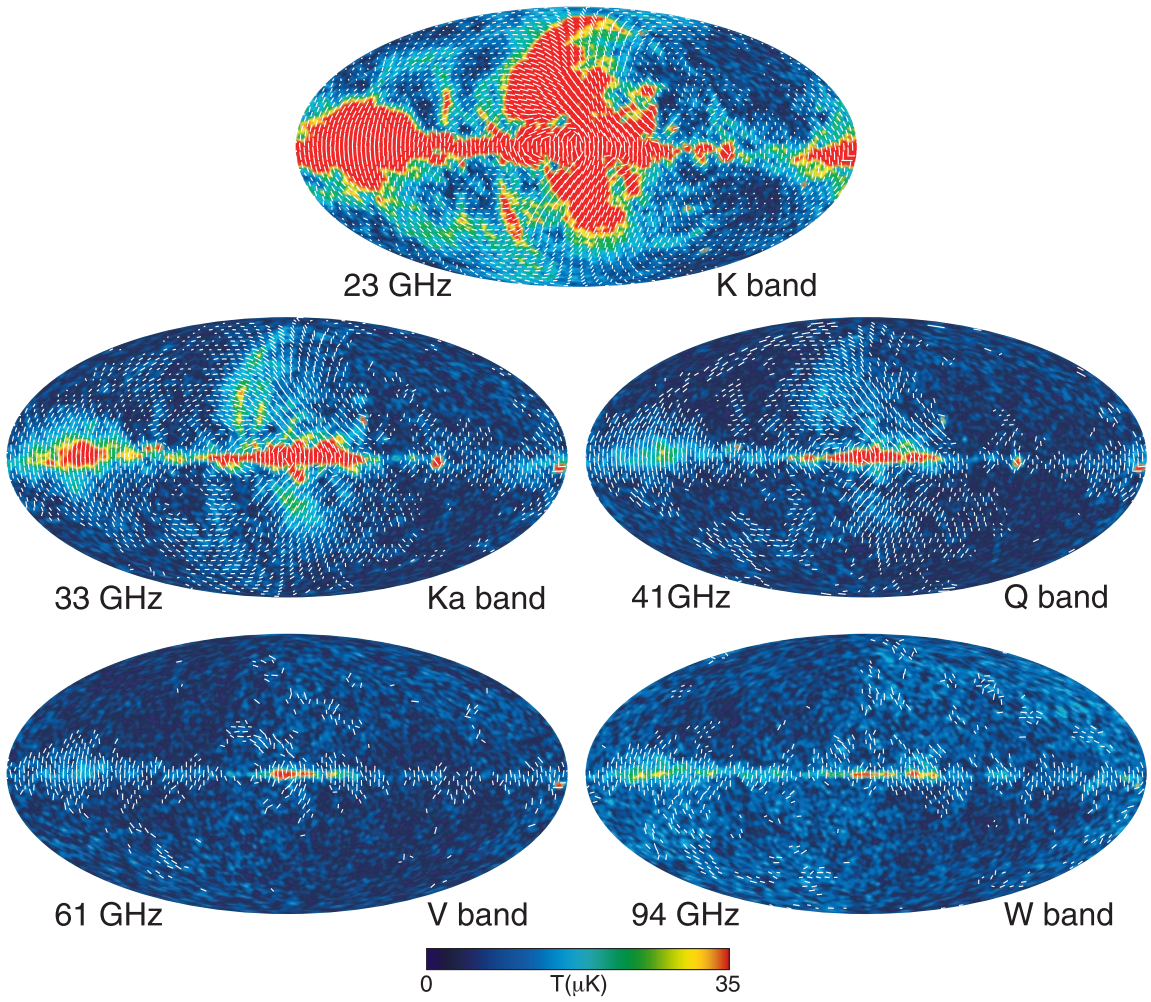

Figure 2.2: Maps of polarized intensity $p \equiv (Q^2 + U^2)^{0.5}$ in Galactic coordinates (smoothed) from WMAP-9; line segments represent the direction of polarization plane for pixels where signal-to-noise > 1 (Figure from Ref. [19]).

a supply of helium-3) to a fraction of 1K. *Planck* is also in an orbit around L2, and spins once every minute. It covers the entire sky in about 1 year.

As an example of a ground-based experiment, we briefly turn to the South Pole Telescope (SPT) [20, 21], keeping in mind that there are a number of experiments currently under construction, and with similar capabilities, such as the Atacama Cosmology Telescope (ACT) [22], POLARBEAR [23], etc. SPT is designed for conducting large-area millimeter- and sub-millimeter-wave surveys of faint, low contrast emission. It is a 10m-diameter off-axis Gregorian telescope operating at the Amundsen-Scott South Pole Station in Antarctica. Extensive shielding ensures low optical loading on the detectors (from stray light reflected from local buildings and the horizon), and therefore low noise. High pointing accuracy and the surface accuracy of the primary mirror enable scanning at high

frequencies, as compared to other experiments of similar type. The receiver is based on a focal plane with 1000 superconducting cryogenically cooled Transition-Edge-Sensor (TES) bolometers, with SQUID-based frequency-domain multiplexer readout. Observations will be done simultaneously in at least three frequency bands, between 95 and 345 GHz. Current width of the survey is 2500 square degrees; the next stage of the experiment will involve a survey with a new polarization-sensitive camera, SPTPol [24].

We conclude this chapter with a few remarks about challenges related to measuring the CMB anisotropies. Aside from technical challenges of recovering such a miniscule signal at frequencies that are hard to observe from the ground, the microwave sky is also contaminated by strong foreground emission from the Galaxy and extragalactic sources. The Galaxy is very bright at these frequencies, due to synchrotron, bremsstrahlung, and dust emission. Far from the Galactic plane, and at frequencies around 100 GHz where the Galactic emission reaches its minimum, contamination is at a level $\lesssim 10\%$. Frequency dependence of the foreground components allows them to be subtracted from the entire CMB map prior to analyzing CMB anisotropies, which is one of the reasons why most CMB experiments strive for multi-wavelength coverage. In addition, in full-sky surveys, pixels close to the Galactic plane are discarded, or masked, since these portions of the sky are dominated by the Galactic emission; a similar procedure is applied to known extragalactic point sources. At the moment, foreground contamination is not limiting the precision of CMB surveys, but in the near future, more detailed studies will be required in order to properly account for foregrounds in polarization maps [2].

Chapter 3

Formalism

In this chapter, we review the formalism used to analyze CMB anisotropies *on the full sky*. In Section 3.1, we focus on the description of temperature, while Section 3.2 focuses on polarization anisotropies. Section 3.3 describes the calculational path from the maps of temperature/polarization to recovering the power spectra and estimating their variances.

3.1 Temperature

In this section, we cover the basics of the theoretical formalism used to describe temperature anisotropies in the CMB. We start by noting that the spherical harmonics $Y_{\ell m}$, which represent a complete orthonormal basis for scalar functions on a sphere[1], are used to decompose temperature anisotropies[2] on the full sky as[3]

$$T(\hat{\mathbf{n}}) = \sum_{\ell=2}^{\infty} \sum_{m=-\ell}^{\ell} T_{\ell m} Y_{\ell m}(\hat{\mathbf{n}}) \tag{3.1}$$

where $\hat{\mathbf{n}}$ represents a unit vector pointing in a given direction on the celestial sphere, $\hat{\mathbf{n}} = (r = 1, \theta, \varphi)$. The inverse transformation (from pixel space to harmonic space) has the form

$$T_{\ell m} = \int d\hat{\mathbf{n}} T(\hat{\mathbf{n}}) Y^*_{\ell m}(\hat{\mathbf{n}}), \tag{3.2}$$

where we use the following normalization

$$\int d\hat{\mathbf{n}} Y_{\ell m}(\hat{\mathbf{n}}) Y^*_{\ell' m'}(\hat{\mathbf{n}}) = \delta_{\ell \ell'} \delta_{m m'}. \tag{3.3}$$

[1] $Y_{\ell m}$'s are the angular portion of the solutions for Laplace's equation, $\nabla f = 0$, where f is a scalar function; they are thus related to Legendre polynomials; see Appendix A.

[2] By "anisotropies", we mean that the temperature map $T(\hat{\mathbf{n}})$ actually represents the difference between the temperature in the direction $\hat{\mathbf{n}}$ and the mean temperature of the CMB sky $T_0 \approx 2.73K$, divided by T_0.

[3] We will often suppress the limits on the sums and use the more compact notation: $\sum_{\ell=2}^{\infty} \sum_{m=-\ell}^{\ell} \to \sum_{\ell m}$.

The main reason to treat the anisotropies in the spherical-harmonic space rather than in pixel space is that the coefficients in the decomposition $T_{\ell m}$ are, to first approximation, Gaussian random variables with zero mean[4], where different ℓ modes are uncorrelated. Therefore, the statistics of the fluctuations are captured by measuring the variance at each ℓ, i.e., the power spectrum C_ℓ^{TT},

$$C_\ell^{TT}\delta_{\ell\ell'}\delta_{mm'} \equiv \langle T_{\ell m} T^*_{\ell' m'} \rangle \,, \tag{3.4}$$

where the mean is taken over the ensemble of all possible realizations of the CMB sky, or by assumption of ergodicity, over all observer positions in the Universe.

Notice also that, since the temperature field is real, and spherical harmonics satisfy

$$Y^*_{\ell m} = (-1)^m Y_{\ell -m}, \tag{3.5}$$

temperature multipole coefficients satisfy the following reality condition

$$T^*_{\ell m} = (-1)^m T_{\ell -m}. \tag{3.6}$$

We show the current state-of-the-art measurements of the TT power spectrum in Figure 3.1, along with the corresponding best-fit theoretical curve. While satellite missions like WMAP are able to map large-scale (low ℓ) anisotropies with astonishing precision, the higher acoustic peaks and the damping tail (high ℓ) are currently best measured with the deep ground-based surveys, such as SPT and ACT.

3.2 Polarization

Two equivalent formalisms for the full-sky treatment of polarization anisotropies are now widely used in the CMB community: the approach introduced by Refs. [3,26] uses differential geometry on a sphere, and the so-called *E-B decomposition*, while the approach introduced by Refs. [27,28] uses spin-weighted spherical harmonics. Since they provide complementary insights into the problems discussed later in this thesis, we combine them as appropriate.

In addition to the map of brightness temperature $T(\hat{\mathbf{n}})$, maps of the Stokes parameters $Q(\hat{\mathbf{n}})$, $U(\hat{\mathbf{n}})$, and $V(\hat{\mathbf{n}})$ complete a description of a polarized radiation field of the CMB, assuming it is a perfect black body[5]. In Cartesian coordinates, components of the electric field of a monochromatic

[4] Some amount of non-Gaussianity is expected in the primordial signal, but other mechanisms for producing non-Gaussian signatures are also known to affect the statistics of the CMB (such as the weak gravitational lensing, for example). They usually require higher-order corrections to the Gaussian CMB sky, which is why Gaussian approximation holds well, at least to first order.

[5] In reality, the CMB should also exhibit small spectral distortions in its frequency spectrum (see, for example, Ref. [29]).

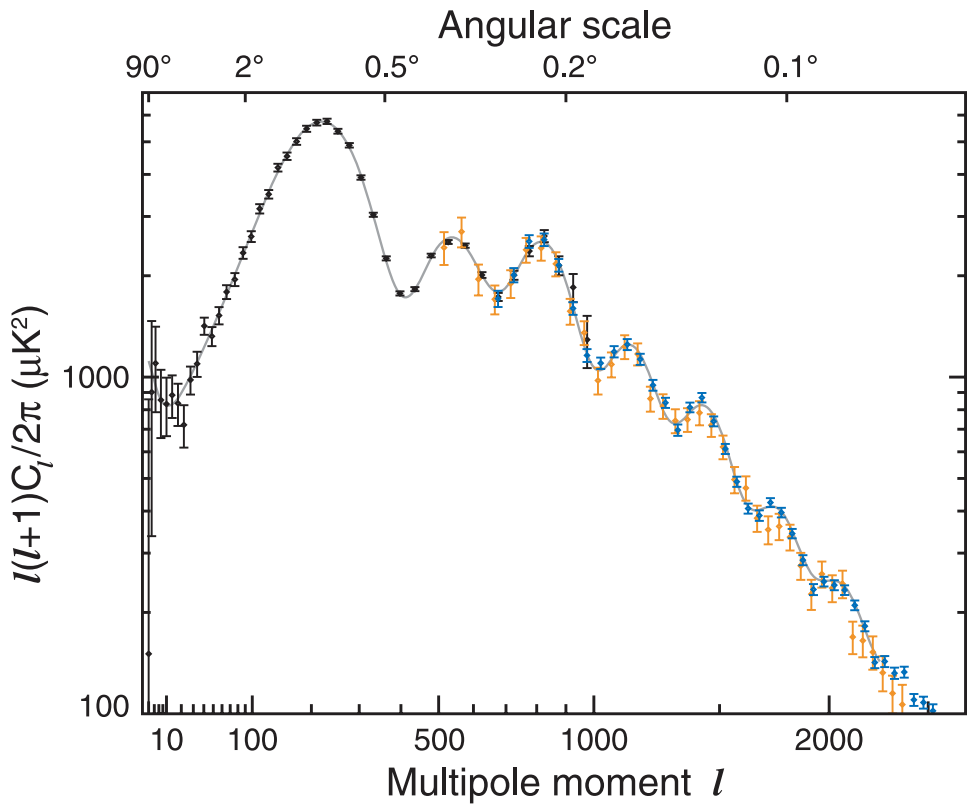

Figure 3.1: Shown are the current best measurements of the TT-power-spectrum multipoles, along with the best-fit curve, from WMAP-9 (black), SPT (blue), and ACT (orange) experiments (Figure from Ref. [25]).

electromagnetic wave of frequency ω_0, propagating along the z direction, are given as [3]

$$\begin{aligned} E_x &= a_x(t)\cos[\omega_0 t - \theta_x(t)] \\ E_y &= a_y(t)\cos[\omega_0 t - \theta_y(t)], \end{aligned} \tag{3.7}$$

in which case, (all four[6]) Stokes parameters are defined as the following time averages

$$\begin{aligned} I &\equiv \langle a_x^2 \rangle + \langle a_y^2 \rangle \\ Q &\equiv \langle a_x^2 \rangle - \langle a_y^2 \rangle \\ U &\equiv \langle a_x a_y \cos[\theta_x - \theta_y] \rangle \\ V &\equiv \langle a_x a_y \sin[\theta_x - \theta_y] \rangle . \end{aligned} \tag{3.8}$$

$Q(\hat{\mathbf{n}})$ and $U(\hat{\mathbf{n}})$ transform as components of a real, symmetric, and trace-free 2×2 tensor field

[6]Notice that I represents the intensity, or the temperature fluctuations; no circular polarization has so far been detected in the CMB, and V is usually assumed to vanish.

on a 2-sphere,

$$P(\hat{\mathbf{n}}) = \frac{1}{\sqrt{2}} \begin{pmatrix} Q(\hat{\mathbf{n}}) & -U(\hat{\mathbf{n}})\sin\theta \\ -U(\hat{\mathbf{n}})\sin\theta & -Q(\hat{\mathbf{n}})\sin^2\theta \end{pmatrix}, \tag{3.9}$$

which can be expanded in terms of *tensor spherical harmonics*, representing a complete orthonormal basis for tensor functions on a sphere, such that[7]

$$P_{ab}(\hat{\mathbf{n}}) = \sum_{\ell=2}^{\infty} \sum_{m=-\ell}^{\ell} [E_{\ell m} Y^E_{(\ell m)ab}(\hat{\mathbf{n}}) + B_{\ell m} Y^B_{(\ell m)ab}(\hat{\mathbf{n}})], \tag{3.10}$$

where we emphasize that there are two distinct components in this decomposition, $Y^E_{\ell m}$ and $Y^B_{\ell m}$, which can be expressed in terms of the usual (spin-zero) spherical harmonics,

$$Y^B_{(\ell m)ab} = \frac{1}{2}\sqrt{\frac{2(\ell-2)!}{(\ell+2)!}}(Y_{(\ell m):ac}\varepsilon^c{}_b + Y_{(\ell m):bc}\varepsilon^c{}_a), \tag{3.11}$$

$$Y^E_{(\ell m)ab} = \sqrt{\frac{2(\ell-2)!}{(\ell+2)!}}(Y_{(\ell m):ab} - \frac{1}{2}g_{ab}Y_{(\ell m):c}{}^c), \tag{3.12}$$

where a colon denotes a covariant derivative on a 2-sphere; g and ε are, respectively, the metric tensor and the Levi-Civita tensor on a unit 2-sphere, given by

$$g = \begin{pmatrix} 1 & 0 \\ 0 & \sin^2\theta \end{pmatrix}, \tag{3.13}$$

and

$$\varepsilon = \begin{pmatrix} 0 & \sin\theta \\ -\sin\theta & 0 \end{pmatrix}. \tag{3.14}$$

The corresponding orthonormality relations read

$$\begin{gathered} \int d\hat{\mathbf{n}}[Y^E_{(\ell m)ab}(\hat{\mathbf{n}})]^* Y^{E,ab}_{(\ell' m')}(\hat{\mathbf{n}}) = \int d[Y^B_{(\ell m)ab}(\hat{\mathbf{n}})]^* Y^{B,ab}_{(\ell' m')}(\hat{\mathbf{n}}) = \delta_{\ell\ell'}\delta_{mm'}, \\ \int d\hat{\mathbf{n}}[Y^E_{(\ell m)ab}(\hat{\mathbf{n}})]^* Y^{B,ab}_{(\ell' m')}(\hat{\mathbf{n}}) = 0. \end{gathered} \tag{3.15}$$

$E_{\ell m}$ and $B_{\ell m}$ are the E mode and the B mode tensor-spherical-harmonic coefficients, respectively. The E mode describes the gradient (curl-free) component of the polarization pattern in the sky (named in analogy with the electric field), while the B mode describes the curl component with a defined handedness (in analogy with the magnetic field); visualizations of both patterns are shown in Figure 3.2. Their power spectra (autocorrelations) are defined as usual,

[7] Notice that we sometimes separate multipole indices from the tensor indicies using parentheses, for clarity; we drop the parentheses when they are unnecessary.

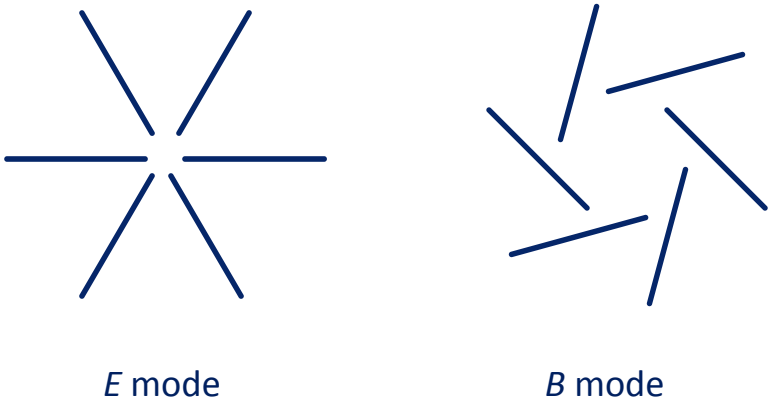

Figure 3.2: Shown are examples of elementary polarization patterns that represent a pure E mode, and a pure B mode. Notice that the E mode is parity-even, while the B mode, obtained by rotating the E mode by 45°, has handedness.

$$\begin{aligned} C_l^{EE}\delta_{\ell\ell'}\delta_{mm'} &\equiv \langle E_{\ell m}E^*_{\ell' m'}\rangle\,, \\ C_l^{BB}\delta_{\ell\ell'}\delta_{mm'} &\equiv \langle B_{\ell m}B^*_{\ell' m'}\rangle\,. \end{aligned} \tag{3.16}$$

We can also define cross-correlations between different modes, and between temperature and polarization,

$$\begin{aligned} C_l^{EB}\delta_{\ell\ell'}\delta_{mm'} &\equiv \langle E_{\ell m}B^*_{\ell' m'}\rangle\,, \\ C_l^{TE}\delta_{\ell\ell'}\delta_{mm'} &\equiv \langle T_{\ell m}E^*_{\ell' m'}\rangle\,, \\ C_l^{TB}\delta_{\ell\ell'}\delta_{mm'} &\equiv \langle T_{\ell m}B^*_{\ell' m'}\rangle\,. \end{aligned} \tag{3.17}$$

We show current state-of-the-art measurements of TE and EE power spectra, as well as the theoretical predictions, in Figures 3.3 and 3.4. Several remarks about these measurements are in order now. Firstly, most of the currently available polarization maps are noise dominated, including those from WMAP. However, that situation will drastically change when *Planck*, SPTPol, ACTPol, and similar experiments deliver the first sets of signal-dominated polarization data, demanding a careful reassessment of analyses applicable in the new regime. Secondly, currently measured cosmological signal consists solely of an E-mode pattern, while the measured B mode still comes from noise. The search for primordial B modes represents one of the "holy grails" of modern cosmology, but there are not, as of yet, precise predictions for the amplitude of this signal. The reason is the following: while the dominant scalar component to primordial fluctuations can give rise to E modes, primordial B modes are generated only by the inflationary gravitational waves, or tensor perturbations, whose amplitude directly depends on the unknown energy scale of inflation.

Should they be detected, they would present the first direct evidence that confirms the inflationary theory and opens a completely new avenue for exploring the physics of the very early Universe. Among secondary sources of the B-mode signal is also the weak gravitational lensing of the CMB by the intervening large-scale structure. It too is expected to be subdominant to the primordial E modes. Figure 3.4 compares the theoretical power spectra generated by different mechanisms.

For Gaussian theories, the six power spectra defined so far (TT, EE, BB, TE, TB, and EB) fully define statistical properties of a temperature and polarization map. However, since the parities of tensor spherical harmonics are $(-1)^\ell$ for $Y_{\ell m}$ and $Y^E_{\ell m}$, and $(-1)^{\ell+1}$ for $Y^B_{\ell m}$, the EB and TB cross-correlations should vanish, $C_\ell^{EB} = C_\ell^{TB} = 0$, as long as the physics that generated the CMB respects parity symmetry[8]. As we will see in Chapters 5 and 6, there are mechanisms that violate this symmetry, giving rise to parity-violating correlations in the CMB, and also to off-diagonal $\ell\ell'$ correlations—a form of non-Gaussianity which we use to test those scenarios.

There is a connection between tensor spherical harmonics and spin-weighted spherical harmonics, which we derive here by expressing the double derivatives in Eqs. (3.12) and (3.11) as [30]

$$Y_{(\ell m):ab} = -\frac{\ell(\ell+1)}{2} Y_{(\ell m)} g_{ab} + \frac{1}{2}\sqrt{\frac{(\ell+2)!}{(\ell-2)!}} [{}_2Y_{(\ell m)}(m_+ \otimes m_+) + {}_{-2}Y_{(\ell m)}(m_- \otimes m_-)]_{ab}, \tag{3.18}$$

where

$$m_\pm \equiv \frac{1}{\sqrt{2}}(\widehat{e}_\theta \mp i\widehat{e}_\varphi), \tag{3.19}$$

and the symbol $\otimes$ denotes a direct product, and the two unit (basis) vectors are

$$\widehat{e}_\theta \equiv \begin{pmatrix} 1 \\ 0 \end{pmatrix}, \qquad \widehat{e}_\varphi \equiv \begin{pmatrix} 0 \\ \sin\theta \end{pmatrix}. \tag{3.20}$$

This substitution leads to the following expressions[9]

$$Y^B_{(\ell m)} = \begin{pmatrix} \frac{i\sqrt{2}}{4}({}_{+2}Y - {}_{-2}Y) & \frac{\sqrt{2}}{4}\sin(\theta)({}_{-2}Y + {}_{+2}Y) \\ \frac{\sqrt{2}}{4}\sin(\theta)({}_{-2}Y + {}_{+2}Y) & \frac{i\sqrt{2}}{4}\sin^2(\theta)({}_{-2}Y - {}_{+2}Y) \end{pmatrix}, \tag{3.21}$$

$$Y^E_{(\ell m)} = \begin{pmatrix} \frac{\sqrt{2}}{4}({}_{+2}Y + {}_{-2}Y) & \frac{i\sqrt{2}}{4}\sin(\theta)({}_{-2}Y - {}_{+2}Y) \\ \frac{i\sqrt{2}}{4}\sin(\theta)({}_{-2}Y - {}_{+2}Y) & -\frac{\sqrt{2}}{4}\sin^2(\theta)({}_{-2}Y + {}_{+2}Y) \end{pmatrix}, \tag{3.22}$$

where the spin-s spherical harmonics are normalized as

$$\int d\widehat{\mathbf{n}}\, {}_sY_{(\ell m)}(\widehat{\mathbf{n}})\, {}_sY^*_{(\ell' m')}(\widehat{\mathbf{n}}) = \delta_{\ell\ell'}\delta_{mm'}. \tag{3.23}$$

[8] Parity transformation is $(\theta \to \pi - \theta,\ \varphi \to \pi + \varphi)$.
[9] We suppress (ℓm) indices for $Y_{\ell m}$'s in these formulas.

As an alternative to using the polarization tensor $P(\hat{\mathbf{n}})$, we will sometimes use the following polarization field

$$p(\hat{\mathbf{n}}) \equiv Q(\hat{\mathbf{n}}) + iU(\hat{\mathbf{n}}) = -\sum_{\ell m} (E_{\ell m} + iB_{\ell m})_2 Y_{\ell m}(\hat{\mathbf{n}}), \tag{3.24}$$

in terms of which the expressions for the E and B modes are

$$E_{\ell m} = \frac{1}{2} \int d\hat{\mathbf{n}} \left[p(\hat{\mathbf{n}})_2 Y^*_{\ell m}(\hat{\mathbf{n}}) + p^*(\hat{\mathbf{n}})_{-2} Y^*_{\ell m}(\hat{\mathbf{n}}) \right] \tag{3.25}$$

and

$$B_{\ell m} = \frac{1}{2i} \int d\hat{\mathbf{n}} \left[p(\hat{\mathbf{n}})_2 Y^*_{\ell m}(\hat{\mathbf{n}}) - p^*(\hat{\mathbf{n}})_{-2} Y^*_{\ell m}(\hat{\mathbf{n}}) \right], \tag{3.26}$$

where we used the following property of the spin-weighted spherical harmonics

$${}_s Y^*_{\ell m} = (-1)^{s+m} {}_{-s} Y_{\ell -m}. \tag{3.27}$$

Note that the E and B modes satisfy the same reality condition of Eq. (3.6) as the temperature multipoles.

3.3 From Maps to Power Spectra

This section describes analytically the calculational road from the CMB temperature and polarization maps to the estimates of the cosmological signal, i.e., the power spectra. Most of this procedure we demonstrate for the case of temperature, but it is readily applicable to the polarization as well. Before we begin, let us first define our notation; the same notation will be used in Chapters 5, 7, and 8, which deal with theoretical considerations related to cosmic birefringence, while a slightly modified notation will be employed when we turn to data analysis in Chapter 6; we point out these changes in the text.

Multipole-coefficient and map symbols X and X' stand for either T, E, or B, such that $X, X' \in \{T, E, B\}$, and $XX' \in \{TT, EE, BB, TE, TB, EB\}$. Absence of a superscript denotes the (theoretical) cosmological signal, either in pixel space, or in harmonic space, uncontaminated by the noise (of instrumental, or astrophysical origin), while the superscript "map" denotes multipoles recovered from a map which include the noise, where the contributions to the noise considered in different problems are clearly specified in the text. An overhat symbol denotes an *estimator*, approximating (but distinct from) a theoretical value. The theoretical power spectra we use are calculated with CMBFAST, or CAMB.

We start by noting that multipole coefficients are reconstructed from a map as

$$T_{\ell m}^{\rm map} = \int d\widehat{\mathbf{n}} T(\widehat{\mathbf{n}}) Y_{\ell m}^*(\widehat{\mathbf{n}}) \approx \frac{4\pi}{N_{\rm pix}} \sum_{i=1}^{N_{\rm pix}} T_i^{\rm map}(\widehat{\mathbf{n}}_i) Y_{\ell m}^*(\widehat{\mathbf{n}}_i), \tag{3.28}$$

where $N_{\rm pix}$ is the total number of pixels in the map, and $T_i^{\rm map}(\widehat{\mathbf{n}}_i)$ is the temperature measured in pixel i in the direction $\widehat{\mathbf{n}}_i$. In theory, any power spectrum is calculated by taking a mean over the ensemble of all possible realizations of the CMB sky, such as those in Eqs. (3.4), (3.16), and (3.17). In practice, we only observe one sky, so the power spectrum is typically *estimated* from multipole coefficients recovered from a map, assuming isotropy (independence on m), and taking the mean over all m modes for a given ℓ, as

$$\widehat{C}_\ell^{TT,{\rm map}} \equiv \frac{1}{2\ell+1} \sum_m T_{\ell m}^{\rm map} T_{\ell' m'}^{{\rm map},\,*}. \tag{3.29}$$

This procedure limits the accuracy of the measurement of C_ℓ's due to a sample variance called *cosmic variance*. Cosmic variance affects most severely the measurements at large angular scales, corresponding to low ℓ multipoles, where a small number of m modes is available at each ℓ (the number of m modes is $2\ell+1$).

In addition to the cosmic-variance limitation, instrumental noise and resolution are also sources of uncertainty in measuring the power spectra[10]. Even though a faithful description of these effects, which we generically refer to as the "noise", is complex and more amenable to simulations than analytic description, it is instructive to understand approximate scaling with key instrumental parameters in the idealized case where the noise can be described fully by a noise power spectrum. We demonstrate this for temperature, but emphasize that the entire calculation is analogous in the case of polarization.

We start by assuming that $T_i^{\rm map}$ and $T_{\ell m}^{\rm map}$ include the cosmological signal, plus noise, such that

$$T_{\ell m}^{\rm map} = T_{\ell m} W_\ell + T_{\ell m}^{\rm noise}, \tag{3.30}$$

where the beam transfer function (or the window function) W_ℓ accounts for the beam smearing, and is usually approximated by a (symmetric) Gaussian as

$$W_\ell \approx \exp^{-l^2\sigma_b^2/2}, \tag{3.31}$$

[10]There are additional contributions that fold into the measurement of multipoles in temperature and polarization and should be accounted for when extracting cosmological signals. These come, for example, from sky cuts, Galactic and extragalactic foregrounds, foreground residuals, instrumental systematics, etc. We address some of these in more detail when we present the analysis of WMAP data, in Chapter 6.

where

$$\sigma_b = \theta_{\rm FWHM}/\sqrt{8\ln 2}, \tag{3.32}$$

and $\theta_{\rm FWHM}$ is the beam full width at half maximum, in radians. In the case of homogeneous Gaussian noise (where every pixel has the same noise variance σ_T^2), uncorrelated to the signal,

$$\left\langle T_i T_j^{\rm noise} \right\rangle = 0, \tag{3.33}$$

and in the absence of pixel-noise correlations,

$$\left\langle T_i^{\rm noise} T_j^{\rm noise} \right\rangle = \sigma_T^2 \delta_{ij}, \tag{3.34}$$

where the noise in polarization is uncorrelated with the noise in temperature, we get

$$\begin{aligned} C_\ell^{TT,{\rm map}} \delta_{\ell\ell'}\delta_{mm'} &\equiv \left\langle T_{\ell m}^{\rm map} T_{\ell' m'}^{{\rm map},\,*} \right\rangle \\ = |W_\ell|^2 \left\langle T_{\ell m} T_{\ell' m'}^* \right\rangle + \left\langle T_{\ell m}^{\rm noise} T_{\ell' m'}^{{\rm noise},\,*} \right\rangle &= \left(|W_\ell|^2 C_\ell^{TT} + C_\ell^{TT,{\rm noise}} \right) \delta_{\ell\ell'}\delta_{mm'}, \end{aligned} \tag{3.35}$$

where we define

$$C_\ell^{TT,{\rm noise}} \equiv \frac{4\pi\sigma_T^2}{N_{\rm pix}}. \tag{3.36}$$

Note that we used Eq. (3.28) for the noise map, and the orthonormality relation for spherical harmonics to arrive at these expressions. The last ingredient to keep in mind is that the pixel-noise variance for polarization is roughly twice that for the temperature,

$$\sigma_E^2 = \sigma_B^2 = 2\sigma_T^2. \tag{3.37}$$

A word of caution on the notation here: some of the "map" power spectra are also denoted by the estimator sign (overhat), while some of them are not. The distinction between them is this: those that bear the overhat sign denote the power estimated from a map, using Eq. (3.29), while those that do not have an overhat are calculated by adding the theoretical signal to the analytic description of the noise, and taking the mean over all sky realizations, as in Eq. (3.35). The first is the power truly calculated from the maps, while the second procedure is a way to *analytically* represent it, where the relation between the two is

$$C_\ell^{TT,{\rm map}} = \left\langle \widehat{C}_\ell^{TT,{\rm map}} \right\rangle. \tag{3.38}$$

Similarly, if the estimator for the power spectrum is *unbiased*, than the following holds

$$C_\ell^{TT} = \left\langle \widehat{C}_\ell^{TT} \right\rangle. \tag{3.39}$$

Once we measure the power spectrum from a temperature/polarization map, we can estimate the cosmological signal as

$$\widehat{C}_\ell^{XX'} = \left(\widehat{C}_\ell^{XX',\mathrm{map}} - C_\ell^{XX',\mathrm{noise}}\right) |W_\ell|^{-2} \,. \tag{3.40}$$

Since there are six power spectra, the uncertainty of this measurement is represented by a 6×6 covariance matrix $\Xi_{AA'}$, where $A \equiv XX'$. This matrix is not diagonal ($\Xi_{AA'} \neq 0$, for $A \neq A'$), since only three multipoles X are used to reconstruct six power spectra. The covariance-matrix elements can be derived starting from its definition and combining the above formulas, as

$$\begin{aligned}
\Xi^\ell_{X_{(1)}X_{(2)},X_{(3)}X_{(4)}} &\equiv \left\langle \left(\widehat{C}_\ell^{X_{(1)}X_{(2)}} - C_\ell^{X_{(1)}X_{(2)}}\right)\left(\widehat{C}_\ell^{X_{(3)}X_{(4)}} - C_\ell^{X_{(3)}X_{(4)}}\right)\right\rangle \\
&= \left(\left\langle \widehat{C}_\ell^{X_{(1)}X_{(2)},\mathrm{map}}\widehat{C}_\ell^{X_{(3)}X_{(4)},\mathrm{map}}\right\rangle - C_\ell^{X_{(1)}X_{(2)},\mathrm{map}}C_\ell^{X_{(3)}X_{(4)},\mathrm{map}}\right)|W_\ell|^{-4} \\
&= |W_\ell|^{-4}\left(\sum_{mm'} \frac{\left\langle X_{(1)\ell m}{}^* X_{(2)\ell' m'} X_{(3)\ell m}{}^* X_{(4)\ell' m'}\right\rangle}{(2\ell+1)^2} - \left\langle X_{(1)\ell m}{}^* X_{(2)\ell' m'}\right\rangle\left\langle X_{(3)\ell m}{}^* X_{(4)\ell' m'}\right\rangle\right) \\
&= \frac{|W_\ell|^{-4}}{(2\ell+1)}\left(\left\langle X_{(1)\ell m}{}^* X_{(3)\ell' m'}\right\rangle\left\langle X_{(2)\ell m}{}^* X_{(4)\ell' m'}\right\rangle + \left\langle X_{(1)\ell m}{}^* X_{(4)\ell' m'}\right\rangle\left\langle X_{(2)\ell m}{}^* X_{(3)\ell' m'}\right\rangle\right) \\
&= \frac{1}{(2\ell+1)}|W_\ell|^{-4}(C_\ell^{X_1X_3,\mathrm{map}}C_\ell^{X_2X_4,\mathrm{map}} + C_\ell^{X_1X_4,\mathrm{map}}C_\ell^{X_2X_3,\mathrm{map}}),
\end{aligned} \tag{3.41}$$

where all multipoles X have superscript "map", which we suppress for clarity. Diagonal components of this matrix approximately provide the variance with which TT, EE, and BB power spectra can be measured,

$$\Xi^\ell_{XX,XX} = \frac{2}{2\ell+1}\left(C_\ell^{XX,\mathrm{map}}\,|W_\ell|^{-2}\right)^2 . \tag{3.42}$$

One more remark about the notation. The two main differences between the notation conventions introduced here and used in all theoretical considerations of this work, and the notation used in the data-analysis portion of this thesis (presented in Chapter 6 and Section 9.1) are the following: 1) in data analysis, the power spectra and multipoles denoted with "map" have already been corrected for the effects of instrumental resolution, i.e., the window function has been divided out; what we call the "noise" will then also have been divided by the square of the window function, and 2) the noise in theoretical derivations is represented by a power spectrum that arises in a simplified model of instrumental noise and instrumental resolution, while in data analysis, the noise model we consider is typically more complicated and cannot be represented analytically.

With this, we conclude the introductory overview of the CMB physics and analysis formalisms and move on to the core subject of this thesis by addressing various physical problems, using the CMB as the main tool.

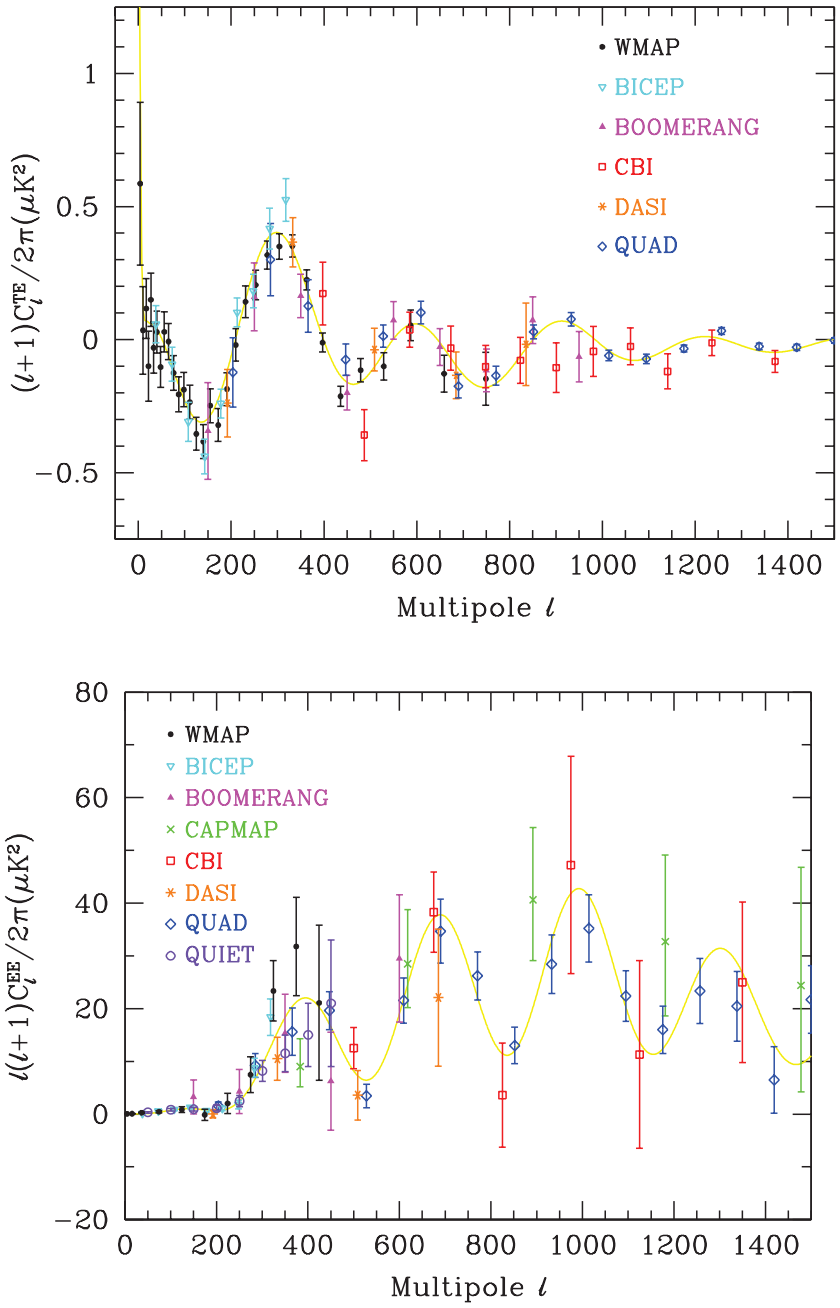

Figure 3.3: Measurements (and best fits) of the TE and EE power spectra from WMAP (black dots), and a number of other CMB experiments (colored symbols); note the unusual normalization of the y-axis in the top panel, chosen so that both low-ℓ and high-ℓ features are visible (plots from Ref. [2]).

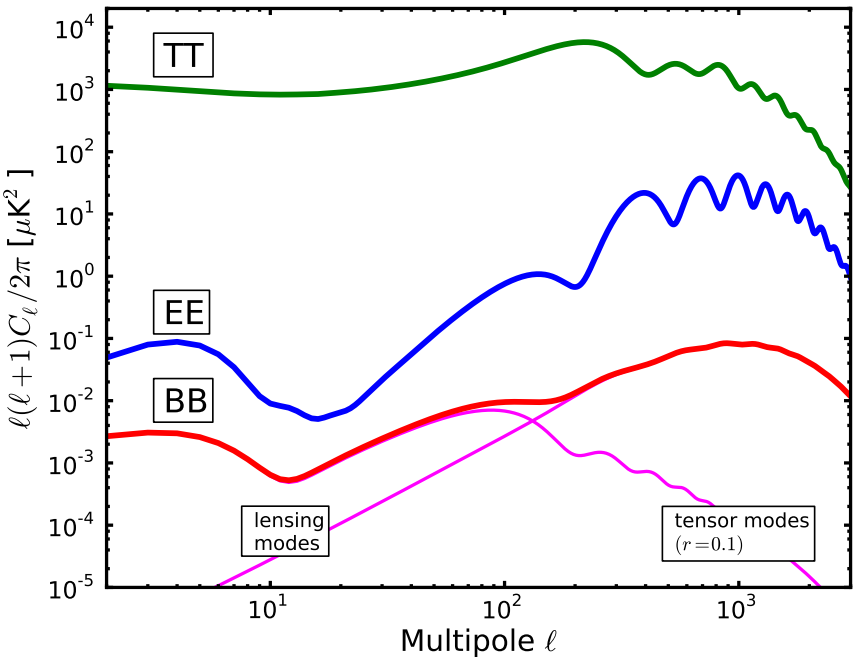

Figure 3.4: Theoretical power spectra, calculated with CAMB using the best-fit WMAP-7 cosmology. The contribution to BB is shown from both weak lensing and primordial gravitational waves (tensor modes), calculated for tensor-to-scalar ratio $r = 0.1$, which is close to its current upper limit. From the amplitude of the signals, it is clear why detection of temperature fluctuations came before the detection of polarization fluctuations, and also why the search for B modes represents such a challenge in a regime where the E modes are still noise dominated. The normalization of C_ℓ's in this figure is adopted as the standard for plotting the power spectra, as it creates a quantity that has the same variance in every $log(\ell)$ interval, and also clearly displays the Sachs-Wolfe plateau for the temperature.

Part III

Testing New Physics: Cosmic Birefringence

This part of the thesis studies CMB signatures of physics beyond the standard models of cosmology and particle physics. We are in particular concerned with the effect of *cosmic birefringence*—a postulated frequency-independent rotation of the plane of polarization of photons that propagate through the Universe [31].

We first review physical scenarios that give rise to cosmic birefringence, motivating the search for direction-dependent (anisotropic) rotation $\alpha(\hat{\mathbf{n}})$ (where $\hat{\mathbf{n}}$ is a direction in the sky) using CMB data sets, and summarize related previous work, in Chapter 4. In Chapter 5, we develop a full-sky formalism for measuring $\alpha(\hat{\mathbf{n}})$ with temperature and polarization maps of the CMB, draw the distinction between rotation and weak lensing of the CMB, and forecast the sensitivity of upcoming and next-generation CMB experiments. In Chapter 6, we revisit previous constraints on the uniform rotation angle, test the validity regime of our formalism using a suite of simulated CMB realizations including the instrumental response, and then perform an optimized analysis of WMAP data to look for the presence of direction-dependent rotation in the sky, evaluating statistical uncertainty and the impact of systematic effects. These measurements provide the first constraint on the rotation-angle power spectrum $C_\ell^{\alpha\alpha}$ down to multipoles corresponding to the resolution of the instrument. We discuss implications of these constraints for quintessence models of dark energy. In Chapter 7, we propose a cross-correlation of the rotation angle with CMB temperature as a new statistical tool to boost signal-to-noise, and help distinguish underlying physical scenarios, in case of detection with future data. Finally, in Chapter 8, we place the effect of cosmic birefringence in the context of other parity-violating physics, in particular chiral gravitational waves from inflation, and explore how accurately the two effects can be distinguished in case the parity-violating EB/TB power spectra are measured in CMB maps.

Chapter 4

Motivation, Phenomenology, and Previous Results

In this chapter, we review the physics behind cosmic birefringence and motivate the search for its anisotropic-rotation signature in full-sky CMB maps, and summarize previous results.

Let us consider an extension of the Standard Model of particles that includes a new scalar degree of freedom ϕ, which has a potential $V(\phi)$ and a cannonical kinetic term in the Lagrangian,

$$\mathscr{L}_\phi = -\frac{1}{2}(\partial_\mu\phi)(\partial^\mu\phi) - V(\phi), \tag{4.1}$$

Its equation-of-state parameter, defined as the ratio of pressure p_ϕ to energy density ρ_ϕ, takes on the following form[1]

$$w_\phi \equiv p_\phi/\rho_\phi = \frac{\frac{1}{2a^2}\dot{\phi}^2 - V(\phi)}{\frac{1}{2a^2}\dot{\phi}^2 + V(\phi)} \tag{4.2}$$

where dots represent derivatives with respect to conformal time, and a is the cosmological scale factor. If the kinetic energy is negligible in comparison to the potential, or, in other words, if the field has slow time evolution, it is said to exhibit *slow roll*, and then we get

$$w \to -1, \qquad \text{for } \dot{\phi} \to 0. \tag{4.3}$$

If such field happens to dominate the energy budget of the Universe, it will drive accelerated expansion. There have been at least two instances in the history of our Universe when acceleration has occurred: one was at very early times, during inflation [32], and the other is the late-time acceleration observed today [33, 34]. Late-time acceleration is ascribed to the dark-energy component that makes about 70% of the energy density in the Universe today, and is measured to have $\omega_{DE} \approx -1$ (within a few-percent measurement error; see [35]). The physical nature of this component is yet

[1] Remember that the energy density is the first entry of the stress-energy tensor corresponding to this field, and the pressure corresponds to each of the elements on the main diagonal; the stress-energy tensor is obtained by taking the derivative of the Lagrangian density of Eq. (4.1) with respect to the metric: $T^{\mu\nu} \equiv \frac{2}{\sqrt{-g}}\frac{\delta(\mathscr{L}_\phi\sqrt{-g})}{\delta g_{\mu\nu}}$.

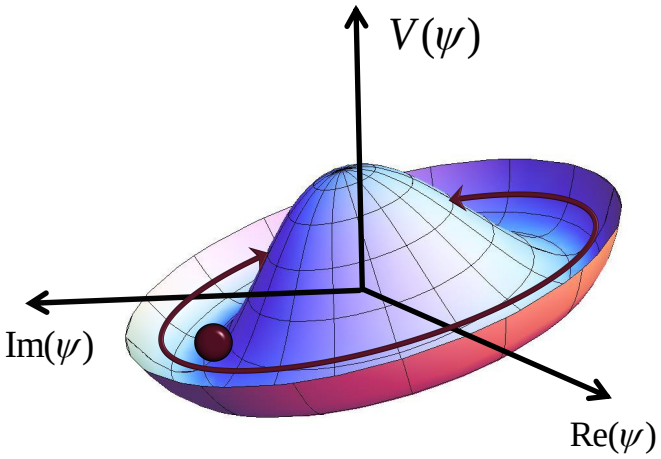

Figure 4.1: We show the potential for the PNGB, given by Eq. (4.4). The mode that goes around the rim of this "Mexican-hat" potential is the PNGB. In this case, the hat is tilted, i.e., the global symmetry is explicitly broken (not exact), so the field acquires a mass. The potential descends from a complete theory that includes a complex scalar ψ.

unknown, but the most popular models include vacuum energy, or *cosmological constant*; modified gravity; and a slowly evolving scalar field, or *quintessence* [36]. If we investigate the third option, the first step is to find a good candidate for quintessence.

Quantum field theories with explicitly (weakly) broken global $U(1)$ symmetry necessarily give rise to pseudo Nambu-Goldstone bosons (PNGB), with a shallow potential (see, e.g., [37]) of the following form

$$V = m^4[1 - \cos(\phi/f)], \tag{4.4}$$

where f is a parameter of the theory. If the symmetry is exact, the field is massless, but if it is weakly broken, the field acquires a small mass m (see Figure 4.1). From a cosmological perspective, a (scalar) PNGB field with this property is a natural candidate for quintessence, since it can drive epochs of accelerated expansion [31]. In addition, many other extensions of the Standard Model of particle physics abound in scalar fields resembling the PNGB, and have nothing to do with quintessence. Cosmic birefringence appears as a generic feature in both of these cases, as a consequence of the Chern-Simons coupling between a PNGB field and electromagnetism. The relevant part of the electromagnetic Lagrangian in this case reads

$$\mathscr{L}_{EM} = -\frac{\beta\phi}{2M} F^{\mu\nu}\widetilde{F}_{\mu\nu} - \frac{1}{4}F^{\mu\nu}F_{\mu\nu}, \tag{4.5}$$

where

$$\widetilde{F}_{\mu\nu} \equiv \epsilon_{\mu\nu\rho\sigma} F^{\rho\sigma}/2 \tag{4.6}$$

is the dual of the electromagnetic field-strength tensor ($F\widetilde{F}$ is often called the *pseudo scalar of electromagnetism*), $\epsilon_{\mu\nu\rho\sigma}$ is the Levi-Civita tensor (totally antisymmetric), and M is a parameter with dimensions of mass. If ϕ is a PNGB, then M is the vacuum expectation value for the broken global symmetry, and β is a coupling [31,38] (see Figure 4.1). There are therefore "natural" candidate scalar fields for dark energy that arise in particle physics (introduced for reasons that have nothing to do with explaining accelerated expansion of the Universe). On the other hand, these fields, such as the PNGB, generically couple to the pseudo scalar of electromagnetism and give rise to cosmic birefringence through the mechanism described below.

The electromagnetic Lagrangian of Eq. (4.5) introduces a modification to the standard Maxwell's equations (see Appendix B for derivation), which results in different dispersion relations for left- and right-circularly polarized photons. Consequently, linearly polarized electromagnetic waves that propagate over cosmological distances undergo cosmic birefringence[2]—a frequency-independent rotation of the plane of polarization by an angle α, where [39]

$$\alpha = \frac{\beta}{M} \int d\tau \left(\frac{\partial}{\partial \tau} - \hat{\mathbf{n}} \cdot \vec{\nabla} \right) \phi = \frac{\beta}{M} \Delta\phi, \tag{4.7}$$

with $\Delta\phi$ being the change in ϕ over the photon trajectory, and τ being the conformal time. For the CMB, the polarization rotation is determined by the change in ϕ since recombination, when the CMB polarization pattern was largely established. See Figure 4.2 for an illustration of this effect.

There is an additional appeal associated with quintessence scenarios with cosmic birefringence. Namely, if we consider a new degree of freedom, we may rightfully be concerned that its other couplings might already forbid its existence, due to strong accelerator constraints on the Standard Model phenomenology—unless there is a symmetry requirement that suppresses these couplings. Ref. [31] has shown that, if *shift symmetry* is required, whereby the action is invariant under the following transformation

$$\phi \to \phi + \text{const}, \tag{4.8}$$

then the only allowed dimension-5 coupling of this scalar to the Standard Model is represented by the Chern-Simons term of Eq. (4.5). Because of the suppression of other interaction terms due to shift symmetry, the new degree of freedom ϕ could thus evade detection in colliders and other lab experiments, but could still be manifest in cosmology through the effect of cosmic birefringence.[3]

[2] In a sense, this effect is similar to birefringence in crystals, and thus the name: it is a birefringence of light in a polarized vacuum with an evolving quintessence.

[3] Let us emphasize here that the field that is the subject of this discussion is *not* an axion field, even though they share some characteristics, such as the existence of the Chern-Simons coupling; laboratory constraints on axions, such as those of PVLAS experiment [40], apply to much more massive fields than the quintessence, which is usually expected to have $m \sim 10^{-33}$eV, or so.

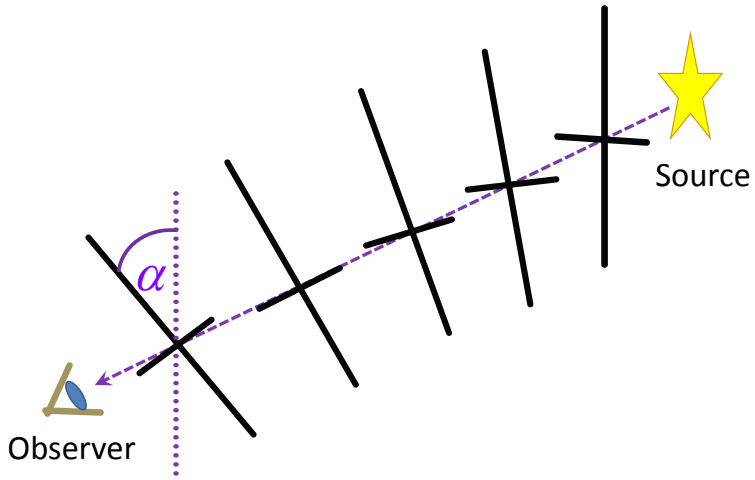

Figure 4.2: This figure illustrates the effect of cosmic birefringence, where polarization at the source is represented by a vertical line on the very right; the direction of polarization progressively changes along the photons' path, so that, by the time they reach the observer, the polarization is rotated by the angle α, proportional to the total change in the field $\Delta\phi$ along the line of sight.

On the other hand, the simplest way to ensure a sustained slow roll for quintessence is precisely to require that $V(\phi)$ respects (approximate) shift symmetry, such as the case for PNGB.

Summarizing what we have stated so far: cosmic birefringence arises generically in quintessence models, and could thus provide one of the preciously rare avenues for testing the microphysics of dark energy; more generally, it is a feature of models that simply include new scalar degrees of freedom, regardless of their time evolution or cosmological role[4].

To search for this effect, we need to identify a polarized source at a cosmological distance; we also need to know the description of its polarization field at the source, so we can compare it with what we observe today. The reason to use a source at a cosmological distance is that the mass-suppression scale M is expected to be large, around the Planck mass,

$$M \approx M_{\rm Pl}, \tag{4.9}$$

corresponding to the energy scale of the new high-energy physics underlying the effective field theory represented by Eq. (4.5).[5]

One of the cosmological sources that has previously been used to look for cosmic birefringence are

[4]Another interesting example is the birefringence that appears in some exotic models for dark matter [41], which we do not explicitly consider here.

[5]This Chern-Simons term is a non-renormalizable term of an effective field theory, expected to descend from a more complete description at high energies.

active galactic nuclei (AGN). For example, Ref. [42] used measurements of the ultraviolet polarization of eight distant radio galaxies distributed across the sky to constrain uniform rotation to

$$\alpha \lesssim 2.2^\circ, \tag{4.10}$$

and Ref. [43] used the same data set to also provide an upper limit on the root-mean-square (RMS) rotation on the sky,

$$\langle \alpha^2 \rangle \lesssim 3.7^\circ. \tag{4.11}$$

Additionally, a detailed understanding of the statistical description of its primordial fluctuations and the largest available lookback time of any other cosmological sources make the CMB a leading background-source candidate to look for cosmic birefringence. The sensitivity of WMAP data to uniform-rotation signal is already similar to AGN—the best current constraint comes from a combined analysis of the WMAP, Bicep [44], and QUAD [45] experiments,

$$-1.4^\circ < \alpha < 0.9^\circ, \tag{4.12}$$

at the 95% confidence level [46]. However, in the case of anisotropic (direction-dependent) rotation, the AGN measurements can only constrain the variance, while the CMB data allow for the reconstruction of individual multipoles of the rotation-angle power spectrum, $C_\ell^{\alpha\alpha}$—which is one of the goals of the work presented in this thesis.

Previous work has thus mostly focused on a special case of a uniform field in the sky, where the rotation angle is the same in every direction. However, if it is driven by a dynamical cosmic scalar ϕ, then ϕ may have spatial fluctuations which would drive anisotropies in the rotation angle,

$$\Delta\alpha(\hat{\mathbf{n}}) = (\beta/M)\delta\phi(\hat{\mathbf{n}}), \tag{4.13}$$

where fluctuations $\delta\phi(\hat{\mathbf{n}})$ are evaluated at recombination. The power spectrum $C_\ell^{\alpha\alpha}$ can be calculated for any model, given the potential $V(\phi)$, using the equations of motion for the fluctuations in ϕ, and projecting them on the sky. This procedure is presented in more detail for a couple of specific models of rotation in Subsections 7.1.1 and 7.1.2. A measurement of the shape of $C_\ell^{\alpha\alpha}$ can thus provide a window into detailed physics of the new cosmic scalar field. Therefore, measuring fluctuations in the rotation angle across the sky is a general quest that goes beyond constraints on a uniform-rotation signal, and can directly probe spatial fluctuations of a cosmic scalar field ϕ. Additionally, higher-multipole measurements can help boost signal-to-noise for detection (see Section 6.6), and can also be the only avenue to look for the signal if there is no monopole (or no uniform rotation), which is the case for a massless field (see Subsection 7.1.1).

We end with a few words to motivate our choice of full-sky analysis to look for $\alpha(\widehat{\mathbf{n}})$. While a flat-sky analysis may be suitable if the rotation-angle power spectrum peaks at small scales, the full-sky formalism will be required to maximize the sensitivity in models such as that in Ref. [47], where the signal-to-noise peaks at low multipoles. There has also been growing attention recently to the possibility of variations in fundamental fields (perhaps remnants of the pre-inflationary Universe) over distance scales comparable to, or larger than, the horizon [48,49]. Observationally, these entail searches for departures from homogeneity/isotropy or departures from statistical homogeneity/isotropy in the CMB or large-scale structure [50]. The full-sky formalism we turn to in Chapter 5 is exact, and can be used to search for the low multipole (e.g., $\ell = 1, 2, 3, \cdots$) moments of $\alpha(\widehat{\mathbf{n}})$ that may arise if ϕ has long-wavelength fluctuations, in addition to, or instead of, the higher-ℓ modes that can also be probed with a survey of a smaller region of the sky[6]. We therefore focus in this thesis on reconstructing the $C_\ell^{\alpha\alpha}$ power spectrum at all scales down to the resolution of the best full-sky CMB data sets available today.

[6]Note that the full-sky formalism is exact, but not necessarily computationally more demanding than the flat-sky calculations.

Chapter 5

Theoretical Considerations

This chapter deals with the formalism and other theoretical considerations related to the search for cosmic birefringence, and similar physical scenarios, using the CMB. It is organized as follows. In Section 5.1, we derive CMB correlations induced or altered by direction-dependent rotation of the CMB polarization pattern. Section 5.2 presents a complete set of minimum-variance estimators for the rotation-angle multipole coefficients, constructed from four temperature-polarization cross-correlations that can be measured in full-sky CMB maps, as well as their variances. In Section 5.3, we show how the signals from rotation and the weak gravitational lensing from the large-scale structure can be geometrically distinguished, and argue that the lensing signal should not bias the rotation measurements. In Section 5.4, we use the full-sky estimator formalism to forecast sensitivity of current, upcoming, and the next-generation satellite experiments. Finally, we conclude and summarize in Section 5.5.

5.1 Effect of Rotation on the CMB Correlations

We now derive the correlations in the CMB maps induced by a post-recombination anisotropic rotation $\alpha(\hat{\mathbf{n}})$ of the polarization, to first order in α. To do this, we first derive the expressions for the rotation-induced E and B modes, noting that the temperature field is not affected. The derivation presented here does not rely on any particular model for the rotation field in the sky, nor does it depend on the physical causes for rotation, making this formalism directly applicable to investigating physical scenarios beyond just cosmic birefringence.

Let us suppose that the polarization at the surface of last scatter is a pure E mode (we re-evaluate this assumption below). If so, a small rotation $\alpha(\hat{\mathbf{n}})$ induces the following change to the polarization tensor

$$\delta P_{ab}(\hat{\mathbf{n}}) = 2\alpha(\hat{\mathbf{n}}) P^r_{ab}(\hat{\mathbf{n}}), \tag{5.1}$$

Material in this chapter was largely adapted from "Derotation of the cosmic microwave background polarization: Full-sky formalism," Vera Gluscevic, Marc Kamionkowski, and Asantha Cooray, *Phys. Rev. D* **80**, 023510 (2009) [4]. Reproduced here with permission,

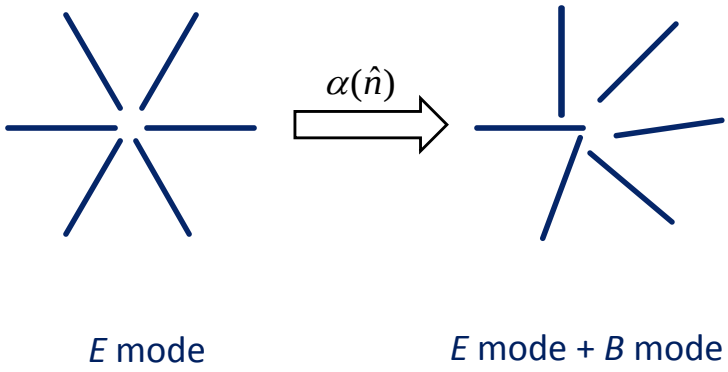

Figure 5.1: This figure illustrates the effect of rotation of a pure E-mode polarization, by an arbitrary amount in every point in the sky. Notice that the resulting polarization pattern is a combination of an E mode and a B mode.

where [51]

$$P^r_{ab}(\hat{\mathbf{n}}) = \sum_{l=2}^{\infty} \sum_{m=-\ell}^{\ell} E_{\ell m} Y^B_{(\ell m)ab}(\hat{\mathbf{n}}). \tag{5.2}$$

A pure E mode thus gets rotated into a B mode, where the presence of this B mode becomes one of the characteristic signatures of rotation (see Figure 5.1 for illustration). Note that Eq. (5.2) is valid only in the limit of small angles, $\alpha(\hat{\mathbf{n}}) \ll 1$. Given that, the B mode will be small compared to the E mode, which satisfies existing empirical constraints. Since the primordial B mode is also constrained to be much smaller than the primordial E mode, and so is the B-mode signal induced by the weak gravitational lensing, the assumption we made about a pure E mode holds well, to first order. Considerations of the higher-order effects are beyond the scope of this work.

Just like the temperature, rotation is also a scalar field in the sky, and can thus be expanded in terms of spherical harmonics,

$$\alpha(\hat{\mathbf{n}}) = \sum_{LM} \alpha_{LM} Y_{LM}(\hat{\mathbf{n}}), \tag{5.3}$$

where α_{LM} are the coefficients of the expansion. Now, using Eqs. (5.1), (5.2), and (5.3), the B mode induced by a small rotation angle from a pure E mode can be expressed as[1]

$$\delta B_{\ell m} = \int d\hat{\mathbf{n}} \delta P_{ab}(\hat{\mathbf{n}}) Y^{B*,ab}_{(\ell m)}(\hat{\mathbf{n}}) = 2 \sum_{LM} \sum_{\ell_2 m_2} \alpha_{LM} E_{\ell_2 m_2} \int d\hat{\mathbf{n}} Y^{B*,ab}_{(\ell m)} Y_{(LM)} Y^B_{(\ell_2 m_2)ab}. \tag{5.4}$$

[1]Notice that we drop explicit dependence on $(\hat{\mathbf{n}})$ in triple-Y integrals, for clarity of the expressions.

Similarly, the induced E mode is

$$\delta E_{\ell m} = \int d\widehat{\mathbf{n}} \delta P_{ab}(\widehat{\mathbf{n}}) Y^{E*,ab}_{(\ell m)}(\widehat{\mathbf{n}}) = 2 \sum_{LM} \sum_{\ell_2 m_2} \alpha_{LM} E_{\ell_2 m_2} \int d\widehat{\mathbf{n}} Y^{E*,ab}_{(\ell m)} Y_{(LM)} Y^{B}_{(\ell_2 m_2) ab}. \tag{5.5}$$

Using Eqs. (3.22) and (3.21), we further obtain

$$Y^{B*,ab}_{(\ell m)} Y^{B}_{(\ell_2 m_2) ab} = \frac{1}{2} ({}_{-2}Y^{*}_{(\ell m)} \times_{-2} Y_{(\ell_2 m_2)} +_{+2} Y^{*}_{(\ell m)} \times_{+2} Y_{(\ell_2 m_2)}), \tag{5.6}$$

and

$$Y^{E*,ab}_{(\ell m)} Y^{B}_{(\ell_2 m_2) ab} = \frac{i}{2} ({}_{+2}Y^{*}_{(\ell m)} \times_{+2} Y_{(\ell_2 m_2)} -_{-2} Y^{*}_{(\ell m)} \times_{-2} Y_{(\ell_2 m_2)}). \tag{5.7}$$

The next step is to use this result in order to rewrite the integrals in Eqs. (5.4) and (5.5) in terms of Wigner 3j symbols. To do that, we need the relation between spin-weighted spherical harmonics and Wigner 3j symbols [30],

$$\begin{aligned} &\int d\hat{n}\, {}_{s_1}Y^{*}_{\ell_1 m_1}(\widehat{\mathbf{n}})\, {}_{s_2}Y_{\ell_2 m_2}(\widehat{\mathbf{n}})\, {}_{s_3}Y_{\ell_3 m_3}(\widehat{\mathbf{n}}) \\ &= (-1)^{m_1+s_1} \sqrt{\frac{(2\ell_1+1)(2\ell_2+1)(2\ell_3+1)}{4\pi}} \begin{pmatrix} \ell_1 & \ell_2 & \ell_3 \\ -m_1 & m_2 & m_3 \end{pmatrix} \begin{pmatrix} \ell_1 & \ell_2 & \ell_3 \\ s_1 & -s_2 & -s_3 \end{pmatrix}. \end{aligned} \tag{5.8}$$

Noting that the spin-spherical harmonics of zero spin are the regular spherical harmonics,

$${}_0Y_{(\ell m)} \equiv Y_{(\ell m)}, \tag{5.9}$$

let us first look at the case of the induced B mode, where we have

$$\begin{aligned} &\int d\hat{n} Y^{B*,ab}_{(\ell m)} Y_{(LM)} Y^{B}_{(\ell_2 m_2) ab} \\ &= \frac{1}{2}(-1)^m \sqrt{\frac{(2\ell+1)(2L+1)(2\ell_2+1)}{4\pi}} \left[\begin{pmatrix} \ell & L & \ell_2 \\ -2 & 0 & 2 \end{pmatrix} + \begin{pmatrix} \ell & L & \ell_2 \\ 2 & 0 & -2 \end{pmatrix} \right] \begin{pmatrix} \ell & L & \ell_2 \\ -m & M & m_2 \end{pmatrix}. \end{aligned} \tag{5.10}$$

We then define[2]

$$\xi^{LM}_{lm\ell_2 m_2} \equiv (-1)^m \sqrt{\frac{(2\ell+1)(2L+1)(2\ell_2+1)}{4\pi}} \begin{pmatrix} \ell & L & \ell_2 \\ -m & M & m_2 \end{pmatrix}, \tag{5.11}$$

and

$$H^{L}_{\ell\ell_2} \equiv \begin{pmatrix} \ell & L & \ell_2 \\ 2 & 0 & -2 \end{pmatrix}. \tag{5.12}$$

[2]Note that the definitions of $\xi^{LM}_{\ell m \ell' m'}$ and $H^{L}_{\ell\ell'}$ differ from those in Ref. [51]; we re-define these quantities in order to avoid division by zero.

Due to the properties of the Wigner 3j symbols (see Appendix A), changing the sign on all three m's brings up a factor of $(-1)^{\ell+\ell_2+L}$, so the sum in Eq. (5.10) vanishes, unless $\ell+\ell_2+L$ =even. Replacing Eqs. (5.10), (5.11), and (5.12) into Eq. (5.4), we come to a relatively simple expression for the rotation-induced B mode,

$$\delta B_{\ell m} = 2\sum_{LM}\sum_{\ell_2 m_2} \alpha_{LM} E_{\ell_2 m_2} \xi^{LM}_{\ell m \ell_2 m_2} H^L_{\ell\ell_2}, \tag{5.13}$$

where the only non-zero terms in the sum are those that satisfy $\ell+\ell_2+L$=even.

Similarly, for the case of the rotation-induced E mode, the properties of the Wigner 3j symbols ensure that if the sum of m's does not vanish, the value of the symbol is zero, so we get

$$\int d\hat{n} Y^{E*,ab}_{(\ell m)} Y_{(LM)} Y^B_{(\ell_2 m_2)ab} = i\xi^{LM}_{\ell m \ell_2 m_2} H^L_{\ell\ell_2}. \tag{5.14}$$

Combining this result with Eq.(5.5), we arrive to

$$\delta E_{\ell m} = 2i\sum_{LM}\sum_{\ell_2 m_2} \alpha_{LM} E_{\ell_2 m_2} \xi^{LM}_{\ell m \ell_2 m_2} H^L_{\ell\ell_2}. \tag{5.15}$$

In Eqs. (5.14) and (5.15), the only non-zero terms are those that satisfy $\ell+\ell_2+L$ =odd. Now that we have obtained the expressions for rotation-induced E and B modes, we can derive the rotation-induced correlations in the CMB temperature and polarization.

Four correlations are modified/induced by the rotation, to first order: EB, EE, TB, and TE (there is also a BB correlation, but it is second order in α, and thus neglected here). Every mode that we detect will contain the sum of the primordial and rotation-induced component,

$$\begin{aligned} E^{\rm tot}_{\ell m} &= E_{\ell m} + \delta E_{\ell m}, \\ B^{\rm tot}_{\ell m} &= \delta B_{\ell m}. \end{aligned} \tag{5.16}$$

Using the definitions of the EE and TE power spectra, and the Eqs. (5.13) and (5.15), we get

$$\begin{aligned} \left\langle B^{\rm tot}_{\ell m} E^{\rm tot,\,*}_{\ell' m'} \right\rangle &= 2\sum_{LM} \alpha_{LM} C^{EE}_{l'} \xi^{LM}_{\ell m \ell' m'} H^L_{\ell\ell'} \\ &= \frac{1}{\sqrt{\pi}} \alpha_{00} C^{EE}_{l'} \delta_{\ell\ell'}\delta_{mm'} + 2\sum_{L\geqslant 1}\sum_{M=-L}^{L} \alpha_{LM} C^{EE}_{\ell'} \xi^{LM}_{\ell m \ell' m'} H^L_{\ell\ell'}, \end{aligned} \tag{5.17}$$

where in the last step we separated explicitly the contribution from the rotation-angle monopole, which we will used in a later discussion of the uniform rotation. We emphasize again that the absence of any superscript on the symbols for the power spectra in these equations denotes primordial contributions (prior to rotation), and the modes with superscript "rot" encompass both primordial

and the rotation-induced parts. Similarly, the rest of the correlations are

$$\left\langle E^{\rm tot}_{\ell m} E^{{\rm tot},\,*}_{\ell' m'} \right\rangle = C_l^{EE}\delta_{\ell\ell'}\delta_{mm'} + 2i\sum_{LM}(C_{\ell'}^{EE} - C_{\ell}^{EE})\alpha_{LM}\xi^{LM}_{\ell m\ell' m'}H^L_{\ell\ell'}, \tag{5.18}$$

$$\left\langle B^{\rm tot}_{\ell m} T^{{\rm tot},\,*}_{\ell' m'} \right\rangle = 2\sum_{LM}\alpha_{LM}C_{\ell'}^{TE}\xi^{LM}_{\ell m\ell' m'}H^L_{\ell\ell'}, \tag{5.19}$$

$$\left\langle E^{\rm tot}_{\ell m} T^{{\rm tot},\,*}_{\ell' m'} \right\rangle = C_{\ell}^{TE}\delta_{\ell\ell'}\delta_{mm'} + 2i\sum_{LM}C_{\ell'}^{TE}\alpha_{LM}\xi^{LM}_{\ell m\ell' m'}H^L_{\ell\ell'}. \tag{5.20}$$

Note that for EB and TB, the sum is taken over the terms that satisfy $\ell+\ell'+L$=even, and in EE and TE, $\ell+\ell'+L$=odd.

The next step is, in a sense, to invert the above four equations in order to obtain an optimal estimator for the rotation-angle multipoles, which can then be evaluated using the measurements of these four cross-correlations from the CMB maps.

5.2 Estimators for Rotation: Full-Sky Formalism

We now focus on building an optimal estimator for the rotation-angle multipoles, $\widehat{\alpha}_{LM}$, using all four temperature-polarization cross-correlations induced by rotation. In this section, we use expressions containing Wigner-3j symbols; in Section 6.2, we revisit this derivation in pixel space for the TB case only, and obtain expressions in terms of the triple-Y integrals. The advantage of the latter is a straightforward implementation in the CMB-analysis software package called HEALPix [52], which we use to analyze WMAP data. However, it is not always possible to conduct calculations in pixel space, in which case one must resort to the expressions presented here.

In the following, we will work under the null assumption, i.e., evaluate all the covariances for the case of *no rotation*. This approach is justified in the regime of small rotation[3]. Furthermore, as we show in Section 6.4, the RMS rotation angle in the sky (calculated from the values in each WMAP pixel) is constrained to be less than about ten degrees. Therefore, the uncertainties estimated based on the null assumption provide good accuracy.

To start, we assume that the primordial CMB temperature/polarization pattern is a realization of a statistically isotropic Gaussian random field, in which case the spherical-harmonic coefficients ($T_{\ell m}$, $E_{\ell m}$, and $B_{\ell m}$) for the *primordial* field are uncorrelated at different angular scales, where $\ell \neq \ell'$. As Eqs. (5.17)–(5.20) show, however, rotation induces *off-diagonal* correlations, i.e., correlations between spherical-harmonic coefficients of different ℓm and $\ell' m'$. This specific non-Gaussian signature is a hallmark of post-recombination rotation of the polarization pattern in the sky. While

[3]Indeed, the uniform rotation angle was previously constrained to be less than about a degree, as pointed out in Chapter 4.

A	$Z^A_{ll'}$
BE	$C^{EE}_{l'}$
EB	C^{EE}_{l}
EE	$-i(C^{EE}_{l'} - C^{EE}_{l})$
BT	$C^{TE}_{l'}$
TB	C^{TE}_{l}
ET	$-iC^{TE}_{l'}$
TE	$-iC^{TE}_{l}$

Table 5.1: The quantities $Z^A_{ll'}$, defined in Eq. (5.21), obtained from Eqs. (5.17)–(5.20).

the correlations of specific ℓm-$\ell' m'$ pairs depend on the azimuthal quantum numbers m and m', they can be parametrized in terms of the rotational invariants (i.e., independent of m),

$$D^{LM,A}_{\ell\ell'} \equiv 2\alpha_{LM} Z^A_{\ell\ell'} H^L_{\ell\ell'}, \tag{5.21}$$

where the quantities $Z^A_{\ell\ell'}$ are given in Table 5.2. Notice that the EB correlator, for a given $\ell\ell'$ pair with $\ell \neq \ell'$, is different than the BE correlator, so we consider *both* BE and EB (and similarly for TE/ET and TB/BT) and then restrict our sums to $\ell' \geq \ell$ to avoid double-counting. We thus have for $\ell > \ell'$, $A = \{BE, EB, TB, BT, TE, ET, EE\}$, while for $\ell = \ell'$, we have $A = \{BE, TE, TB, EE\}$. With these shorthands,

$$\left\langle X^{\rm tot}_{\ell m} (X'_{\ell' m'})^{\rm tot,\,*} \right\rangle = \sum_{LM} D^{LM,XX'}_{\ell\ell'} \xi^{LM}_{\ell m \ell' m'}, \tag{5.22}$$

where we emphasize again that the superscript "tot" represents combined contribution from primordial + rotation-induced signal, while the absence of any superscript denotes just the primordial signal (for either multipole coefficients, or the power spectra).

We now suppose that we have a measurement of the spherical-harmonic coefficients $T^{\rm map}_{\ell m}$, $E^{\rm map}_{\ell m}$, $B^{\rm map}_{\ell m}$, obtained from a CMB temperature and polarization maps. These receive contributions from the true signal on the sky, reduced by the ℓ-space window function W_ℓ (where we assume a Gaussian beam of width $\theta_{\rm FWHM}$), and a contribution from detector noise (see Section 3.3 for more details). The predictions for the rotational invariants for the *map* are

$$D^{LM,XX',{\rm map}}_{\ell\ell'} = D^{LM,XX'}_{\ell\ell'} W_\ell W_{\ell'}. \tag{5.23}$$

Following Refs. [50, 51, 53], the minimum-variance estimator for each $D^{LM,XX',{\rm map}}_{\ell\ell'}$ is[4]

$$\widehat{D}^{LM,XX',{\rm map}}_{\ell\ell'} = (G_{\ell\ell'})^{-1} \sum_{mm'} X^{\rm map}_{\ell m} X'^{,{\rm map},*}_{\ell' m'} \xi^{LM}_{\ell m \ell' m'}, \tag{5.24}$$

[4]Note that the definition of $G_{\ell\ell'}$ differs from that in Refs. [50, 51].

where we use (see Appendix A),

$$\sum_{mm'} (\xi^{LM}_{\ell m\ell' m'})^2 = G_{\ell\ell'} \equiv \frac{(2\ell+1)(2\ell'+1)}{4\pi}. \tag{5.25}$$

Recall also that for EB and TB, only the terms in Eq. (5.24) that satisfy $\ell+\ell'+L$ =even are non-vanishing, while for EE and TE only $\ell+\ell'+L$=odd terms are non-vanishing.

The variances with which $\widehat{D}^{LM,XX',\mathrm{map}}_{ll'}$ can be measured for each XX' can also be calculated; moreover, measurements for different XX' are correlated, for the same $\ell\ell'$. The corresponding covariance is given by

$$\mathcal{C}^{\ell\ell'}_{AA'} \equiv G_{\ell\ell'} \left(\left\langle \widehat{D}^{LM,A,\mathrm{map}}_{\ell\ell'} \widehat{D}^{LM,A',\mathrm{map}}_{\ell\ell'} \right\rangle - \left\langle \widehat{D}^{LM,A,\mathrm{map}}_{\ell\ell'} \right\rangle \left\langle \widehat{D}^{LM,A'\mathrm{map}}_{\ell\ell'} \right\rangle \right). \tag{5.26}$$

Notice that this covariance resembles (and is similarly defined and derived as) the covariance for the power spectra presented earlier in Eq. (3.41); the difference is the scaling with $H^L_{\ell\ell'}$ and the rotation-angle multipoles. In principle, $\mathcal{C}^{\ell\ell'}_{AA'}$ is a 7×7 matrix (in AA' space) for $\ell \neq \ell'$ and 4×4 for $\ell = \ell'$. However, the matrix is sparsely populated in AA' space; it can be written in block-diagonal form, since the EB and TB correlators are non-vanishing only for $\ell+\ell'+L$=even while those for TE and EE are non-vanishing only for $\ell+\ell'+L$=odd. We derive explicit expressions for the relevant entries of $\mathcal{C}^{\ell\ell'}_{AA'}$ in the following.

We first recall that each $\widehat{D}^{LM,A,\mathrm{map}}_{\ell\ell'}$ (i.e., each $\ell\ell'$ and AA', for a given LM) provides a measurement of α_{LM}, through

$$(\widehat{\alpha}_{LM})^A_{\ell\ell'} = \widehat{D}^{LM,A,\mathrm{map}}_{\ell\ell'} / F^{L,A}_{\ell\ell'}, \tag{5.27}$$

in terms of

$$F^{L,A}_{\ell\ell'} \equiv 2 Z^A_{\ell\ell'} H^L_{\ell\ell'} W_\ell W_{\ell'}. \tag{5.28}$$

The variance and covariance of $(\widehat{\alpha}_{LM})^A_{\ell\ell'}$ are given simply in terms of those for $\widehat{D}^{LM,A,\mathrm{map}}_{\ell\ell'}$, scaled by the appropriate factors of $F^{L,A}_{\ell\ell'}$.

We then choose to construct an optimal estimator $\widehat{\alpha}_{LM}$ by minimizing its variance. A minimum-variance estimator is obtained by summing all of the individual estimators $(\widehat{\alpha}_{LM})^A_{\ell\ell'}$, for a fixed LM, with inverse-variance weighting (and taking into account also the covariances). The estimator thus reads

$$\widehat{\alpha}_{LM} = \sigma^2_L \sum_{\ell'\geq l} G^L_{\ell\ell'} \sum_{AA'} F^{L,A'}_{\ell\ell'} \widehat{D}^{LM,A,\mathrm{map}}_{\ell\ell'} \left[(\mathcal{C}^{\ell\ell'})^{-1} \right]_{AA'}, \tag{5.29}$$

and its variance

$$\sigma^{-2}_L = \sum_{\ell'\geq \ell} G^L_{\ell\ell'} \sum_{AA'} F^{L,A}_{\ell\ell'} F^{L,A'}_{\ell\ell'} \left[(\mathcal{C}^{\ell\ell'})^{-1} \right]_{AA'}. \tag{5.30}$$

The $\ell\ell'$ sums must satisfy triangle inequalities given in Eq. (A.12), and the AA' sums are over

$\{EB, BE, TB, BT, EE, TE, ET\}$ for $\ell \neq \ell'$, and $\{EB, TB, EE, TE\}$ for $\ell = \ell'$, and the matrix inversion is in the AA' space.

We further assume that the noise is homogeneous (with the same variance in each pixel), uncorrelated with the data, and uncorrelated between different pixels. We also assume that the noise in temperature is uncorrelated with the noise in polarization. If so, then the power spectra for the map are given by Eq. (3.35), for $A \in \{TT, EE, BB\}$, where the corresponding noise power spectra are given by (or analogous to) Eq. (3.36). The instrumental-noise contributions to the cross-power spectra in this case vanish,

$$C_\ell^{EB,\mathrm{noise}} = C_\ell^{TB,\mathrm{noise}} = C_\ell^{TE,\mathrm{noise}} = 0. \tag{5.31}$$

Now we can calculate the desired covariances using Eqs. (5.24) and the usual definitions of the power spectra C_ℓ^A. For EB, for $\ell \neq \ell'$, we have

$$\begin{aligned} \mathcal{C}_{BE,BE}^{\ell\ell'} &= C_\ell^{BB,\mathrm{map}} C_{\ell'}^{EE,\mathrm{map}}, \\ \mathcal{C}_{EB,EB}^{\ell\ell'} &= C_{\ell'}^{BB,\mathrm{map}} C_\ell^{EE,\mathrm{map}}, \\ \mathcal{C}_{EB,BE}^{\ell\ell'} &= \mathcal{C}_{BE,EB}^{\ell\ell'} = 0, \end{aligned} \tag{5.32}$$

and for $\ell = \ell'$,

$$\mathcal{C}_{BE,BE}^{\ell\ell} = C_\ell^{BB,\mathrm{map}} C_\ell^{EE,\mathrm{map}}. \tag{5.33}$$

The covariances for BT and TB are the same, with the replacements $E \to T$. There are also covariances between the TB and EB estimators. For $\ell \neq \ell'$, they read

$$\begin{aligned} \mathcal{C}_{BE,BT}^{\ell\ell'} &= C_\ell^{BB,\mathrm{map}} C_{\ell'}^{TE,\mathrm{map}}, \\ \mathcal{C}_{EB,TB}^{\ell\ell'} &= C_{\ell'}^{BB,\mathrm{map}} C_\ell^{TE,\mathrm{map}}, \\ \mathcal{C}_{BE,TB}^{\ell\ell'} &= \mathcal{C}_{EB,BT}^{\ell\ell'} = 0, \end{aligned} \tag{5.34}$$

and for $\ell = \ell'$,

$$\mathcal{C}_{BE,BT}^{\ell\ell} = C_\ell^{BB,\mathrm{map}} C_\ell^{TE,\mathrm{map}}. \tag{5.35}$$

For EE,

$$\mathcal{C}_{EE,EE}^{\ell\ell'} = (1 + \delta_{\ell\ell'}) C_\ell^{EE,\mathrm{map}} C_{\ell'}^{EE,\mathrm{map}}. \tag{5.36}$$

For the TE case, for $\ell \neq \ell'$, we have

$$\begin{aligned}
\mathcal{C}^{\ell\ell'}_{TE,TE} &= C_\ell^{TT,\rm map} C_{\ell'}^{EE,\rm map}, \\
\mathcal{C}^{\ell\ell'}_{ET,ET} &= C_{\ell'}^{TT,\rm map} C_{\ell}^{EE,\rm map}, \\
\mathcal{C}^{\ell\ell'}_{TE,ET} &= \mathcal{C}^{\ell\ell'}_{ET,TE} = C_\ell^{TE,\rm map} C_{\ell'}^{TE,\rm map},
\end{aligned} \tag{5.37}$$

and for $\ell = \ell'$,

$$\mathcal{C}^{\ell\ell}_{ET,ET} = C_\ell^{TT,\rm map} C_{\ell}^{EE,\rm map} - \left(C_\ell^{TE,\rm map}\right)^2. \tag{5.38}$$

There are also TE-EE covariances. However, since TE and EE will turn out to almost always be weaker probes of the rotation (see Section 5.4), we do not include these additional expressions here.

As an example (and for clarity), let us now explicitly write down the expressions for the estimator and its variance (uncertainty) in the case where we use only information from the BE correlator,

$$\widehat{\alpha}_{LM} = \sigma_L^2 \sum_{\ell' \geq \ell} (1+\delta_{\ell\ell'})^{-1} G_{\ell\ell'} \left[\frac{F^{L,BE}_{\ell\ell'} \widehat{D}^{LM,BE,\rm map}_{\ell\ell'}}{C_\ell^{BB,\rm map} C_{\ell'}^{EE,\rm map}} + (\mathrm{B} \leftrightarrow \mathrm{E}) \right], \tag{5.39}$$

and

$$\sigma_L^{-2} = \sum_{\ell' \geq \ell} (1+\delta_{\ell\ell'})^{-1} G_{\ell\ell'} \left[\frac{(F^{L,BE}_{\ell\ell'})^2}{C_l^{BB,\rm map} C_{\ell'}^{EE,\rm map}} + (\mathrm{B} \leftrightarrow \mathrm{E}) \right]. \tag{5.40}$$

The $\ell\ell'$ sums here are over values that satisfy $\ell + \ell' + L =$even. The estimator and variance for TB are the same after the replacement $E \to T$.

We now perform two cross-checks of the above expressions. First, we take the flat-sky limit of the expression in Eq. (5.40), valid for the full sky, and compare it to the flat-sky results of Ref. [54]. Secondly, we reduce our expressions to those corresponding to the case where the rotation field only has the monopole, and compare them with what we expect to obtain for the case of uniform rotation.

For the first test, we work out the EB case, but the other three estimators (from TB, EE, and TE) follow analogously. From Eqs. (5.40) and (5.28), we get

$${\sigma_L}^{-2} = 4 \sum_{\ell' > \ell} (H^L_{\ell\ell'})^2 G^L_{\ell\ell'} (W_\ell W_{\ell'})^2 \left[\frac{(C_{\ell'}^{EE})^2}{C_\ell^{BB,\rm map} C_{\ell'}^{EE,\rm map}} + \frac{(C_{\ell}^{EE})^2}{C_{\ell'}^{BB,\rm map} C_{\ell}^{EE,\rm map}} \right]. \tag{5.41}$$

The two terms in this equation are the same under the exchange of ℓ and ℓ'. Thus, after re-naming the indices on one of the two terms, we get the sums over $\ell < \ell'$ and $\ell > \ell'$, which covers the whole range of ℓ's[5]. We are left with

$$(\sigma_L)^{-2} = 4 \sum_{\ell\ell'} \mathcal{X}^L_{\ell\ell'} G_{\ell\ell'} (H^L_{\ell\ell'})^2, \tag{5.42}$$

[5]Note that, when we switch to integration, as shown further on in the text, the $\ell = \ell'$ term is of measure zero, and can be ignored.

where we have defined

$$\mathcal{X}_{\ell\ell'} \equiv (W_\ell W_{\ell'})^2 \frac{\left(C_{\ell'}^{EE}\right)^2}{C_{\ell'}^{EE,\rm map} C_\ell^{BB,\rm map}}. \tag{5.43}$$

We now derive the limit of high multipoles.[6] We start by using the approximation [30],

$$H^L_{\ell\ell'} \approx \cos 2\varphi_{\ell\ell'} \begin{pmatrix} \ell & \ell' & L \\ 0 & 0 & 0 \end{pmatrix}, \tag{5.44}$$

for the $\ell+\ell'+L$=even case. From Eqs. (5.25) and (5.44), we have

$$G_{\ell\ell'}(H^L_{\ell\ell'})^2 \xrightarrow{L,\ell,\ell'\to\infty} \frac{\ell\ell'}{\pi} \begin{pmatrix} \ell & \ell' & L \\ 0 & 0 & 0 \end{pmatrix}^2 \cos^2 2\varphi_{\ell\ell'}. \tag{5.45}$$

From Eq. (5.8), this gives, for large L,

$$(\sigma_L)^{-2} \xrightarrow[L,\ell,\ell'\to\infty]{} 4\sum_{\ell\ell'} \mathcal{X}_{\ell\ell'} \sqrt{\frac{\ell\ell'}{2\pi L}} \int d\hat{n} Y_{\ell 0} Y_{\ell' 0} Y_{L0} \cos^2 2\varphi_{\ell\ell'}. \tag{5.46}$$

Given that

$$\int_0^{2\pi} \frac{d\varphi_\ell}{2\pi} e^{im\varphi_\ell} = \delta_{m,0}, \tag{5.47}$$

Eq. (5.46) can be rewritten using

$$\begin{aligned} &\sum_{mm'M} \sum_{\ell\ell'} \sqrt{\frac{\ell\ell'}{2\pi L}} \int d\hat{n} Y^*_{\ell m} Y_{\ell' m'} Y_{LM} \delta_{M,0} \delta_{m,0} \delta_{m',0} \\ &= \sum_{mm'M} \sum_{\ell\ell'} \sqrt{\frac{\ell\ell'}{2\pi L}} \int d\hat{n} Y^*_{\ell m} Y_{\ell' m'} Y_{LM} \int \frac{d\varphi_\ell d\varphi_{\ell'} d\varphi_L}{(2\pi)^3} e^{i(M\varphi_L + m'\varphi_{\ell'} - m\varphi_\ell)}. \end{aligned} \tag{5.48}$$

We then use relations from Ref. [30]

$$e^{i\cdot\vec{\ell}\cdot\vec{n}} \approx \sqrt{\frac{2\pi}{\ell}} \sum_m i^m Y_{\ell m} e^{im\varphi_\ell}, \tag{5.49}$$

$$\delta(\vec{L} - (\vec{\ell} - \vec{\ell}')) = \int \frac{d\hat{n}}{(2\pi)^2} e^{i(\vec{L}-\vec{\ell}+\vec{\ell}')\cdot\hat{n}} \approx \int \frac{d\hat{n}}{(2\pi)^2} \sum_{mm'M} Y^*_{\ell m} Y_{\ell' m'} Y_{LM} \sqrt{\frac{(2\pi)^3}{\ell\ell' L}} e^{i(M\varphi_L + m'\varphi_{\ell'} - m\varphi_\ell)}, \tag{5.50}$$

[6] If L is large, then the triangle inequalities and the requirement for non-flat triangles ensures that ℓ and ℓ' are also large.

and replace the sum with the integral,

$$\sum_{\ell\ell'} \int d\varphi_\ell \, d\varphi_{\ell'} \, \ell\ell' \leftrightarrow \int \int d^2\vec{\ell} \, d^2\vec{\ell}'. \tag{5.51}$$

Finally, by combining Eqs. (5.48)–(5.51) and Eq. (5.46), and after integrating over $d\varphi_L$, we obtain the flat-sky limit,

$$(\sigma_L)^{-2} \xrightarrow[L,\ell,\ell'\to\infty]{} 4 \int \frac{d^2\ell'}{(2\pi)^2} \cos^2 2\varphi_{\ell'\ell} (W_\ell W_{\ell'})^2 \frac{(C_{\ell'}^{EE})^2}{C_\ell^{BB,\mathrm{map}} C_{\ell'}^{EE,\mathrm{map}}}, \tag{5.52}$$

which can be shown to agree with the results of Ref. [54][7].

Additionally, to illustrate the difference between the flat-sky and full-sky analysis, we numerically evaluate the flat-sky formula, and compare those results to the full-sky expressions for the variance of the EB estimator, for a fixed instrumental noise and resolution. As expected, the two results are in good agreement at high multipoles, where the flat sky makes a valid approximation (better than a fraction of a percent for $L \gtrsim 50$), while the discrepancy increases up to $\sim 4\%$ at lower L's. In general, the full-sky formalism is exact, and rarely more computationally expensive than the flat-sky, so we resort to it in this work.

We now turn to the second test, and derive the variance for the $L = 0$ term only, in which case all the representation-theory coefficients can be readily evaluated. We focus only on the EB case. From Eqs. (5.42) and (5.43) (for $\ell = \ell'$), after evaluating the coefficients for $L = 0$, we get the variance of the uniform-rotation estimator to be

$$(\sigma_{00})^{-2} = \frac{1}{\pi} \sum_\ell \frac{\left[C_\ell^{EE} (W_\ell)^2\right]^2 (2\ell+1)}{C_\ell^{EE,\mathrm{map}} C_\ell^{BB,\mathrm{map}}}. \tag{5.53}$$

On the other hand, the B mode induced by small rotation from a pure E mode is given by Eq. (5.1). The induced EB power spectrum in that case is simply

$$C_\ell^{EB,\mathrm{tot}} = 2\alpha C_\ell^{EE}, \tag{5.54}$$

and estimators for the rotation can be expressed for each ℓm pair as

$$\widehat{\alpha}^{\ell m} = \frac{E_{\ell m}^{\mathrm{map}} B_{\ell m}^{\mathrm{map}}}{2 C_\ell^{EE} W_\ell^2}. \tag{5.55}$$

[7] After combining their Eqs. (7) and (8) and results from their Table 1, we arrive to the same expression.

The variance is then calculated from all ℓm pairs as

$$\sigma^{-2} = \sum_{\ell=0}^{\infty} \sum_{m=-\ell}^{\ell} \frac{1}{\left\langle (\widehat{\alpha}^{\ell m})^2 \right\rangle} = \sum_{\ell} (2\ell+1) \frac{4[C_\ell^{EE} (W_\ell)^2]^2}{C_\ell^{EE,\mathrm{map}} C_\ell^{BB,\mathrm{map}}}, \tag{5.56}$$

where the factor of $(2\ell+1)$ comes from the sum over m, because the terms in the sum have effectively only index ℓ. For $L = 0$, Eq. (5.56) reduces precisely to Eq. (5.53), once the factor of $\sqrt{4\pi}$ by which α and α_{00} differ is taken into account[8].

In conclusion, both the agreement of our full-sky results with the previous flat-sky calculations and the uniform-rotation test validate the derivations presented in this section.

5.3 Rotation vs. Weak Lensing

Here we briefly demonstrate that the effects of rotation and weak gravitational lensing [30,55–64] on the CMB polarization are orthogonal to each other and can thus be distinguished geometrically with a full-sky map. If this were not the case, we should be concerned with a method of disentangling the two effects, since the estimator for the rotation would suffer a large bias from the lensing contributions, and the corresponding uncertainties would need to be corrected as well.

To begin, recall that if we start with a pure E mode at the surface of last scatter, rotation induces a B mode, given by Eq. (5.4), where the only non-zero terms are those that satisfy $L+\ell+\ell_2 =$even. However, if we consider the effect of weak lensing, a pure–E-mode polarization tensor changes by

$$\delta P_{ab} = (\nabla_c \varphi)(\nabla^c P_{ab}), \tag{5.57}$$

where only in this section φ denotes the projection of the gravitational potential along the line of sight (to be distinguished from the previous use of this symbol to denote a coordinate on the sky). Thus, the B mode induced by weak lensing is

$$\delta B_{\ell m} = \int d\widehat{\mathbf{n}} \delta P_{ab}(\widehat{\mathbf{n}}) Y^{B*,ab}_{(\ell m)}(\widehat{\mathbf{n}}) = 2 \sum_{LM} \sum_{\ell_2 m_2} \varphi_{LM} E_{\ell_2 m_2} \int d\widehat{\mathbf{n}} Y^{B*,ab}_{(\ell m)} (\nabla_c Y_{(LM)})(\nabla^c Y^E_{(\ell_2 m_2) ab}). \tag{5.58}$$

The parity of the spherical harmonic Y_{LM} is $(-1)^L$. The parity of the E-mode term in the integral is $(-1)^{\ell_2}$, and the parity of the B-mode term is $(-1)^{\ell+1}$. The parity of the integrand in Eq. (5.58) is thus $(-1)^{L+\ell+\ell_2+1}$. Therefore, the integral is non-vanishing only for terms that satisfy $L+\ell+\ell_2 =$odd.

We conclude that the rotation induces B modes that satisfy $L+\ell+\ell_2 =$even, while for weak lensing we have $L+\ell+\ell_2 =$odd (see Eqs. (5.4) and (5.13)), so that the two effects are orthogonal. Finally, another relevant point for the analysis of the rotation signal is that the weak lensing affects the

[8] This factor comes about because of the normalization of spherical harmonics, so that the physical uniform rotation on the sky and the monopole coefficient are related by $\alpha = \alpha_{00}/\sqrt{4\pi}$.

temperature map, while the rotataion does not, which provides an additional avenue to distinguish their relative contributions.

5.4 Forecasts

We now calculate forecasts for the sensitivity of different CMB experiments to detecting rotation. We do so by numerically evaluating the expression of Eq. (5.30) for the variance of $\widehat{\alpha}_{LM}$, for a range of L-modes, given appropriate instrumental noise levels and resolutions. We perform the calculations for a fixed cosmology, using the primordial power spectra obtained with CMBFAST with WMAP-5-year [65] best-fit cosmological parameters: $\Omega_b h^2 = 0.02267$, $\Omega_c h^2 = 0.1131$, $\Lambda = 0.726$, $n_s = 0.960$, $\tau = 0.084$, and a power spectrum normalized to WMAP-5.

We analyze three different experiments: (i) CMBPol's (EPIC-2m) 150 GHz channel with resolution $\theta_{\rm FWHM} = 5'$, taking the relevant parameters as given in Ref. [66], a noise-equivalent temperature NET$= 2.8\mu{\rm K}\sqrt{\rm sec}$, and the observation time $t_{\rm obs} = 4$ yr; (ii) *Planck*'s 143 GHz channel, with $\theta_{\rm FWHM} = 7.1'$, NET $= 31\mu{\rm K}\sqrt{\rm sec}$, and $t_{\rm obs} = 1.2$ yr; (iii) WMAP-5, with $\theta_{\rm FWHM} = 21'$, $\sigma_T = 30\mu$K, and $\sigma_P = 42.6\mu$K [50]. The NET parameters specified for *Planck* and CMBPol are related to the temperature/polarization pixel-noise variances as

$$\sigma_T^2/N_{\rm pix} = f_{\rm sky}^0({\rm NET})^2/t_{\rm obs}, \tag{5.59}$$

where $f_{\rm sky}^0$ is fraction of the sky observed[9], here assumed to be unity.

The variances are shown for each of the three experiments in Figure 5.2, for estimators constructed separately from EB, EE, TB, and TE correlations. The first thing to notice here is that both the lower noise and the higher resolution contribute to about two orders of magnitude improvement in the sensitivity to rotation from WMAP to *Planck*, and would lead to yet more than another order-of-magnitude improvement in CMBPol. This is illustrated in more detail in Figure 5.3, where the variances in the EB and TB estimators are compared for all three experiments. We can also see that, at low multipoles (below L of about 200), the most sensitive estimators for all three experiments are those derived from the EB and TB correlations. This is the case because of the absence of any TB or EB correlation under the assumption (justified by the current upper limits to the B mode amplitude) of no B modes at the surface of last scatter.

For WMAP, we find a TB-estimator variance of 8.3° at $L = 0$, which is consistent with the current constraints on uniform rotation[10] [65, 67]. The dipole and quadrupole components of the

[9] The fraction of the sky *observed* should be distinguished from the fraction of the sky *used in the analysis*, which we denote $f_{\rm sky}$. For satellite experiments, $f_{\rm sky}^0 \approx 1$ usually, and it is used to estimate the noise power spectrum, while $f_{\rm sky} \approx 0.7$, since the pixels around the Galactic plane are typically covered by an analysis mask, cutting out about 30% of the surveyed sky.

[10] Note that we calculate the multipole moments of rotation, so a constraint on a uniform rotation α corresponds to a monopole constraint of $\alpha_{00} = \sqrt{4\pi}\alpha$. Thus, an upper limit $\alpha_{00} = 8.3°$ is equivalent to $\alpha = 2.3°$.

rotation have the same variances as the monopole ($L = 0$), since the variance remains fairly flat out to L of about 100, in all three instruments. Above $L \approx 400$, the variance increases rapidly. This happens when the exponential part of the window functions becomes dominant, due to the finite angular resolution of the instrument. Also, since the correlation angle for polarization is about ten times smaller than that for temperature, the exponential tail in the EE-estimator case becomes prominent at higher multipoles than in the TE case. The variance from the EB estimator at $L = 0$ is 46.2° for WMAP, and thus not constraining. The TE-estimator variance quickly drops below the EB-estimator variance (at $L \approx 20$) and below the TB-estimator variance (at $L \approx 150$). However, the variance σ_L at these L's is so large ($\gtrsim 100$ degrees) that the measurements are not at all constraining. Similar features are apparent in plots for the other two experiments.

For *Planck*, the variances of the EB and TB estimators are more comparable, and the constraints to all rotation multipoles in the range from L of 0 to about 300 come from the EB variance. At $L = 0$ the variance is $14'$ and $24'$, for the EB- and TB-estimator variances, respectively. *Planck* can thus provide an order-of-magnitude better sensitivity to the uniform rotation than WMAP. For high multipoles, above $L \approx 400$ or so, the TE-estimator variance becomes the smallest one. At $L \approx 800$, a rapid rise in all four variances is visible, due to the limitations in angular resolution and the correlation angle of the polarization.

For CMBPol, the EB-estimator variance is the smallest in the whole range of multipoles from 0 to 1000. At $L = 0$, the EB and TB values are, respectively, 22" and 63", which is better than *Planck* by more than an order of magnitude. Similarly to WMAP and *Planck* variances, we observe a rapid rise in the variance above $L \approx 1000$, corresponding to the resolution limitations and/or the polarization correlation length.

In Figure 5.4, we show the variance for the combined minimum-variance estimator, obtained from all four cross-correlations, with inverse-variance weighting. We have not included the covariance between the four estimators in this numerical calculation. However, this omission should make negligible difference for WMAP and CMBPol, where the variance is determined primarily by TB and EB, respectively; the *Planck* curve may be increased, but only slightly. The run of this combined variance with L differs very little from the smallest (constraining) variance (that comes from TB in the case of WMAP, and EB in the case of *Planck* and CMBPol), since that term typically dominates the weighted sum. In other words, the estimator obtained from TB for WMAP, and from EB for higher-sensitivity experiments is very close to being exactly the minimum-variance estimator; very little is gained by adding the information from the other three correlations.

5.5 Summary and Conclusions

In this chapter, we derived the complete set of minimum-variance quadratic estimators for a direction-dependent rotation of the CMB polarization, and provided a recipe, given a full-sky map, for measuring the rotation angle as a function of position in the sky. Namely, if primordial perturbations are assumed to be Gaussian (as predicted by inflation), then the rotation introduces a characteristic non-Gaussian signal in the polarization map. More specifically, if primordial perturbations are Gaussian, then the spherical-harmonic coefficients $E_{\ell m}$ and $B_{\ell m}$ of the polarization map are statistically independent for different ℓ and m. However, the rotation introduces off-diagonal correlations, i.e., correlations between different ℓm pairs, which can then be measured to recover the rotation angle. We also evaluated the variances with which the rotation-angle spherical-harmonic coefficients can be measured for WMAP, *Planck*, and CMBPol, providing forecasts for the sensitivity of each of these satellite experiments. Our results indicate that EB and TB correlations will provide more sensitive probes of the rotation angle than TE and EE correlations (at most angular scales), and that EB becomes better, relative to TB, as the instrumental noise is reduced. We have checked that our results for the variances recover prior results, both analytically and numerically, in the flat-sky limit. As an additional check, we showed that our expression for the monopole variance corresponds to that derived for a uniform rotation.

Furthermore, we discussed the use of parity considerations in distinguishing the effects of rotation and of weak lensing on the CMB temperature/polarization maps. There is a subtlety related to this, worth noting again: we assumed that the polarization pattern at the surface of last scatter is a pure E mode, and calculated B modes induced by rotation, pointing out that they are orthogonal to those induced by weak lensing. However, the rotation may also affect the lensing-induced modes, producing secondary effects. Proper treatment of these higher-order effects requires a more complicated analysis, which is beyond the scope of this thesis and is left for future work.

We have elucidated the all-sky formalism; one of the next steps in this context is to work out algorithms for recovery of the rotation angle for a map with partial sky coverage, such as those forthcoming from deep ground-based observations that are currently underway. We anticipate that analogous techniques for determining the cosmic-shear deflection angle may be adapted for this purpose.

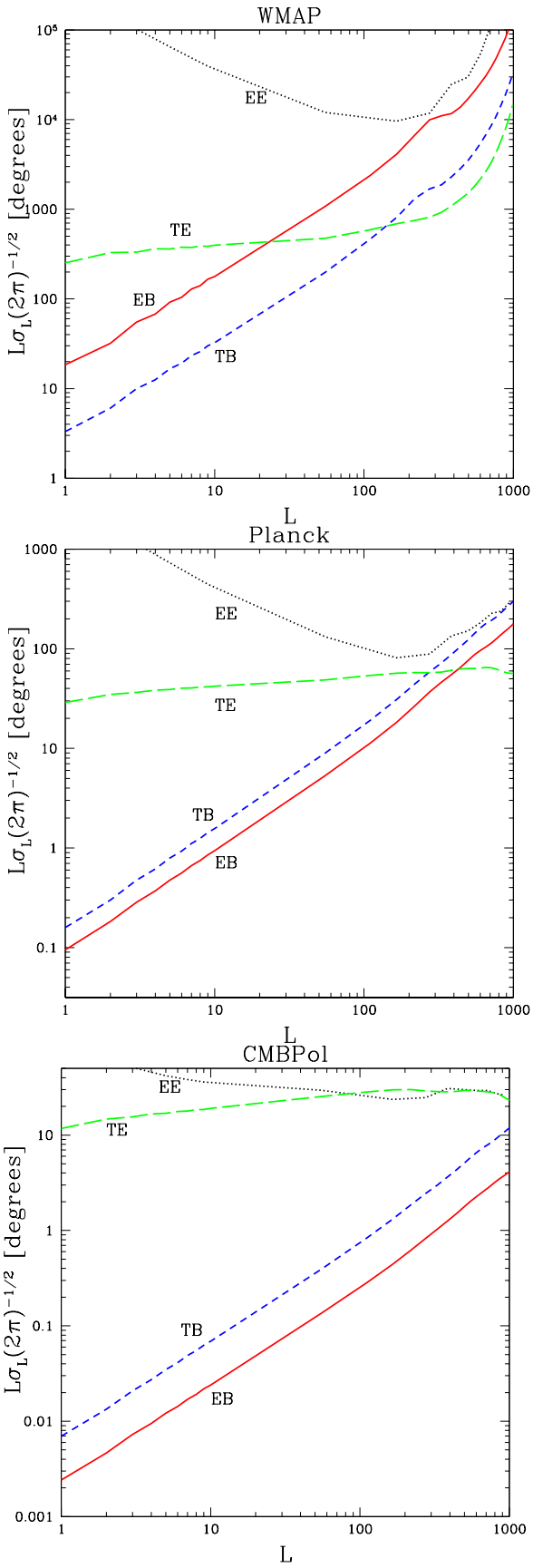

Figure 5.2: Variances for the estimator of the rotation-angle multipole coefficients from all four correlations, for WMAP, *Planck*, and CMBPol. At a large range of multipoles, where the constraints are meaningful, the minimum-uncertainty estimator for *Planck* and CMBPol comes from the EB correlation, and for WMAP from the TB correlation.

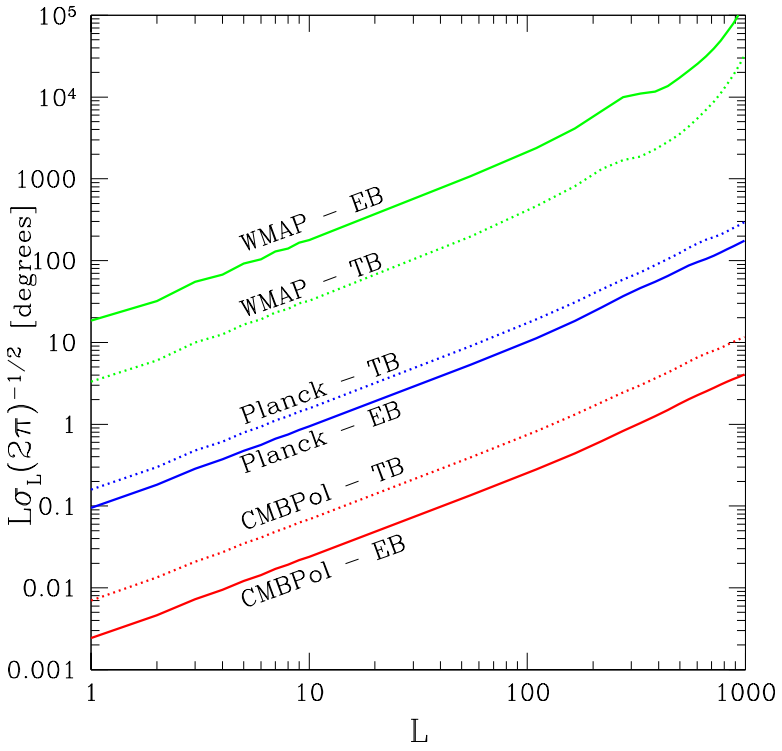

Figure 5.3: The best constraints to the rotation-angle multipole coefficients, i.e., the variances for its estimators from the EB and TB correlations, compared for three different experiments. Notice that *Planck* gives about two orders of magnitude improvement with respect to WMAP, and CMBPol is one order of magnitude more sensitive than *Planck*.

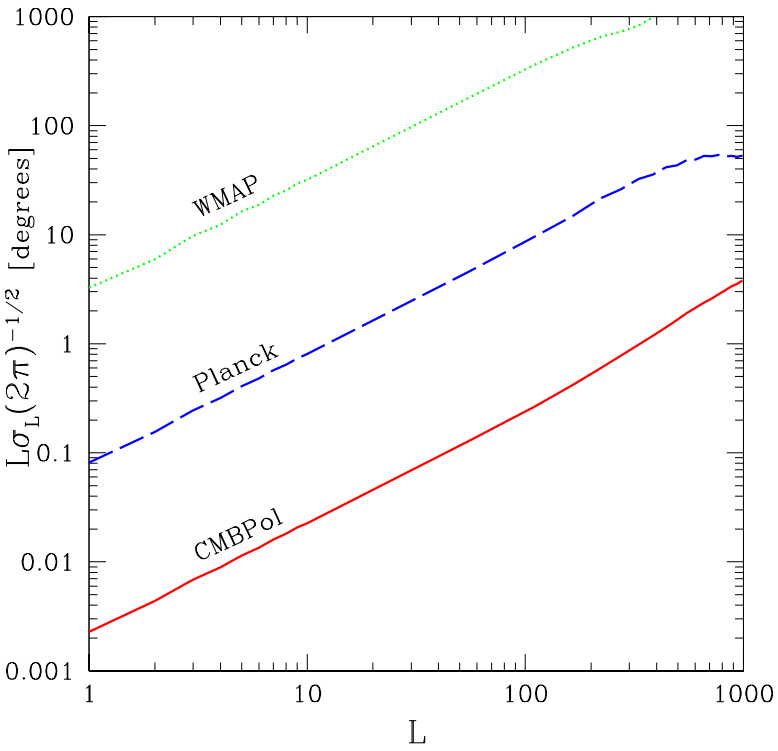

Figure 5.4: The combined variance of the rotation-angle multipole coefficients, obtained from all four cross-correlations, evaluated for WMAP, *Planck* and CMBPol. Note that, due to the inverse-variance summation, the smallest of the four variances dominates the shape and amplitude of the curves for each experiment.

Chapter 6

Data Analysis

In this chapter, we analyze WMAP 7-year temperature and polarization maps, applying the full-sky formalism of Chapter 5 to search for direction-dependent rotation of CMB polarization, from cosmic birefringence. It is organized as follows. In Section 6.1, we describe the data and auxilliary tools (such as sky masks) used in the analysis. In Section 6.2, we rewrite our optimal estimator for the rotation-angle multipole coefficients in pixel space, which facilitates numerical calculations; in the entire chapter, we focus solely on the estimator constructed from TB measurements, as it is expected to have the best sensitivity and yield maximum signal-to-noise at most multipoles, given WMAP noise levels. We also present an estimator for the rotation-angle autocorrelation $C_L^{\alpha\alpha}$ and discuss our data-based de-biasing technique. In Section 6.3 we briefly turn to discussing the type of non-Gaussianity induced by direction-dependent rotation, so as to clarify which modes in temperature and polarization maps contribute most of the signal for reconstructing the rotation map. In Section 6.4, we revisit the current constraints on RMS rotation angle in the sky, coming from the TE power spectrum, in order to further justify small-angle approximation used to interpret our final results. In Section 6.5, we discuss in detail the simulations used in the analysis, and present our test run to demonstrate the validity of the analysis method. In Section 6.6, we present the key results: the first model-independent constraints on directional fluctuations of the rotation angle, down to the resolution of the instrument (i.e., constraints on $C_L^{\alpha\alpha}$ multipoles, up to $L = 512$), and also the implied constraint on a scale-invariant model for $C_L^{\alpha\alpha}$. In Section 6.7, we discuss systematic effects and demonstrate that neither polarized point sources, foregrounds, nor asymmetric beams are expected to significantly impact our results. We discuss the implications of the null measurement for quintessence models for dark energy in Section 6.8, and conclude and summarize in Section 6.9.

Material in this chapter was largely adapted from "First CMB constraints on direction-dependent cosmological birefringence from WMAP-7," Vera Gluscevic, Duncan Hanson, Marc Kamionkowski, and Christopher Hirata, *Phys. Rev. D* **86**, 103529 (2012) [5]. Reproduced here with permission,

6.1 WMAP 7-year Data

We now turn to applying the formalism presented in the earlier sections to search for rotation in the CMB maps made by the WMAP satellite. In this section, we describe in detail the data set we use for this purpose.

We use the full-resolution (corresponding to HEALPix resolution of $N_{\rm side} = 512$) co-added 7-year sky maps that contain foreground-reduced measurements of the Stokes I, Q, and U parameters in three frequency bands: Q (41 GHz), V (61 GHz), and W (94 GHz), available at the LAMBDA website [8]. A summary of the instrumental parameters most relevant to this analysis is provided in Table 6.1.

Band	$\theta_{\rm FWHM}$	Δ_T [μKarcmin]	Δ_P [μKarcmin]
Q (41 GHz)	34'	316	544
V (61 GHz)	24'	387	589
W (94 GHz)	22'	467	693

Table 6.1: Relevant instrumental parameters: beam full-width half maximum and approximate map noise for temperature and polarization for the three frequency bands we use in the analysis [8].

Even though WMAP mapped 4π sterradians of the sky, about 30% (depending on the wavelength) around the plane of our Galaxy is heavily contaminated with various foregrounds and must be discarded prior to the analysis. This is done by "masking out the Galaxy", i.e., setting the pixel values in the contaminated portion of the sky to zero. Known point sources and any other localized contamination are treated in the same way. We therefore apply the seven-year temperature $KQ85y7$ mask with 78.27% of the sky admitted, and a polarization $P06$ mask with 73.28% of the sky admitted. These are the fiducial masks we use in the analysis of both data maps and simulated maps. They are constructed to remove diffuse emission based on the data in K and Q bands, and on a model of thermal dust emission, while the point sources are masked based on a combination of external catalog data and WMAP-detected sources. For more information about the fiducial exclusion masks, see Ref. [68] and Figure 6.1.

6.2 Optimized Estimators and De-biasing Procedure

In preparation to apply the rotation formalism to WMAP data, we rewrite the estimator for the rotation-angle spherical-harmonic coefficients $\widehat{\alpha}_{LM}$ and their variances in the form that is convenient for implementation with the CMB-analysis software package HEALPix. Namely, instead of working with Wigner-3j symbols, we leave parts of the expressions in terms of triple-Y integrals in pixel space (position space). We then construct the estimator $\widehat{C}_L^{\alpha\alpha}$ for the rotation-angle autocorrelation $C_L^{\alpha\alpha}$, and discuss the method for de-biasing this measurement. The goal of this analysis is to measure the

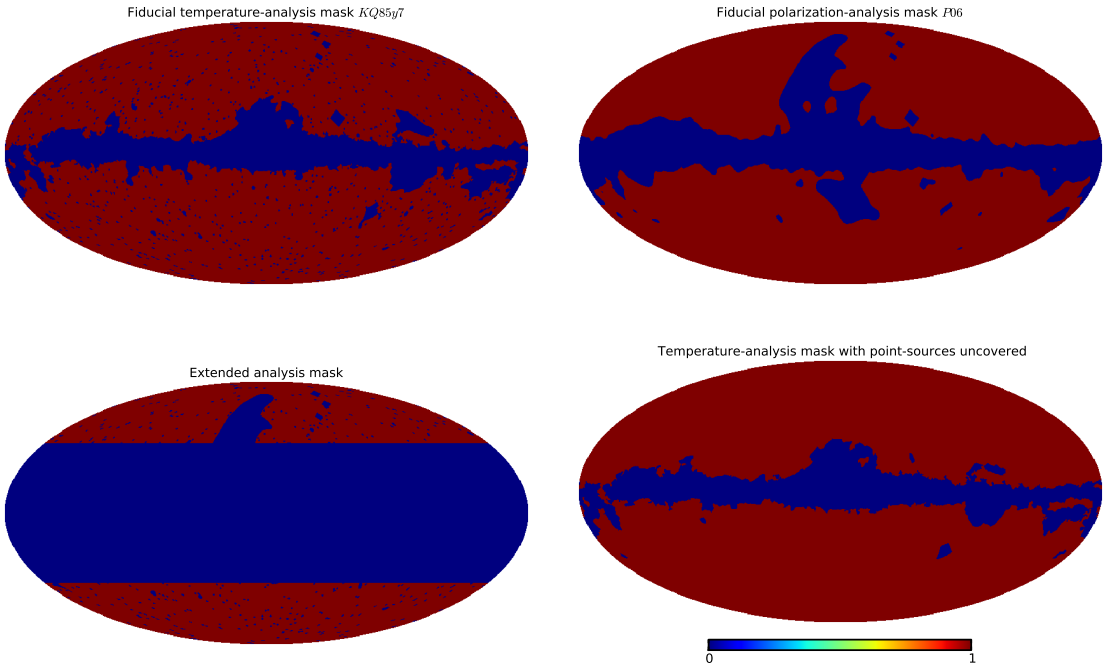

Figure 6.1: Fiducial temperature-analysis mask (with $\sim$ 78% of the sky admitted), fiducial polarization-analysis mask ($\sim$ 73%), extended mask ($\sim$ 33%), and the temperature-analysis mask with point sources uncovered ($\sim$ 82%). Fraction of the sky admitted of the combined fiducial masks for polarization and temperature is $\sim$ 68%, which is twice the sky admitted as compared to the extended mask. For more details on the use of the latter two masks, see Section 6.7.

rotation-angle power spectrum, or otherwise put an upper limit on a range of its multipoles, down to the resolution of WMAP. Formulas presented in this section are directly incorporated into our analysis pipeline.

In the presence of rotation, the polarization field acquires a phase factor,

$$p^{\rm tot}(\hat{\mathbf{n}}) \equiv [Q+iU](\hat{\mathbf{n}}) = p(\hat{\mathbf{n}})e^{2i\alpha(\hat{\mathbf{n}})}, \tag{6.1}$$

where the absence of a superscript denotes the polarization in the absence of rotation, which we refer to here as the "primary polarization". To obtain an estimate of the phase factor $e^{2i\alpha(\hat{\mathbf{n}})}$ from the polarization field in Eq. (6.1), we require a tracer of $p(\hat{\mathbf{n}})$. The primary polarization is generated by Thomson scattering of the local temperature quadrupole, so the observed temperature field may be used for this purpose. Due to projection effects, the local temperature quadrupoles at last scattering appear on the sky as a curvature of the temperature field. The estimator for the rotation angle then involves projecting the temperature field into a map as a spin-2 quantity (which evaluates the curvature) and looking for correlation with the polarization field which varies as a function of position in the sky. We turn to a rigorous derivation of the estimator in the following.

On the full sky, the polarization field can be decomposed in terms of spin-2 spherical harmonics ${}_2Y_{lm}(\hat{\mathbf{n}})$, as shown in Eq. (3.24), where E and B modes represent polarization patterns of opposite parity [28, 69]. The primary E-mode polarization signal (sourced by the dominant scalar perturbations) is detected with high significance in WMAP-7 data [46], while the primary B modes (sourced by the subdominant tensor perturbations) have only been constrained with upper limits. For this reason, most of the constraining power for rotation in WMAP comes from the search for the rotation of the primary E mode into an observed B mode. The induced B mode is given as [4, 51] (see also Eq. (3.26))

$$B_{\ell m} = \frac{i}{2}\int d\hat{\mathbf{n}}[p(\hat{\mathbf{n}})e^{2i\alpha(\hat{\mathbf{n}})}{}_2Y^*_{\ell m}(\hat{\mathbf{n}}) - p(\hat{\mathbf{n}})^* e^{-2i\alpha(\hat{\mathbf{n}})}{}_{-2}Y^*_{\ell m}(\hat{\mathbf{n}})]. \tag{6.2}$$

This B mode is correlated with the primary E mode (from which it originated), and through it also with the temperature anisotropies. The presence of rotation therefore gives rise to anomalous EB and TB correlations, and both these power spectra can be used to search for the rotation. It is, however, worth keeping in mind that individual multipoles of the E-mode polarization signal are still noise dominated, whereas the temperature is measured at $S/N > 1$, for a large number of multipoles, in every frequency band of the WMAP-7 data. Therefore, at WMAP-7 noise levels the temperature field makes a better tracer of the primary E mode than the observed E mode itself. For this reason, on most angular scales, the search for a TB correlation, which we focus on here, provides the best constraint on rotation (see Ref. [4] and Section 5.4).

Assuming the primary polarization is a pure E mode at the surface of last scatter, the rotation-induced TB correlation reads [4, 51] (see also Section 5.2)

$$\begin{aligned}&\left\langle B^{\rm tot}_{\ell m} T^{\rm tot,\,*}_{\ell' m'}\right\rangle \\ &= \int d\hat{\mathbf{n}} C^{TE}_{\ell'}\left[\frac{1}{2}\sin(2\alpha)[{}_2\mathrm{Y}_{\ell'\mathrm{m}'}{}_2\mathrm{Y}^*_{\ell\mathrm{m}} + {}_{-2}\mathrm{Y}_{\ell'\mathrm{m}'}{}_{-2}\mathrm{Y}^*_{\ell\mathrm{m}}] - \frac{\mathrm{i}}{2}\cos(2\alpha)[{}_2\mathrm{Y}_{\ell'\mathrm{m}'}{}_2\mathrm{Y}^*_{\ell\mathrm{m}} - {}_{-2}\mathrm{Y}_{\ell'\mathrm{m}'}{}_{-2}\mathrm{Y}^*_{\ell\mathrm{m}}]\right],\end{aligned} \tag{6.3}$$

where we suppress the $\hat{\mathbf{n}}$ dependence for clarity. The two contributions to the correlation, sin and cos, have opposite parities, where only terms that satisfy $\ell+\ell'+L=$even, and $\ell+\ell'+L=$odd, respectively, contribute to the sum. Power spectrum $C^{TE}_{\ell'}$ is the correlation between the temperature and the primary E mode, which we calculate using CAMB.

So far, we have not assumed anything about the magnitude of the rotation per pixel in CMB maps. As discussed in Chapter 4, from a combination of CMB data sets, the uniform rotation was previously constrained to be less than about a degree; the observations of quasars suggest an upper bound on the RMS of $\alpha(\hat{\mathbf{n}})$ of just a few degrees; and the measurement of the TE correlation from WMAP-7 data implies a somewhat weaker constraint on RMS rotation of less than about ten degrees (see Section 6.4 for details on this last calculation). Motivated by these results, in the rest of this work, we adopt a small–rotation-angle limit. The numerical results we present in Section 6.6

do not depend on the validity of this assumption, but their interpretation as an upper limit of the rotation-angle autocorrelation $C_L^{\alpha\alpha}$ does; this subtlety is discussed in more detail in Sections 6.5 and 6.6.

In the limit of small rotation angle, only the sine term contributes to the observed TB which then reads

$$\left\langle B_{lm}^{\rm tot} T_{l'm'}^{\rm tot,*} \right\rangle \approx \int d\hat{\mathbf{n}} C_{\ell'}^{TE} \alpha(\hat{\mathbf{n}}) [{}_2Y_{\ell'm'}(\hat{\mathbf{n}}) {}_2Y_{\ell m}^*(\hat{\mathbf{n}}) + {}_{-2}Y_{\ell'm'}(\hat{\mathbf{n}}) {}_{-2}Y_{\ell m}^*(\hat{\mathbf{n}})]. \tag{6.4}$$

A TB correlation generated by weak gravitational lensing of the CMB is of opposite parity, with $\ell+\ell'+L=$odd, and does not represent a source of bias for measuring a small-rotation signal (as discussed in detail in Section 5.3). In addition, the effect of lensing is not internally observable at WMAP noise levels, even with an optimal estimator [70]. We therefore do not consider lensing further in this section.

From Eq. (6.4), it is evident that scale-dependent birefringence induces correlations between temperature and polarization modes at different wavenumbers (multipoles) ℓ, ℓ'; i.e., it produces a statistically anisotropic imprint on the covariance matrix of the observed CMB. Each $\ell\ell'$ pair measured in the maps may therefore be used as an estimate of the rotation-angle multipole α_{LM}, provided that it satisfies the usual triangle inequalities[1], as well as the parity condition $\ell+\ell'+L=$even. The prescription for combining all $\ell\ell'$ estimates in order to produce a minimum-variance quadratic estimator is explained in detail in Ref. [4] and in Section 5.2, and is somewhat similar to the prescription presented in Ref. [58]. Here, we only present the final expressions for the TB estimator,

$$\widehat{\alpha}_{LM} = N_L \int d\hat{\mathbf{n}} Y_{LM}(\hat{\mathbf{n}}) \left[\sum_{\ell m} \bar{B}_{\ell m}^* {}_2Y_{\ell m}(\hat{\mathbf{n}}) \sum_{\ell' m'} C_{\ell'}^{TE} \bar{T}_{\ell' m'} {}_2Y_{\ell' m'}^*(\hat{\mathbf{n}}) + (\text{complex conjugate}) \right], \tag{6.5}$$

where N_L is an L-dependent normalization and the barred quantities denote inverse-variance filtered multipoles. For full-sky coverage and homogenous noise in pixel space, the expressions for these quantities read

$$\begin{aligned} \bar{B}_{\ell m} &\equiv \frac{B_{\ell m}^{\rm map}}{C_\ell^{BB,\rm map}}, \\ \bar{T}_{\ell' m'} &\equiv \frac{T_{\ell' m'}^{\rm map}}{C_{\ell'}^{TT,\rm map}}. \end{aligned} \tag{6.6}$$

The unbarred $B_{\ell m}^{\rm map}$ and $T_{\ell' m'}^{\rm map}$ are the observed temperature and polarization multipoles corrected for the combined instrumental beam and pixelization transfer function[2] W_ℓ, and the TT and BB

[1] These are the inequalities that the triple-Y integrals, or Wigner-3j symbols, must satisfy; see Appendix A for more details.

[2] Note that W_ℓ in this section includes the pixelization transfer function which approximates smoothing of the signal fluctuations as they are binned into pixels; this is a small effect which should be taken into account in the actual data analysis, even though we neglected it in previous theoretical considerations of Chapter 5.

power spectra are analytic estimates of the cosmological signal (under the null assumption of no rotation) + noise power spectrum in a given frequency band,

$$\begin{aligned} C_\ell^{TT,\mathrm{map}} &\equiv C_\ell^{TT} + C_\ell^{TT,\mathrm{noise}}/W_\ell^2, \\ C_\ell^{BB,\mathrm{map}} &\equiv C_\ell^{BB} + C_\ell^{BB,\mathrm{noise}}/W_\ell^2. \end{aligned} \tag{6.7}$$

Notice that we use slightly different notation than in Section 3.3 and Chapter 5; here, symbols with "tot" and "map" denote quantities already corrected for the beam and pixelization transfer function W_ℓ. In the idealized case of full-sky coverage and homogeneous instrumental noise, the estimator normalization N_L is calculable analytically and is equal to the inverse of the estimator variance,

$$N_L = \left(\sum_{\ell\ell'} \frac{(2\ell+1)(2\ell'+1)}{4\pi} \frac{(C_{\ell'}^{TE})^2}{C_\ell^{BB,\mathrm{map}} C_{\ell'}^{TT,\mathrm{map}}} (H_{\ell\ell'}^L)^2 \right)^{-1}, \tag{6.8}$$

where

$$H_{\ell\ell'}^L = \begin{pmatrix} \ell & L & \ell' \\ -2 & 0 & 2 \end{pmatrix} + \begin{pmatrix} \ell & L & \ell' \\ 2 & 0 & -2 \end{pmatrix}, \tag{6.9}$$

again, slightly differently defined than in Chapter 5. The objects in parentheses are Wigner-3j symbols, as before.

In the non-idealized case of real data, the simple analytic inverse-variance filters presented in Eqs. (6.6) and (6.7) are suboptimal, in the sense that the associated estimator variance is not truly minimized. To obtain a true minimum-variance estimate, computationally more involved filters are required [70]. In practice, however, we find that the full-sky expressions for the estimator in Eq. (6.5) provide a very good approximation to its behavior on the cut sky. Namely, the analytic expression for its variance, given by Eq. (6.8), is consistent with the full variance recovered from a suite of Monte Carlo simulations (described in detail in Section 6.5) when the simple inverse-variance filters are used in the presence of sky cuts[3]. This result motivates us to continue using the simple inverse-variance filters and the corresponding analytic expressions for the estimator normalization.

The insensitivity to the presence of the Galactic mask that we observe here can be interpreted as a consequence of the following properties. First, the estimator of Eq. (6.5) is a product of inverse-variance filtered T and B maps in position space, which are local functions of the data. The inverse-variance filters are local in pixel space (they resemble Gaussians with a width of a few arcmins, corresponding to the resolution in a given frequency band), and so the mask boundaries remain localized after filtering. Additionally, the estimator is an even function of the temperature map (see Eq. (6.5)—it contains a second derivative of the temperature field performed by ${}_2Y_{\ell' m'}$), and so it is relatively insensitive to the discontinuities introduced by the analysis mask. These properties put the

[3]The appropriate correction for the fraction of the sky admitted by the analysis masks must be included in this case, however; more details on this in Section 6.5.

rotation estimator $\widehat{\alpha}_{LM}$ in sharp contrast with the estimators for the gravitational-lensing potential, where the dependence on the gradient of the temperature field renders the lensing reconstruction very sensitive to sky cuts [71].

A word of caution before we proceed. In order to apply the full-sky formalism to the cut sky (after contaminated portions of the sky have been masked), all measured power spectra need to be corrected[4] by a factor of $\sim 1/f_{\rm sky}$. Unless otherwise noted, $f_{\rm sky}$ is calculated as the fraction of the pixels that the mask admits. We include this factor when appropriate in the following derivation.

Once the rotation-angle multipoles are measured, using the estimator of Eq. (6.5), their auto-correlation can be estimated as

$$C_L^{\widehat{\alpha}\widehat{\alpha}} \equiv \frac{1}{f_{\rm sky}(2L+1)} \sum_M \widehat{\alpha}_{LM} \widehat{\alpha}^*_{LM}. \tag{6.10}$$

This represents a sum over the $\langle TBTB \rangle$ trispectrum, where T and B denote the temperature and B-mode multipole moments. This estimator for $C_L^{\alpha\alpha}$ is non-zero, even in the absence of rotation, due to the presence of Wick contractions from the primary CMB and the instrumental noise. They produce the *noise bias* $C_L^{\alpha\alpha,\ \rm noise}$, and must be subtracted from the measurement of $C_L^{\widehat{\alpha}\widehat{\alpha}}$, in order to recover an estimate $\widehat{C}_L^{\alpha\alpha}$ of the rotation-induced signal $C_L^{\alpha\alpha}$,

$$\widehat{C}_L^{\alpha\alpha} = C_L^{\widehat{\alpha}\widehat{\alpha}} - C_L^{\alpha\alpha,\rm noise}. \tag{6.11}$$

For Gaussian CMB+noise fluctuations, the noise bias can be identified with the three disconnected Wick contractions of the trispectrum which $C_L^{\widehat{\alpha}\widehat{\alpha}}$ probes:

$$\begin{aligned} &(a) \quad TBTB \\ &(b) \quad TBTB \\ &(c) \quad TBTB. \end{aligned} \tag{6.12}$$

We neglect contraction (a), which only couples to the $L = 0$ mode of $\widehat{\alpha}_{LM}$, and also contraction (c), as it is negligible[5]. In the absence of statistical anisotropy (i.e., for full-sky coverage and homogeneous instrumental noise), the contraction (b) between two real fields with multipoles $\ell m, \ell' m'$ carries a set of delta functions $\delta_{\ell\ell'}\delta_{mm'}$, and the realization-dependent noise bias may be written explicitly in terms of the observed power spectra. If $C_L^{\widehat{\alpha}\widehat{\alpha}}$ is evaluated by cross-correlating the f_1, f_2, f_3, and

[4] When multipole coefficients are calculated from a map where a fraction $1 - f_{\rm sky}$ of the pixels is masked (i.e., signal set to zero), the usual full-sky expression for their variance (i.e., the power spectrum, as calculated in Eq. (3.29)) is underestimated by a factor of $f_{\rm sky}$, because the variance corresponding to the masked pixels is effectively zero.

[5] In our simulations, we verify that this term has indeed a negligible numerical contribution.

f_4 frequency-band maps, the analytic expression for this *isotropic bias* follows from Eq. (6.5),

$$C_L^{\alpha^{f_1 f_2}\alpha^{f_3 f_4},\mathrm{noise,iso}} \equiv \langle \widehat{\alpha}_{LM} \widehat{\alpha}^*_{LM} \rangle_{\mathrm{Gauss,iso}} = \\ N_L^2 \sum_{\ell\ell'} \frac{(2\ell+1)(2\ell'+1)}{4\pi} (H^L_{\ell\ell'} C^{TE}_{\ell'})^2 \frac{\widehat{C}^{TT,f_1 f_3,\mathrm{map}}_{\ell'} \widehat{C}^{BB,f_2 f_4,\mathrm{map}}_{\ell}}{(C^{TT,f_1 f_1,\mathrm{map}}_{\ell'} C^{BB,f_2 f_2,\mathrm{map}}_{\ell} C^{TT,f_3 f_3,\mathrm{map}}_{\ell'} C^{BB,f_4 f_4,\mathrm{map}}_{\ell})}, \tag{6.13}$$

where the power spectra in the denominator of Eq. (6.13) are the simple analytic inverse-variance filters. The $\widehat{C}^{TT,f_1 f_3,\mathrm{map}}_{\ell'}$ and $\widehat{C}^{BB,f_2 f_4,\mathrm{map}}_{\ell}$ are measured by cross-correlating data maps in the frequency bands f_1 and f_3, or f_2 and f_4 respectively, and corrected by the factor of $1/f^{\mathrm{T}}_{\mathrm{sky}}$ and $1/f^{\mathrm{P}}_{\mathrm{sky}}$, corresponding to the temperature and polarization analysis mask, respectively. Most of the power in temperature comes from CMB fluctuations, and the B-mode power is mostly noise if $f_2 = f_4$, and negligible otherwise. Therefore, since the instrumental noise is independent for different frequency bands, the largest contribution to the noise bias can be eliminated by cross-correlating estimates of $\widehat{\alpha}_{LM}$ obtained from two different frequency bands.

In reality, we work with a masked sky which has been observed with inhomogeneous noise levels, and Eq. (6.13) does not provide a perfect description of the noise bias, although it is an excellent first approximation. This leads us to utilize a two-stage de-biasing procedure in which we subtract both the data-based isotropic bias of Eq. (6.13), and an additional Monte-Carlo–based correction, in order to correct for the effects of sky cuts and inhomogeneity of the instrumental noise. The total noise bias $C_L^{\alpha\alpha,\ \mathrm{noise}}$ is the sum of the two contributions,

$$C_L^{\alpha\alpha,\mathrm{noise}} \equiv C_L^{\alpha\alpha,\mathrm{noise,iso}} + C_L^{\alpha\alpha,\mathrm{noise,MC}}. \tag{6.14}$$

We estimate $C_L^{\alpha\alpha,\mathrm{noise,MC}}$ from a set of WMAP realizations generated with no rotation signal (described in Section 6.5), analyzed in the same way as the data itself. For each realization, we calculate the appropriate $C_L^{\alpha\alpha,\mathrm{noise,iso}}$, and, averaging over many realizations, we obtain $C_L^{\alpha\alpha,\mathrm{noise,MC}}$ as

$$C_L^{\alpha\alpha,\mathrm{noise,MC}} \equiv \langle C_L^{\widehat{\alpha}\widehat{\alpha}} - C_L^{\alpha\alpha,\mathrm{noise,iso}} \rangle_{\mathrm{sims}}. \tag{6.15}$$

This two-stage procedure reduces the sensitivity of our estimator to uncertainties in the CMB and instrumental-noise model, as compared to the case where the entire bias is recovered from Monte Carlo analysis. With the two-stage procedure, the largest (isotropic) contribution to the bias is evaluated directly from the power spectra of the observed maps, and is specific to the CMB realization at hand; subtracting it from the bispectrum naturally takes care of any noise (bias) contribution that might arise from the uncertainty in the background cosmology or in the noise description used to generate Monte Carlo simulations. The procedure is equivalent to simply omitting the terms in the expression for the bispectrum which we know come from sources other than the rotation signal.

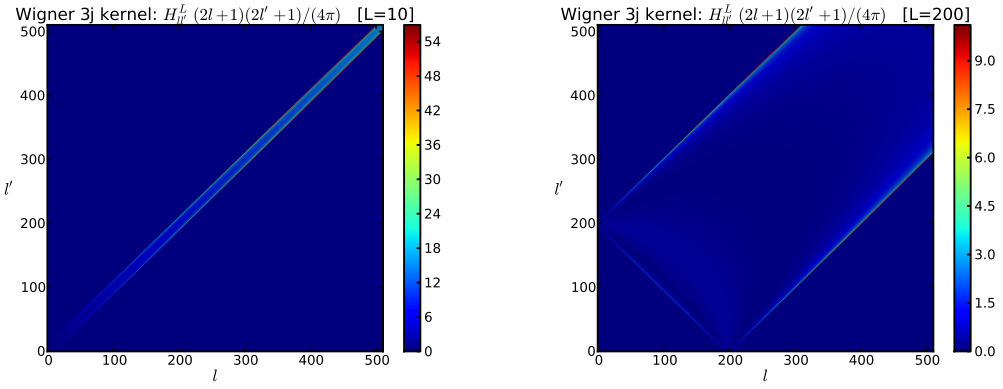

Figure 6.2: The Wigner-3j geometric factors in the summands of Eqs. (6.5) and (6.13), for $L = 10$ and 200. The geometric factor is non-zero only in the region of the $\ell\ell'$ space where the triangle inequalities, and parity conditions are satisfied. The dominant contribution comes from the triangles in which $L \sim \ell$, or $L \sim \ell'$, i.e., where either the temperature or the polarization mode has a length scale comparable to the length scale of the rotation-angle mode.

As shown in Section 6.6, we find consistency of the results obtained with either the calculation of the trispectrum as a four-point autocorrelation of the maps in the same band, or the calculation of the trispectrum from cross-band correlations, which have an almost negligible noise bias.

6.3 Geometry of the Estimators

For completeness, to illustrate the shape in harmonic space of the statistical anisotropy introduced by birefringent rotation, we show here the power-spectrum kernel, as well as the geometric Wigner-3j contributions to the kernels in the $\ell\ell'$ space from Eq. (6.5) in Figures 6.2, and 6.3. The structure of the power-spectrum kernel originates from the polarization and temperature power spectra, so that the terms that correspond to the acoustic peaks in the primordial TT and TE power spectra have the largest contribution to the sums over ℓ and ℓ'. The geometric weight (corresponding to the Wigner-3j symbols discussed in Section 5.2) dictates the shape of the $\ell\ell' L$ triangles generated by the rotation at a scale L. The terms where either ℓ, or ℓ' is close in value to L have the largest contribution. The combination of the geometric weight and the power-spectra weight dictates the size of the statistical uncertainty at any particular L. The interplay of the two, for example, produces a peak at $L \sim 270$, apparent in all the plots of the noise bias presented in this work (see, for example, Figure 6.7). The local maximum in the variance of $\widehat{C}^{\alpha\alpha}_L$ also appears at this scale.

6.4 Constraints on RMS Rotation Revisited

We argued in Chapter 4 that the small-angle approximation and the null assumption are proven to hold, by non-detection of rotation in WMAP data. Our results in Section 6.6 will demonstrate

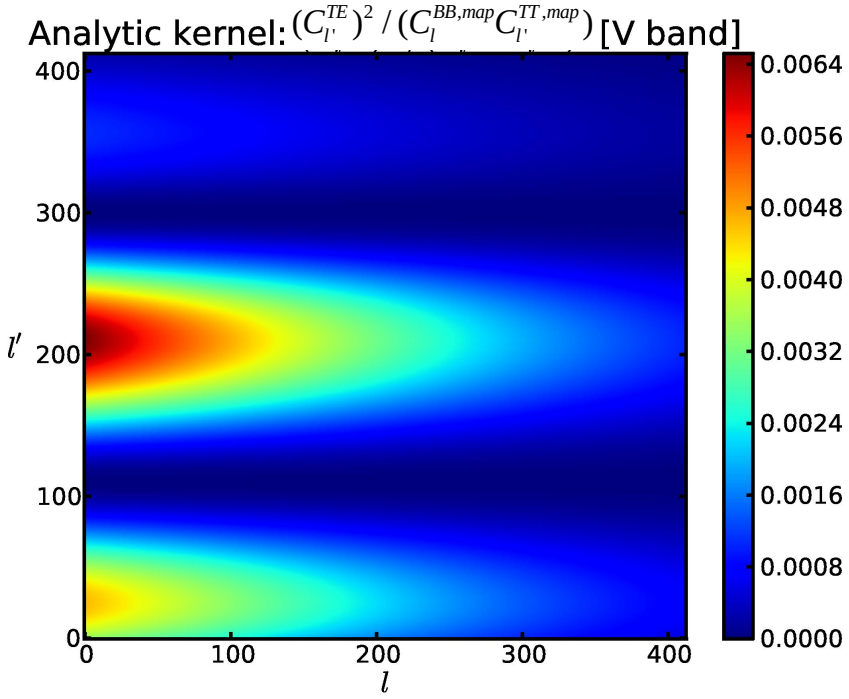

Figure 6.3: The power-spectrum kernel of the summands in Eqs. (6.5) and (6.13) is shown. The types of triangles that contribute the most to the isotropic bias of $C_L^{\hat{\alpha}\hat{\alpha}}$ are set by the geometric properties of spin-2 Wigner-3j symbols illustrated by the kernel shown in Figure 6.2, which is modulated by this kernel to produce summands in the expression for the bias.

that this is true for uniform rotation; here, we repeat previous WMAP analysis that provides an upper limit to the pixel variance (or the RMS) of rotation from the measurement of the TE power spectrum.

If the primordial B mode is small compared to the primordial E mode, and the rotation field is independent of the CMB, the measured TE power spectrum reads (see also Figure 6.4)

$$C_\ell^{TE,\mathrm{tot}} = \langle \cos[2\alpha(\hat{\mathbf{n}})] \rangle \, C_l^{TE}, \tag{6.16}$$

where the mean is taken over all realizations of the rotation field, and it does not depend on the direction $\hat{\mathbf{n}}$. In the case the probability distribution for α is a Gaussian centered at zero and with a width $\langle \alpha(\hat{\mathbf{n}})^2 \rangle^{1/2}$, the expectation value in Eq. (6.16) is simply related to the pixel-variance of α,

$$\langle \cos[2\alpha(\hat{\mathbf{n}})] \rangle = e^{-2\langle \alpha(\hat{\mathbf{n}})^2 \rangle}. \tag{6.17}$$

Therefore, an estimate of this expectation value and its uncertainty, obtained from the TE measurement as compared to the primordial power spectrum C_l^{TE}, provides an upper limit of the rotation-angle pixel-variance. Using the expressions for a minimum-variance estimator and its vari-

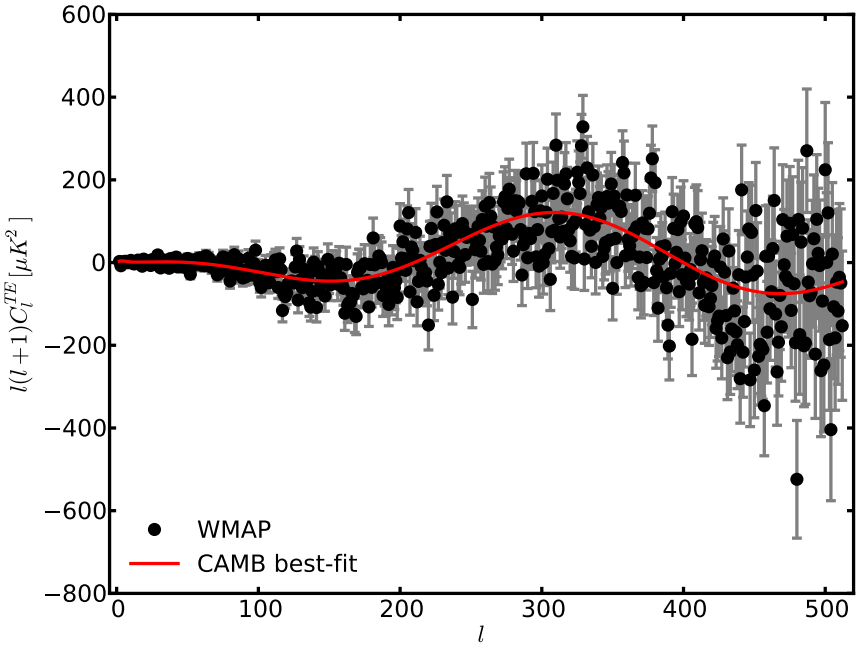

Figure 6.4: TE power spectrum measured from WMAP-7 data (black) is compared to the primordial power spectrum, generated using CAMB for the best-fit cosmology, with no rotation (red, solid). Both power spectra are adopted from Ref. [8]. The uncertainty on this measurement (gray error bars) leaves room for a maximal rotation-angle RMS of roughly 9.5°.

ance (analogous to those of Eqs. (9.9) and (9.10)), we obtain[6]

$$\langle \cos[2\alpha(\hat{\mathbf{n}})] \rangle = 0.997 \pm 0.050, \tag{6.18}$$

implying an upper limit on the rotation RMS of

$$\left\langle \alpha(\hat{\mathbf{n}})^2 \right\rangle^{1/2} \lesssim 9.5^\circ. \tag{6.19}$$

6.5 Simulations and Test Run

We now describe our Monte Carlo simulations of the observed CMB maps, and also present results of a test run for a toy model of rotation, to ensure that our formalism and analysis method recover the signal accurately.

We produce a suite of simulated WMAP observations, to test the normalization of our α_{LM}

[6]Note that this constraint also follows from the 21σ confidence-level detection of the TE power spectrum, reported by Ref. [46].

estimates, calculate their variance and the noise bias $C_L^{\alpha\alpha,\ \rm noise}$ of Eq. (6.11). We produce simple simulations of the WMAP data with the following procedure:

1. Generate CMB-sky temperature and polarization realizations for the best-fit "LCDM+SZ+ALL" WMAP-7 cosmology of Ref. [8].

2. Convolve simulated CMB skies with a symmetric experimental beam. For the WMAP band maps, we use an effective beam calculated as the average beam transfer function for all differencing assemblies at a given frequency.

3. Add simulated noise realizations based on the published I, Q, U covariance matrices within each pixel. We do not make any attempt to generate noise with pixel-to-pixel noise correlations, although we do exclude multipoles with $l < 100$ from our analysis, as this is where most of the correlated noise resides. We demonstrate that there is consistency of $\widehat{C}_L^{\alpha\alpha}$ estimates constructed from autocorrelations and cross-correlations of maps with independent noise realizations, and so are justified in neglecting correlated noise in our analysis.

We do not include Galactic foreground residuals or unresolved point sources in our simulations, but we address their possible impact on our results in Section 6.7.

In order to demonstrate the recovery of the cosmic-birefringence signal using the minimum-variance estimator formalism and the de-biasing method discussed in Section 6.2, we generate a suite of simulations that include a rotation signal, i.e., where the polarization maps are rotated by realizations of a scale-invariant power spectrum,

$$C_L^{\alpha\alpha} = A C_L^{\alpha\alpha,\rm fiducial} \equiv A \frac{131\rm deg^2}{L(L+1)}, \tag{6.20}$$

where we choose the amplitude of this fiducial model so that it gives a signal-to-noise ratio of order 1 at low L for WMAP V band, and an RMS rotation-angle on the sky of 10°, satisfying the small-angle approximation[7]. We apply analysis masks to each simulated map, and then analyze the map cross-correlations, recovering $\widehat{\alpha}_{LM}$ multipoles. We then compute the power spectrum using Eq. (6.10). Due to the interaction of the power distribution at different scales in the map with the geometry of the analysis mask, the $f_{\rm sky}$ factor is in principle a function of the multipole moment L, which typically starts smaller than the average[8] value at low L's, and converges towards the average value at high L's. Since most of the signal for the model of Eq. (6.20) (which we come back to in Section 6.6) comes from low L's, we evaluate the exact L dependence, and substitute the $f_{\rm sky}(L)$ function in Eq. (6.10).

[7] It is important that the model satisfies the small-angle approximation, as our calculation of the bias from Monte Carlo analysis is based on the null assumption. In the regime where this approximation is not satisfied, higher-order corrections will be necessary to recover the rotation-angle power spectrum from the measured $\langle TBTB\rangle$ trispectrum.

[8] The "average" here is the usual $f_{\rm sky}$ fraction associated with a mask, equal to the fraction of the pixels that the mask admits.

In order to evaluate the exact L-dependence of $f_{\rm sky}$, we generate a large number of $\alpha(\hat{\mathbf{n}})$ realizations of the power-spectrum model of Eq. (6.20), mask the sky with the fiducial analysis mask, and then recover the input power spectrum in the usual way, i.e., take the pseudo-C_L of the masked map. The $f_{\rm sky}(L)$ shown in Figure 6.5 is the average ratio of the output (recovered) to the input (signal) power, as a function of the multipole moment L.

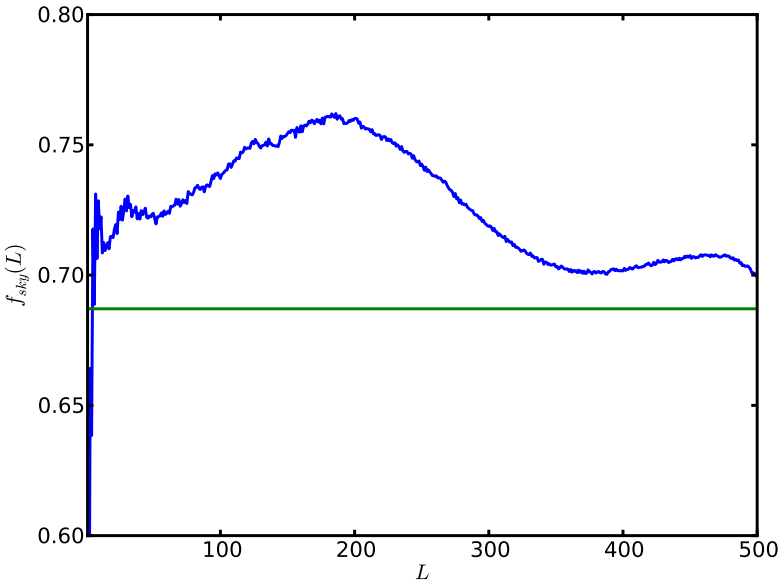

Figure 6.5: The L dependence of the $f_{\rm sky}$ factor used for the reconstruction of a scale-invariant rotation-angle power spectrum. The horizontal (green) line at $f_{\rm sky} = 0.68$ represents the fraction of pixels admitted by the mask.

Figure 6.6 shows the results of the test run, comparing the input $C_L^{\alpha\alpha}$ power spectrum to the mean of the reconstructed power from a large number of simulations, and demonstrate a successful recovery of the signal. In Section 6.6, we apply the same signal-reconstruction method to WMAP-7 data.

To conclude this section, we note one subtlety necessary for the correct interpretation of the results of our analysis. The expression for the estimator of Eq. (6.5) only recovers the rotation-angle multipole in the small-angle regime. In the general case of arbitrarily large rotation, Eq. (6.5) provides an exact estimate of the multipoles of another observable quantity: $\frac{1}{2}\sin[2\alpha(\hat{\mathbf{n}})]$. Strictly speaking, our de-biasing procedure also relies on the small-angle approximation, since $C_L^{\alpha\alpha,{\rm noise,MC}}$ is calculated from a suite of null simulations. It is therefore necessary to inquire which regime corresponds to a particular model of rotation before interpreting our results as a constraint on such a model. However, the fiducial model we use as an example here satisfies this assumption (producing an RMS rotation of $\sim 10^\circ$). In this particular case, the difference between the two power spectra

(of α and of $\frac{1}{2}\sin[2\alpha]$) is mainly contained in the 15% difference in their amplitudes. It is thus possible to recover the rotation-angle power spectrum by simply rescaling the measured power for this case—the fact we use in Section 6.6 to constrain this model from WMAP data.

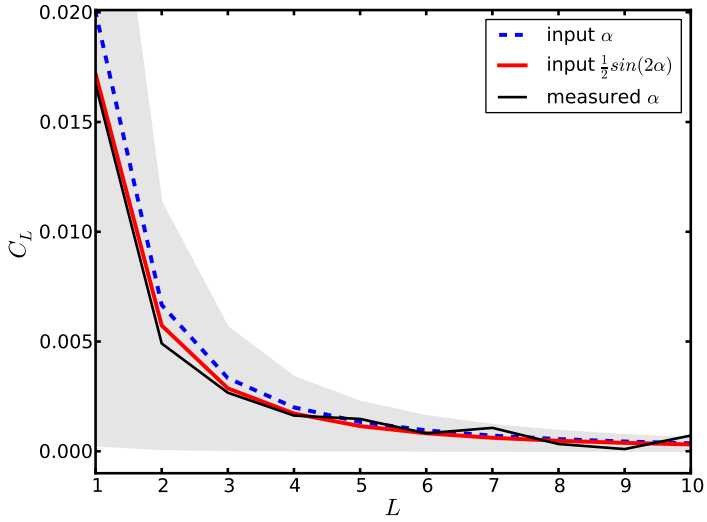

Figure 6.6: The recovery of the rotation signal with our analysis method is demonstrated using a suite of simulations that include realizations of a rotated sky. Blue dashed line is the input-signal power spectrum of $C_L^{\alpha\alpha}$, red thick line represents the power spectrum of $\frac{1}{2}\sin[2\alpha(\hat{\mathbf{n}})]$, and the thin black line is the mean recovered power from the simulations; the gray region is a 1σ–confidence-level interval calculated from the same suite of simulations.

6.6 Results: Constraints on $C_l^{\alpha\alpha}$

In this section, we present the results of our analysis to look for rotation from cosmic birefringence in WMAP data. Before continuing, let us first clarify some of our notation. The rotation-angle power spectra are marked with four frequency bands as $[f_1 f_2][f_3 f_4]$. This means that the two estimates of α_{LM} needed to evaluate the power spectrum are obtained by cross-correlating band f_1 with f_2, and f_3 with f_4, respectively. Here, the temperature multipoles are measured from f_1 and f_3, and the B modes are obtained from the maps in f_2 and f_4 bands. We measure five different cross-band correlations: [VV][VV], [QV][QV], [QQ][VV], [WV][WV], and [WW][VV], but since the results for all of them are qualitatively the same, here we only show plots for a characteristic subset.

Figures 6.7, 6.8, and 6.9 show the measurement of the rotation-angle autocorrelation, before and after de-biasing, and different components of the noise bias described in Section 6.2. The blue and gray areas in the middle panels represent 1σ and 3σ confidence-level intervals, respectively, derived from the null-hypothesis (no rotation) Monte Carlo analysis described in Section 6.5. We see no significant deviations from zero in any of the five cross-band correlations—our results are consistent

with $\alpha_{LM} = 0$, within 3σ at each multipole, in the range from $L = 0$ to 512.[9] We bin the power and list the measurements for all multipoles in Table 6.2. As an additional consistency check, the upper limit we obtain on the uniform rotation angle, given as $\alpha \equiv \alpha_{00}/\sqrt{4\pi}$, is in good agreement with previous WMAP results [46], as shown in Table 6.3.

As we pointed out in Section 6.5, in the general case of arbitrarily large rotation, our method provides an exact estimate of the autocorrelation of the quantity $\frac{1}{2}\sin[2\alpha(\hat{\mathbf{n}})]$, rather than the rotation angle itself; when the small-angle approximation is satisfied, this quantity and its power spectrum assymptote to $\alpha(\hat{\mathbf{n}})$ and $C_L^{\alpha\alpha}$, respectively. In order to evaluate the regime corresponding to a particular model, we note that the RMS fluctuation typical of realization of a power spectrum $C_L^{\alpha\alpha}$ is given by

$$\langle \alpha(\hat{n})^2 \rangle^{1/2} = \sqrt{\sum_L \frac{2L+1}{4\pi} C_L^{\alpha\alpha}}. \tag{6.21}$$

In the event of a breakdown of the small-angle approximation, the values in Table 6.2 should be interpreted as constraints on the autocorrelation of $\frac{1}{2}\sin[2\alpha(\hat{\mathbf{n}})]$, rather than α itself[10]. Evaluating Eq. (6.21) for the uncertainty levels quoted in Table 6.2 would erroneously lead to a conclusion that a large RMS rotation is allowed by the WMAP data. We show that the upper limit on the RMS rotation is roughly 9.5° in Section 6.4, and we again note that previous studies of quasar data imply an even stronger constraint of $\sim 4°$ [43].

L bin	[VV][VV]	[QV][QV]	[QQ][VV]	[WV][WV]	[WW][VV]
26	2.65±1.87	1.61±2.44	1.05±1.62	0.72±2.03	-0.43±1.34
77	1.86±2.58	0.70±2.84	1.57±2.36	1.03±2.70	0.17±2.04
128	1.07±1.33	1.00±1.36	0.27±1.17	3.04±1.35	0.96±1.02
179	1.40±1.49	-1.29±1.65	-0.31±1.15	-0.40±1.48	0.66±1.13
230	-1.90±1.76	-4.47±1.96	1.87±1.36	-3.36±1.97	-0.69±1.33
282	4.31±2.23	3.17±2.42	2.04±2.21	2.14±2.42	-0.20±1.90
333	1.98±2.39	-0.25±2.60	4.59±1.80	2.62±2.45	-1.11±1.96
384	0.81±1.78	-1.71±1.93	1.97±1.51	1.22±1.71	1.93±1.52
435	-0.40±1.64	-0.19±1.80	1.53±1.26	-1.03±1.74	-1.65±1.30
486	3.22±1.75	0.78±1.93	1.02±1.39	2.69±1.84	-0.28±1.27

Table 6.2: Results for the measurement of $\widehat{C}_L^{\alpha\alpha}$ [degrees^2] are listed, as recovered from five different cross-band correlations. The 1σ confidence intervals are calculated with a suite of Gaussian-sky simulations, described in Section 6.5. The results are binned, with the central L value of each bin listed in the Table; the width of each bin is $\Delta L \sim 51$.

The null result shown here is model independent, but it can be translated into an upper limit

[9] Of course, a closer inspection of some of the ℓ bins in some cross-band correlations might be interpreted as 1σ-2σ *detection* instead of null result within a 3σ confidence interval. However, since the birefringent rotation we are looking to detect is a frequency-independent effect, we would expect *consistency in all band-cross correlations*, which we do not observe, at any of the multipoles. Therefore, we are justified in quoting our cleanest cross-band measurements as upper limits on the rotation-angle power-spectrum multipoles.

[10] In addition, the de-biasing procedure would possibly need to be adjusted in order to include higher-order corrections which might affect the results presented here.

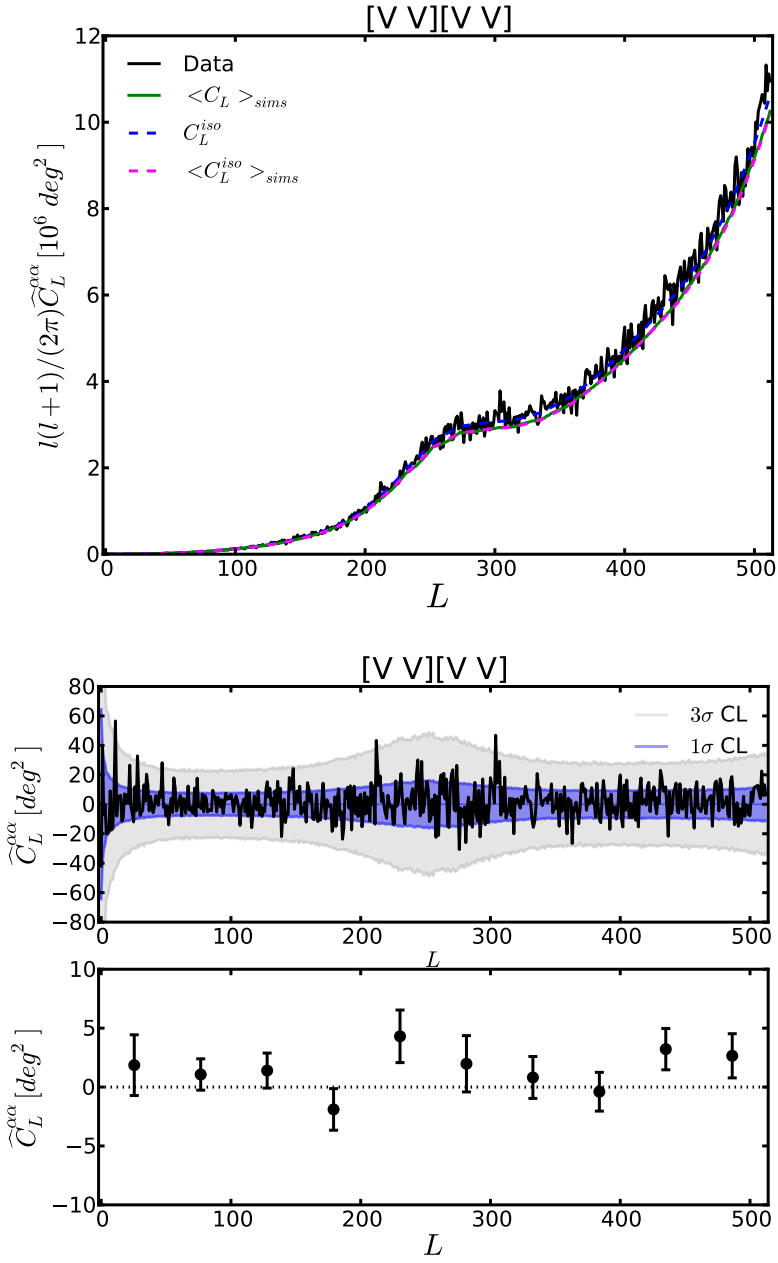

Figure 6.7: Top panel: Measurement of the rotation-angle power spectrum from V band, shown before de-biasing, along with the components of the noise bias: Monte-Carlo measurement of the null-hypothesis mean $\langle \widehat{C}_L^{\alpha\alpha} \rangle$ (solid green), isotropic noise bias (blue dashed), and the mean isotropic bias (magenta dashed). Middle panel: The same power spectrum after de-biasing, with 1σ and 3σ confidence interval. Bottom panel: binned version of the middle-panel power spectrum. The results are consistent with zero within 3σ.

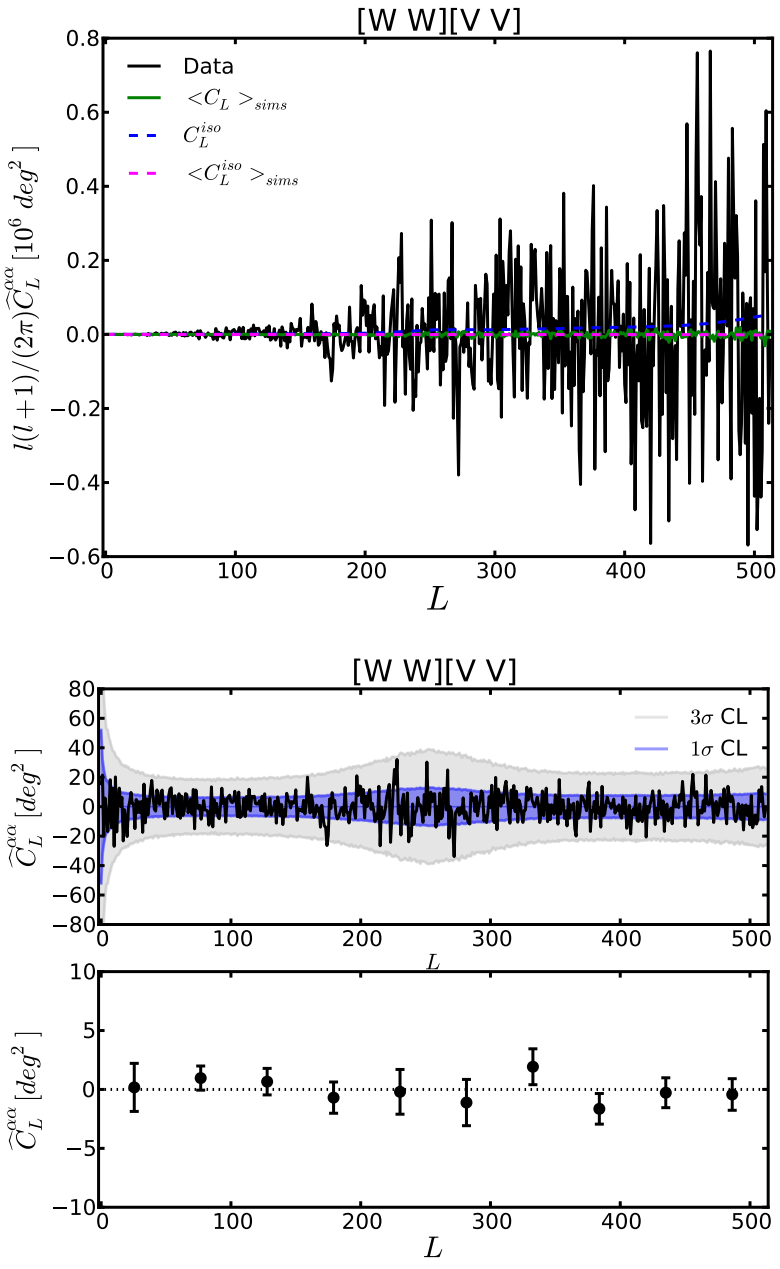

Figure 6.8: Same as Figure 6.7, for $[f_1 f_2][f_3 f_4]$=[WW][VV].

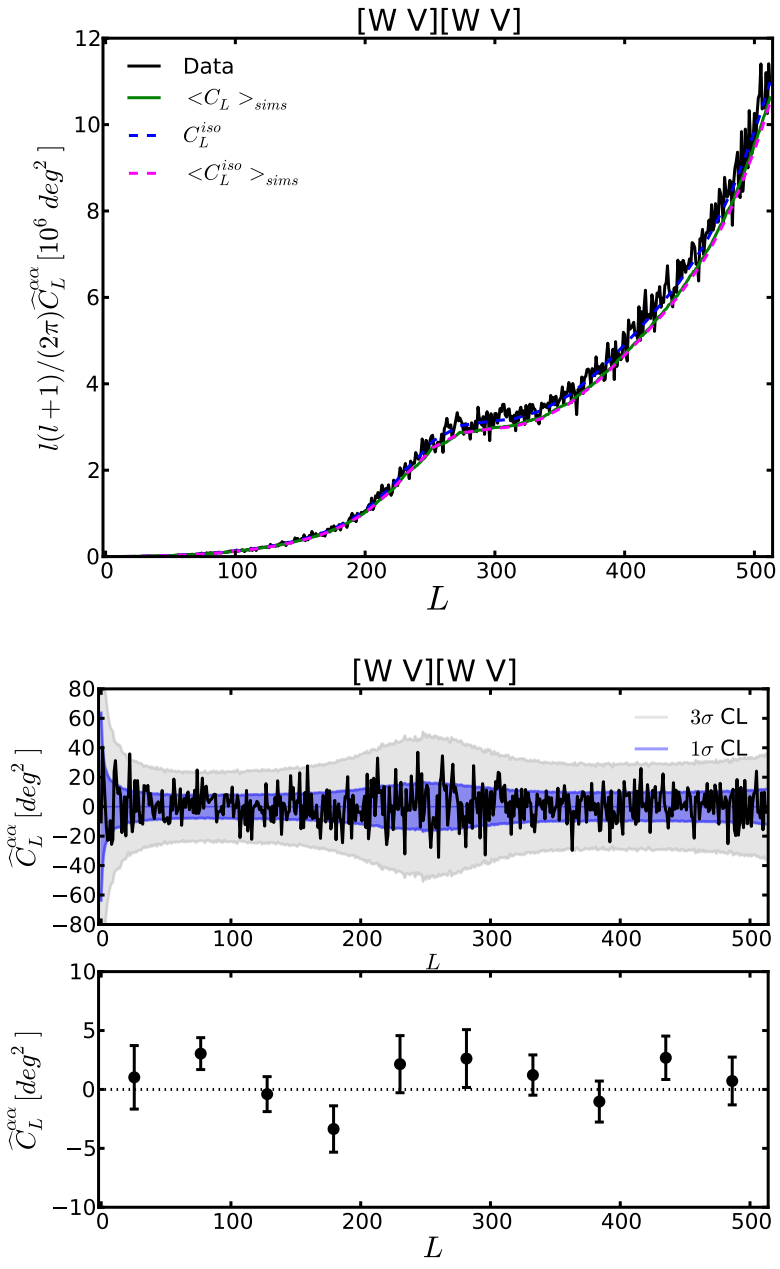

Figure 6.9: Same as Figure 6.7, for $[f_1 f_2][f_3 f_4]$=[WV][WV].

$[f_1 f_2]$	$\alpha \pm 1\sigma$ [°]
[VV]	-0.9 ± 2.3
[QV]	-0.5 ± 2.4
[QQ]	0.9 ± 2.8
[WV]	-2.2 ± 2.4
[WW]	-1.8 ± 2.7

Table 6.3: Uniform-rotation angle α with a 1σ confidence interval, from five cross-band correlations of WMAP-7; the correction factor of $1/f_{\rm sky}$ is applied to each measurement here. The uncertainties are consistent with the $\pm 1.4°$ uncertainty on the uniform-rotation angle reported by the WMAP team [46] for a joint analysis of the Q-, V- and W-band data, after accounting for the fact that we analyze the bands individually (resulting in slightly larger error bars).

on the amplitude of any specific model of rotation. As a generic example, we focus on a scale-invariant rotation-angle power spectrum[11] of Eq. (6.20). The best-fit amplitude is evaluated from all multipoles in the range $0 \leq L \leq 512$, using a Fisher-matrix minimum-variance estimator, as in Ref. [7]

$$\widehat{A} = \sigma_A^2 \sum_L \frac{C_L^{\alpha\alpha,\rm fiducial} \widehat{C}_L^{\alpha\alpha}}{\rm var(\widehat{C}_L^{\alpha\alpha})}, \tag{6.22}$$

where

$$\sigma_A = \left(\sum_L \frac{(C_L^{\alpha\alpha,\rm fiducial})^2}{\rm var(\widehat{C}_L^{\alpha\alpha})} \right)^{-1/2} \tag{6.23}$$

is the analytic expression for the variance of $\widehat{A}$, and $\rm var(\widehat{C}_L^{\alpha\alpha})$ is the variance of the estimated rotation-angle power spectrum, calculated from a suite of null-hypothesis simulations. We note that the measured $\widehat{C}_L^{\alpha\alpha}$ have been corrected by $f_{\rm sky}(L)$ (see Section 6.5; the correction is calculated specifically for this model) only in this portion of the analysis interpretation. For the presentation of the model-independent results, we use the average value, $f_{\rm sky} \sim 0.68$. Most of the constraint here comes from low L's: 50% of the sum in Eq. (9.10) comes from $L = 1$, and 90% from $L < 10$.

Even though the analytic expression above provides a good estimate of the statistical variance, because the constraint comes primarily from low-L modes, the probability distribution of $\widehat{A}$ is significantly non-Gaussian. To capture this non-Gaussianity in our analysis, we again generate a suite of null-hypothesis Monte Carlo simulations and recover the 68% and 99% confidence-level intervals from these simulations. The corresponding probability distributions for $\widehat{A}$ are shown in Figure 6.10.

The best-fit values for the quadrupole amplitude $\widehat{C}_2^{\alpha\alpha}$ and associated confidence intervals are listed in Table 6.4; consistency with zero is apparent within 3σ for all cross-band correlations we analyzed. The tightest constraint on the quadrupole amplitude of a scale-invariant rotation-angle

[11] Such a power spectrum would be acquired by a massless scalar field which was a spectator during inflation, for example; specific rotation models are discussed in some more detail in Chapter 7.

power spectrum comes from [WW][VV]. It is

$$\sqrt{C_2^{\alpha\alpha}/(4\pi)} \lesssim 1^\circ, \tag{6.24}$$

with 68% confidence[12].

$[f_1 f_2][f_3 f_4]$	$\widehat{C}_2^{\alpha\alpha} \pm 1\sigma(\pm 3\sigma)$ [deg^2]
[VV][VV]	$11.4^{+15.8}_{-16.9}(^{+79.0}_{-27.7})$
[QV][QV]	$29.6^{+18.8}_{-18.3}(^{+70.3}_{-33.4})$
[QQ][VV]	$19.8^{+14.3}_{-13.9}(^{+51.6}_{-46.6})$
[WV][WV]	$16.8^{+15.9}_{-16.9}(^{+79.0}_{-27.7})$
[WW][VV]	$3.0^{+14.0}_{-13.9}(^{+43.3}_{-42.9})$

Table 6.4: Measurement of the quadrupole amplitude of a scale-invariant rotation-angle power spectrum for different cross-band correlations, with 68% and 99% confidence-level intervals, recovered from a suite of null-hypothesis simulations. Consistency with zero within 3σ is apparent for all cross-band correlations, and the tightest constraint comes from [WW][VV].

6.7 Control of Systematics

In addition to the statistical uncertainty, there is also a systematic error for the measurement of the uniform rotation angle, owing to uncertainty in the detector polarization angles [46]. This systematic uncertainty should only apply to the monopole of α. The direction-dependent part is only sensitive to the extent that it affects the statistical noise bias, and this is mitigated by our data-dependent de-biasing procedure. There are, however, other sources of systematic error that can potentially bias our estimates and add uncertainties to the rotation-angle measurements. In this section, we investigate the impact of asymmetry of the instrumental beams, unresolved polarized point sources, and foreground residuals from unremoved/unmasked Galactic emission.

6.7.0.1 Beam Asymmetries

The fast spin and precession rates of the WMAP scan strategy, coupled with the yearly motion of the satellite around the ecliptic, enforce that any bias to $\widehat{\alpha}_{LM}$ originating from scan-strategy related systematics, like beam asymmetry, must be confined to $M = 0$ modes in ecliptic coordinates [72]. Furthermore, the smoothness of the scan strategy on large scales (dictated by the ∼70-degree opening angle of the detectors[13], and the large 22.5-degree amplitude of the hourly satellite precession), ensure that any such bias falls off quickly as a function of L. The estimates of C_2, as we discuss in Section 6.6, are most sensitive to the low-L modes of $\widehat{C}_L^{\alpha\alpha}$, so to test for the presence of beam-asymmetry contamination, we rotate our coordinate system to ecliptic coordinates, and re-derive a constraint

[12]Note that the conversion between the amplitude A and the quadrupole is $C_2 = A \times 131\text{deg}^2/6$.
[13]This is one half of the separation angle of the two telescope beams.

on C_2 from $L < 10$, $M = 0$ modes. We see no departure from the null hypothesis in this case where it should be maximal, and so conclude that beam asymmetries are not a significant source of bias for our measurements.

6.7.0.2 Unresolved Point Sources

To test the impact of unresolved point sources on our results, we repeat our analysis after unmasking the portion of the maps associated with detected point sources (but not Galactic contamination). Compared to our fiducial analysis, the measurement points for $\widehat{C}_L^{\alpha\alpha}$ shift by $\lesssim 1\sigma$, where σ represents the statistical error from our foreground-free Monte Carlo analysis; see Figure 6.11. This shift provides a conservative upper limit on the systematic uncertainty that point-source residuals can produce, assuming that the bright detected population has comparable polarization properties to those of the fainter sources. The unresolved point-source power at WMAP frequencies is dominated by unclustered radio sources, with fluxes close to the detection threshold, and so this is a reasonable assumption. We note that there is no overall bias, as the direction of scatter does not appear to be correlated for different multipoles. Of course, the contribution of radio point sources to the map is a steep function of the flux cut, and by unmasking all detected point sources our estimate of potential bias and uncertainty is overly conservative. Given a model for radio-source number counts (per flux) dN/dS, we can scale these results to the levels of contamination expected at the actual WMAP source detection threshold of (conservatively) ~ 1 Jy. Any bias $\Delta\widehat{C}_L^{\alpha\alpha}$ (which we do not see evidence for, even in the unmasked map) will scale with the point-source trispectrum as

$$\Delta\widehat{C}_L^{\alpha\alpha} \propto \int_{S=0}^{S_{\rm cut}} S^4 \frac{dN}{dS} dS, \tag{6.25}$$

while the uncertainty on $\widehat{C}_L^{\alpha\alpha}$ will scale with the point-source power as

$$\sigma\left(\widehat{C}_L^{\alpha\alpha}\right) \propto \left(\int_{S=0}^{S_{\rm cut}} S^2 \frac{dN}{dS} dS\right)^2. \tag{6.26}$$

Evaluating these terms for the dN/dS model of Ref. [73], we find that Δ and σ should be suppressed by factors of 0.005 and 0.06, respectively, when moving from a flux cut of 10 Jy (no masking) to 1 Jy. We find even smaller (though comparable in magnitude) results using the simpler $dN/dS \propto S^{-2.15}$ model of Ref. [74]. This implies that any bias from unresolved sources should be completely negligible, and any increase in uncertainty due to their contribution to the observed power should be $\lesssim 0.1\sigma$, where σ represents the statistical error from our point-source–free Monte Carlo analysis. In conclusion, we expect the unresolved point sources to produce a negligible systematic uncertainty in the measurement of $\widehat{C}_L^{\alpha\alpha}$ from WMAP.

6.7.0.3 Foreground Residuals

An additional conceivable source of systematic uncertainty might result from Galactic foregrounds. To explore the extent to which such uncertainty might affect our results, we perform two tests. In the first, we repeat our analysis on non-foreground-reduced maps, to test the effect of the presence of unsubtracted foregrounds. In the second, we repeat the foreground-reduced analysis using a mask which excludes a larger fraction of the low-Galactic-latitude sky. We construct this conservative mask by combining the fiducial $KQ85y7$ analysis mask with the extended mask of Ref. [8], and additionally masking out pixels with Galactic latitudes in the range of $\pm 40^\circ$; the mask admits only about 33% of the sky, approximately half the sky admitted in our fiducial analysis (see Figure 6.1). The function of this test is to explore the effect of residuals left by the foreground subtraction procedure, which should be stronger close to the Galactic plane. The measurement of $\widehat{C}_L^{\alpha\alpha}$ is scaled appropriately to account for the fractional sky coverage and the results from the two modified analyses are compared with the results of the fiducial analysis in Figure 6.12. In the first case, the change in the measurements is negligible compared to the statistical uncertainty. In the second case, the scatter between the two results is consistent with the difference in sky coverage (producing up to 40% larger scatter for the extended-mask data points). The measurements show no apparent bias in either case. These results imply that foregrounds and foreground residuals are not likely to make a large systematic contribution to our estimated statistical uncertainty, at least for the case of the most constraining cross-band correlation [WW][VV] of WMAP.

6.8 Implications for Quintessence Scenarios

In this section, we discuss the implications of the constraints presented in Section 6.6 for models where cosmic birefringence is caused by a quintessence field, assumed to drive the accelerated expansion of the Universe today.

As captured by Eq. (4.7), the amount of birefringent rotation in any given direction is proportional to the amount by which the birefringence-inducing field ϕ has evolved along the photons' path $\Delta\phi$, multiplied by the strength of the Chern-Simons coupling β, and inversely proportional to the characteristic mass scale of the underlying theory. We can now inquire how the constraints on $C_\ell^{\alpha\alpha}$ affect the allowed M-β parameter space for quintessence models. To do this, we first need to specify which model for $V(\phi)$ we are interested in, since the potential controls the value of $\Delta\phi$; in other words, there is no model-independent answer to this inquiry. Even though careful model building and selection is beyond the scope of this thesis, we attempt to illustrate the constraining power of the current, upcoming, and futuristic CMB data sets, in the context of a class of commonly considered quintessence models.

The "natural" energy scale M of the underlying theory is typically set around the Planck mass

$M_{\rm Pl}$, and parameter β is expected to be close to unity [31], regardless of the specific form of the potential V,

$$M \approx M_{\rm Pl}, \qquad \beta \approx 1. \tag{6.27}$$

If we now assume ϕ is a PNGB (as these fields are quite common in particle physics and make natural candidates for scalars with slow roll), and set the density-weighted average equation-of-state parameter as far away from cosmological-constant value of -1 as allowed by current supernovae observations [35],

$$\langle w_\phi \rangle \approx -0.95, \tag{6.28}$$

and also request that the current fractional energy density in the field ϕ accounts for the dark energy today,

$$\Omega_\phi \approx 0.7, \tag{6.29}$$

and finally solve the equation of motion for ϕ (see Subsection 7.1.1) under these conditions, we get that the field ϕ evolves by [6]

$$\Delta\phi \approx 0.01 M_{\rm Pl}, \tag{6.30}$$

since last scattering until today. Substituting these values into Eq. (4.7) then gives a value for the birefringent-rotation angle of about a degree—matching the level of current constraint on the monopole of $\alpha(\hat{\mathbf{n}})$. In other words, with WMAP data, we have started probing the "natural" regime of rotation angles for a fairly generic class of PNGB quintessence models. Lowering this limit by more than an order of magnitude with *Planck* data, or data from the forthcoming ground-based surveys like SPTPol, or ACTPol, would then start excluding large portions of the preferred parameter space for these models.[14].

One additional thing to note is that the constraints on the anisotropies in the rotation angle might also have a competitive constraining power when it comes to probing spatial fluctuations in the quintessence field, since the commonly-considered observational probes, such as large-scale structure, galaxy surveys, and supernova surveys, impose only weak constraints on fluctuations in quintessence[15] (see, for example, [75,76]). Investigating this avenue further is an interesting direction for future work.

[14]The caveat is, of course, the fact that this order-of-magnitude calculation tightly depends on the measurements of the equation-of-state parameter; for values closer to -1, the constraints become weaker.

[15]This result is expected, for several reasons. Directional fluctuations in the equation-of-state parameter should be on the order of 1 part in 10^5, while the Poisson noise from the measurements is overwhelmingly larger. In addition, any kind of survey of astrophysical objects will involve considerations related to non-linear growth of structure which is much harder to understand than the linear system such as the CMB.

6.9 Summary and Conclusions

In this section, we implemented the minimum-variance quadratic-estimator formalism presented in Chapter 5 to search for direction-dependent cosmic birefringence with WMAP 7-year data.

We obtained the first CMB measurement of the rotation-angle power spectrum $C_\ell^{\alpha\alpha}$, in the range from $\ell = 0$ to 512, finding consistency with zero at each multipole. We then derived an upper limit for the signal, by simulating a suite of Gaussian-sky realizations with no rotation, including symmetric beams, noise realizations appropriate for each WMAP frequency band, Q-U correlations, and sky cuts. We investigated the impact of foregrounds and polarized diffuse point sources on the reported constraints, and came to the conclusion that they do not represent significant sources of systematic error. We also used this null result to get a 68% confidence-level upper limit of $\sqrt{C_2^{\alpha\alpha}/(4\pi)} \lesssim 1^\circ$ on the quadrupole of a scale-invariant rotation-angle power spectrum. This constraint is a factor of 2 stronger than the one obtained previously from quasar observations [43] (see Subsection 7.1.1). This is not surprising, since, as we argued earlier, the CMB analysis has a significant advantage over the AGN analysis for this purpose: it provides a measurement of the rotation-angle power at each individual multipole, and has better sensitivity to models with significant power at high multipoles. Additionally, we discussed how different modes in the CMB maps contribute to the non-Gaussian signal from rotation at a multipole L, showing that most of the contribution comes from $L\ell\ell'$ triangles where either $\ell \sim L$, or $\ell' \sim L$. We also revisited previous constraints on RMS rotation from the TE power spectrum, in order to further justify the small-angle assumption used to interpret the results and perform power-spectrum de-biasing. Finally, we discussed the implications of our constraints on $C_\ell^{\alpha\alpha}$ for PNGB quintessence, arguing that the current upper limit corresponds to the amount of rotation expected in some relatively generic scenarios, pointing out that the upcoming data from *Planck* will have the power to start rejecting interesting regions of parameter space.

In conclusion, with 7 years' worth of integration time with WMAP, we were able to constrain the uniform rotation to less than about a degree. It will be interesting to see the results of this analysis, as applied to data from *Planck*, SPTPol, ACTPol, and other upcoming experiments, which will, for the first time, provide signal-dominated polarization measurements.

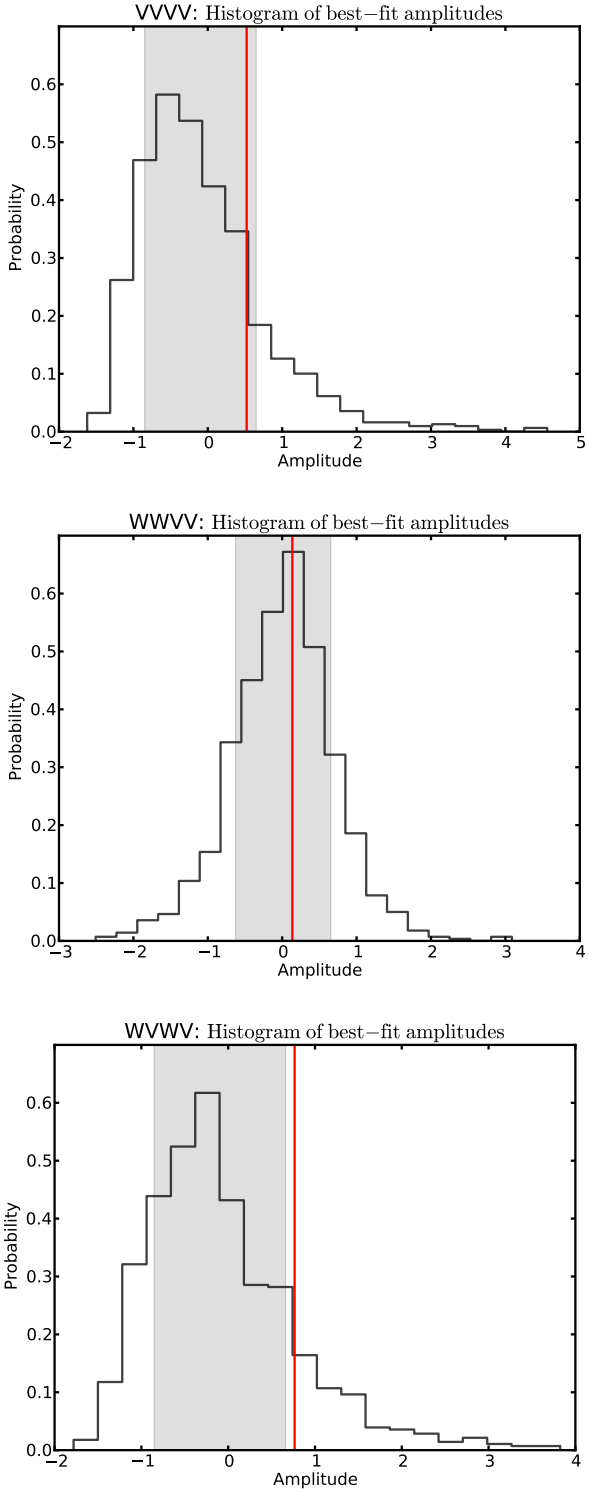

Figure 6.10: Probability distributions of the best-fit amplitude $\widehat{A}$ of the scale-invariant rotation power $C_L^{\alpha\alpha}$ recovered from a suite of null-hypothesis simulations are shown for some representative cross-band correlations. The gray-shaded area denotes a 68% confidence interval around the mean value; the red vertical line represents the measurement of the best-fit $\widehat{A}$. We find consistency with zero within 3σ for all five measurements.

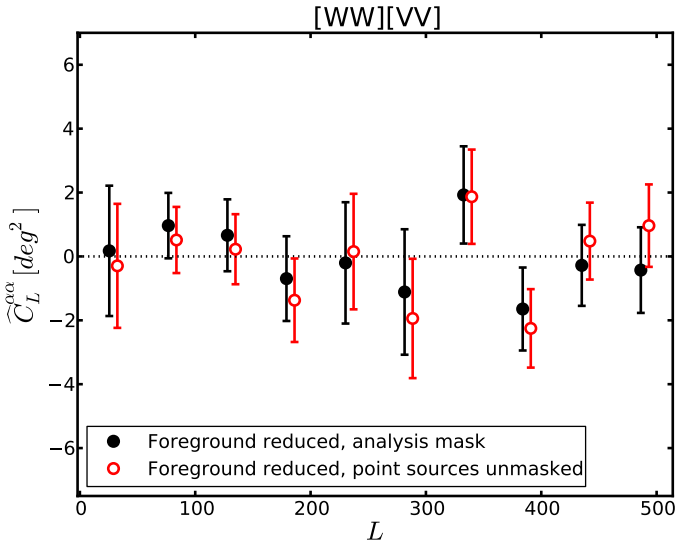

Figure 6.11: Measurement of $\widehat{C}_L^{\alpha\alpha}$ from [WW][VV]. Results shown in black are obtained by using the analysis mask that covers all the point sources brighter than $\sim$ 1Jy, while the results in red (empty circles) are obtained after unmasking all the point sources. There is no apparent bias and the difference in every bin is less than the statistical uncertainty, despite the extreme variation in the source contamination. Scaling arguments in Section 6.7 imply that the unresolved point sources have a negligible contribution to the estimated measurement uncertainty for the most constraining cross-band correlation in WMAP.

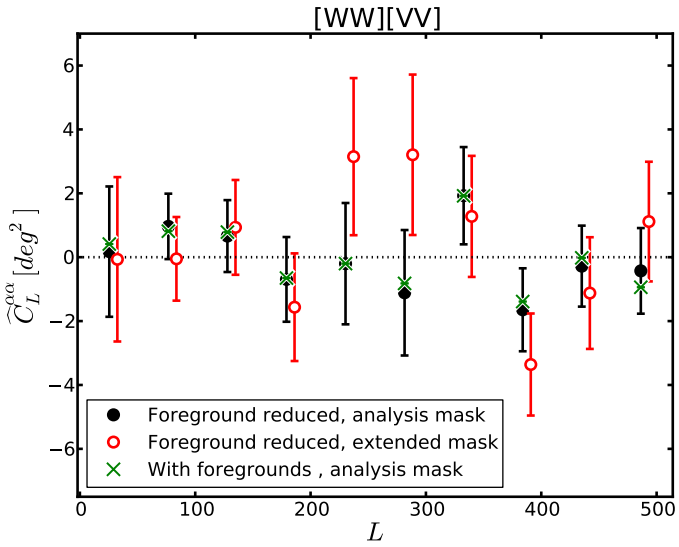

Figure 6.12: Measurement of $\widehat{C}_L^{\alpha\alpha}$ from [WW][VV] cross-band correlation, with the corresponding statistical uncertainty obtained from a suite of null-hypothesis foreground-free simulations. Black filled circles are measurements obtained from the foreground-reduced maps after applying the fiducial analysis mask, and they represent our fiducial results of Figure 6.8. The colored data points (and the associated error bars) correspond to the two test analyses: the green x's are obtained from the maps prior to foreground subtraction, but using the fiducial mask, while the red empty circles are measurements obtained from foreground-reduced maps, after applying an extended mask (with an additional $\sim 35\%$ of the sky covered around the Galactic plane). The results from the two tests show no apparent bias. For the case of non-foreground-reduced analysis, the difference from the fiducial measurements is negligible compared to the statistical uncertainty. For the extended-mask case, the scatter between the two results is consistent with the difference in sky coverage. This implies that foregrounds and foreground residuals should not have a drastic impact on the estimated measurement uncertainty for WMAP.

Chapter 7

Outlook: Cross-correlation of Rotation with Temperature

In this chapter, we explore the possibility that cosmic-birefringence signal may be correlated with primordial density perturbations, and thus also with temperature fluctuations in the CMB. The plan of this chapter is as follows. In Section 7.1, we work out the signal predictions for direction-dependent $\alpha(\hat{\mathbf{n}})$ for two distinct physical scenarios: a massless-scalar-field model (in which there is no uniform rotation and no cross-correlation with the temperature pattern $T(\hat{\mathbf{n}})$), and a PNGB quintessence model with adiabatic primordial perturbations seeded during inflation. In Section 7.2, we derive a minimum-variance estimator for $C_L^{\alpha T}$ and compare the detectability of $C_L^{\alpha\alpha}$ and $C_L^{\alpha T}$, for current and futuristic CMB experiments. Throughout this chapter, we focus only on the EB estimator for the rotation angle, as it is expected to provide the best sensitivity with upcoming and future experiments (see Section 5.4).

7.1 Scenarios for Anisotropic Rotation

7.1.1 Massless Scalar Field

In the first scenario, we suppose that the ϕ field is simply a massless scalar with a potential that vanishes,

$$V(\phi) = 0. \tag{7.1}$$

In this case, the value of the field is completely uncorrelated with primordial density perturbations[1] [47]. If ϕ is effectively massless during inflation, there will be a scale-invariant power spectrum of

Material in this chapter was largely adapted from "Cross-correlation of cosmological birefringence with CMB temperature," Robert Caldwell, Vera Gluscevic, and Marc Kamionkowski, *Phys. Rev. D* **84**, 043504 (2011) [6]. Reproduced here with permission, ©(2011) by the American Physical Society.

[1] We imagine that some mechanism has nullified the quantum-gravity effects that generically break global symmetries [77, 78].

perturbations to ϕ,

$$P_{\delta\phi}(k) = H_I^2/2k^3, \tag{7.2}$$

with an amplitude fixed by the Hubble parameter H_I evaluated during inflation[2], where k is a wavenumber. If we split the field into a smooth background component and a perturbation on top of it,

$$\phi(\vec{x},\tau) \to \phi(\tau) + \delta\phi(\vec{x},\tau), \tag{7.3}$$

the evolution of the homogeneous background component (which is not a function of the spatial coordinates represented by $\vec{x}$) is given by the following equation of motion

$$\ddot{\phi} + 2\mathcal{H}\dot{\phi} + a^2 V' = 0, \tag{7.4}$$

where

$$\mathcal{H} \equiv \dot{a}/a, \tag{7.5}$$

a is the scale factor, dots denote derivatives with respect to conformal time τ, and the prime denotes derivative with respect to ϕ. For a vanishing potential, this equation has only a decaying and a constant solution, so the value of the field is fixed in time in each causally disconnected region of the early Universe. This precludes the scalar-field perturbations from having any correlation with perturbations in the matter/radiation density. This is manifest in the absence of any source term in the perturbed equation of motion for the scalar field,

$$\delta\ddot{\phi} + 2\mathcal{H}\delta\dot{\phi} - k^2\delta\phi = 0, \tag{7.6}$$

where we set

$$(d\phi/d\tau) = 0, \qquad V = 0. \tag{7.7}$$

A solution to Eq. (7.6) is a transfer function

$$T_k(\tau) \propto j_1(k\tau)/(k\tau), \tag{7.8}$$

where j_1 denotes a spherical Bessel function. The transfer function describes the conformal-time evolution of a given Fourier mode of wavenumber k, during matter domination.

The power spectrum $C_L^{\alpha\alpha}$ for the rotation angle is then

$$C_L^{\alpha\alpha} = 4\pi \left(\frac{\beta}{M}\right)^2 \int \frac{k^2\,dk}{2\pi^2} P_\phi(k) \left[j_L(k\Delta\tau) T_k(\tau_{\rm lss})\right]^2 = \frac{1}{\pi}\left(\frac{\beta H_I}{M}\right)^2 \int \frac{dk}{k} \left[j_L(k\Delta\tau) T_k(\tau_{\rm lss})\right]^2, \tag{7.9}$$

[2]It is also imaginable that a white-noise spectrum of ϕ fluctuations is imprinted by some post-inflation phase transition, but we will not consider that scenario here.

where $\Delta\tau$ is the conformal-time difference between last scattering and today, and $\tau_{\rm lss}$ is the conformal time at the last scattering. For large angular scales the transfer function evaluates to

$$T_k(\tau_{\rm lss}) \approx 1, \qquad \text{for } L \lesssim 100, \tag{7.10}$$

in which case

$$C_L^{\alpha\alpha} \approx \frac{(\beta H_I/M)^2}{2\pi L(L+1)}, \qquad \text{for } L \lesssim 100. \tag{7.11}$$

The upper limit on a scale-invariant power spectrum derived from WMAP-7 data, presented by Eq. (6.24), provides a limit on the relevant combination of model parameters,

$$\beta H_I/M \lesssim 0.1, \tag{7.12}$$

which is 2 times stronger than the one implied by previous studies of AGN data [43]. We therefore choose a fiducial amplitude of the power spectrum such that this combination of parameters is 0.2, to match the current 2σ upper limit. The left-hand panel of Figure 7.1 shows the result of a numerical calculation for $C_L^{\alpha\alpha}$ of Eq. (7.38), for a range of amplitudes equal to, or smaller than the current constraint.

The CMB temperature power spectrum is given by

$$C_\ell^{TT} = \frac{2}{\pi}\int k^2\, dk\, \left[\Delta_{T,\ell}(k)\right]^2 P_\Psi(k), \tag{7.13}$$

where $P_\Psi(k)$ is the primordial power spectrum for the gravitational potential Ψ, and $\Delta_{T,\ell}(k)$ is the transfer function that quantifies the contribution of a density mode of wavenumber k to C_ℓ^{TT}, and may be obtained from numerical Boltzmann codes, such as CMBFAST or CAMB.

As discussed above, scalar-field fluctuations are not sourced by the gravitational potentials for this $V = 0$ model. Similarly, energy-density fluctuations in the scalar field have only second-order corrections due to the fluctuations $\delta\phi$, and so their effect on gravitational potentials is also small. In this case, the αT cross-correlation power spectrum vanishes,

$$C_L^{\alpha T} = 0. \tag{7.14}$$

7.1.2 Quintessence

In the second scenario, we suppose that ϕ is a quintessence field with a non-zero potential and a homogeneous component that undergoes time evolution. In this case, gravitational-potential per-

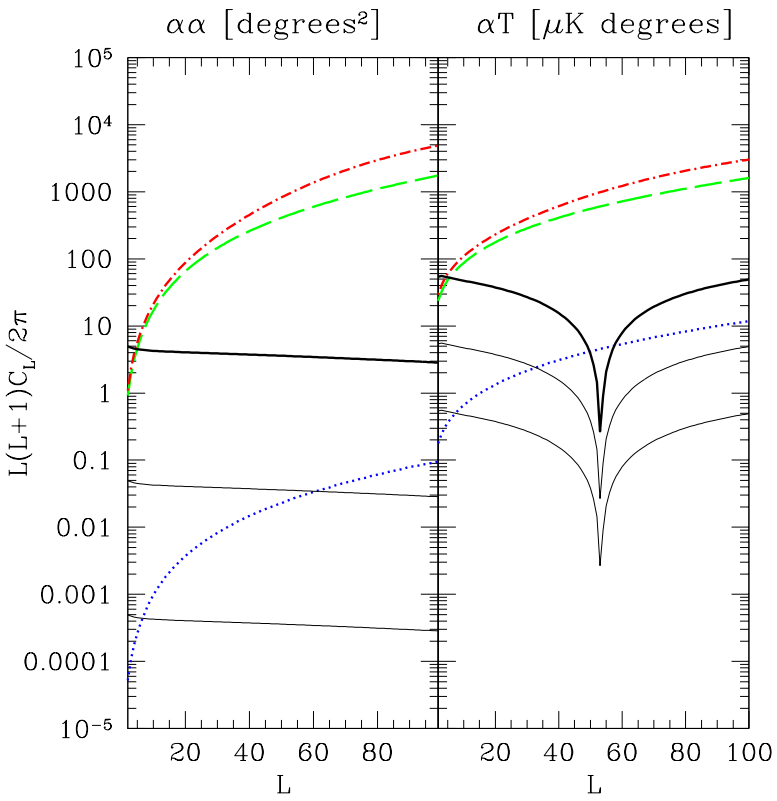

Figure 7.1: Shown are the power spectra for the rotation angle $C_L^{\alpha\alpha}$ and its cross-correlation with the CMB temperature $C_L^{\alpha T}$ (logarithm of the absolute value), for a PNGB quintessence model in which the rotation-angle fluctuations are driven by the scalar-field fluctuations at the last-scattering surface. The black solid curves are the theoretical predictions for (from top to bottom) $A = 1$, 0.1, and 0.01, where A is the power-spectrum amplitude for the rotation-angle autocorrelation, in the units of the maximum currently allowed amplitude at 2σ confidence level. We also show the noise power spectra anticipated for SPIDER (red, dot-dashed), *Planck* (green, dashed), and CMBPol (blue, dotted). The autocorrelation power spectrum for a massless quintessence is the same as the one shown in the left panel, while the αT cross-correlation vanishes. All of our numerical integrations are done in the synchronous gauge, using a modified version of CMBFAST.

turbations directly source (and are also sourced by) scalar-field fluctuations. A cross-correlation between the birefringent-rotation angle and CMB-temperature fluctuations is therefore inevitable, although its amplitude and detailed features depend on the specific potential V. We now derive $C_L^{\alpha\alpha}$ and $C_L^{\alpha T}$ for the case of a PNGB quintessence with a potential given by Eq. (4.4), as expected if ϕ is an axion-like field.

Since every CMB photon that comes from a given direction $\hat{\mathbf{n}}$ last scattered at the spacetime point in the direction $\hat{\mathbf{n}}$ when the Universe had some fixed temperature, $\alpha(\hat{\mathbf{n}})$ is determined by the value of ϕ at that point of spacetime. In other words, the rotation-angle anisotropies $\alpha(\hat{\mathbf{n}})$ are determined by the synchronous-gauge scalar-field perturbations $(\delta\phi)_{\rm syn}$ at the last-scattering surface.

We first suppose that the initial value of ϕ is set by some post-inflationary physics, so that the

primordial perturbation to ϕ is adiabatic[3]. In this case, $(\delta\phi)_{\rm syn}$ initially vanishes. We then evolve the scalar-field–perturbation equation of motion forward in time, from the early radiation-dominated epoch, to the last-scattering surface. This equation of motion reads

$$\delta\ddot{\phi} + 2\mathcal{H}\delta\dot{\phi} + a^2 V''\delta\phi - \nabla^2\delta\phi = -\frac{1}{2}\dot{h}\dot{\phi}, \tag{7.15}$$

in the synchronous gauge, and

$$\delta\ddot{\phi} + 2\mathcal{H}\delta\dot{\phi} + a^2 V''\delta\phi - \nabla^2\delta\phi = \dot{\phi}(3\dot{\Phi} + \dot{\Psi}) - 2a^2 V'\Psi, \tag{7.16}$$

in the conformal-Newtonian/longitudinal gauge, where definitions of the metric variables Φ, Ψ, η, and h are given in Ref. [79]. The subsequent evolution of the scalar field is not adiabatic, meaning that $(\delta\phi)_{\rm syn,lss}$ does not necessarily vanish at the last-scattering surface, even though all the matter and radiation perturbations do. We take an initial value of ϕ, and values for the model parameters m and f such that, today, the fractional energy density of the Universe carried by the quintessence field is[4]

$$\Omega_\phi = 0.7, \tag{7.17}$$

and the density-weighted average equation-of-state parameter[5]

$$\langle w \rangle \approx -0.95, \tag{7.18}$$

which gives

$$\Delta\phi = 0.045\, M_{\rm Pl}, \tag{7.19}$$

for the change in the scalar field between decoupling and today. However, the power spectra presented in Figure 7.1 will be similar for any quintessence potential that has $w_\phi \to -1$ at early times.

We now derive an analytic approximation for $(\delta\phi)_{\rm syn,lss}$, which allows for the numerical results for the power spectra to be reproduced with high accuracy. For this purpose, we switch to the conformal-Newtonian/longitudinal gauge and make the approximation that decoupling takes place well into matter domination. We assume that most of the growth in perturbations happens during this epoch. For $w_\phi \to -1$, the V'' term in Eq. (7.16) is negligible. Additionally, in the superhorizon limit, valid for multipoles $L \lesssim 100$, we can neglect the spatial-gradient term. The simplified equation

[3] By "post-inflationary physics", we are actually referring to the period of reheating. Also, note that the choice of exact initial conditions does not make much difference for a quintessence field with a negative equation-of-state parameter. This is because the fluctuations in such field are always decaying away until much after recombination.

[4] This number is chosen so as to agree with the current measurement of the energy density trapped in the dark-energy component, often modeled with a quintessence field, such as the one discussed here.

[5] The evolution of ϕ here is set up so that w starts at -1 (no roll), and then gets more positive (significant evolution starts at z of a few; observations are constraining this density-average w, rather than just its present-day value, when interpreted for models with an evolving scalar field.

of motion is then,

$$\delta\ddot{\phi} + 2\mathcal{H}\delta\dot{\phi} \approx -2a^2V'\Psi. \tag{7.20}$$

Aside from the homogeneous solutions that are either constant or decaying, it also has an inhomogeneous solution that grows as

$$(\delta\phi)_{\rm con} \approx -a^2\tau^2V'\Psi/27, \tag{7.21}$$

during matter domination. The potential derivative V' can be expressed, using the quintessence slow-roll approximation, from

$$a^2V' \approx -3\mathcal{H}\dot{\phi}. \tag{7.22}$$

Also, the pressure p_ϕ and energy density ρ_ϕ of the scalar, and its equation-of-state parameter w_ϕ, given by Eq. (4.2), satisfy

$$p_\phi + \rho_\phi = \frac{1}{a^2}\dot{\phi}^2, \tag{7.23}$$

so that

$$\dot{\phi}^2 = a^2\rho_\phi(1+w_\phi), \tag{7.24}$$

with

$$\rho_\phi = \Omega_\phi\rho_c, \tag{7.25}$$

and where

$$\rho_c = 3H^2M_{Pl}^2/(8\pi) \tag{7.26}$$

is the critical density today. We then find

$$(\delta\phi)_{\rm con} = \frac{4}{9}\left[\frac{3}{8\pi}\Omega_\phi(1+w_\phi)\right]^{1/2} M_{Pl}\Psi. \tag{7.27}$$

Finally, going back to the synchronous gauge, by using the gauge-transformation equations presented in Ref. [79],

$$(\delta\phi)_{\rm syn} = (\delta\phi)_{\rm con} - \alpha_{MB}\dot{\phi}(\delta\dot{\phi})_{\rm syn} = (\delta\dot{\phi})_{\rm con} - \alpha_{MB}\ddot{\phi}, \tag{7.28}$$

after noting that[6]

$$\alpha_{MB} \approx (2/3)\Psi/\mathcal{H}, \tag{7.29}$$

during matter domination, we arrive at the synchronous-gauge scalar-field perturbation at the last-scattering surface,

$$(\delta\phi)_{\rm syn,lss} = -\frac{2}{9}\left(\frac{3\Omega_{\phi,\rm lss}(1+w_{\phi,\rm lss})}{8\pi}\right)^{1/2} M_{\rm Pl}\Psi, \tag{7.30}$$

where the equation-of-state parameter $w_{\phi,\rm lss}$ and the energy-density parameter $\Omega_{\phi,\rm lss}$ are evaluated

[6] We use α_{MB} to denote parameter α from Ref. [79], not to be confused with the notation we use for the rotation angle α.

at recombination.

We proceed to derive the initial conditions in the conformal-Newtonian/longitudinal gauge, for the sake of completeness, which can then be used to evolve Eq. (7.16). To obtain the initial conditions in this gauge, we use Eq. (7.28), where

$$\alpha_{MB} = (1/2)\Psi/\mathcal{H}, \tag{7.31}$$

during radiation domination. At early times, deep in the radiation era, we can set the fractional energy-density perturbation in the radiation field to [79]

$$\delta_r = -2\Psi, \tag{7.32}$$

and assume that the equation-of-state parameter $w_\phi \to -1$, and changes slowly with time. Furthermore, using Eq. (7.23), and the perturbation in the energy density,

$$(\delta\rho_\phi)_{\rm con} = \frac{1}{a^2}\dot{\phi}\dot{\delta\phi} + V'(\phi)\delta\phi - \frac{1}{a^2}\dot{\phi}^2\Phi, \tag{7.33}$$

while the adiabatic initial conditions require that the entropy-density perturbation vanishes at early times, so that

$$\mathcal{S} \equiv \frac{\delta\rho_\phi}{\rho_\phi + p_\phi} - \frac{\delta\rho_r}{\rho_r + p_r}. \tag{7.34}$$

Inserting these assumptions into the gauge-transformation equations, and noting that $\delta\phi$ vanishes in the synchronous gauge, we get the initial conditions for the scalar-field perturbations in the conformal-Newtonian/longitudinal gauge[7],

$$\begin{aligned} (\delta\phi)_{\rm con} &= \frac{1}{2}\frac{\dot{\phi}}{\mathcal{H}}\Psi, \\ (\dot{\delta\phi})_{\rm con} &= \dot{\phi}\Phi - \frac{3}{2}\dot{\phi}\Psi - \frac{1}{2}\frac{a^2V'}{\mathcal{H}}\Psi. \end{aligned} \tag{7.35}$$

The primordial power spectrum for the gravitational potential, for large scales (small k) is

$$P_\Psi = \frac{9}{25}\frac{2\pi^2}{k^3}\Delta^2_{\mathcal{R}}, \tag{7.36}$$

where, for simplicity, we take the scalar spectral index to be $n_s = 1$, and the curvature-perturbation amplitude $\Delta^2_{\mathcal{R}}(k_0) = 2.43(\pm 0.11) \times 10^{-9}$ [68]. To evolve the power spectrum from primordial to the last-scattering surface, we need to multiply it by transfer functions, which are a suppression factor for small scales (large k's). The power spectrum for the birefringent-rotation angle in this

[7] These initial conditions can also be derived by requiring that $\mathcal{S}$ and $\dot{\mathcal{S}}$ vanish at early times.

quintessence model is then

$$C_L^{\alpha\alpha} = \frac{2}{27}\Omega_\phi(1+w_\phi)\left(\frac{\beta M_{\rm Pl}}{M}\right)^2 \int \frac{k^2\,dk}{2\pi^2} P_\Psi(k)[j_L(k\Delta\tau)T_k(\tau_{\rm lss})]^2. \tag{7.37}$$

For large scales, $L \lesssim 100$, Eq. (7.10) again holds, so we can simplify the power spectrum to[8]

$$C_L^{\alpha\alpha} \simeq 3.5\times10^{-11}\frac{(\beta H_I/M)^2}{L(L+1)}\Omega_\phi(1+w_\phi), \qquad \text{for } L \lesssim 100. \tag{7.38}$$

In other words, $C_L^{\alpha\alpha}$ for the quintessence scenario will be scale-invariant, as in the case of a massless scalar field, in the small-L limit, as shown in Figure 7.1.

However, in the case of quintessence, there will also be a cross-correlation with the CMB temperature, since the CMB temperature is determined largely by the potential Ψ at last scattering. From Eqs. (7.13) and (7.37), we get

$$C_L^{\alpha T} = -\frac{4\pi}{3}\sqrt{\frac{\Omega_\phi(1+w_\phi)}{6\pi}}\frac{\beta M_{\rm Pl}}{M}\int \frac{k^2\,dk}{2\pi^2} P_\Psi(k)\Delta_{T,L}(k)j_L(k\Delta\tau)T_k(\tau_{\rm lss}). \tag{7.39}$$

The absolute value of this cross-correlation is also shown in Figure 7.1.

7.2 Prospects for Detection

Since the best sensitivity to detecting rotation-angle coefficients α_{LM} will ultimately come from the EB cross-correlation (as shown in Section 5.4), here we restrict our attention only to EB and analyze detectability of $C_L^{\alpha\alpha}$ and $C_L^{\alpha T}$ by, first deriving, and then numerically evaluating expressions for corresponding noise power spectra, and finally comparing the noise to the signal calculated for specific models presented in Section 7.1.

Using the same assumptions, definitions, and notation as in Chapter 5, we rewrite the minimum-variance estimator for the rotation-angle spherical-harmonic coefficients of Eq. (5.39) as

$$\widehat{\alpha}_{LM} = C_L^{\alpha\alpha,\rm noise}\sum_{mm',\ell'\geq l}\xi^{LM}_{\ell m\ell' m'}[V^L_{\ell\ell'}E^{\rm map}_{\ell' m'}B^{\rm map}_{\ell m} + V^L_{\ell'\ell}E^{\rm map}_{\ell m}B^{\rm map}_{\ell' m'}], \tag{7.40}$$

where,

$$V^L_{\ell\ell'} \equiv \frac{F^{L,BE}_{\ell\ell'}}{(1+\delta_{\ell\ell'})C_\ell^{BB,\rm map}C_{\ell'}^{EE,\rm map}}, \tag{7.41}$$

and also

$$F^{L,EB}_{\ell\ell'} = F^{L,BE}_{\ell'\ell}. \tag{7.42}$$

Under the null hypothesis of no rotation, the expectation value of the estimator in Eq. (7.40) is zero,

[8] We arrive at this by combining Eqs. (8) and (12) of Ref. [6].

and its variance is the $\alpha\alpha$ noise power spectrum, as given in Ref. [4],

$$C_L^{\alpha\alpha,\rm noise} \equiv \left\langle |\widehat{\alpha}_{LM}|^2 \right\rangle = \left[\sum_{\ell\ell'} \frac{(2\ell+1)(2\ell'+1)(F_{\ell\ell'}^{L,BE})^2}{4\pi C_\ell^{BB,\rm map} C_{\ell'}^{EE,\rm map}} \right]^{-1}. \tag{7.43}$$

The usual noise power spectra, which include instrumental noise and resolution, are defined and calculated as before,

$$\begin{aligned} C_\ell^{TT,\rm noise} &\equiv \frac{4\pi f_{\rm sky}^0 (\rm NET)^2}{t_{\rm obs}}, \\ C_\ell^{EE,\rm noise} = C_\ell^{BB,\rm noise} &\equiv 2C_\ell^{TT,\rm noise}, \\ C_\ell^{EB,\rm noise} = C_\ell^{TB,\rm noise} &\equiv 0, \end{aligned} \tag{7.44}$$

where $t_{\rm obs}$ is the total observation time, $f_{\rm sky}^0$ is the fraction of the sky surveyed (taken to be different from 1 only for SPIDER [10]; see Table 8.1), and NET is the noise-equivalent temperature, which we use here instead of the pixel-noise variance σ_T^2 (see Eqs. (3.36) and (5.59)). As before, we assume no cross-correlation between the noise in polarization and temperature, and apply the null assumption of no B modes in the signal, so there are no TB and EB correlations. The power spectrum $C_\ell^{BB,\rm map}$ thus contains only the contribution from instrumental noise.

We note here that weak gravitational lensing and primordial gravitational waves both induce a contribution to the B mode. However, the power spectrum for this B mode should be smaller than that of the noise, even for a futuristic mission like CMBPol [7], and so our sensitivity estimates should be unaffected by neglecting it. While weak gravitational lensing also induces off-diagonal EB correlations, the EB correlations from weak lensing can be distinguished geometrically from those due to birefringent rotation (see Section 5.3).

If the polarization pattern at the last scattering is a realization of a statistically isotropic field, then there are $2L+1$ statistically independent M modes for each L in $\widehat{\alpha}_{LM}$. In this case, each M mode provides an independent estimator of the rotation power spectrum, $C_L^{\alpha\alpha}$. The minimum-variance estimator, prior to the $f_{\rm sky}$ correction for the masked portion of the sky[9], is (see Eq. (6.10))

$$\widehat{C}_L^{\alpha\alpha} = \frac{1}{2L+1} \sum_{M=-L}^{L} |\widehat{\alpha}_{LM}|^2. \tag{7.45}$$

Each $\widehat{\alpha}_{LM}$ is a sum of products of Gaussian random variables and is thus not a Gaussian random variable. However, if the number of terms in the sum is large, the central-limit theorem holds, and $\widehat{\alpha}_{LM}$ can be approximated as Gaussian. In this case, the expression for the variance of $\widehat{C}_L^{\alpha\alpha}$ takes

[9] We fold in this correction in just a few lines; the reason to leave it out for now is simply to be consistent with the notation used in the Section 3.3 which is concerned only with simplified analytic understanding of the noise power spectra, rather than with the convenience for reconstruction from real data maps. Since the topic of this section are forecasts of sensitivity, we resort to the same notation.

on a simple form,

$$\left(\Delta\widehat{C}_L^{\alpha\alpha}\right)^2 \approx \frac{2}{f_{\rm sky}(2L+1)}\left(C_L^{\alpha\alpha,{\rm noise}}\right)^2, \tag{7.46}$$

where $f_{\rm sky}$ is, as before, the fraction of the sky used in the analysis[10], taken here to be 0.8 for Planck and CMBPol, and 0.5 for SPIDER.

In analogy with the derivation in Ref. [3] of the estimator for C_ℓ^{TE} (or, following the expressions for the power-spectra covariances of Section 3.3), the estimator for $C_L^{\alpha T}$ is

$$\widehat{C}_L^{\alpha T} = \frac{1}{2L+1}\sum_{M=-L}^{L}\widehat{\alpha}_{LM}(T_{LM}^{\rm map})^* W_L^{-1}, \tag{7.47}$$

where $T_{LM}^{\rm map}$ is the temperature spherical-harmonic coefficient obtained from a map, as usual. Under the null hypothesis, $T_{LM}^{\rm map}$ has no correlation with any $B_{\ell m}$, and it is correlated with $E_{\ell m}$ only for $\{LM\} = \{\ell m\}$, and uncorrelated otherwise. The estimator $\widehat{\alpha}_{LM}$ depends on a large number of $E_{\ell m}$ modes but does not include $\{\ell m\} = \{LM\}$. There is therefore no correlation (under the null hypothesis) of $\widehat{\alpha}_{LM}$ and $T_{LM}^{\rm map}$; i.e., there is no noise contribution to $C_L^{\alpha T}$. The full expression for its variance (which is a six-point correlation function), after applying Wick's theorem and the properties of Wigner-3j symbols (see Appendix A), reads

$$\begin{aligned}(\Delta\widehat{C}_L^{\alpha T})^2 = \frac{(C_L^{\alpha\alpha,{\rm noise}})^2 C_L^{BB,\ {\rm noise}}}{4\pi W_L^2}[2(V_{LL}^L)^2(C_L^{TE,\ {\rm map}})^2 + \sum_\ell [2\frac{(2\ell+1)^2}{(2L+1)^2}(V_{\ell\ell}^L)^2 C_l^{EE,\ {\rm map}} C_L^{TT,{\rm map}} \\ +(1+\delta_{\ell L})(V_{\ell L}^L)^2(C_L^{TE,{\rm map}})^2] + \sum_{\ell\ell'}(1+\delta_{\ell\ell'})\frac{(2\ell+1)(2\ell'+1)}{(2L+1)}(V_{\ell\ell'}^L)^2 C_L^{TT,{\rm map}} C_{\ell'}^{EE,{\rm map}}].\end{aligned} \tag{7.48}$$

Again, if $\widehat{\alpha}_{LM}$ is approximately Gaussian, then the expression for the variance, in analogy with the variance of C_ℓ^{TE} (see Ref. [3], or Section 3.3), simplifies to

$$\left(\Delta\widehat{C}_L^{\alpha T}\right)^2 \approx \frac{1}{f_{\rm sky}(2L+1)} C_L^{\alpha\alpha,{\rm noise}} C_L^{TT,{\rm map}} W_L^{-2}. \tag{7.49}$$

To check the validity of this expression for the purpose of calculating the sensitivity of future CMB experiments to the rotation signal, we compare it to the full expression of Eq. (7.48), and confirm that the numerical results agree up to a level of a few percent. Thus, without any loss in accuracy, Eq. (7.49) can be used instead of Eq. (7.48).

We now return to the two scenarios for cosmic-birefringence rotation which predict that the rotation α is a realization of a random field with the power spectra $C_L^{\alpha\alpha}$ and $C_L^{\alpha T}$ presented in Figure 7.1. Our aim here is to evaluate the smallest signal amplitude detectable by measurement of the rotation alone, as well as the smallest amplitude detectable by measurement of the rotation-temperature cross-correlation.

[10] To be distinguished from $f_{\rm sky}^0$, the fraction of the sky surveyed.

We write the power spectra as

$$C_L^{\alpha\alpha} \equiv A^2 C_L^{\alpha\alpha,\mathrm{fiducial}},$$
$$C_L^{\alpha T} \equiv A C_L^{\alpha T,\mathrm{fiducial}}, \tag{7.50}$$

where the fiducial model ($A = 1$) is the quintessence model in Figure 7.1 with the largest amplitude allowed by current rotation-angle constraints at 2σ level. The inverse variance with which the amplitude A^2 of $C_L^{\alpha\alpha}$ can be obtained from the rotation-angle autocorrelation can be evaluated using the Fisher-matrix formalism [80] as

$$\frac{1}{\left[\Delta(A^2)\right]^2} = \sum_L \left(\frac{\partial C_L^{\alpha\alpha}}{\partial (A^2)}\right)^2 \frac{1}{\left(\Delta \widehat{C}_L^{\alpha\alpha}\right)^2} = \sum_L \left(\frac{C_L^{\alpha\alpha,\mathrm{fiducial}}}{\Delta \widehat{C}_L^{\alpha\alpha}}\right)^2. \tag{7.51}$$

Similarly, the inverse variance with which the amplitude A of $C_L^{\alpha T}$ can be obtained from the cross-correlation of the rotation with the temperature is

$$\frac{1}{(\Delta A)^2} = \sum_L \left(\frac{\partial C_L^{\alpha T}}{\partial A}\right)^2 \frac{1}{\left(\Delta \widehat{C}_L^{\alpha T}\right)^2} = \sum_L \left(\frac{C^{\alpha T,\mathrm{fiducial}}}{\Delta \widehat{C}_L^{\alpha T}}\right)^2. \tag{7.52}$$

From these relations, we can estimate the signal-to-noise ratio for measurement of A^2 from $C_L^{\alpha\alpha}$ to be

$$(S/N)_{\alpha\alpha} = A^2 / \left[\Delta(A^2)\right], \tag{7.53}$$

and the signal-to-noise for measurement of A from $C_L^{\alpha T}$ to be

$$(S/N)_{\alpha \mathrm{T}} = A/(\Delta A). \tag{7.54}$$

We evaluate these expressions for our fiducial model ($A = 1$), for different instrumental parameters and present the results in Table 8.1. The smallest A detectable at the 2σ level from $C_L^{\alpha T}$ and $C_L^{\alpha\alpha}$ are $2\Delta A$ and $\left[2\Delta(A^2)\right]^{1/2}$, respectively.

We now evaluate the largest possible signal-to-noise and the smallest detectable amplitude A for three satellite-based CMB polarization experiments: (i) SPIDER's 150 GHz channel, as described in Ref. [10], (ii) *Planck*'s 143 GHz channel, as described in Ref. [81], and (iii) CMBPol's (EPIC-2m) 150 GHz channel, as described in Ref. [11]. We obtain the CMB temperature-polarization power spectra from CMBFAST, using WMAP-7 cosmological parameters [46]. The instrumental parameters we use are listed in Table 8.1.

Figure 7.1 shows the noise power spectra[11] $C_L^{\alpha\alpha,\mathrm{noise}}$ and $C_L^{\alpha T,\mathrm{noise}}$ obtained by evaluating expres-

[11]Note that there is a difference in normalization between the *noise* and the *variance*: $C_L^{XX',\mathrm{noise}} \equiv$

Instrument	$f^0_{\rm sky}$	$f_{\rm sky}$	$\theta_{\rm FWHM}$ [arcmin]	NET [μK $\sqrt{\rm sec}$]	$t_{\rm obs}$ [year]	$(S/N)_{\alpha\alpha}$	$(S/N)_{\alpha T}$
SPIDER	0.5	0.5	60	3.1	0.016	9	7
Planck	1	0.8	7.1	62	1.2	11	9
CMBPol/EPIC	1	0.8	5	2.8	4	2×10^5	1200

Table 7.1: Key instrumental parameters we use for the three experiments considered in Section 7.2: beamwidth, noise-equivalent temperature, and observation time. The last two columns list signal-to-noise ratios (S/N) for the messurement of birefringent-rotation angle autocorrelation and its cross-correlation with the CMB temperature, for a fiducial quintessence model ($A = 1$) shown in Figure 7.1. Note that the signal-to-noise scales with the signal amplitude as $(S/N)_{\alpha\alpha} \propto A^2$ and $(S/N)_{\alpha\rm T} \propto A$.

sions derived in this section. For $C_L^{\alpha T}$, strictly speaking, there is no instrumental-noise contribution, only the *effective noise*, arising from cosmic variance. Table 8.1 also lists the projected signal-to-noise ratios, assuming $A = 1$, for all three experiments.

In conclusion, we find that SPIDER and *Planck* may already have the sensitivity to detect not only the rotation signal, but also its cross-correlation with the temperature, in the optimistic scenario of $A \sim 1$, where the signal is just below the current detection limit[12]. In both cases, the sensitivity to the signal may be improved if both $C_L^{\alpha T}$ and $C_L^{\alpha\alpha}$ are measured in tandem. A futuristic mission like CMBPol should have sensitivity to a signal as small as $A \sim 10^{-5}$, and a detection of the cross-correlation of very high signal-to-noise may be obtained if $A \sim 1$.

7.3 Summary and Conclusions

If a quintessence field gives rise to cosmic birefringence, then a correlation between the rotation-angle fluctuations and CMB-temperature fluctuations is inevitable. We calculated this cross-correlation assuming the initial quintessence perturbations are adiabatic and seeded during inflation. We also discussed, by way of contrast, a scenario in which the birefringence-inducing field is just a massless scalar field that has no correlation with primordial perturbations.

We then derived the minimum-variance estimator for the $C_L^{\alpha T}$ power spectrum that can be obtained from CMB temperature and polarization maps. We found that measurement of this cross-correlation may improve sensitivity to the rotation signal in some cases where the signal would otherwise be only marginally detectable. We further showed that a high signal-to-noise measurement of this cross-correlation is conceivable with forthcoming and future CMB experiments if the rotation-angle power-spectrum amplitude is near its current upper limit, and can thus provide another empirical handle with which to probe new physics indicated by cosmic birefringence.

$\sqrt{(2L+1)/2}\Delta\widehat{C}_L^{XX'}$, where $XX' = \{\alpha\alpha, \alpha T\}$. It is customary to plot the noise power spectra, even though the variance enters the expressions for signal-to-noise.

[12] Here we have assumed that the errors to the rotation-angle estimators are approximately Gaussian. However, if the signal is barely detectable (for example, for SPIDER in case $A \sim 1$), then this assumption may break down, and if so, the precise quantitative forecasts for the signal-to-noise may differ slightly.

We have restricted our attention to the EB estimator for the rotation angle, as it is expected to provide the best sensitivity. However, there may be some improvement, though probably small, with the inclusion of the TE, TB, and EE estimators for the rotation. We leave this calculation for future work. Likewise, we have left more careful investigation of the impacts of partial-sky analysis, foregrounds, uneven noise, and the effect of cosmic birefringence on cosmological parameter extraction [82] for future work.

We have refrained from discussing details of the quintessence model here, as the angular dependence of the cosmic-birefringence power spectra at superhorizon scales at the time of recombination, $L \lesssim 100$, is insensitive to these details. The dependence of the amplitudes of the $C_L^{\alpha\alpha}$ and $C_L^{\alpha T}$ power spectra is given in terms of the quintessence parameters Ω_ϕ and w_ϕ at the last-scattering surface by Eqs. (7.37) and (7.39). However, if the quintessence field couples to the pseudoscalar of electromagnetism, it is natural to expect it to be a PNGB field. In this case, ϕ is frozen at early times leading to spatial variations in α at small scales ($L \gtrsim 100$) that are unobservably small. However, additional fluctuations in α may be produced during the epoch of reionization, which is another potentially interesting direction for future research.

For the massless scalar field, the uniform rotation angle is expected to be zero, and so a search for the fluctuations is essential to detect the signal. For quintessence, however, the uniform rotation is expected to be non-zero and generically quite a bit larger than the fluctuations, which, given the current best constraint may imply a relatively small amplitude of the fluctuations power spectrum. However, we have shown that future experiments, like CMBPol, may be sensitive to a fluctuation amplitude as small as $\sim 10^{-5}$ of the current upper limit to the uniform rotation, which, if detected, would help distinguish between different birefringence scenarios. Moreover, the fluctuation amplitude in the quintessence scenario could be larger than a measured uniform-rotation angle. This could occur if, for example, the uniform-rotation angle (which can only be recovered mod π) happens to be close to an integer multiple of π. It will be interesting, with forthcoming precise CMB maps, to address these questions empirically rather than through theoretical speculation.

Chapter 8

Parity Violations Beyond Standard Models

Both inflation [32] and late-time cosmic acceleration [33] require new physics beyond general relativity and the standard models of particle physics and cosmology. Since the Standard Model of particles violates parity within the weak sector and is presumably only a low-energy limit of a grand unified theory, it is natural to inquire whether there are manifestations of parity violation in the new physics responsible for cosmic inflation and/or late-time acceleration.

One such possibility arises if a quintessence field couples to the pseudo-scalar of electromagnetism that manifests as rotation of the polarization of light that propagates through the Universe, producing the effect of a uniform[1] cosmic birefringence we explored in Chapters 5 and 6. Beyond cosmic birefringence, parity violation has, for example, been introduced in inflation through modifications of gravity that produce a difference in the amplitude of right (R) and left (L) circularly polarized gravitational waves in the inflationary gravitational-wave background. We refer collectively to these inflationary mechanisms as *chiral gravity*.

Since the CMB polarization can be decomposed into two modes of opposite parity—E modes, or the gradient part, and B modes, or the curl part (see Section 3.2)—a cross-correlation between the E and B modes, and similarly between the temperature modes T and the B mode, would, if detected, be a sign of parity violation [83], making the CMB maps an excellent test ground to look for signatures of parity-violating physics. Chiral gravitational waves induce TB and EB power spectra at the CMB last-scattering surface [83, 84], while cosmic birefringence induces parity violation by rotating the primordial polarization afterwards [83, 85]. An early analysis of CMB data suggested a possible birefringence signal with rotation angle $\sim 6^\circ$ [67], but current constraints are less than a few degrees (see Chapter 4). Ref. [86] showed that WMAP does not have enough sensitivity to test

Material in this chapter was largely adapted from "Testing parity-violating mechanisms with cosmic microwave background experiments," Vera Gluscevic and Marc Kamionkowski, *Phys. Rev. D* **81**, 123529 (2010) [7].

[1] Only uniform rotation representa parity violation; multipoles above the monopole do not, as they average out to zero on the whole sky.

chiral gravity, and discussed prospects for detection of chiral gravitational waves with *Planck* and CMBPol.

In this chapter, we quantify how well the effects of uniform rotation in the sky (such as that originating from cosmic birefringence) and chiral gravity can be constrained and distinguished from each other, in case of a positive detection of EB and/or TB power spectra. In Section 8.1 we conveniently parametrize gravitational chirality and discuss its effect on the CMB maps; similarly, we review the effects of uniform rotation in Section 8.2. These two sections also present forecasts for detecting these signals separately with WMAP, SPIDER, *Planck*, CMBPol (EPIC), and a cosmic-variance–limited experiment. Section 8.3 quantifies the degeneracy between the two signals, in case of detection of EB/TB power spectra. Section 8.4 revisits the current constraints and forecasts for detectability of primordial gravity waves, using BB and also TB power spectra. Section 8.5 discusses possible B-mode contamination of the birefringent signal and the chiral-gravity signal, from other cosmological sources, such as weak gravitational lensing and primordial B modes, and their effect on our results. Finally, we summarize and give concluding remarks in Section 8.6. Throughout this chapter, we use ΛCDM model consistent with WMAP-5 [65] best-fit cosmology.[2]

8.1 Gravitational Chirality

Scenarios for gravitational chirality previously considered in the literature include[3]:

- *Addition of the Chern-Simons terms* to the Einstein-Hilbert action [83]. If there is some new physics that violates parity and time-reversal symmetry, that appears at a large energy scale, and involves a scalar field whose time evolution violates time-reversal, then the low-energy effective Lagrangian should include terms that are a generalization of those in Eq. (4.1) responsible for cosmic birefringence. In addition, the same physics can give rise to the following terms

$$\mathscr{L}_\phi = f(\phi) R^\lambda_{\sigma\mu\nu} \widetilde{R}^{\sigma\mu\nu}_\lambda, \tag{8.1}$$

  where $R^\lambda_{\sigma\mu\nu}$ is the Riemann tensor, and $\widetilde{R}^{\sigma\mu\nu}_\lambda$ its dual. In this scenario, the scalar could be a present-day field (like that in scalar-tensor theories of gravity, or the quintessence) in which case Solar-System tests constrain Chern-Simons gravity, as suggested in Ref. [87]. Here, we consider the case where ϕ is identified with the inflaton, so the only observable consequences are produced during inflation and imprinted on the CMB. While the coupling does not change the background dynamics, it can be shown to induce a difference in amplitudes of L and R

[2] When the numerical part of this work was done, only the 5-year results from WMAP were available; we note, however, that updating cosmological parameters and appropriate constraints to WMAP-9-year results should not affect our results in any significant way.

[3] Notice that these scenarios might come from similar underlying physics, but we mention them separately, as they are discussed in the literature.

primordial gravity waves, by amplifying R, while attenuating L, as they propagate inside the horizon. The accumulated difference becomes frozen when the modes exit the horizon, and it alters the statistical properties of the CMB during recombination, by inducing non-vanishing TB and EB power spectra. It is worth noting here that parity-violating gravitational Chern-Simons term is ubiquitous in string theory, the only current candidate for a unifying theory.

- *Chiral gravity*, whereby a different gravitational constant is associated with R and L gravitons [84]. As suggested in Ref. [84], since R and L graviton polarizations are two genuinely separate degrees of freedom, there is nothing in the theory forcing the L and R Newton's constants to the same value. It can also be shown that the difference between the two values would drive a discrepancy in the amplitudes of primordial L and R gravity waves.

- *Gravity at a Lifshitz point*, as a formulation of quantum gravity in 4-dimensions [88]. The associated action necessarily contains a Cotton tensor, which violates parity invariance, so we can expect as its robust prediction circular polarization of primordial gravitational waves, or gravitational chirality.

In all these inflationary mechanisms, which we refer to collectively as *chiral gravity*, linearized gravity prefers one handedness (i.e., it is chiral), so the power spectra of the L and R gravitational waves may have different amplitudes and thus induce non-vanishing TB and EB power spectra at the last-scattering surface. Measurements of these power spectra can therefore provide an estimate of the chiral asymmetry, with a variance due to the finite precision of the instrument and cosmic variance.

We first want to quantify the chirality by introducing an appropriate chirality parameter and show how the CMB polarization map depends on this parameter. To have B modes at the last-scattering surface, we need primordial gravitational waves, or in other words, a non-zero tensor-to-scalar ratio,

$$r \equiv A_t/A_s, \qquad A_t = \frac{r}{1+r}, \tag{8.2}$$

where A_t and A_s are, respectively, the fractional contributions of tensor and scalar modes to the TT quadrupole. Each one of the six CMB temperature/polarization power spectra—TT, EE, BB, TE, TB, and EB—have a tensor component proportional to A_t, while TT, EE, and TE additionally have a scalar component proportional to A_s. The tensor-to-scalar ratio r is constrained to be $\lesssim 0.22$ at a 95% confidence level [65] with WMAP-5.[4]

As demonstrated in Ref. [86], parity-odd TB and EB power spectra are proportional to the difference of the L- and R-mode contributions to the gravitational-wave (tensor) power spectra, $P^{t,L}(k)$ and $P^{t,R}(k)$,

$$C_\ell^{XX'} = (4\pi)^2 \int k^2 dk [P^{t,L}(k) - P^{t,R}(k)] \Delta_\ell^X(k) \Delta_\ell^{X'}(k), \tag{8.3}$$

[4]Current constraint with WMAP-9 results is even lower: $r \lesssim 1.3$ at a 95% confidence level [25].

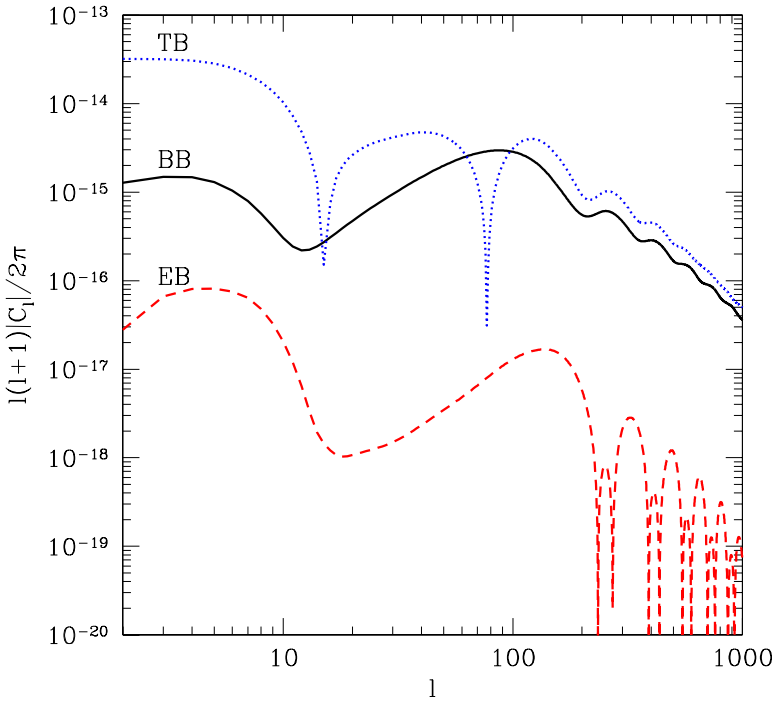

Figure 8.1: B-mode power spectra for $r = 0.22$ and $\Delta\chi = 0.2$.

while the tensor-contributions to the parity-even power spectra—TT, EE, BB, and TE—are

$$C_\ell^{XX'} = (4\pi)^2 \int k^2 dk [P^{t,L}(k) + P^{t,R}(k)] \Delta_\ell^X(k) \Delta_\ell^{X'}(k), \tag{8.4}$$

where $\Delta_\ell^X(k)$ is the radiation transfer function for X, and $X, X' = \{T, E, B\}$, as before. Following Ref. [86], we define a chirality parameter $\Delta\chi$ as

$$\begin{aligned} P^{t,L}(k) &\equiv \frac{1}{2}(1 + \Delta\chi) P^t(k), \\ P^{t,R}(k) &\equiv \frac{1}{2}(1 - \Delta\chi) P^t(k), \end{aligned} \tag{8.5}$$

where

$$P^t(k) \equiv P^{t,L} + P^{t,R}. \tag{8.6}$$

Maximal parity violation occurs when there are gravitational waves of only one handedness: $\Delta\chi = 1$ corresponds to fully left-handed, and $\Delta\chi = -1$ to fully right-handed gravitational waves. To illustrate, we show the three B-mode power spectra alculated using a modified version of CMBFAST for $r = 0.22$ and $\Delta\chi = 0.2$, in Figure 8.1.

To calculate the uncertainty with which $\Delta\chi$ can be estimated with different CMB experiments we use a Fisher-matrix analysis [80], employing the null hypothesis, $C_\ell^{EB} = C_\ell^{TB} = 0$. This ensures that the TB and EB power spectra do not have cross-correlations with the other four power spectra.

Instrument	$\theta_{\rm FWHM}$ [arcmin]	NET [μK$\sqrt{\rm sec}$]	$t_{\rm obs}$ [years]
WMAP-5	21	650	5
SPIDER	60	3.1	0.016
Planck	7.1	62	1.2
CMBPol	5	2.8	4
CV-limited	5	0	1.2

Table 8.1: Instrumental parameters from Ref. [9–11,50], for the five CMB experiments considered in the text. The parameters are the beamwidth, noise-equivalent temperature, and observation time.

The reciprocal value of the variance $\sigma^2_{\Delta\chi}$ is then given by [3]

$$\sigma^{-2}_{\Delta\chi} = \sum_\ell \sum_{A,A'} \frac{\partial C^A_\ell}{\partial \Delta\chi} \frac{\partial C^{A'}_\ell}{\partial \Delta\chi} [\Xi^\ell]^{-1}_{AA'}, \tag{8.7}$$

where the inversion is in AA' space, $A, A' = \{TB, EB\}$, and Ξ_ℓ is the TB-EB part of the power-spectrum covariance matrix[5] (see also Section 3.3 for definitions). The partial derivatives in Eq. (8.7) can be evaluated by noting from Eqs. (8.3) and (8.5) that

$$(\partial C_\ell^{TB/EB}/\partial\Delta\chi) = C_\ell^{TB/EB}(\Delta\chi = 1). \tag{8.8}$$

We obtain the TB/EB power spectra by modifying CMBFAST and using a ΛCDM model consistent with WMAP-5 parameters.

We now forecast the sensitivities to chiral gravity of the following five experiments: (i) WMAP-5, (ii) SPIDER's 150 GHz channel, (iii) *Planck*'s 143 GHz channel, (iv) CMBPol's (EPIC-2m) 150 GHz channel, and (v) a cosmic-variance–limited experiment. The corresponding instrumental parameters are given in Table 8.1. We use $\sigma_P = \sqrt{2}\sigma_T$ as before (see Section 3.3). We take $f^0_{\rm sky} = 1.0$ (the fraction of the sky surveyed), and $f_{\rm sky} = 0.7$ (the fraction of the sky used in the analysis), for all experiments, except for SPIDER, where $f^0_{\rm sky} = f_{\rm sky} = 0.5$.

Figure 8.2 shows the 1σ uncertainty of the estimate of $\Delta\chi$, as a function of tensor-to-scalar ratio r. The error increases with decreasing r, which implies the existence of a critical value of r below which a 1σ-level detection becomes impossible, even for maximal allowed signal (when $\sigma_{\Delta\chi} \geq 1$). This value is far above the upper limit for WMAP-5 (compare to results from Ref. [86]), and so WMAP-5 can provide no constraints on chiral gravity. Prospects are more optimistic for the upcoming and next-generation CMB data releases. The critical r is about 0.064 for SPIDER, 0.082 for *Planck*, 0.0079 for CMBPol, and 0.0023 for the cosmic-variance–limited experiment. If r is just below the WMAP-5 detection limit of 0.22, $\Delta\chi$ will be detectable at the 1σ level if it is greater than 0.46, 0.51, 0.18, and 0.11 for these four experiments, respectively. If we consider the 3σ confidence level,

[5] Note that under the null hypothesis $\Delta\chi = 0$, the 2×2 TB-EB part of the inverted 6×6 covariance matrix is the same as the inverse of the 2×2 TB-EB matrix.

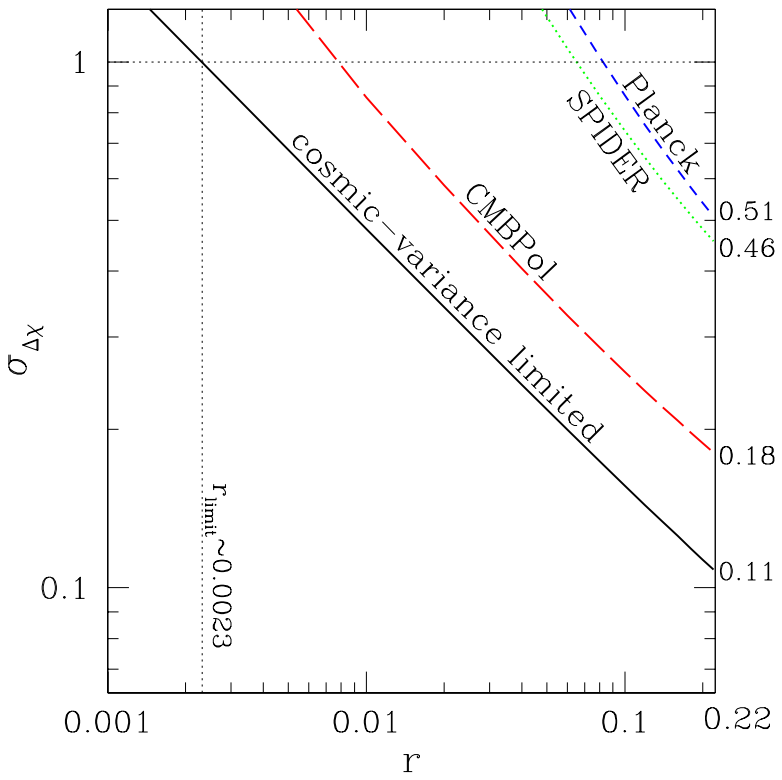

Figure 8.2: 1σ uncertainty on the gravitational-chirality parameter $\Delta\chi$ for five different CMB experiments, for the fiducial value of $\Delta\chi = 0$. The horizontal dotted line is at $\sigma_{\Delta\chi} = 1$ and represents maximal parity violation. In the region above this line, the chirality is non-detectable. Note that the WMAP-5 curve lies entirely above the non-detection line.

the corresponding lowest detectable values are larger by a factor of ~ 3.

To conclude this section, we show how different multipoles ℓ contribute to the sum of Eq. (8.7), separating the contribution from TB and EB, in Figure 8.3. In this plot, only the TB/EB summands of Eq. (8.7) are plotted against ℓ, for $r = 0.22$, for SPIDER, Planck, and CMBPol. The off-diagonal terms that contain the covariance between TB and EB are negligible. The major contribution to $\sigma_{\Delta\chi}^{-2}$ for all five experiments comes from the TB power spectrum, from low multipoles, $\ell \lesssim 7$. Thus, large angular scales in TB contain most of the information about gravitational chirality in the primordial signal.

8.2 Uniform Rotation

In this section, we rewrite all the relevant formulas needed to compare the effects of primordial chiral gravitational waves to uniform rotation from cosmic birefringence. We also re-evaluate the prospect for detecting uniform rotation with various CMB experiments.

If linear polarization at each point on the sky is rotated by an angle[6] $\Delta\alpha$, TB and EB power

[6]Notice the change in notation: previously used symbol α denoting a uniform-rotation angle is now substituted by

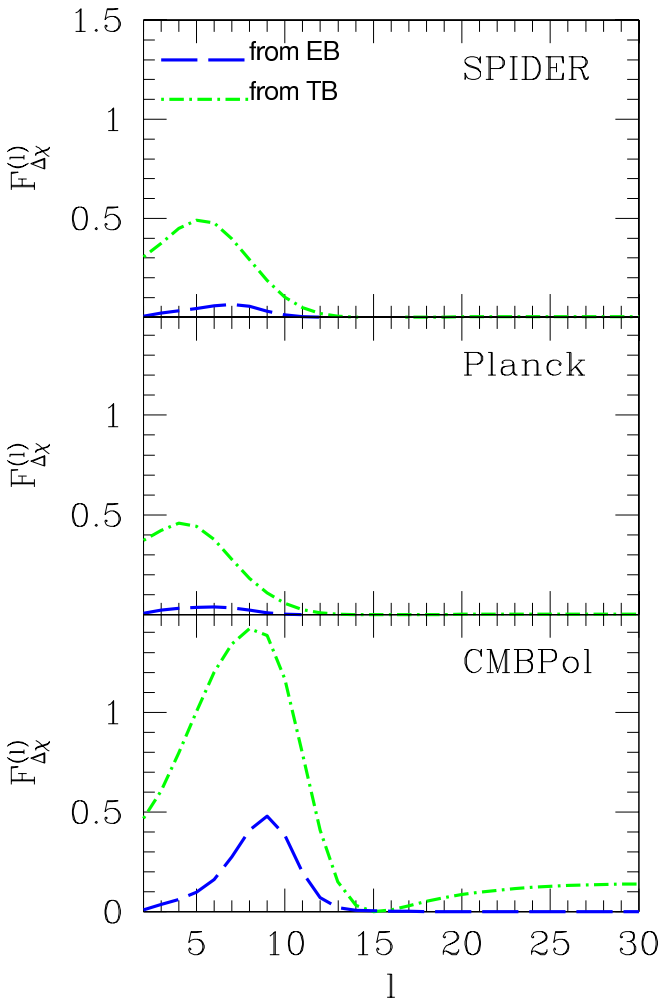

Figure 8.3: Diagonal (TB-TB and EB-EB) summands of Eq. (8.7), for $r = 0.22$, are plotted against the multipole ℓ to show that the constraint to $\Delta\chi$ comes primarily from the TB power spectrum at $l \lesssim 7$.

spectra are induced,

$$C_\ell^{TB,\mathrm{rot}} = 2\Delta\alpha C_\ell^{TE}, \qquad C_\ell^{EB,\mathrm{rot}} = 2\Delta\alpha C_\ell^{EE}. \tag{8.9}$$

The uncertainty $\sigma_{\Delta\alpha}$ to which $\Delta\alpha$ can be measured is given by

$$\sigma_{\Delta\alpha}^{-2} = \sum_\ell \sum_{A,A'} \frac{\partial C_\ell^A}{\partial \Delta\alpha} \frac{\partial C_\ell^{A'}}{\partial \Delta\alpha} [\Xi^\ell]^{-1}_{AA'}. \tag{8.10}$$

Using the same instrumental parameters as in Section 8.1, and for $r = 0.22$, we obtain the following 1σ uncertainties for the uniform rotation angle: 3.2° from WMAP-5, 0.9° from SPIDER, 15.9′ from Planck, 10.7” from CMBPol, and 1.9 μarcsec from a cosmic-variance–limited experiment—all in good agreement with previous forecasts (see Refs. [4, 54, 83] and Section 5.4).

$\Delta\alpha$, to match the notation for the chirality parameter, $\Delta\chi$.

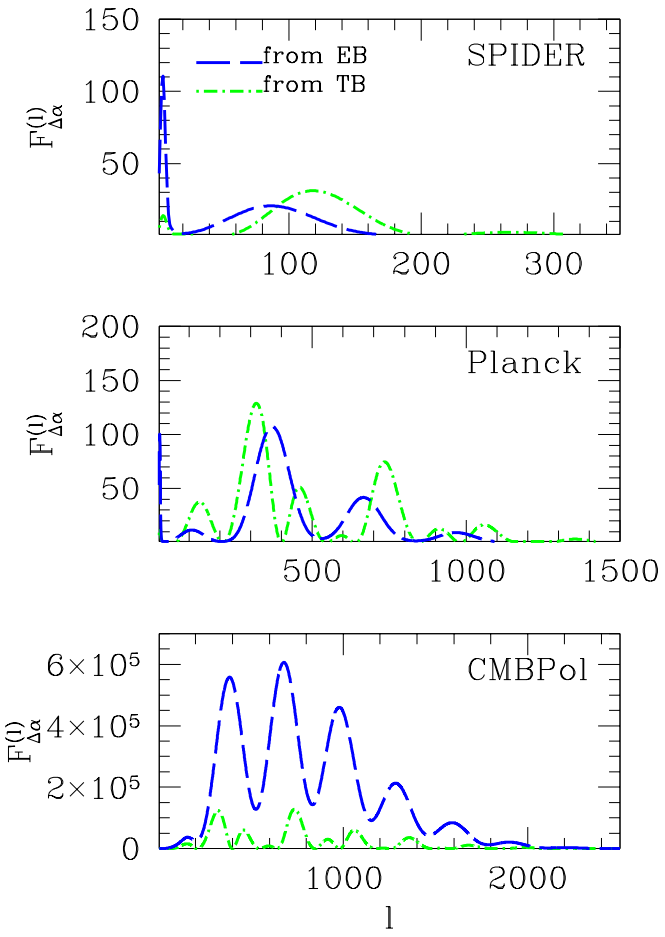

Figure 8.4: Diagonal (TB-TB and EB-EB) summands of Eq. (8.10), for $r = 0.22$, are plotted against the multipole ℓ to show that the constraints to $\Delta\alpha$ from upcoming and future CMB experiments will come primarily from ℓ's of $\sim$100, 500, or 700 (depending on the experimental sensitivity).

In Figure 8.4, we plot, separately, the contributions from only TB and only EB correlation to the sum in Eq. (8.10), as a function of multipole moment ℓ, for the cases of SPIDER, *Planck*, and CMBPol, for $r = 0.22$. The off-diagonal terms that contain the covariance between TB and EB are small. The dominant contribution to the constraint on $\Delta\alpha$ comes from the TB correlation for WMAP-5, and from EB for the higher-precision experiments. Different multipoles give the leading summands in $\sigma_{\Delta\alpha}^{-2}$ for different experimental sensitivities, but unlike the case of chiral gravitational waves, small angular scales ($l \gtrsim 100$) always dominate the sum.

8.3 Separating Chiral Gravity from Uniform Rotation

In this section, we ask how well the effects of chiral gravity and uniform rotation can be distinguished, assuming that a TB/EB power spectrum has been detected in CMB maps.

To first order in $\Delta\alpha$ and $\Delta\chi$, the TB/EB power spectrum is a sum of a part $C_\ell^{A,\mathrm{chi}}$ due to chiral

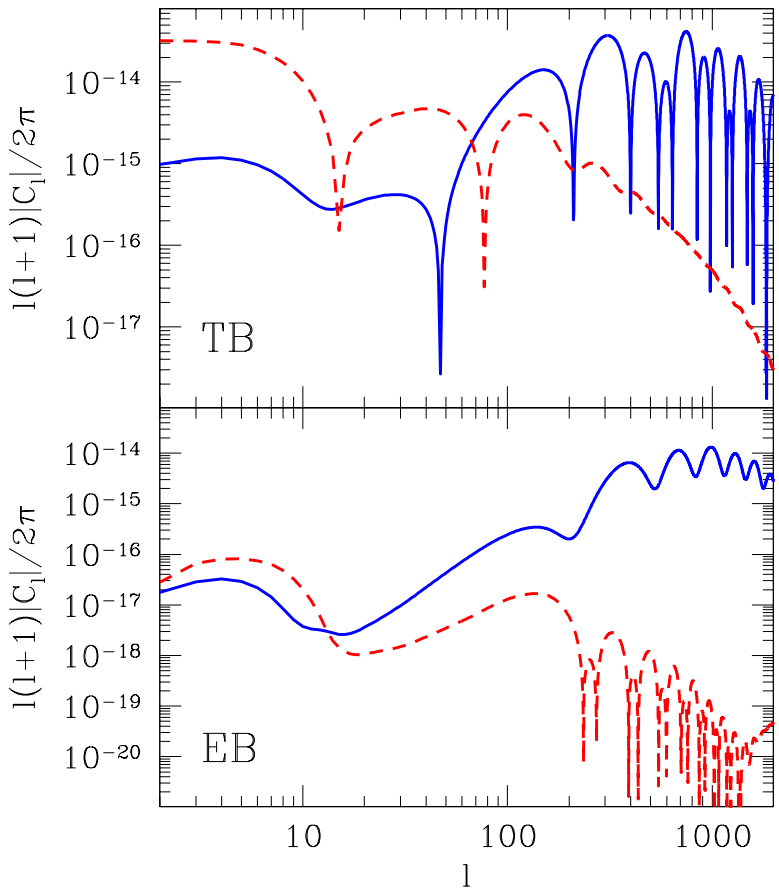

Figure 8.5: Theoretical curves representing TB and EB power spectra from primordial chiral gravitational waves for $\Delta\chi = 0.2$ and $r = 0.22$ (dashed red curves), and from uniform rotation for $\Delta\alpha = 5'$ (solid blue curves).

gravitational waves and a part $C_\ell^{A,\rm rot}$ due to uniform rotation. The combined EB and TB power spectra are

$$\begin{aligned} C_\ell^{TB,\rm tot} &= \Delta\chi C_\ell^{TB,t}(\Delta\chi = 1) + 2\Delta\alpha C_\ell^{TE}, \\ C_\ell^{EB,\rm tot} &= \Delta\chi C_\ell^{EB,t}(\Delta\chi = 1) + 2\Delta\alpha C_\ell^{EE}, \end{aligned} \tag{8.11}$$

where the superscript t indicates the tensor-induced part of the power spectrum, while the absence of it denotes the full power spectrum, including the scalar part, which we denote with superscript s. Figure 8.5, which shows $C_\ell^{A,\rm chi}$ and $C_\ell^{A,\rm rot}$, demonstrates that the contributions from these two mechanisms are qualitatively different. Our goal now is to quantify how well they can be distinguished, given a finite precision of the temperature/polarization maps.

The Fisher matrix for $\Delta\alpha$ and $\Delta\chi$ has the following entries

$$\mathcal{F}_{ij} = \sum_\ell \sum_{A,A'} \frac{\partial C_\ell^A}{\partial a_i} \frac{\partial C_\ell^{A'}}{\partial a_j} [\Xi^\ell]^{-1}_{AA'}, \tag{8.12}$$

where $i, j = \{1, 2\}$; a_i and a_j are the elements of $\vec{a} = (\Delta\alpha, \Delta\chi)$; $A, A' = \{TB, EB\}$; and $\mathcal{F}$ is the inverse of the covariance matrix between $\Delta\alpha$ and $\Delta\chi$. The derivatives in Eq. (8.12) can be calculated using Eq. (8.11), and $[\Xi^\ell]^{-1}_{AA'}$ is the inverse of the TB-EB covariance matrix defined in Section 3.3, where the inversion is in AA' space. Once again, we employ the null hypothesis[7] $\Delta\alpha = \Delta\chi = 0$.

Figure 8.6 shows 1σ error ellipses in the $\Delta\alpha$-$\Delta\chi$ parameter space, for WMAP-5, SPIDER, *Planck*, and CMBPol, for a range of tensor-to-scalar ratios. In addition, each plot shows a 1σ-error ellipse for a different set of fiducial values: $\Delta\chi = 0.2$ and $\Delta\alpha = 5$". The ellipses for this model are merely shifted in the $\Delta\alpha$-$\Delta\chi$ space, but are otherwise not significantly different from the null-hypothesis ellipses.

From Figure 8.6, we see that once we take into account the covariance between $\Delta\alpha$ and $\Delta\chi$, the results differ very slightly from the two cases where we had only one of these two effects acting on the CMB (the ellipses show very little tilt in $\Delta\alpha$-$\Delta\chi$ space). We conclude that if non-vanishing TB/EB power spectra are measured with high statistical significance, we will be able to distinguish uniform rotation from gravitational chirality to a high degree of precision.

This result can also be explained in terms of the features apparent in Figures 8.3 and 8.4, which show that the $\Delta\chi$ constraint comes primarily from TB at low ℓ's, while the $\Delta\alpha$ constraint comes primarily from EB at high ℓ's.

8.4 Constraints on Tensor-to-Scalar Ratio Revisited

We now examine a claim of Ref. [84] that if the gravitational-wave background is chiral, it may be more easily detected through the TB signal than the BB signal, due to a the boost in the amplitude obtained by cross-correlating a weak signal (B modes) with a strong one (T modes), rather than with itself.

Under the null hypothesis of no gravitational waves, the error with which the tensor-to-scalar ratio can be measured, from just one power spectrum A (where $A \in \{BB, TB, EB\}$) is

$$\sigma_r^{-2} = \sum_\ell \left(\frac{\partial C_\ell^A}{\partial A_t}\right)^2 \left(\Xi_{AA}^\ell\right)^{-1}, \tag{8.13}$$

where the inversion is in ℓ space. Remember that these power spectra are simply proportional to r,

$$(\partial C_\ell^A / \partial r) \propto C_\ell^A (r = 1). \tag{8.14}$$

[7] Even in the case where we work around non-zero fiducial values, the effect of the off-diagonal terms is negligible and the covariance matrix can be treated as a block-diagonal matrix to good precision. In addition, the cross-terms between TB/EB and the other four power spectra in Eq. (8.12) vanish, to the first order in small parameters, so we really only need to consider TB and EB separately.

The relevant covariance-matrix entries are obtained from Eqs. (3.35) and (3.41), for

$$C_\ell^{BB} = C_\ell^{TB} = C_\ell^{EB} = 0, \tag{8.15}$$

and they read

$$\Xi_{BB}^\ell = \frac{2}{2\ell+1}\left(C_\ell^{BB,\mathrm{map}}|W_l|^{-2}\right)^2 = \frac{2}{2\ell+1}\left(C_\ell^{BB,\mathrm{noise}}|W_l|^{-2}\right)^2, \tag{8.16}$$

$$\begin{aligned}\Xi_{TB,TB}^\ell &= \frac{1}{2\ell+1}|W_l|^{-4}\left[\left(C_\ell^{TB,\mathrm{map}}\right)^2 + C_\ell^{TT,\mathrm{map}}C_\ell^{BB,\mathrm{map}}\right] \\ &= \frac{1}{2\ell+1}C_\ell^{BB,\mathrm{noise}}|W_l|^{-2}\left[C_\ell^{TT,s} + C_\ell^{TT,\mathrm{noise}}|W_l|^{-2}\right],\end{aligned} \tag{8.17}$$

where we have employed the null hypothesis in the second equality in each of these equations. The expressions are similar for EB, with the substitute $T \to E$.

Given that the current data already provide signal-dominated temperature measurements,

$$C_\ell^{TT,\mathrm{noise}} \ll C_\ell^{TT}, \tag{8.18}$$

for the low ℓ, at which the gravitational-wave signal arises, we can set

$$C_\ell^{TT,\mathrm{noise}} \approx 0. \tag{8.19}$$

Moreover,

$$C_\ell^{TB} \sim \beta(C_\ell^{BB}C_\ell^{TT})^{1/2}, \qquad \text{with } \beta \sim 0.1. \tag{8.20}$$

As a result, while the summand for σ_r^{-2} from BB is $\sim (C_\ell^{BB}/C_\ell^{BB,\mathrm{noise}})^{-2}$, that from TB is $\sim C_\ell^{BB}/C_\ell^{BB,\mathrm{noise}}$. Thus, in the limit of sufficiently high signal-to-noise, $C_\ell^{BB,\mathrm{noise}} \to 0$, the BB signal provides a better probe (i.e., probes smaller σ_r). In other words, the value of the cross-correlation with T is ultimately limited by cosmic variance (as is also the cross-correlation with E), while the BB sensitivity improves without limit as the instrumental noise is reduced. The importance of TB is also weakened slightly given that

$$C_\ell^{TB} < [C_\ell^{TT}C_\ell^{BB}]^{1/2}. \tag{8.21}$$

It is true that in the opposite limit, where instrumental noise is large, TB is more sensitive to gravitational waves (with $\Delta\chi = 1$) than TT. However, this limit is only of academic interest, as it encompasses the regime of r that is already ruled out by temperature measurements.

To make these arguments more quantitatively precise, we have evaluated σ_r for BB, TB, and

Instrument	from BB	from TB	from EB
WMAP-5	0.68	0.37	3.03
SPIDER	0.011	0.051	0.20
Planck	0.026	0.071	0.30
CMBPol	1.57×10^{-5}	0.0018	0.0062

Table 8.2: The projected 1σ uncertainty σ_r on the tensor-to-scalar ratio for a maximal chiral-gravitational-wave background with $\Delta\chi = 1$, from measurements of three different power spectra, for several CMB experiments.

EB (for $\Delta\chi = 1$) for WMAP-5, SPIDER, *Planck*, and CMBPol; the results are shown in Table 8.2. We see that the sensitivity to gravitational waves with future experiments will come primarily from BB measurements, with only marginal improvement from TB measurements. While the TB sensitivity of WMAP-5 is better than that of BB, the smallest r detectable with either is already larger than the upper limit obtained from TT measurements.

In conclusion, we showed here that, while TB may improve the sensitivity to a chiral-gravitational-wave background, it does so only marginally, with most of the sensitivity due primarily to BB (see also Ref. [86]).

8.5 Possible B-mode Contamination

We now briefly examine the degree of contamination that the reconstruction of the parity-violating signals considered in this chapter might suffer from other cosmological sources of B modes—the primordial tensor modes and the weak lensing of the CMB.

Chiral-gravitational-wave signal and the *uniform-rotation* signal represent parity violations. Only such effects that exhibit *overall* preferred handedness in the sky can induce EB and TB *power spectra*, to first order. Weak lensing and the fluctuations in the rotation angle that average to zero on the whole sky, for example, only induce off-diagonal correlations in the maps, where $\ell \neq \ell'$. Therefore, the lensing signal does not mimmic parity-violating signals, and so should not bias the measurements discussed in this chapter.

However, it is worth noting that the expressions of Eq. (8.9) hold true only to first order in small parameters, $\Delta\alpha$ and r. Second-order contribution to $C_\ell^{EB,rot}$ can arise due to rotation of a primordial B mode into an E mode. This contribution is, however, negligible even in the case where r takes on the maximal value allowed by current observations. Likewise, the additional contribution due to late-time rotation of a lensing-induced B mode is also negligible (second order in small parameters).

On the other hand, when calculating the uncertainties, we include both the weak-lensing[8] and primordial B modes, in order to account for their contribution to the overall noise power. To

[8]The lensing surface is assumed to be located after the last-scattering surface, and before most of the rotation can take place.

illustrate these different contributions, we compare them to the instrumental noise in Figure 8.7. From this figure, it is evident that the noise power is dominated by the instrumental noise/resolution at high ℓ's, and by the primordial BB at low ℓ's. For the case of chiral gravitational waves, for example, there is no need to include the contribution from the weak lensing, since the constraints to $\Delta\chi$ come from large scales (below ℓ of 10 or so), where weak lensing has no power[9].

8.6 Summary and Discussion

In this chapter, we first revisited the sensitivity of current and future CMB experiments to chiral-gravitational-wave background leftover from inflation, and to uniform rotation from cosmic birefringence, separately. We showed that the WMAP polarization data are not precise enough to provide any information about gravitational chirality, even for the case where the tensor-to-scalar ratio is just below the current upper limit. *Planck* and SPIDER may be able to make a marginal detection, but only if r and $\Delta\chi$ are both close to their maximal allowed values. CMBPol may probe gravitational chirality over a larger range of the r-$\Delta\chi$ parameter space. As an illustration, the smallest amount of gravitational chirality detectable at the 3σ level with a cosmic-variance–limited experiment (if r is at its maximal allowed value) corresponds to about 65% of the gravitational-wave background being of one handedness, and 35% of another. In an analogous analysis, we show that Planck has a 1σ sensitivity to a uniform rotation of about $16'$, while a cosmic-variance–limited experiment could reach down to rotation angles of about 2μarcsec.

We then showed that there is no strong degeneracy between $\Delta\alpha$ and $\Delta\chi$ parameters. In other words, the effects of chiral gravity and uniform rotation can be easily distinguished, provided that the TB/EB power spectra are clearly detected. However, the same results can be interpreted as to infer that a marginal (e.g., 3σ) detection of $\Delta\alpha$ could be due, alternatively, to gravitational chirality at some level. For example, if CMBPol were to measure $\Delta\alpha \approx 15$" and find $r = 0.1$, then the corresponding TB/EB detection could alternatively be attributed, with similar statistical significance, to gravitational chirality with $\Delta\chi = 0.6$. If, however, the earlier suggestion of a TB/EB signal corresponding to a rotation angle of 6° [67] had held up, it could *not* have been attributed to chiral gravity, as the implied value of $\Delta\chi$ would have been in the unphysical regime $\Delta\chi \gg 1$. The plot that summarizes these results is shown in Figure 8.6.

Furthermore, we re-examined an earlier claim that, if the gravitational-wave background is chiral, it may be more easily detected through the TB signal than the BB signal. We demonstrated that, while TB may improve the sensitivity, it does so only marginally, due to cosmic-variance limitation; BB remains the most sensitive probe for the noise regime of *Planck* and next-generation CMB experiments.

[9] We note here that these conclusions hold for a full-sky analysis; in the case of cut-sky, a more careful treatment of this issue may be required.

A few more notes on distinguishing these two parity-violating effects. If a parity-violating signal is detected in the CMB and attributed to uniform rotation from cosmic birefringence, it may be possible to test it further with observations of cosmological radio sources [89]. Off-diagonal correlations in the CMB may also provide additional information on cosmic birefringence, if the rotation angle is position dependent [4, 51, 54], as suggested in Refs. [47, 90], and discussed in detail in Chapter 5. A parity-violating signal from chiral gravity waves might be distinguished from that due to cosmic birefringence through direct detection of the gravitational-wave background at shorter wavelengths [91–94]. Finally, it may be that any signals of chiral gravity in the CMB may be corroborated, within the context of specific alternative-gravity theories, by a variety of other observations and measurements [95].

Finally, we emphasized that we do not expect weak lensing by the large-scale structure to be a significant contaminant in detecting a signal from chiral gravity and/or cosmic birefringence, with *Planck* or CMBPol. For the case of direction-dependent rotation, the contribution of the weak leansing can be geometrically distinguished from the effects of rotation, as discussed in Section 5.3. We examined potential contamination for the case of parity-violating signals, and showed that in the case of chiral gravity, most of the signal is imprinted in the large-scale inhomogeneities, where weak lensing has no power. On the other hand, for uniform rotation, the corresponding correction to the variance due to weak lensing turns out to be numerically small—less than 10% for CMBPol, and negligible for all other instruments we considered (except for a cosmic-variance–limited experiment where we analyzed un-lensed maps only).

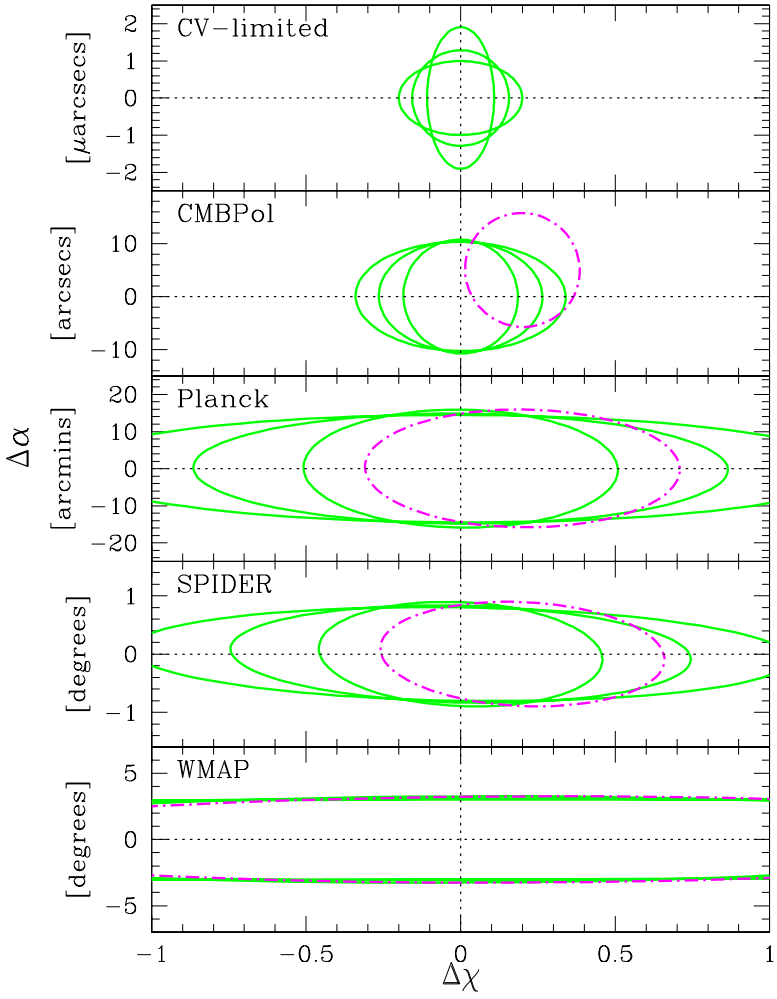

Figure 8.6: Constraints on the allowed $\Delta\alpha$-$\Delta\chi$ parameter space are shown for the case of null detection with different experiments (in case of null detection, the area outside the ellipse is excluded at a 68% confidence level). The solid-line ellipses on each plot are for the fiducial value of zero for both parameters, and for the following values of tensor-to-scalar ratios (going from the narrowest to the widest ellipse in the $\Delta\chi$ direction): 0.22, 0.1, and 0.06. The dot-dashed ellipse in each plot is for $r = 0.22$, for a model with $\Delta\chi = 0.2$ and $\Delta\alpha = 5$". In both models, the tilt of the ellipses is negligible, which means that the two signals are separable to high accuracy, provided a detection with high statistical significance. Thus, the combined constraints on both parameters are almost the same as those calculated individually in Sections 8.1 and 8.2.

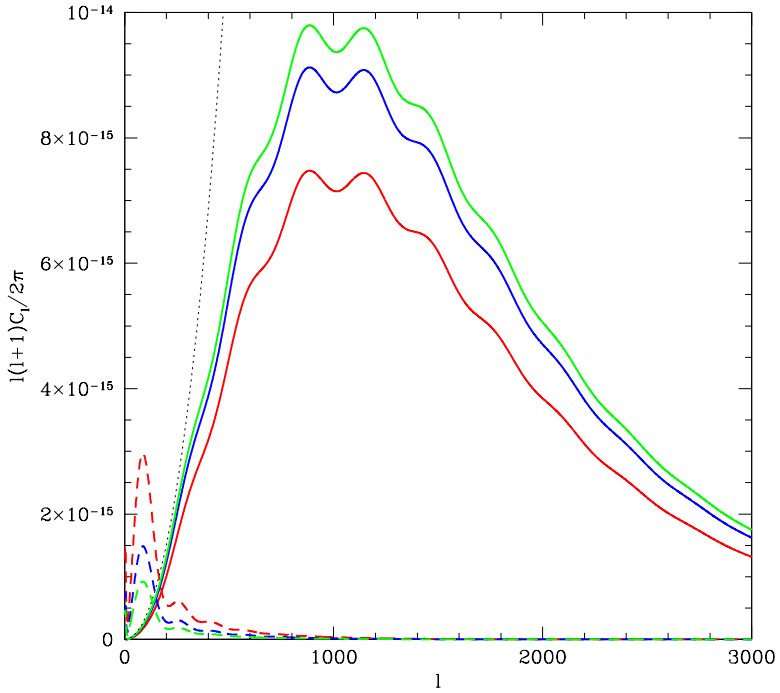

Figure 8.7: BB power spectra from primordial gravitational waves (dashed lines), and from the weak lensing of the primordial E modes (solid lines), for $r = 0.22$ (red), $r = 0.1$ (blue), and $r = 0.06$ (green). The dotted black line is appropriately normalized instrumental-noise power spectrum for CMBPol. Note that the instrumental noise dominates at high multipoles, due to the limited resolution of the experiment. The lensed maps are obtained from CMBFAST code for the same set of cosmological parameters we use throughout this chapter.

Part IV

Probing Old Times: Cosmic Reionization

Since recombination at the age of ∼380 000 years ($z \approx$1100), the Universe stayed mostly neutral for the next 100 million years or so ($z \approx$ 20–30), when the first astrophysical sources of light were born and started a phase transition from the cosmic "dark ages" to the ionized and star-lit Universe we observe today. Details of the epoch of reionization (EoR) are still unclear, and currently available observational constraints are few.

Lyα absorption in the spectra of distant quasars suggests that the tail end of reionization occurred at a redshift $z \gtrsim 6$ [96], but the implications of these measurements are difficult to interpret precisely [97]. Recent measurements of the density of Lyα emitters at high redshift also imply a transition from neutral to ionized intergalactic medium (IGM) occured at $z \lesssim$ 6–7, or so [98]. Large-scale anisotropy in the CMB polarization spectra (the "reionization bump", visible at $\ell \lesssim 10$ in Figure 3.4), implies an integrated optical depth to Thomson scattering of CMB photons off free electrons of $\tau \approx 0.074 \pm 0.034$, which places the redshift of reionization at $z_r \approx 10.6 \pm 1.4$, with 68% confidence [46, 99], if reionization occurred everywhere suddenly (i.e., if the ionized fraction[10] $x_i(z)$ is a step function). However, analytic considerations [100–102] and numerical simulations [103] have long established the current paradigm of an inhomogeneous reionization process [104], where regions of ionized gas, seeded by the first star-forming galaxies, grew and eventually coalesced, filling the entire volume of the IGM. If so, then reionization may have occurred over a range of redshifts. Recent results from the EDGES experiment [105], a low-frequency survey looking to detect a global reionization signal by observing a step function in the frequency spectrum of the sky, placed a lower limit on the duration of the EoR, $\Delta z \gtrsim 0.06$, at 95% confidence level. Finally, observations from the SPT CMB survey have provided an upper limit on the duration of the EoR for specific reionization scenarios (under assumptions that the mechanism of reionization accords with prevailing theoretical models), $\Delta z \lesssim 7.9$, at 95% confidence level [106], by constraining the kinetic-Sunyaev-Zel'dovich signal [107] from bulk motions of ionized bubbles during the EoR.

Properties of ionizing sources (their clustering, masses, radiation spectra, feedback mechanisms, etc.) control details of the IGM tomography (size distribution of the bubbles as a function of redshift, and the overall ionized fraction), and so confronting theoretical predictions about the tomography with direct observations of the EoR is one of the most active and challenging areas of research in modern cosmology.

There are several avenues currently explored for probing details of the EoR; in this part of the thesis, we focus on the following two: reionization signatures imprinted on the CMB, and redshifted 21-cm signal from neutral hydrogen during EoR. These are complimentary ways to tie observables to the description of the ionization structure during the EoR. While the 21-cm mapping allows for 3D tomography of neutral hydrogen (since scanning in frequency space corresponds to mapping in redshift z), the CMB can only recover a projection in 2D plane of the sky. On the other hand, the

[10] The ionized fraction x_i is defined as the ratio of the number of protons to the total number of hydrogen atoms.

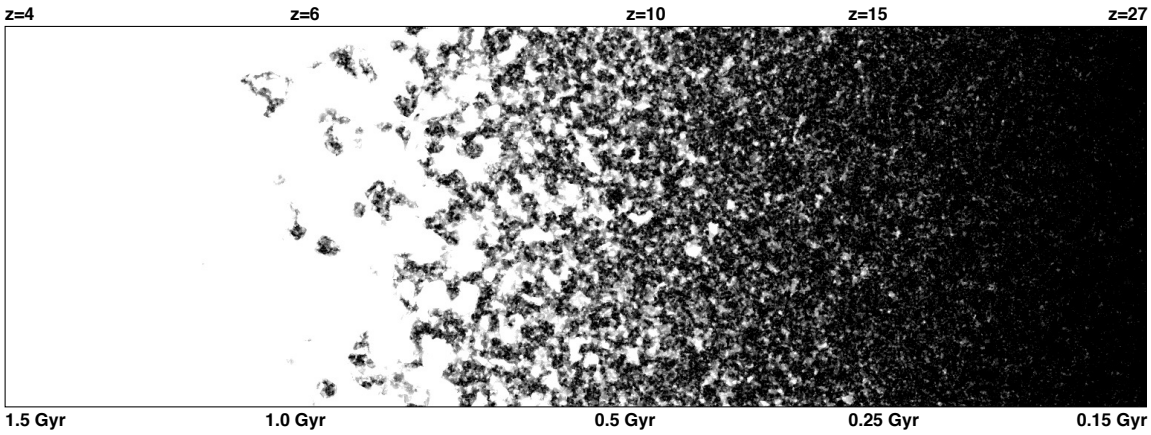

Figure 8.8: A slice through redshifts from one of the simulations of the EoR is shown. Black represents neutral, and white ionized IGM. Notice the inhomogeneous ionization structure in the mid-phases of the reionization process, where regions of ionized gas form around sources of radiation, expand, and merge to complete the EoR at low redshifts. (Figure from Ref. [106]).

21-cm spectral line probes neutral fraction during the EoR, while the CMB probes ionized fraction through the integrated optical depth all the way to the last-scattering surface.

In this thesis, we first use currently available CMB data to constrain simple phenomenological models of reionization and discuss implications for future work (Chapter 9). We then diverge from the CMB and investigate statistical tools which can be applied to the maps of the redshifted 21-cm signal—the goal of many low-frequency radio arrays currently under construction (Chapter 10).

Chapter 9

Reionization Signatures in the CMB

There are three main mechanisms that affect the statistics of the CMB during the EoR [108]: (i) Thomson scattering of the local CMB quadrupole off the free electrons in ionized regions adds large-scale power to polarization anisotropies; (ii) Doppler shift of the CMB photons scattered off ionized regions with peculiar motions gives rise to the kinetic Sunaiev-Zel'dovich effect; and (iii) the screening of the last-scattering surface due to Thomson scattering damps CMB anisotropies by a factor of $e^{-\tau(\hat{\mathbf{n}})}$, where, sourced by the inhomogeneities in the ionized fraction during the *patchy* middle phase of the EoR, the integrated optical depth varies as a function of the position $\hat{\mathbf{n}}$ in the sky [108],

$$\tau(\hat{\mathbf{n}}, z) = \sigma_T n_{p,0} \int_0^z dz' \frac{(1+z')^2}{H(z')} x_i(\hat{\mathbf{n}}, z'), \tag{9.1}$$

where σ_T is the Thomson-scattering cross-section, $n_{p,0}$ is the present-day nuber density of protons, and $x_i(\hat{\mathbf{n}}, z)$ is the ionization fraction in direction $\hat{\mathbf{n}}$ at redshift z. In this chapter, we study the effects of *patchy screening* on the CMB.

Anisotropic screening of the small-scale fluctuations produces a B-mode polarization that is correlated in a characteristic way with the temperature and with the E mode [108, 109], and it also modulates the power in the temperature map. Statistically, the effect on the CMB maps is very similar to the effect of anisotropic rotation we discussed in earlier chapters. In fact, the minimum-variance-estimator formalism used to search for $\alpha(\hat{\mathbf{n}})$ in CMB maps can easily be adapted for reconstruction of $\tau(\hat{\mathbf{n}})$ and its power spectrum $C_L^{\tau\tau}$, which is the approach we use in this chapter.

In Section 9.1, we outline the formalism adapted for reconstruction of the optical-depth map $\tau(\hat{\mathbf{n}})$ proposed by Ref. [108]. In Section 9.2, we interpret prior null searches for a modulation of CMB power [110] in terms of an upper limit to optical-depth fluctuations. We then apply the minimum-

Material in this chapter was largely adapted from "Patchy screening of the cosmic microwave background by inhomogeneous reionization," Vera Gluscevic, Duncan Hanson, and Marc Kamionkowski, *Phys. Rev. D* **87**, 047303 (2013) [13]. Reproduced here with permission, ©(2013) by the American Physical Society.

variance estimator of Ref. [108] to WMAP-7 data to search for patchy screening by measuring the off-diagonal TB correlations. We derive an upper limit to all multipoles of the power spectrum $C_L^{\tau\tau}$ up to $L = 512$, and discuss possible systematic effects that might affect our results. In Section 9.3, we discuss implications of these constraints for a simple phenomenological reionization model whose parameters might serve as figures of merit for future experiments. We also revisit predictions for future experiments and discuss constraints on the parameter space imposed by the recent results from the EDGES [105] experiment. Finally, we conclude and summarize in Section 9.4.

9.1 Patchy Reionization

Patchy-reionization signal can be traced either through its effect on the CMB power spectra or using the off-diagonal correlations induced by directional variation of τ. However, the effect on the power spectra is small on all angular scales, and will be difficult to disentangle from other secondary anisotropies, such as lensing and low-redshift kinetic Suniaev-Zel'dovich effect[1] [108, 114–119]. We therefore focus on the reconstruction from off-diagonal correlations proposed by Ref. [108]. This formalism is directly analogous to the minimum-variance–estimator formalism we used to look for direction-dependent rotation from cosmic birefringence (discussed in detail in Chapter 5), the main difference being the opposite parities of $\widehat{\alpha}_{LM}$ and $\widehat{\tau}_{LM}$ estimators. We briefly review the main formulas in the following.

Patchy screening suppresses primary[2] anisotropies, so the observed temperature fluctuation and polarization are, respectively,

$$\begin{aligned} T^{\rm obs}(\widehat{\mathbf{n}}) &= e^{-\tau(\widehat{\mathbf{n}})}\Delta T(\widehat{\mathbf{n}}), \\ p^{\rm obs}(\widehat{\mathbf{n}}) \equiv Q(\widehat{\mathbf{n}}) + iU(\widehat{\mathbf{n}}) &= e^{-\tau(\widehat{\mathbf{n}})}p(\widehat{\mathbf{n}}), \end{aligned} \tag{9.2}$$

where Q and U are the usual Stokes parameters. All six temperature and polarization correlations in the CMB can, in principle, be used to reconstruct the map of $\tau(\widehat{\mathbf{n}})$.[3] The EB estimator will ultimately provide the best sensitivity to patchy screening [4, 109], once low-noise polarization measurements are available with future CMB experiments. With WMAP and *Planck*, however, the best sensitivity is achieved with the TT correlation, which we discuss in Section 9.2. Here, we derive a constraint to patchy screening from the TB correlation, as a proof of principle for future application of this analysis method. The estimator for the optical-depth fluctuation is [4, 109] (see also Section

[1] For example, currently favored patchy-reionization models produce BB power spectra with an amplitude of $\sim 0.01\mu$K, which is an order of magnitude lower than the one expected from weak lensing [107, 111–113].

[2] By "primary" here, we mean those generated before reionization.

[3] Note that this was *not* the case with direction-dependent rotation of polarization maps, where temperature was not affected.

6.2),

$$\widehat{\tau}_{LM} = -iN_L \int d\widehat{\mathbf{n}}\, Y_{LM}(\widehat{\mathbf{n}}) \left[\sum_{\ell m \ell' m'} \bar{B}^*_{\ell m 2} Y_{\ell m}(\widehat{\mathbf{n}}) C^{TE}_{\ell'} \bar{T}_{\ell' m' 2} Y^*_{\ell' m'}(\widehat{\mathbf{n}}) + \text{complex conjugate} \right], \quad (9.3)$$

where the sum is only over $\ell + \ell' + L = $ odd. Barred quantities $\bar{B}_{lm}$ and $\bar{T}_{lm}$ represent the inverse-variance–filtered multipoles,

$$\begin{aligned} \bar{B}_{\ell m} &\equiv B^{\rm map}_{\ell m} / C^{BB,{\rm map}}_{\ell}, \\ \bar{T}_{\ell m} &\equiv T^{\rm map}_{\ell m} / C^{TT,{\rm map}}_{\ell}, \end{aligned} \quad (9.4)$$

where the TT and BB power spectra are analytic estimates of the total (signal plus noise) power spectrum, as defined in Chapter 6,

$$C^{XX,{\rm map}}_{\ell} \equiv C^{XX}_{\ell} + C^{XX,{\rm noise}}_{\ell} W^{-2}_{\ell}, \quad (9.5)$$

in a given frequency band, for $XX \in \{TT, BB\}$, and $B^{\rm map}_{\ell m}$ and $T^{\rm map}_{\ell m}$ are the observed temperature and polarization multipoles, recovered from the maps and corrected for the combined instrumental-beam and pixelization transfer function W_ℓ. The normalization N_L can be calculated either analytically or using Monte Carlo simulations. Note that the estimator of Eq. (9.3) is equivalent to the real part of the rotation-angle estimator in of Eq. (6.5), the only difference being the parity condition. In Chapter 6, we demonstrated that the full-sky formalism with the full-sky inverse-variance-filtering procedure described above is justified in spite of the sky cuts introduced by masking the Galaxy.

The TB correlations sought by this estimator can in principle also be generated by re-scattering of CMB photons and by the kinetic-Sunyaev-Zel'dovich effect from re-scattering. However, Ref. [108] showed that the estimator is relatively insensitive to the kinetic-Sunyaev-Zel'dovich effect, and also that only the large-scale ($\ell \lesssim 40$) temperature fluctuations are sensitive to the former mechanism. In order to avoid large-scale contamination from pixel-pixel noise correlations in WMAP, we discard $T^{\rm map}_{\ell m}$ and $E^{\rm map}_{\ell m}$ multipoles below $l = 100$ from our analysis anyway, so we effectively probe only patchy screening.

The estimator for the corresponding power spectrum of fluctuations of τ is

$$C^{\widehat{\tau}\widehat{\tau}}_L \equiv \frac{1}{f_{\rm sky}(2L+1)} \sum_M \widehat{\tau}_{LM} \widehat{\tau}^*_{LM}, \quad (9.6)$$

where, as before, $f_{\rm sky}$ represents the fraction of the sky admitted by the analysis mask, correcting for the fact that the full-sky analysis is applied to the maps where a portion of the pixel values (mostly around the Galactic plane) was set to zero. When evaluated for the fixed cosmology of WMAP-7 best-fit parameters, and for the noise levels appropriate for the experiment in consideration, this four-point correlation provides a biased estimate of $C^{\tau\tau}_L$, where the bias mostly arises from the

inhomogeneous pixel noise and the sky cuts. However, if this trispectrum is estimated by cross-correlating the $\widehat{\tau}_{LM}$ signal estimated from one frequency band with the same signal estimated from another frequency band, the largest contribution to its bias vanishes, because the instrumental noise is uncorrelated in different frequency bands. The leftover bias can be evaluated and subtracted by running a suite of null-hypothesis (no patchy signal) Monte Carlo simulations. We therefore generate a suite of null simulations, as described in Section 6.5, and use data-based de-biasing technique of Section 6.2. We also use the null simulations to recover the statistical uncertainty for each measurement following the procedure described in Chapter 6.

9.2 Current Constraints from CMB

We now show the results that the analysis method described in Chapter 6, adapted for the search for patchy screening in WMAP-7 data, yields. The results are shown only for the cleanest band-cross correlation [WW][VV], where the estimate of τ_{LM} recovered from the W frequency band is cross-correlated with the estimate from the V frequency band. Prior to the analysis, we mask out the Galaxy and the known point sources using the fiducial 7-year analysis masks available at the LAMBDA website [8] (where for the combined mask $f_{\rm sky} \approx 68\%$). After subtracting the bias, we recover a de-biased estimate $\widehat{C}_L^{\tau\tau}$ of the power spectrum at each multipole up to $L = 512$; Figure 9.1 shows the binned measurements with estimated uncertainties. At all multipoles, we recover consistency with zero within the 3σ confidence level.

Our simulations do not include polarized point sources nor foreground residuals. In order to test their impact on our estimates of the power spectrum and associated statistical uncertainty, we perform the tests described in Section 6.7. The results of these tests are shown in Figures 9.2 and 9.3, which demonstrate that the foregrounds and point sources do not significantly affect the results reported in Figure 9.1.

9.3 Interpretation: Simple Analytic Model for Reionization

To understand the implications of the results of Section 9.2, we consider a simple parametrization of inhomogeneous reionization in which optical-depth fluctuations are described by white noise smoothed on angular scales

$$\theta_C \equiv \pi/L_C, \tag{9.7}$$

corresponding to the following power spectrum

$$C_L^{\tau\tau} = (4\pi/L_C^2)(\Delta\tau)^2 e^{-L^2/L_C^2}, \tag{9.8}$$

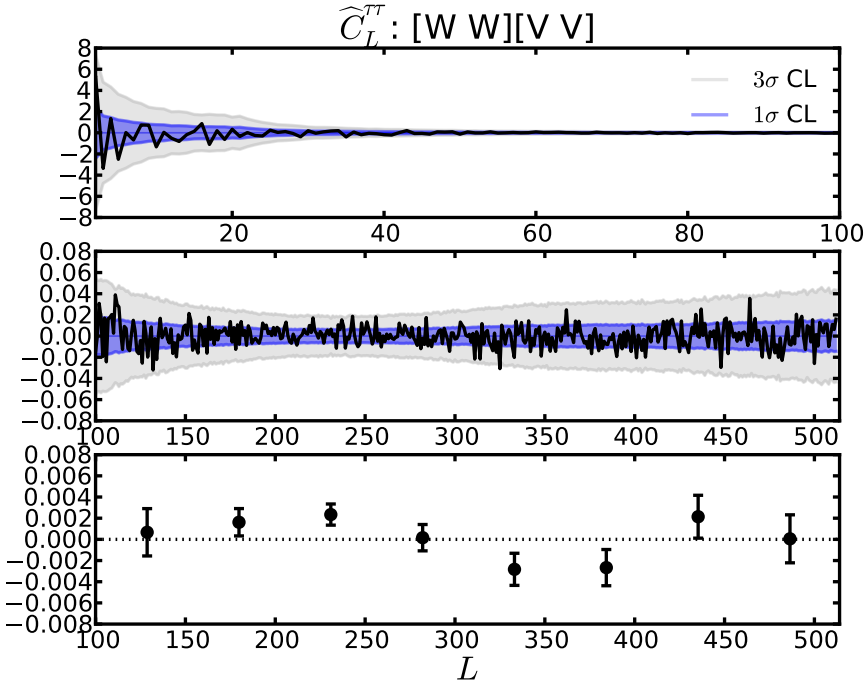

Figure 9.1: The top two panels show the measurements of the power spectrum of fluctuations in optical depth τ, recovered from off-diagonal TB correlations, with corresponding 1σ and 3σ confidence-level intervals, for all multipoles down to the resolution limit of WMAP-7. A binned version of this plot, with associated statistical uncertainty, is shown in the bottom panel. The first two bins are -0.0085 ± 0.1264 at $L = 26$, and 0.0029 ± 0.0056 at $L = 77$; they are omitted for the sake of clearer presentation. The measurements are consistent with zero at all multipoles.

plotted in Figure 9.5 for several values of L_C. We constrain the parameters $\Delta\tau$ and L_C with the Fisher-matrix minimum-variance estimate for the amplitude,

$$\widehat{(\Delta\tau)^2} = (\sigma[(\Delta\tau)^2])^2 \sum_L C_L^{\tau\tau,\mathrm{fiducial}} \widehat{C}_L^{\tau\tau} / \mathrm{var}(\widehat{C}_L^{\tau\tau}), \tag{9.9}$$

where

$$\left(\sigma[(\Delta\tau)^2]\right)^{-2} = \sum_L (C_L^{\tau\tau,\mathrm{fiducial}})^2 / \mathrm{var}(\widehat{C}_L^{\tau\tau}) \tag{9.10}$$

is roughly the inverse-variance with which $(\Delta\tau)^2$ can be measured, $\mathrm{var}(\widehat{C}_L^{\tau\tau})$ is the variance of the power spectrum, estimated from a suite of simulations with no patchy screening, and $\widehat{C}_L^{\tau\tau}$ are the unbinned measurements from WMAP-7 maps. Since the results are consistent with no signal, the variance provides a constraint on $(\Delta\tau)^2$, which we show as a function of the model parameter L_C in Figure 9.6. We also show in Figure 9.6 the upper limit to $(\Delta\tau)^2$ inferred from upper limits to the power of TT modulation discussed in Ref. [110]. Given that the mean optical depth is known to be $\tau \sim 0.1$, it is clear that our bound $\Delta\tau \lesssim 1$, from TB is far from constraining, and that

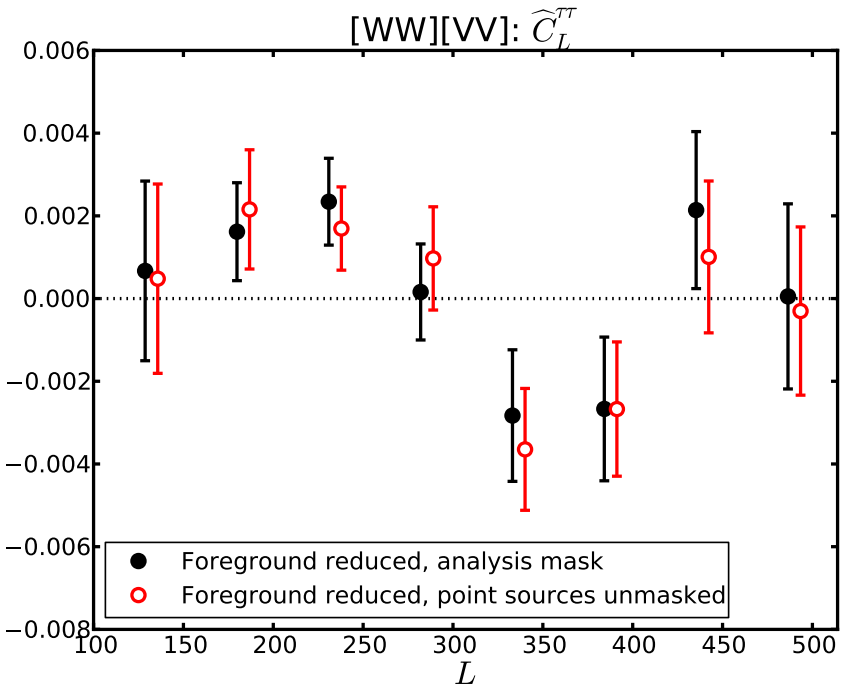

Figure 9.2: Measurement of $\widehat{C}_L^{\tau\tau}$ from off-diagonal TB correlations in WMAP-7 data. Results shown in black (filled circles) are obtained by using the analysis mask that covers all the point sources brighter than ~ 1 Jy, while the results in red (empty circles) are obtained after unmasking all the point sources. In spite of the large difference in the source contamination, the two results differ by much less than the statistical uncertainty, and no overall bias is observed.

$\Delta\tau \lesssim 0.01 - 0.1$, from TT is at best marginally constraining.

While the power spectrum of Eq. (9.8) describes a particular patchy pattern on the sky, it does not rely on any specific description of the underlying reionization process. We now take a step further in this direction, and consider what happens if every point in the Universe goes suddenly from neutral to ionized, at slightly different times, so that a "reionization surface", as observed from Earth, is "crinkled" on a comoving scale of

$$R_C \approx 200\,\mathrm{Mpc}\,(L_C/150)^{-1}. \tag{9.11}$$

We refer to this simple analytic reionization model as the *crinkly-surface model* (see Figure 9.4 for illustration). During matter domination, this smoothing scale, or bubble size, corresponds at a reionization redshift $z_r \sim 10$ to a redshift interval

$$\Delta z \approx R_C z_r^{1/2} \Omega_m^{1/2} H_0/c. \tag{9.12}$$

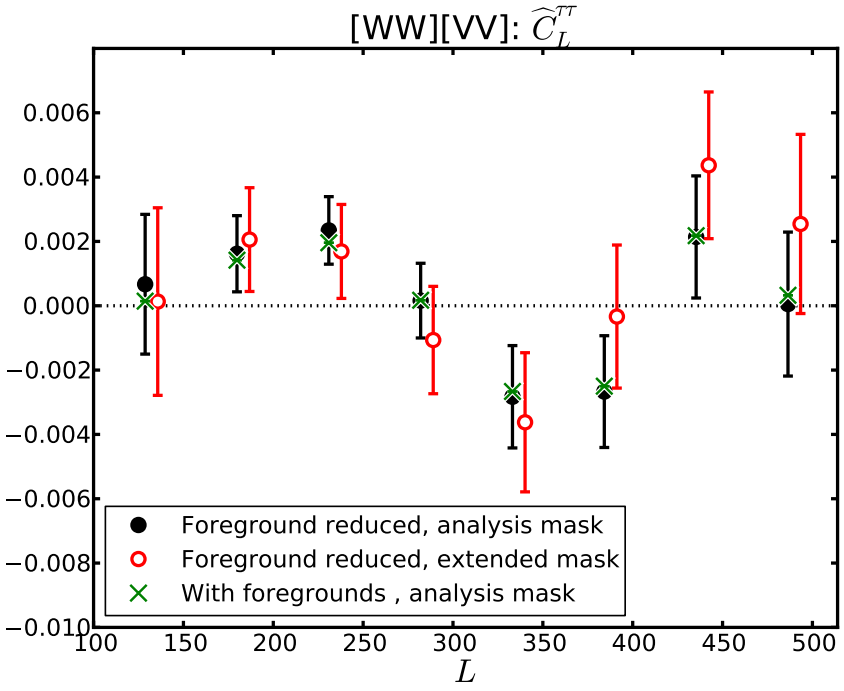

Figure 9.3: Measurement of $\widehat{C}_L^{\tau\tau}$ from off-diagonal TB correlations in WMAP-7 data. Black filled circles represent the measurements obtained from the foreground-reduced maps after applying the fiducial analysis mask (the fiducial result of Figure 9.1). The rest of the data points correspond to the two test cases: the green x's are obtained from the maps prior to foreground subtraction, but using the fiducial mask, while the red empty circles are measurements obtained from foreground-reduced maps after applying an extended mask, shown in Figure 6.1. No overall bias is observed in the two cases, and all three results are consistent, within the estimated statistical uncertainty.

Since the optical depth scales with the reionization redshift as

$$\tau \propto z^{3/2}, \tag{9.13}$$

we find that a bubble size R_C induces an optical-depth fluctuation

$$\Delta\tau \approx 0.01(R_C/200\,\mathrm{Mpc}). \tag{9.14}$$

There is thus a rough scaling,

$$(\Delta\tau) \approx 0.01\,(L_C/150)^{-1}, \tag{9.15}$$

between the optical-depth-fluctuation amplitude and the correlation multipole L_C for the crinkly-surface model, represented by a thick band (to indicate roughly the theory uncertainty) in Figure 9.6. Figure 9.6 also shows the expectations we obtained for the (model-independent) sensitivities of *Planck* and CMBPol-EPIC in this parameter space [120], and the constraint on the crinkly-surface

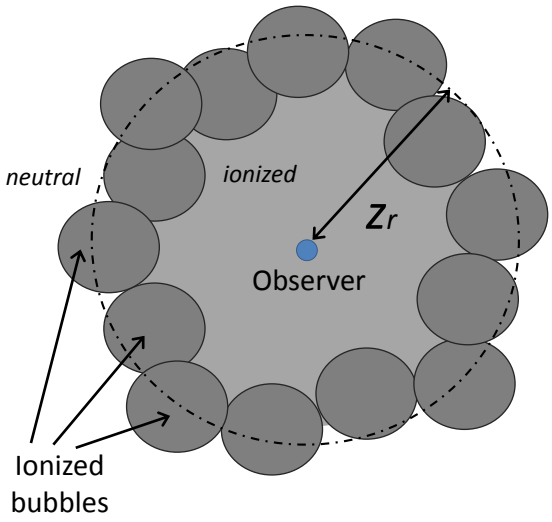

Figure 9.4: Depiction of the crinkly-surface model for reionization: as ionized bubbles of the same radius R_C nucleate at different places at slightly different times, completing the reionization process when they 3D-tile the entire volume of IGM. The surface of reionization then appears crinkled, with characteristic scale corresponding to R_C, as seen from a distance of $z \sim z_r$.

model implied by the EDGES results ($\Delta z \gtrsim 0.06$, at 95% confidence).

Notice at the end that the upper-limit lines in Figure 9.6 are not tied to the crinkly-surface interpretation; they simply constrain the patchy pattern in the sky, produced by an arbitrary reionization model, and described by Eq. (9.8). The gray band, however, is model-dependent and represents the preferred region of this parameter space, under the assumption of crinkly-surface reionization described above. Latter is also true for the EDGES exclusion region. (Both the gray region and the EDGES-excluded region are calculated using the scaling relations valid for the crinkly-surface model.)

A wider range of reionization scenarios can be described by a "Swiss cheese" model in which bubbles of size R_C are spread over a larger redshift range [107], so that each line of sight crosses, on average, N bubbles. The RMS optical-depth fluctuation in Eq. (9.8) would, for fixed R_C, then be reduced by a factor $N^{1/2}$, relative to the crinkly-surface model. Thus, both the gray-shaded area and the EDGES excluded region in Figure 9.6 would be reduced by $N^{1/2}$. Note that kinetic-Sunyaev-Zel'dovich fluctuations should increase in sensitivity as N increases [106, 107] to complement the reduced sensitivity of patchy screening in this limit.

9.4 Summary and Conclusions

The directional dependence of the optical depth $\tau(\hat{\mathbf{n}})$ to Thomson scattering of CMB photons encodes information about the morphology of the ionized regions during the EoR. In this chapter, we used

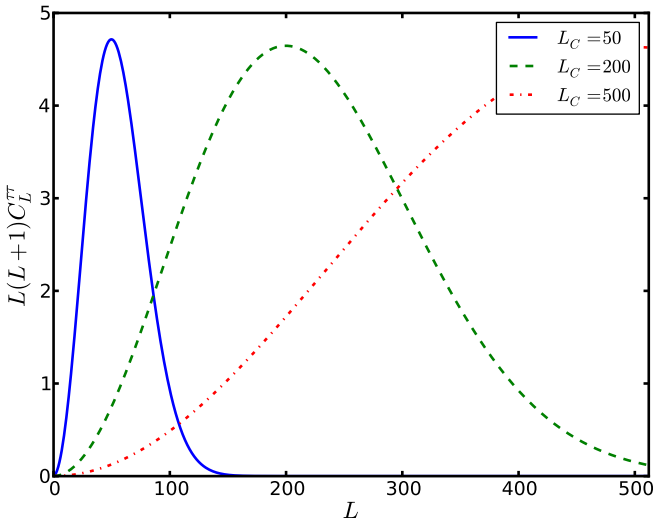

Figure 9.5: Family of simple patchy-reionization models, given by Eq. (9.8), for $\Delta\tau = 1$, and different values of L_C.

WMAP-7 temperature and polarization data to derive a bound on the individual multipoles of the optical-depth power spectrum up to $L = 512$, or bubble sizes larger than ~ 60 Mpc comoving. We then interpreted these null results in terms of a bound on an RMS optical-depth fluctuation $\Delta\tau$ in a model of white-noise fluctuations with coherence angle θ_C. While the bound derived proves to be too weak to constrain realistic models, and probes bubble sizes larger than those ($R_C \lesssim 10$ Mpc) favored in current reionization models, our result provides a proof of principle that such analyses can be carried out with future data. We then note that data from the forthcoming *Planck* satellite and from a subsequent post-*Planck* project should approach the realistic parameter space. Before such optical-depth-fluctuation searches are carried out in the future, though, several issues will need to be understood. For example, the estimator in Eq. (9.3) has the same parity as that for the lensing potential (see Section 5.3 and Ref. [71]), and further modeling of the $\Delta\tau$ and lensing signals, and/or de-lensing of the CMB, will be necessary for a CMB detection in the optical-depth fluctuation with *Planck* or future-generation experiments.[4]

[4]This is the opposite from what we concluded for the estimator for direction-dependent rotation; the difference comes from the fact that, in the case of rotation vs. weak lensing, different temperature and polarization multipoles were contributing to constraints of the two effects, due to the parity requirements. This is no longer the case for patchy reionization, where the lensing signal must be removed prior to the analysis.

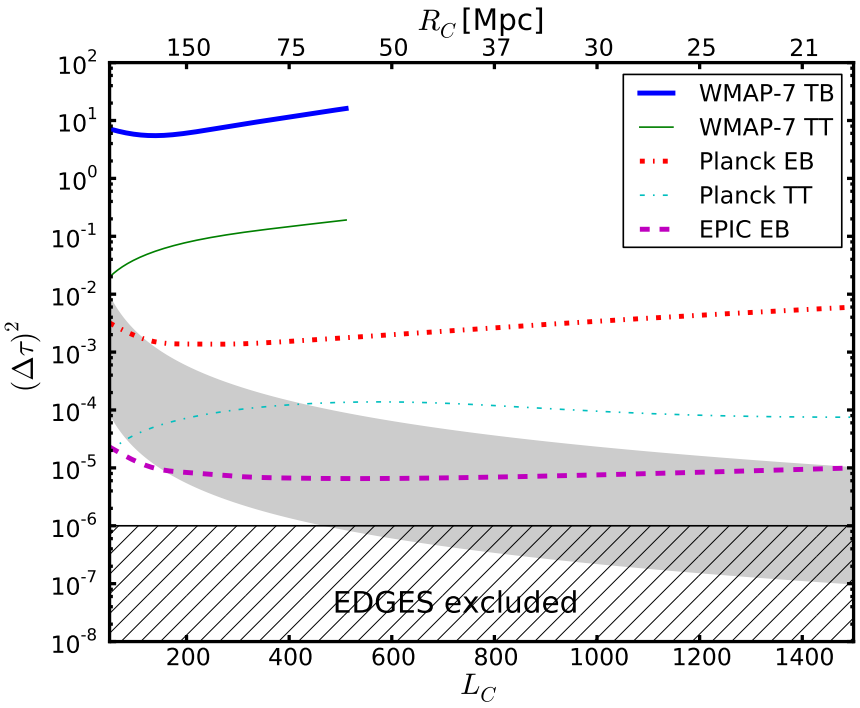

Figure 9.6: Shown are the 1σ confidence-level upper limits from WMAP-7 TT and TB off-diagonal correlations, on the amplitude $(\Delta\tau)^2$ of the patchy-screening model given in Eq. (9.8), as a function of the coherence-scale parameter L_C. Also shown are sensitivity forecasts for experiments with map noise of 27μKarcmin and 1μKarcmin, and beam width of $7'$ and $5'$, corresponding to *Planck* and CMBPol-EPIC–like mission, respectively. The values expected for a reionization surface that is crinkled on scales R_C are indicated by the gray band. Also shown is the portion of this parameter space (under the assumption of the crinkly-surface scenario) excluded by EDGES.

Chapter 10

Statistics of the 21-cm Signal

Among the most promising observational probes of the EoR is the 21-cm spectral line, from hyperfine splitting in the ground state of hydrogen, with an energy of 5.9×10^{-6}eV that corresponds to the rest-frame frequency of 1420 MHz. The redshifted 21-cm emission from neutral regions of the IGM during reionization is estimated to be a 1% correction (in terms of emission or absorption, depending on the redshift) to the energy density of the CMB. It is expected to display angular structure and frequency structure, due to the inhomogeneities in the gas density, ionized fraction x_i, and spin temperature [121] of the emitting gas.

Statistical detection of the large-scale brightness fluctuations in redshifted 21-cm emission is within the scope of a number of experiments that are presently being built, such as the Murchison Widefield Array (MWA) and the Low Frequency Array (LOFAR) (for reviews see, e.g., [122, 123]). In this context, it is important to develop appropriate statistical tools to be employed in analyzing the incoming data. Such development is facilitated by the fact that the N-body and radiative-transfer simulations of reionization have begun to reach the large scales of order 100 comoving Mpc [103, 124, 125] needed to capture the evolution of the IGM during the EoR. These simulated data cubes can be used to test various statistical tools proposed for extracting information about the properties of the IGM during reionization.

So far, studies of the statistics of the 21-cm fluctuations have mainly focused on the power spectrum of the brightness temperature T_b [126–128]. While this statistic is fully representative at the onset of the EoR, where the Gaussian primordial density fluctuations drive the 21-cm fluctuations, it ceases to be so at later times. Namely, as the reionization process advances, the mapping between the hydrogen density and T_b becomes highly non-linear (as evidenced, for instance, by the bounded domain, $x_i \in [0, 1]$), which results in non-Gaussianity of the *probability distribution function* (PDF) of T_b. For this reason, various authors have started exploring alternative and complementary statistics (see, e.g., [129–131]), in particular the PDFs and difference PDFs of the 21-cm brightness

Material in this chapter was largely adapted from "Statistics of 21-cm fluctuations in cosmic reionization simulations: PDFs and difference PDFs," Vera Gluscevic and Rennan Barkana, *MNRAS* **408**, pp. 2373-2380 (2010) [12].

temperature [123, 132]. In this chapter, we test these two statistics on six different simulated data cubes of Ref. [103]. These data cubes are results of different astrophysical inputs that produce various reionization histories, all of which are allowed by the current observational constraints. We measure the one-point PDFs and difference PDFs and analyze their properties.

The plan of the Chapter is as follows: in Section 10.1 we briefly describe the simulation runs used in this work. In Section 10.2 we then present the measured one-point PDFs along with the best fits of the model proposed by Ref. [132], and discuss the main parameters driving the PDF shape. We next present in Section 10.3 the first measurements of difference PDFs for the same set of simulations and analyze their properties. We conclude and summarize in Section 10.4.

10.1 21-cm Simulations

In order to interpret future observations of the high-redshift Universe, we need to understand the morphology of HII regions[1] during reionization, in particular their size distribution and how it is affected by the properties of the ionizing sources, gas clumping and source suppression from photoheating feedback. For this purpose, Ref. [103] ran a 1024^3 N-body simulation in a box of size $65.6h^{-1} \approx 94$ Mpc to model the density field, post-processing it using a suite of radiative-transfer simulations. The authors assumed a standard ΛCDM cosmology, with $n_s = 1$, $\sigma_8 = 0.9$, $\Omega_m = 0.3$, $\Omega_\Lambda = 0.7$, $\Omega_b = 0.04$ and $h = 0.7$. The outputs are stored at 50 million year intervals, roughly between redshifts 6 and 16.

The radiative-transfer code assumes sharp HII fronts, which are traced at sub-grid scales. The properties of the sources are chosen in most cases so that reionization ends near $z \sim 7$. A soft ultraviolet spectrum that scales as ν^4 is assumed for each source. The typical luminosity of a halo of mass m is taken to be[2]

$$\dot{N}(m) = 3 \times 10^{49} m/(10^8 M_\odot), \tag{10.1}$$

in ionizing photons per second. This corresponds to a halo star formation rate of

$$\dot{S}(m) = f_{\rm esc}^{-1}\, m/(10^{10} M_\odot), \tag{10.2}$$

in units of $M_\odot\,{\rm yr}^{-1}$, for an escape fraction of $f_{\rm esc}$ and a Salpeter initial mass function. The N-body simulation resolves haloes down to $10^9 M_\odot$, but since the effect of smaller mass haloes cannot be neglected, the effect of haloes down to $10^8 M_\odot$ is included in some of the runs with a merger tree (see Table 10.1).

For the purpose of measuring PDFs and difference PDFs, we choose six runs, labeled as in

[1] HII stands for ionized hydrogen.
[2] $M_\odot$ is one solar mass.

Simulation	Merger tree haloes	$\dot{N}$ [photons sec^{-1}]	Comments
$S1$	Yes	$2 \times 10^{49} M_8$	-
$S4$	No	$C_{S4} M_8$	Includes only haloes with $m > 4 \times 10^{10} M_\odot$.
$C5$	No	$6 \times 10^{49} M_8$	Structure on small scales; $C_{\rm cell} = 4 + 3\delta_{\rm C}$.
$F2$	Yes	$2 \times 10^{49} M_8$	Includes feedback on $m < M_J/2$; $\tau_{SF} = 20\,$Myr.
$M2$	No	$9 \times 10^{49} M_8$	Includes minihaloes with $m_{\rm mini} > 10^5 M_\odot$.
$Z1$	Yes	$1 \times 10^{50} M_8$	Higher source efficiency (early reionization).

Table 10.1: Details of the radiative-transfer simulations from Ref. [103]. Merger tree haloes: 'Yes' means that the halo resolution is supplemented with a merger tree down to $10^8 M_\odot$; C_{S4} is calibrated such that there is the same output of ionizing photons in each time step as in S1; M_8 denotes the halo mass in units of $10^8 M_\odot$; $C_{\rm cell}$ is the sub-grid clumping factor; $\delta_{\rm C}$ is the baryonic overdensity smoothed on the cell scale; τ_{SF} is the time-scale over which the cool gas in the source is converted into stars; and M_J is the linear-theory Jeans mass.

Ref. [103]: S1, S4, C5, F2, M2 and Z1. These runs differ by the efficiency of the sources and by the halo-mass resolution. Some runs include feedback from photoheating, which suppresses source formation within ionized regions. Others investigate the impact of clumping, i.e., IGM density inhomogeneities, and include a sub-grid clumping factor $C_{\rm cell}$ different from unity. Finally, some runs account for the presence of minihaloes, which are dense absorbers for ionizing photons and thus tend to extend the process of reionization. A summary of the parameters of each of the six runs is presented in Table 10.1. The list of the redshift slices for each data cube is shown in Table 10.2. For more details about the simulations, see Ref. [103].

Simulation	Redshift slices
$S1$	$6.9, 7.3, 7.7, 8.2, 8.7, 9.4, 10.1, 11.1, 12.3, 13.9, 16.2$
$S4$	$7.3, 7.7, 8.2, 8.7, 9.4, 10.1, 11.1, 12.3, 13.9, 16.2$
$C5$	$6.6, 6.9, 7.3, 7.7, 8.2, 8.7, 9.4, 10.1, 11.1, 12.3, 13.9, 16.2$
$F2$	$6.3, 6.6, 6.9, 7.3, 7.7, 8.2, 8.7, 9.4, 10.1, 11.1, 12.3, 13.9, 16.2$
$M2$	$6.9, 7.3, 7.7, 8.2, 8.7, 9.4, 10.1, 11.1, 12.3, 13.9, 16.2$
$Z1$	$10.1, 11.1, 12.3, 13.9, 16.2$

Table 10.2: List of the simulation runs and corresponding redshift slices discussed in this work. The redshift outputs for each simulation are spaced in 50 Myr intervals.

10.2 One-point PDFs

We measure the one-point PDFs of the observed brightness temperature T_b of the redshifted 21-cm emission, in the six simulation runs of Ref. [103]. We measure T_b in a 32^3 grid, i.e., T_b is averaged over cells of size of 2.9 comoving Mpc, at each of the redshifts listed in Table 10.2. Note that this scale is much larger than the spatial resolution of the simulations; it is chosen by balancing the requirement to be large enough to fall close to the general range of the upcoming observations (corresponding to a resolution of arcminutes), with the need to be small enough compared to the simulation box to give a reasonable statistical sample. The PDFs are shown in Figure 10.1.

As seen in Figure 10.1, the one-point PDFs are Gaussian-like at the highest redshifts and highly non-Gaussian at lower redshifts. The Gaussian shape of the PDFs at the beginning of reionization, when the Universe is almost completely neutral, is driven by the primordial fluctuations in the density field of the emitting IGM gas. At lower redshifts and near the end of reionization, the completely ionized gas does not emit at 21-cm, while the brightness temperatures of the leftover patches of neutral gas are still governed by the density-field inhomogeneities. At these redshifts, entirely ionized cells contribute to the increasingly dominant delta function at $T_b = 0$ mK, while the emission from the partially neutral cells maintains a Gaussian around a higher T_b. The interplay between these two types of cells sets the shape of the PDFs as the reionization proceeds.

In Figure 10.1, we also plot the best fit of a Gaussian + Exponential + (Dirac) Delta function model (GED model) for the 1-pt PDFs. This is an "empirical" model (i.e., based on simulation data), suggested by Ref. [132]:

$$p(T_b) = \begin{cases} P_D \delta_D(T_b) + a\, \mathrm{e}^{\lambda T_b} \; ; & T_b \leqslant T_L \; , \\ c_G\, \mathrm{e}^{-\frac{(T_b - T_G)^2}{2\sigma_G^2}} \; ; & T_b > T_L \; . \end{cases} \tag{10.3}$$

To get a smooth curve, the values of the two functions and their first derivatives are matched at the brightness temperature $T_b = T_L$, leaving (after normalization) four independent parameters for the GED model: the joining point of the exponential and the Gaussian function T_L, the mean of the Gaussian T_G, its standard deviation σ_G, and its maximum value c_G.

From the best fit of the GED model to the PDF in each redshift slice for each of the simulated data cubes, we obtain the value of the probability fraction contained in the delta function (at T_b's around zero) P_D, in the Gaussian (at high T_b's), P_G, and in the exponential part of the model (which interpolates between the delta function and the Gaussian) P_E. These parameters can be reconstructed from observations and must sum to unity, to ensure a normalized PDF. The variation of P_D, P_E, P_G, T_G, T_L, and σ_G with the global ionized fraction $\bar{x}_i$ is shown in Figure 10.2. The evolution of $\bar{x}_i$ with redshift for each of the simulation runs is also shown.

When we fit the GED model, while its δ_D function portion is meant to capture the PDF spike

near $T_b = 0$ mK (at low redshifts), we do not attempt to model (or resolve in the data) the shape of this spike. Thus, we exclude the lowest-temperature bin before fitting the GED model, and derive P_D in three different ways: from the required overall normalization of the PDF to unity; then also directly, i.e., without the model fitting, from the total number count in the first bin of the T_b PDF; finally, we measure the one-point PDFs of x_i, and estimate P_D from the number count in the highest bin of this PDF (the cells in this bin have $x_i \geq 0.95$). These three different estimates of P_D are compared for all six simulation runs in Figure 10.3. In this figure, we show that the difference in P_D calculated from the cell counts and from the GED model is negligible, which indicates that this model represents the data faithfully. The values of P_D as measured indirectly (from fitting the GED model) yield an accurate estimate of the fraction of fully ionized cells. In the limit of infinite resolution, P_D would equal $\bar{x}_i$ and so directly measure the reionization history, while in reality P_D measures a low-resolution, smoothed-out version of the reionization history.

Comparing the various simulation runs, we find that small-scale structure has a relatively minor effect on the 21-cm PDF during reionization, at least for the present implementation of sub-grid astrophysics, and when the final reionization redshift is held (relatively) fixed. Compared to our fiducial case (S1), we have three simulations where mainly the small-scale structure has been adjusted: a scenario with photoheating feedback (F2), one with evaporating minihaloes (M2), and one with increased sub-grid clumping (C5). The latter two also do not have merger-tree source haloes. Figures 10.1 and 10.2 show that these scenarios have the effect of stretching out cosmic reionization, especially by delaying its progress early on, when the rarity of high-mass haloes makes feedback effective (F2), or the still-high density makes recombinations important (C5), or the minihaloes have not yet photo-evaporated (M2). However, in all these scenarios, the 21-cm PDF at a given stage (as measured by $\bar{x}_i$) is fairly unchanged. In particular, the evolution of the probabilities P_D, P_E, P_G, and the parameters T_G and T_L is rather similar for these three scenarios and S1.

Strong changes in the properties of the ionizing sources do have more of an effect on the evolution of the PDF. For example, a higher source luminosity (Z1) leads to earlier reionization by somewhat more massive haloes. Even early in reionization, the ionized bubbles are already rather large (compared to the fixed pixel scale at which the PDF is measured), which changes the PDF shape and the reconstructed GED-model parameters. Also, since reionization in this case occurs at higher redshifts, when the Universe is denser, the mean 21-cm brightness is higher, leading to higher values of T_G and T_L compared to the lower-redshift cases. Furthermore, even without changing the redshift range, if the ionized sources lie in much more massive haloes (S4) than in the S1 case, the impact on the PDFs is noticeable. In this case, the ionized bubbles (produced by larger and more strongly clustered sources) grow larger than the effective PDF resolution quite early in reionization, so that P_D is larger than in the other cases (mostly at the expense of P_E), and is generally closer to the value of $\bar{x}_i$.

In summary, we find that $\bar{x}_i$ is the main parameter determining the one-point 21-cm PDFs. In particular, various modifications in the small-scale structure have only a minor effect on the PDF evolution versus $\bar{x}_i$ (as quantified by the parameters of the GED-model fits). This suggests that analysis of features of the observed one-point PDFs can be used to reconstruct the global reionization history relatively independently of any assumptions about the astrophysics on unresolved sub-grid scales. On the other hand, the typical mass of source haloes, and the typical reionization redshift, have more of an effect. It is important to note, though, that observations will provide independent constraints on these major parameters. The redshift will obviously be measured, and, for example, the span of the reionization epoch will constrain the typical halo mass driving this process. Note also from Figure 10.2 that in all the simulation runs, the Gaussian probability P_G can be taken as a rough estimate of the cosmic neutral fraction $(1 - \bar{x}_i)$.

While the one-point PDF is interesting, it will be rather difficult to measure with the upcoming generation of instruments, mainly due to comparatively bright foregrounds and the associated thermal noise. In particular, Ref. [132] found that the one-point PDF can only be reconstructed from upcoming observations if the analysis is made on the basis of quite strict (and not easily tested) assumptions that the real PDF is very similar in shape to that measured in numerical simulations. This difficulty motivates the use of an alternative statistical tool that should have a much higher signal-to-noise ratio for a given observation, namely the *difference PDF* proposed by Ref. [123]. In Section 10.3 we present the first numerical measurements of difference PDFs, specifically using the same six simulated data cubes, and we discuss their properties.

10.3 Difference PDFs

The PDF of the difference in the 21-cm brightness temperatures,

$$\Delta T_b \equiv |T_{b1} - T_{b2}|, \tag{10.4}$$

at two separate points in the sky (or, analogously, at two cells in the simulated data cube) was previously proposed [123] as a useful statistic for describing the tomography of the IGM during the EoR. More precisely, if we consider two points separated by a distance r, then the distribution of ΔT_b is given by the difference PDF $p_\Delta(\Delta T_b)$, normalized as

$$\int p_\Delta \Delta T_b = 1. \tag{10.5}$$

The motivation for introducing this statistic is at least threefold. Firstly, the effective number of data points available for reconstructing the difference PDF is much larger than for the one-point PDF (by roughly a factor of the number of pixels divided by two, though the pixel pairs must be

divided up into bins of distance r). Secondly, the difference PDF (which is a major piece of the two-point PDF) is a generalization which not only includes the information in the commonly considered power spectrum or two-point correlation function (which can be derived from the variance of the difference PDF), but also yields additional information. And thirdly, being a PDF of a difference in T_b, it avoids the mean sky background and fits naturally with the temperature differences measured via interferometry.

We present the first measurements of difference PDFs, for the same set of simulation runs of Ref. [103] that we used to discuss the properties of the one-point PDF in Section 10.2. The difference PDFs for all the redshifts of $S1$ are shown in Figure 10.4. For each of the other five simulation runs, we show difference PDFs at three representative redshifts in Figure 10.5. In Figures 10.4 and 10.5, every redshift has 6 distance bins, logarithmically spaced, and each distance bin has 20 temperature bins, linearly spaced. The range in distance is chosen so that it covers basically the full range from the resolution (pixel) scale to the largest separations found within the 94 comoving Mpc data cube.

Even for the one-point PDF, there is no good analytical model that matches simulations, possibly because the PDF is sensitive to the reionization topology, and specifically to the way in which the complex-shaped ionized bubbles partially overlap the box-shaped pixels. This led Ref. [132] to base their analysis on the PDF as measured in a simulation, and to consider an empirical model for fitting the PDF shape. Similarly, in the case of the difference PDF, the analytical model of Ref. [123] does not quantitatively match the result that we find in the simulations, but we can nonetheless use the model and the discussion in Ref. [123] to develop a qualitative understanding of the difference PDF and how best to analyze it.

At high redshifts, when the PDF is nearly Gaussian, the difference PDF (which is defined using the absolute value of ΔT_b) should approximately be a half-Gaussian. Non-linear density fluctuations, though, give a slower decaying tail at high ΔT_b than would be expected for a pure Gaussian. As reionization develops with time, the difference PDF becomes a superposition of three contributing terms: The pixel pairs in which both pixels are fully ionized, those in which one pixel is (partly) neutral and the other ionized, and those where both are neutral. We explicitly show these three contributions in Figure 10.6 for one redshift near the midpoint of reionization in the $S1$ simulation. The both-ionized pixel pairs basically give the δ_D function at zero ΔT_b; the amount of probability in this δ_D function is physically meaningful, as discussed below. The pairs in which one pixel is neutral and the other ionized tend to be well separated in T_b, and so this contribution is responsible for the high ΔT_b peak, at $\Delta T_b \sim 13$ mK in the case plotted there. As we consider smaller r, the T_b values of the two points that are separated by r become more strongly correlated, making it difficult for one to be ionized and the other neutral, and so this contribution declines at smaller r. At the same time, as we reduce r, this contribution becomes more highly concentrated at small values of ΔT_b, since at small separations, if one pixel is fully ionized, then the second one tends to be at least highly ionized,

making their T_b difference small. Note also that the ionized+neutral contribution drops suddenly at $\Delta T_b \sim 1.5$ mK, but this is due to the fact that some of the probability in this region that should be included under ionized+neutral is incorrectly swept up under the both-ionized δ_D function, which is dominant at ΔT_b near zero. This is an unavoidable effect of the finite (2.9 Mpc) resolution of our gridded field. Since in practice we define a "fully ionized" pixel as having an ionization fraction of 95% or higher, some highly ionized pixels are classified as fully ionized. A higher resolution map, with a definition closer to 100% ionization, would move this artificial drop-off closer to $\Delta T_b = 0$. Those pairs in which both pixels are neutral peak at $\Delta T_b = 0$, and give a contribution with a roughly half-Gaussian shape, at all separations r.

The difference PDF as a function of separation transitions between two limits. The $r \to \infty$ limit corresponds to two uncorrelated points, for which p_Δ is essentially a convolution of the one-point PDF p with itself. As long as r is large enough to maintain a weak correlation, p_Δ keeps its large-r limit and only varies slowly as r is decreased. Once r becomes small enough for a significant correlation (which is positive in the physical regimes considered here), it becomes harder to produce a large difference ΔT_b between the two correlated points (as noted above, even when one is fully ionized and the other is not); p_Δ thus becomes more strongly concentrated near $\Delta T_b = 0$, approaching a δ_D function at $\Delta T_b = 0$ as $r \to 0$.

The correlation between cells, referred to above, probes different physical effects at different redshifts. Before reionization, this is the density correlation, which arises from large-scale modes in the initial fluctuations. During reionization, the correlation of T_b is dominated by ionization, so that points close enough together to be in the same ionized bubble (or in strongly correlated nearby bubbles) will have strongly correlated 21-cm brightness temperatures. Thus, by inspecting the plots, one can make a rough estimate of the average size of an ionized bubble at low redshifts, or the typical density-fluctuation correlation length at high redshifts. This effective correlation length is the first separation bin at which the difference PDF at high ΔT_b drops significantly below its value at larger separations. For example, in Figure 10.4, the average bubble size can be seen to increase beyond 10 comoving Mpc during the late stages of reionization.

As in the case of the one-point PDF, the difference PDF is relatively insensitive to variations in the small-scale sub-grid physics, as tested by the various simulation runs. Figure 10.7 displays a comparison of the difference PDFs for the six different reionization runs, for various comoving distance bins, at the redshift where $\bar{x}_i$ is closest to the value of 0.4 (i.e., in the midst of the reionization process). We also show the corresponding one-point PDFs, for easy comparison. Similarly to p (as discussed in Section 10.2), the large ionized bubbles and correlation length in the case of reionization by massive, rare sources stretch p_Δ out to higher values of ΔT_b (as seen in the Z1 run and, especially, S4). Our findings are consistent with those of Ref. [103] and with the general theoretical expectation that clustered groups of galaxies determine the spatial distribution of ionized bubbles [133] which is

then driven by large-scale modes and is mainly sensitive to the overall bias of the ionizing sources.

We next proceed to measure the parameter analogous to P_D, but this time for the case of difference PDFs. This parameter, which we denote ΔP_D, represents the (number) fraction of pairs for which $\Delta T_b \approx 0$. In the reality of having limited resolution, it is the fraction of pairs for which ΔT_b falls within the lowest-temperature bin. Ideally, this value would directly measure the fraction of pairs in which both cells are fully ionized, but the finite resolution adds a contribution from pairs that do not satisfy this condition, but nonetheless have matching brightness temperatures to within the bin size.

Just as P_D in the one-point PDF measures a low-resolution version of the reionization history, so can ΔP_D be considered as measuring a low-resolution version of the ionization correlation function [123]. In particular, in the limit of infinitely high resolution, ΔP_D would precisely measure the joint ionization probability of two points as a function of their separation. In this case, we would expect ΔP_D to vary from the corresponding value of P_D, at $r \to 0$, down to P_D^2, at $r \to \infty$ (where each pixel in the pair is independently ionized with probability P_D). While these relations are not exact with finite resolution, they do provide a rough guide for what to expect. We show the value of ΔP_D in Figure 10.8, for the redshifts of each simulation at which the δ_D function at $\Delta T_b \approx 0$ is visible. A comparison with the corresponding values of P_D (shown in Figure 10.3) shows that the above theoretical behavior is satisfied only approximately, since the fully ionized pairs make up only a fraction of ΔP_D. Still, Figure 10.8 shows the flat asymptote of ΔP_D at large r, and its rise as r drops below the correlation length (although r does not quite reach small enough values to see the flat $r \to 0$ asymptote).

We have illustrated how the difference PDF encodes information about the EoR, in particular by separating out information on the ionization correlations (unlike the power spectrum analysis, in which the ionization and density correlations are mixed together). We note that a model for the PDF (such as the GED model) is insufficient for constructing an analytical model fit for the difference PDF, since the latter depends on additional information regarding the correlations on various scales. We leave for future work a more quantitative analysis of the features of the difference PDF and their relation to the properties of the ionizing sources and the reionization history.

10.4 Summary and Conclusions

Upcoming low-frequency radio observations will use the MWA, LOFAR, and similar instruments to survey the sky for redshifted 21-cm emission. Analyzing this data will require extraction of a small signal on top of the overwhelming foregrounds, so the detection is expected to be achieved only statistically. It is therefore important to develop appropriate statistical tools that can be used to gain information about the history of reionization from these observations.

In this chapter, we examined PDFs and difference PDFs, using six different simulations from Ref. [103]. We showed that the PDFs are highly non-Gaussian in the midst of the reionization process, and are thus a complementary statistic to the commonly discussed power spectrum. As a way to analyze the PDFs, we examined the evolution of the parameters of the best-fit GED model with the global ionized fraction $\bar{x}_i$. In particular, the δ_D function portion of the probability (P_D) measures a low-resolution, smoothed-out version of the reionization history (i.e., $\bar{x}_i$ as a function of redshift).

We also presented the first numerical measurements of difference PDFs; specifically, we measured difference PDFs for the same set of simulation runs from Ref. [103]. We argued that the larger data set and the nature of this statistic can be significant advantages in the presence of bright foregrounds. The difference PDF can be physically understood as arising from three contributions: pixel pairs in which both, one, or neither of the pixels is ionized. As an illustration of the information that can be deduced from the difference PDFs, we considered the typical correlation length, which corresponds to the average size of an ionized bubble during reionization, or the typical density-fluctuation correlation length, at the onset of the EoR. The difference PDF also has a delta-function portion (ΔP_D), which measures a low-resolution, smoothed-out version of the ionization correlation function at each redshift.

We found that increasing small-scale clumping, and including photoheating feedback or mini-haloes has only a small effect on the one-point and difference PDFs (considered at a given $\bar{x}_i$), at least within the range of assumptions covered by the simulations that we considered. On the other hand, we showed that the PDFs are highly sensitive to the properties of the ionizing sources, so that measuring them can help distinguish between reionization driven by large versus small haloes, and help unveil information about the first sources of light in the Universe. These conclusions parallel those of Ref. [103], highlighting the fundamental fact that the spatial structure of reionization is driven by large-scale modes and depends mainly on the overall bias of the ionizing sources [129,133].

As one of the future steps, it will be interesting to more precisely quantify the properties of difference PDF and establish the relation between their features and the properties of the IGM during the EoR. It would also be interesting to explore the PDFs and difference PDFs in alternative reionization scenarios, such as those dominated by x-ray sources or a decaying dark matter particle. Contrasting different scenarios may lead to a fuller understanding of the information content of the specific PDF shapes that we measured.

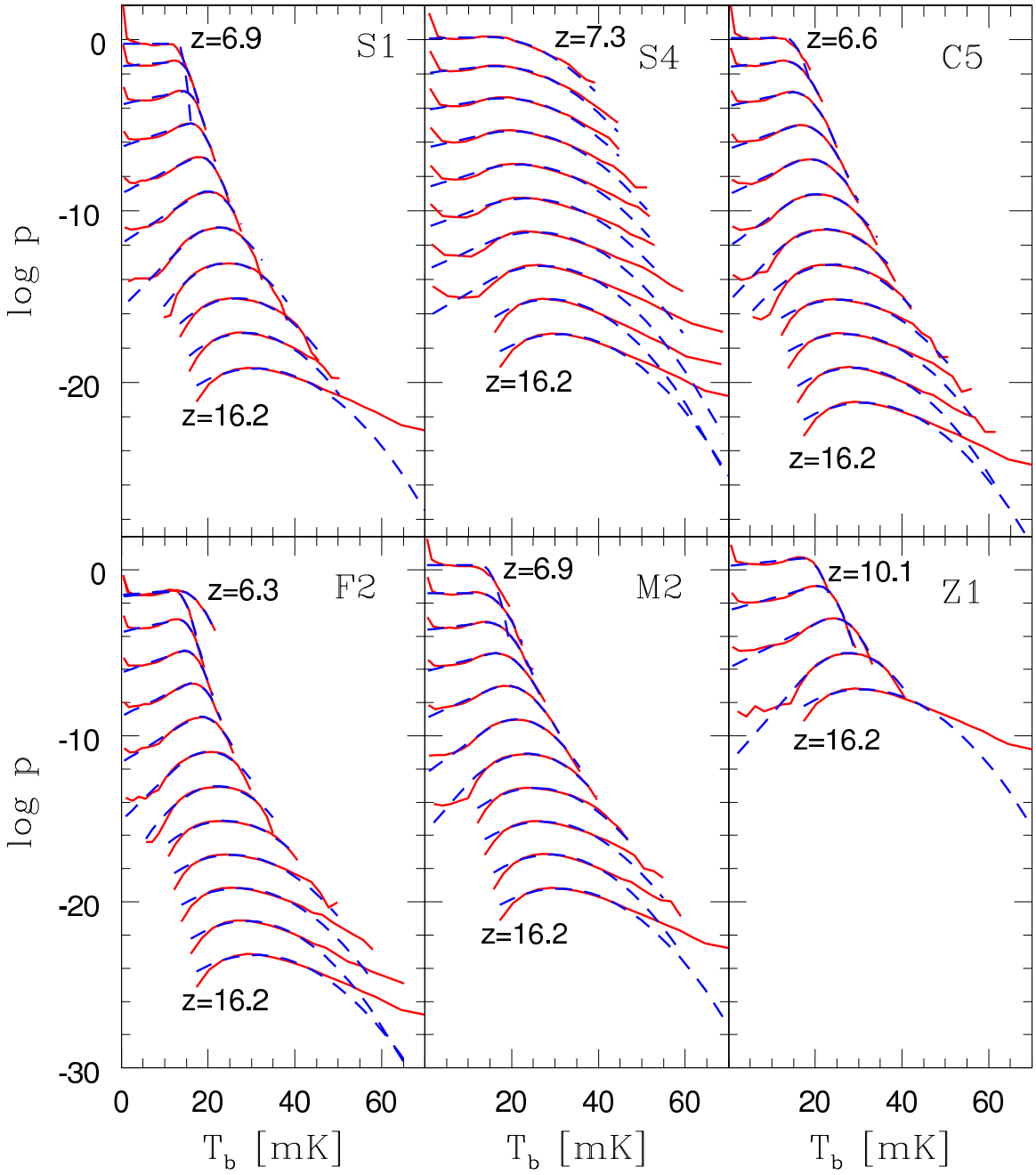

Figure 10.1: One-point PDFs for six different simulation runs, at the redshifts listed in Table 10.2. The y-axis is the logarithm of $p(T_b)$, where p represents the number fraction of points (i.e., pixels, or data-cube cells) at a given T_b, normalized by the temperature-bin size. The units of p are mK^{-1}. There are 20 evenly spaced temperature bins in each curve. The size of a bin at each redshift is set by the temperature range of the cells at that redshift. The top PDF in each plot is at the lowest redshift of the data cube, and the redshift increases downward. The i-th PDF in each plot is shifted down the vertical axis by $2(i-1)$ in logarithmic space, for clarity. We show the measured PDFs (solid red curves) as well as the best fits of the GED model (dashed blue curves).

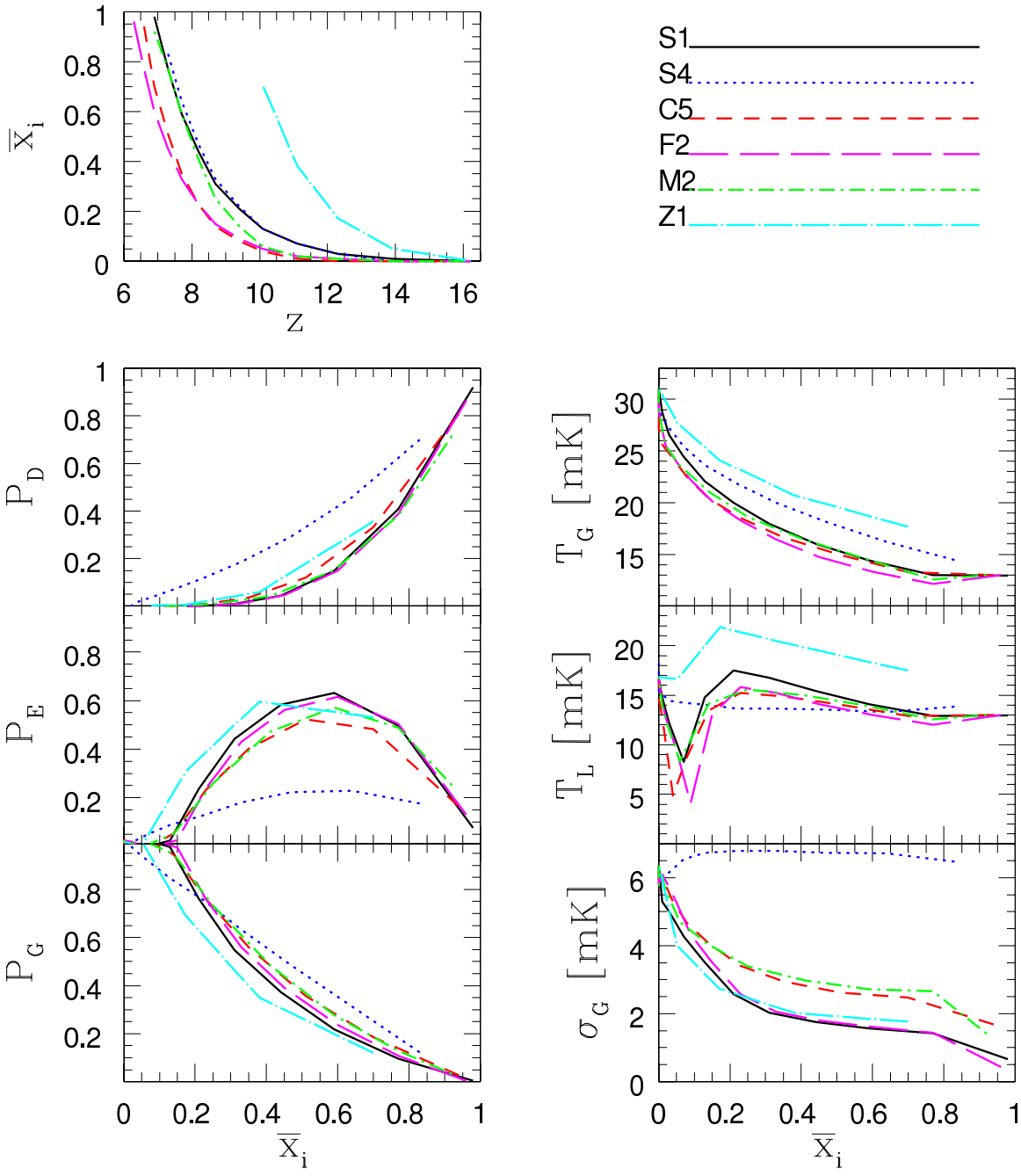

Figure 10.2: Top panel: evolution of the global ionized fraction $\bar{x}_i$ with redshift z, for each of the six simulation runs. Other panels show how various parameters derived from the best-fit GED model to the 21-cm PDF evolve as the reionization proceeds. P_D, P_E, and P_G are, respectively, the fractional probability in the delta function, the exponential, and the Gaussian part of the PDF; T_L is the joining point of the exponential and the Gaussian, T_G is the mean of the Gaussian, and σ_G is its variance. There are four free parameters in the fit to each PDF.

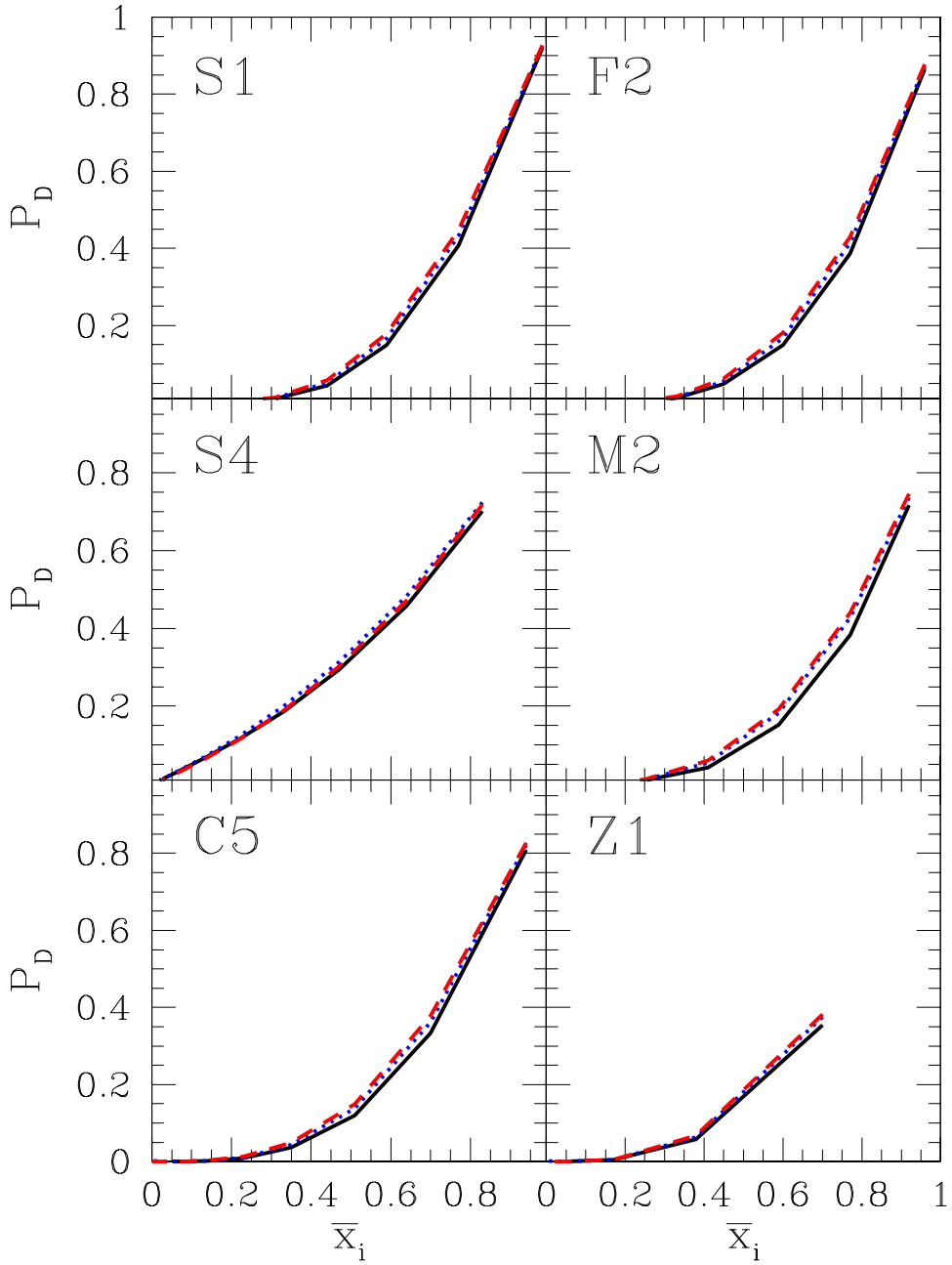

Figure 10.3: Three different measurements of P_D are shown versus $\bar{x}_i$. These include P_D as calculated from the best fit of the GED model (solid black curve), directly from the measured PDF of T_b, i.e., the fraction of pixels that fall within the lowest-temperature bin (dotted blue curve), and directly from the measured PDF of x_i, i.e., the fraction of pixels that fall within the highest-x_i bin (dashed red curve). Results for the six different simulation runs are shown.

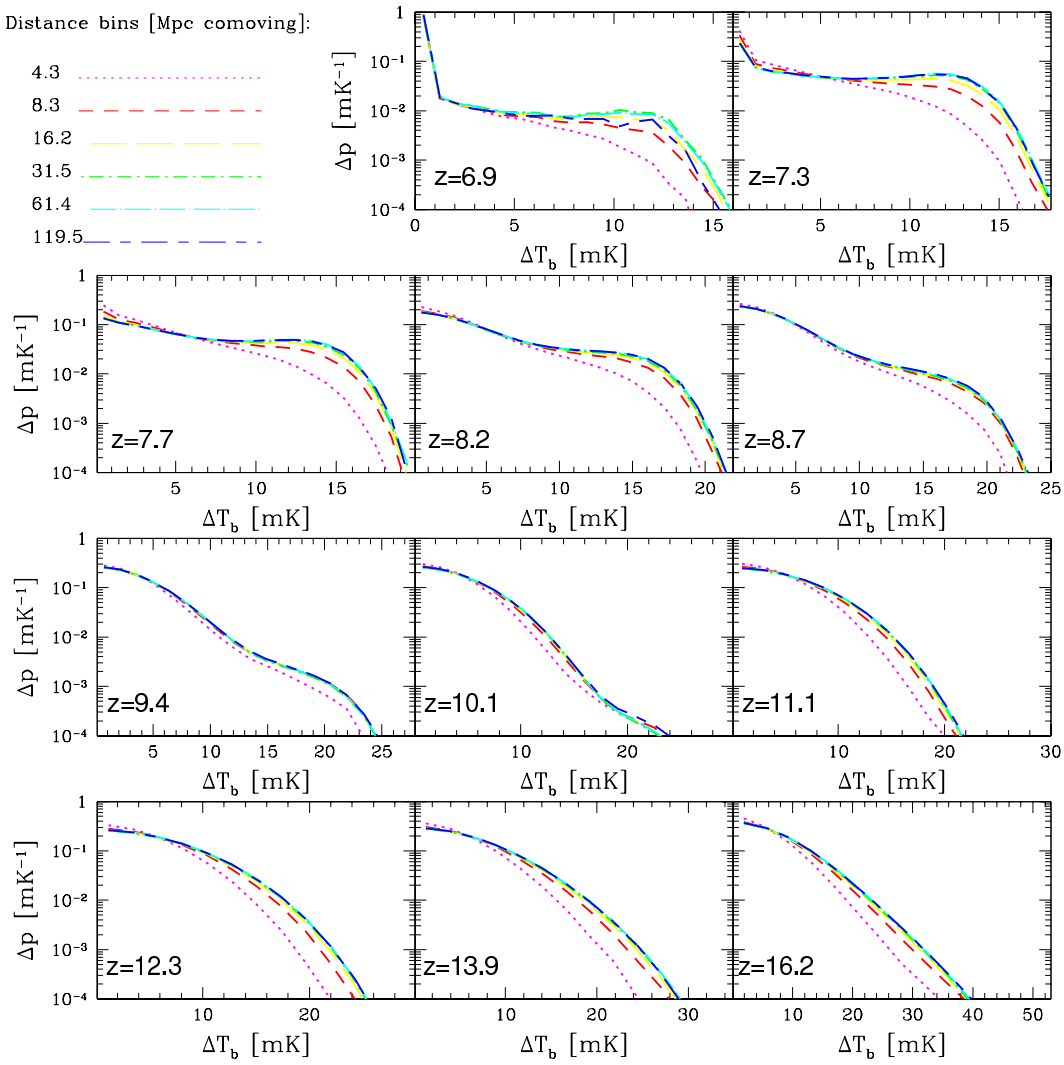

Figure 10.4: Difference PDFs are shown for all the output redshifts of the $S1$ simulation. The x-axis is the brightness temperature difference ΔT_b for pairs of cells, and the y-axis, p_Δ, is the number fraction of pairs of cells at a given separation, r, with a given ΔT_b (normalized by the size of the ΔT_b bin). Different curves indicate different r bins (the legend indicates the central values of the logarithmic bins).

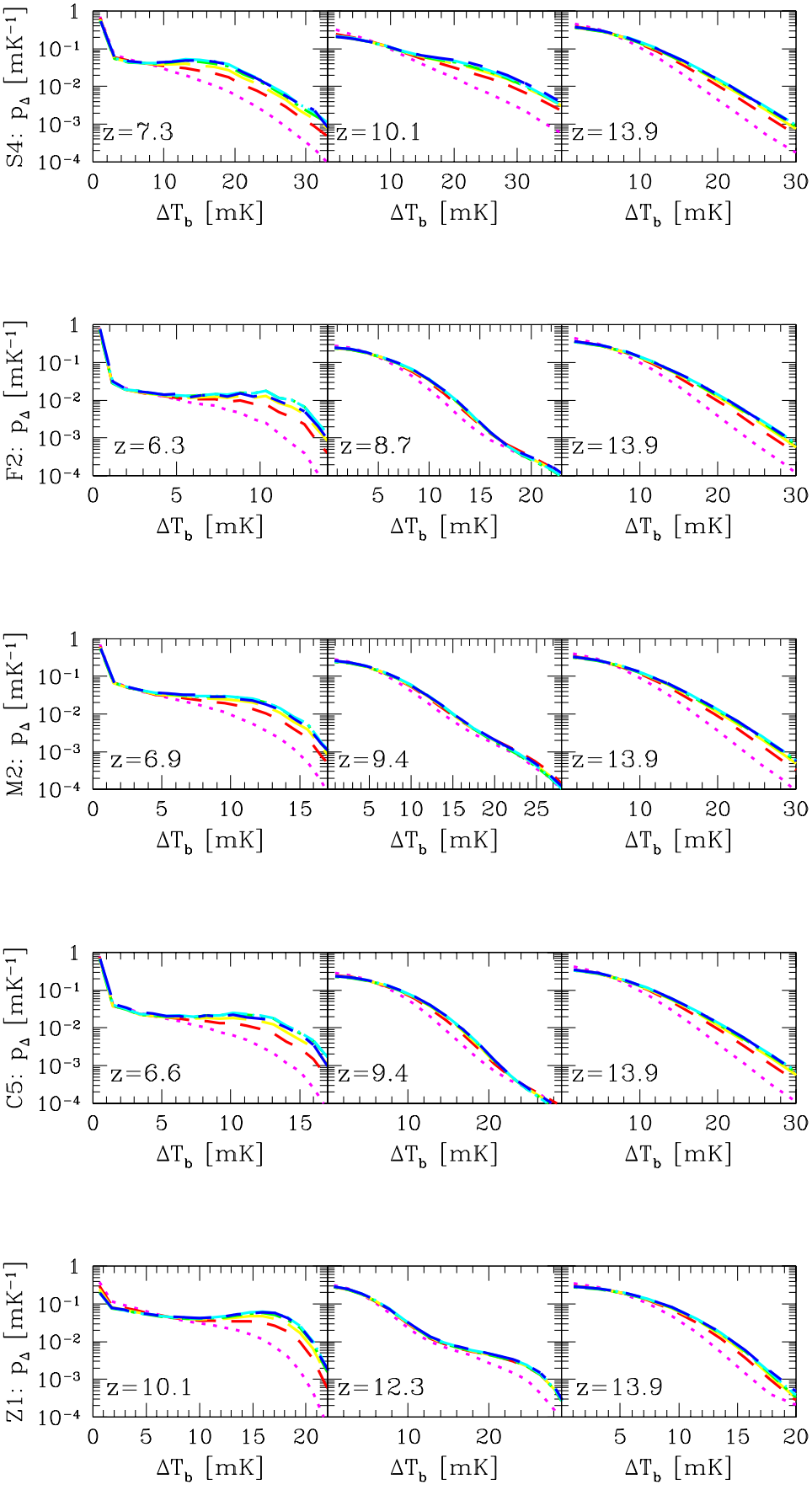

Figure 10.5: This figure is a smaller version of Figure 10.4: difference PDFs for the rest of the simulation runs are shown for three representative redshifts (i.e., early, mid, and late reionization). The legend is the same as in Figure 10.4.

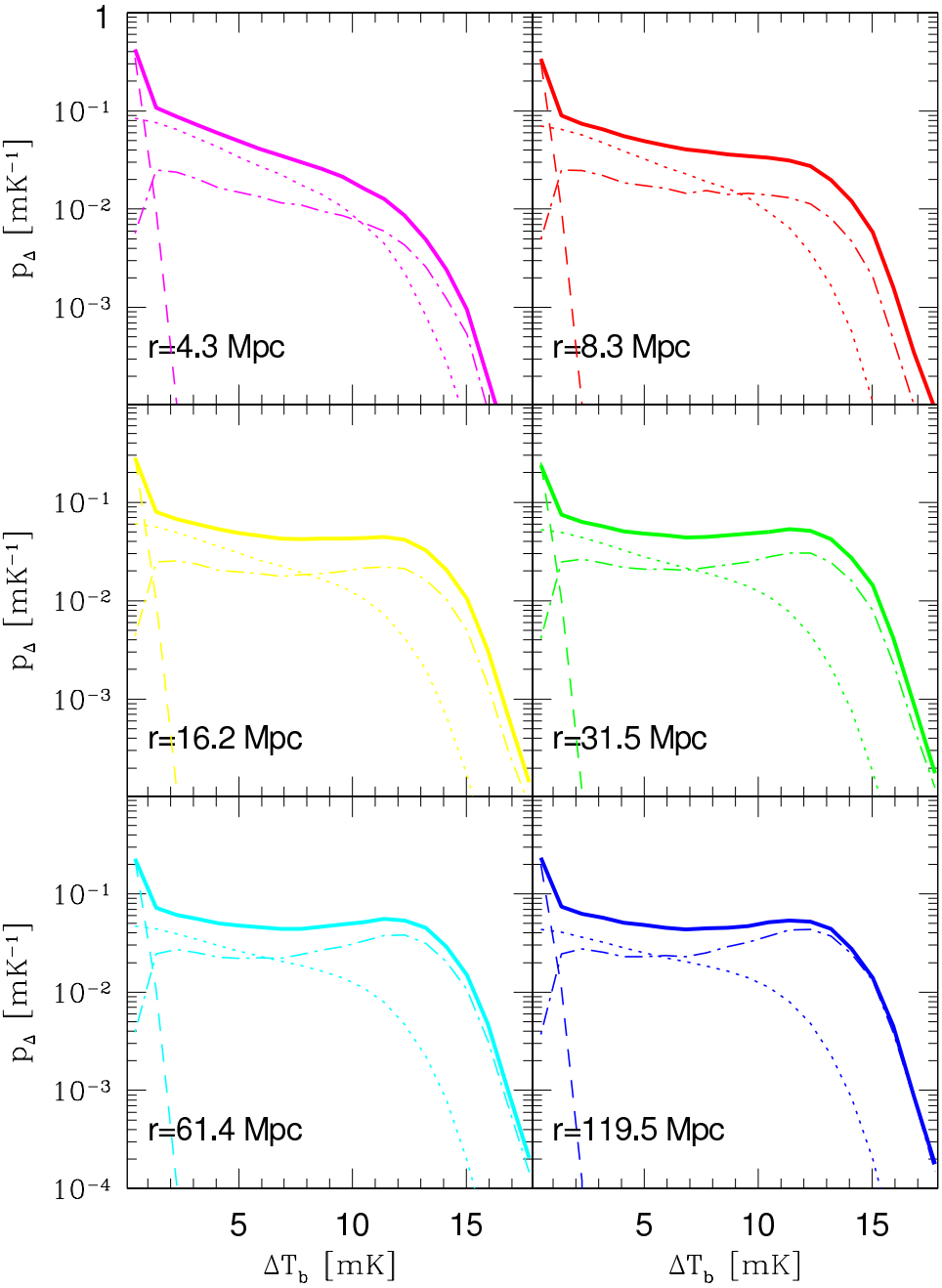

Figure 10.6: Separate contributions to the difference PDF, for the S1 simulation at $z = 7.3$. We show the contribution of pixel pairs in which both cells are fully ionized (dashed curves, capturing the δ_D functions at zero ΔT_b), pairs in which one cell is fully ionized (dot-dashed curves), and pairs in which neither of the cells is fully ionized (dotted curves). The total p_Δ (solid curves) is the sum of these three contributions.

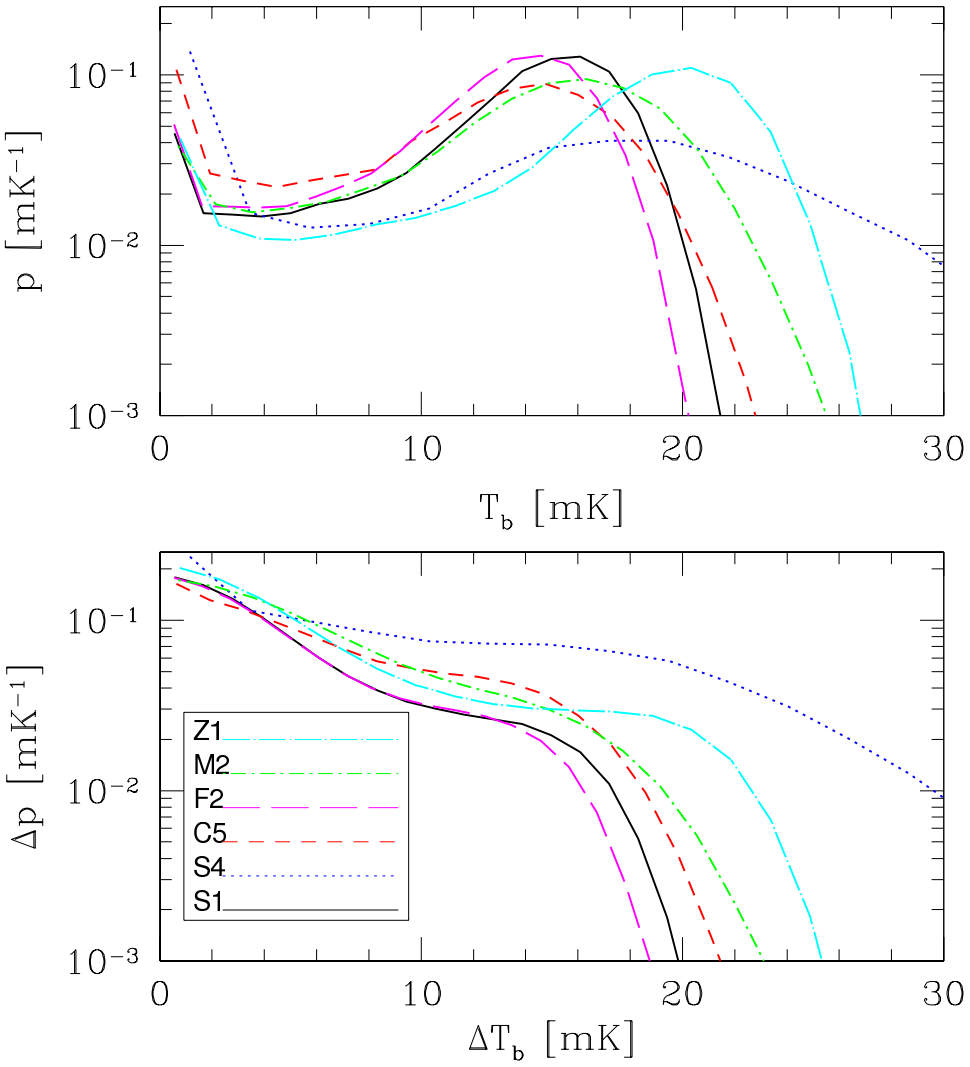

Figure 10.7: Comparison of the one-point PDFs (upper panel) and difference PDFs (lower panel), for all six simulation runs, at $r = 16.2$ comoving Mpc. Each simulation run is shown at the redshift for which the value of the global ionized fraction $\bar{x}_i$ is closest to 0.4, i.e. in the midst of the reionization process.

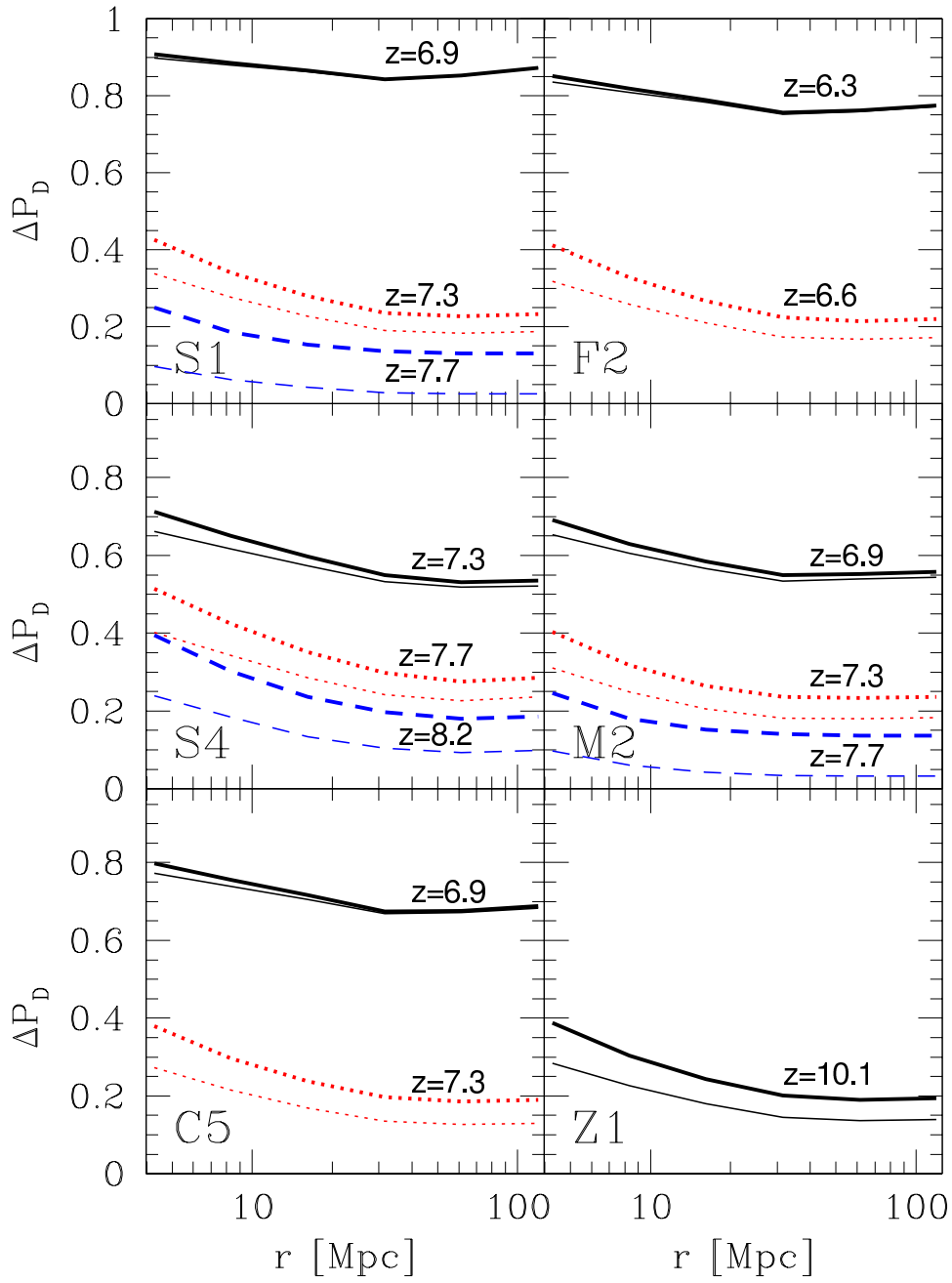

Figure 10.8: ΔP_D parameter (thick lines), measured from difference PDFs as the value of the zero-temperature-difference bin, for all six simulation runs, is shown for the redshifts where it is non-vanishing. It represents the fractional probability in the delta function around $\Delta T_b \approx 0$, i.e., the number fraction of pairs of cells which are either both fully ionized, or both at the same brightness temperature. We see that this value tends to asymptote to the corresponding P_D, at $r \sim 0$, as expected for fully correlated cells. The thin lines of the same type and color represent the part of the corresponding ΔP_D that originates from pairs where both cells are fully ionized.

Part V

General Conclusions

In this thesis, we explored two very different topics: signatures of new (potentially parity-violating) physics, and the epoch of cosmic reionization. We now conclude with a few general remarks regarding future research directions.

First, the formalism and analysis method developed to search for cosmic birefringence and chiral gravity in the CMB are readily applicable to investigating other signatures that will open up a "gold mine" of information for cosmology in the next decade. One example is the weak gravitational lensing of the CMB, and another we already started exploring in this thesis—the signature that reionization inhomogeneities have imprinted on the CMB. Second, all our theoretical considerations were based on analyzing higher-order statistics, which are rapidly becoming important for unearthing tiny deviations from the concordance model of cosmology, and perhaps are the main direction that CMB science is headed in the future. Thirdly, the work of this thesis was only concerned with data from full-sky CMB surveys; however, a particularly interesting avenue has just started opening up with the advent of deep, small-area ground-based surveys, such as SPT and ACT, whose data might become highly relevant for related searches in the future. Also, the CMB measurements of upcoming data sets, from both *Planck* and the ground-based observations, are entering a new regime of signal-dominated polarization measurements—it will be interesting to see how these might challenge or confirm some of the results presented here. Finally, we have briefly focused on tools of 21-cm cosmology, by investigating different statistics for analyzing planned low-frequency radio observations whose aim will be to map the redshifted 21-cm signal from reionization—a direction which by itself represents one of the most active areas of cosmology research. To unify it with the CMB-themed part of this thesis, let us just point out that a cross-correlation between the 21-cm maps and the maps of patchy screening of the CMB could have a potential to unveil tomography of the intergalactic medium, far exceeding either one of the two approached alone—a prospect well worth exploring.

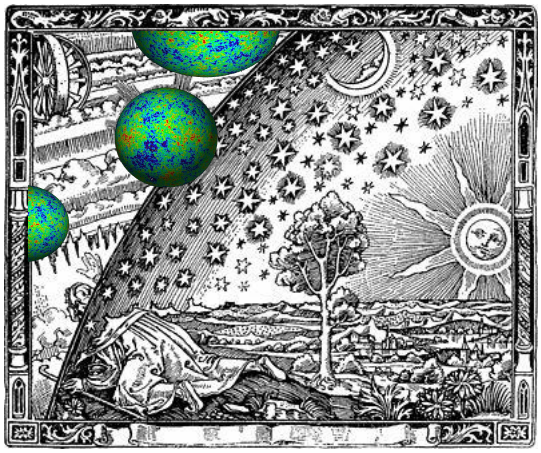

Figure 10.9: Modified *Flammarion* engraving

Appendix A

Wigner-3j Symbols

Here we list some useful relations regarding the Wigner-3j symbols (abundantly used in Chapter 5 of this thesis).

We start by providing a useful way to define spherical harmonics, using Legendre polynomials,

$$Y_{\ell m}(\theta,\varphi)=\sqrt{\frac{(2\ell+1)}{4\pi}\frac{(\ell-m)!}{(\ell+m)!}}P_\ell^m(\cos\theta)e^{im\varphi}. \tag{A.1}$$

The metric tensor and its inverse on a unit 2-sphere (i.e., on the *sky*) is

$$g=\begin{pmatrix}1 & 0\\ 0 & \sin^2\theta\end{pmatrix}, \tag{A.2}$$

$$g^{-1}=\begin{pmatrix}1 & 0\\ 0 & \frac{1}{\sin^2\theta}\end{pmatrix}. \tag{A.3}$$

The Levi-Civita tensor on a unit 2-sphere is

$$\varepsilon=\begin{pmatrix}0 & \sin\theta\\ -\sin\theta & 0\end{pmatrix}. \tag{A.4}$$

An orthonormal basis on a unit 2-sphere is

$$\widehat{e}_\theta\equiv\begin{pmatrix}1\\ 0\end{pmatrix},\qquad \widehat{e}_\varphi\equiv\begin{pmatrix}0\\ \sin\theta\end{pmatrix}. \tag{A.5}$$

Some useful properties of the Wigner 3j symbols and related quantities include

$$\begin{pmatrix}\ell_1 & \ell_2 & \ell_3\\ m_1 & m_2 & m_3\end{pmatrix}=(-1)^{\ell_1+\ell_2+\ell_3}\begin{pmatrix}\ell_1 & \ell_2 & \ell_3\\ -m_1 & -m_2 & -m_3\end{pmatrix}, \tag{A.6}$$

$$\begin{pmatrix} \ell_1 & \ell_2 & \ell_3 \\ m_1 & m_2 & m_3 \end{pmatrix} = \begin{pmatrix} \ell_2 & \ell_3 & \ell_1 \\ m_2 & m_3 & m_1 \end{pmatrix}, \tag{A.7}$$

$$\begin{pmatrix} \ell_1 & \ell_2 & \ell_3 \\ m_1 & m_2 & m_3 \end{pmatrix} = (-1)^{\ell_1+\ell_2+\ell_3} \begin{pmatrix} \ell_2 & \ell_1 & \ell_3 \\ m_2 & m_1 & m_3 \end{pmatrix}, \tag{A.8}$$

$$\begin{pmatrix} \ell & \ell & 0 \\ m & -m & 0 \end{pmatrix} = \frac{(-1)^{\ell-m}}{\sqrt{2\ell+1}}, \tag{A.9}$$

$$m_1 + m_2 + m_3 \neq 0 \Rightarrow \begin{pmatrix} \ell_1 & \ell_2 & \ell_3 \\ m_1 & m_2 & m_3 \end{pmatrix} = 0, \tag{A.10}$$

$$\sum_{m_1 m_2} (2\ell_3 + 1) \begin{pmatrix} \ell_1 & \ell_2 & \ell_3 \\ m_1 & m_2 & m_3 \end{pmatrix} \begin{pmatrix} \ell_1 & \ell_2 & \ell_3{}' \\ m_1 & m_2 & m_3{}' \end{pmatrix} = \delta_{\ell_3 \ell_3{}'} \delta_{m_3 m_3{}'}. \tag{A.11}$$

They also satisfy triangle inequalities,

$$\begin{aligned} L &\leq \ell + \ell', \\ L &\geq |\ell - \ell'|, \end{aligned} \tag{A.12}$$

The relation between spin-zero spherical harmonics and Wigner 3j symbols is

$$\int d\hat{n} Y_{\ell_1 m_1}(\widehat{\mathbf{n}}) Y_{\ell_2 m_2}(\widehat{\mathbf{n}}) Y_{\ell_3 m_3}(\widehat{\mathbf{n}}) = \sqrt{\frac{(2\ell_1+1)(2\ell_2+1)(2\ell_3+1)}{4\pi}} \begin{pmatrix} \ell_1 & \ell_2 & \ell_3 \\ m_1 & m_2 & m_3 \end{pmatrix} \begin{pmatrix} \ell_1 & \ell_2 & \ell_3 \\ 0 & 0 & 0 \end{pmatrix}. \tag{A.13}$$

Appendix B

Maxwell's Equations with Chern-Simons Coupling

In this chapter, we derive Maxwell's equations in curved spacetime, modified by the presence of an electromagnetic Chern-Simons coupling of photons to a dynamical scalar field ϕ, considered in Part III of this thesis.

We consider the following Lagrangian density

$$\mathscr{L} = \sqrt{-g}(-\frac{1}{4}F^{\mu\nu}F_{\mu\nu} - \frac{\beta}{4M}\phi\varepsilon_{\mu\nu\rho\sigma}F^{\mu\nu}F^{\rho\sigma}) \equiv \mathscr{L}_1 + \mathscr{L}_1, \tag{B.1}$$

and the metric element

$$ds^2 = -a^2(1+2\Psi)dt^2 + a^2(1-2\Phi)d\vec{x}^2, \tag{B.2}$$

with the usual definition of the symbols. We begin by sketching out the derivation of the first and second Maxwell's equations, and then focus on the third and fourth, which are relevant for the derivation of the birefringent rotation angle in Eq. (4.7).

Let us begin by expanding the Euler-Lagrange equation,

$$\frac{\partial\mathscr{L}}{\partial A_\alpha} - \nabla_\beta\frac{\partial\mathscr{L}}{\partial(\nabla_\beta A_\alpha)} = 0, \tag{B.3}$$

noting that in the absence of currents[1] the first term vanishes, and the second term has contributions from the standard electromagnetic part $\mathscr{L}_1$, and from the Chern-Simons term $\mathscr{L}_2$. Substituting

$$\frac{\partial(\nabla_\mu A_\nu)}{\partial(\nabla_\sigma A_\rho)} = \delta_\mu{}^\sigma\delta_\nu{}^\rho, \tag{B.4}$$

and

$$F_{\mu\nu} \equiv \partial_\mu A_\nu - \partial_\nu A_\mu \tag{B.5}$$

[1]Since we are only interested in propagation of photons in a vacuum, we set the current to zero.

into

$$\mathscr{L}_1 = -\sqrt{-g}\frac{1}{4}g^{\mu\lambda}g^{\nu\sigma}F_{\mu\nu}F_{\lambda\sigma}, \tag{B.6}$$

and plugging the new expression into the Euler-Lagrange equation for $\mathscr{L}_1$, we get the usual result[2],

$$\nabla_\beta \frac{\partial \mathscr{L}_1}{\partial(\nabla_\beta A_\alpha)} = \nabla_\beta(\sqrt{-g}F^{\alpha\beta}). \tag{B.7}$$

We further use Eqs. (B.4) and (B.5) and expand $\mathscr{L}_2$ as

$$\mathscr{L}_2 = -\sqrt{-g}\frac{\beta}{4M}\phi\varepsilon_{\mu\nu\rho\sigma}g^{\mu\lambda}g^{\nu\gamma}g^{\rho\delta}g^{\sigma\xi}F_{\lambda\gamma}F_{\delta\xi}, \tag{B.8}$$

to get

$$\frac{\partial \mathscr{L}_2}{\partial(\nabla_\beta A_\alpha)} = -\sqrt{-g}\frac{\beta}{4M}\phi[(\varepsilon^{\beta\alpha}{}_{\rho\sigma} - \varepsilon^{\alpha\beta}{}_{\rho\sigma})F^{\rho\sigma} + (\varepsilon_{\mu\nu}{}^{\beta\alpha} - \varepsilon_{\mu\nu}{}^{\alpha\beta})F^{\mu\nu}] = -\sqrt{-g}\frac{\beta}{M}\phi F^{\mu\nu}\varepsilon_{\mu\nu}{}^{\beta\alpha}, \tag{B.9}$$

where in the last step we used antisymmetry of the Levi-Civita tensor,

$$\varepsilon^{\beta\alpha}{}_{\rho\sigma} = -\varepsilon^{\alpha\beta}{}_{\rho\sigma}, \tag{B.10}$$

renamed indicies $\rho\sigma \to \mu\nu$, and employed the following property

$$\varepsilon^{\beta\alpha}{}_{\mu\nu} = \varepsilon_{\mu\nu}{}^{\beta\alpha}. \tag{B.11}$$

Finally, remembering the definition of the dual of the electromagnetic field-strength tensor, we can write the full Euler-Lagrange equation (including the Chern-Simons term) in curved spacetime as[3]

$$\nabla_\mu(\sqrt{-g}F^{\mu\nu}) + \nabla_\mu(2\frac{\beta}{M}\phi\sqrt{-g}\widetilde{F}^{\mu\nu}) = 0. \tag{B.12}$$

Explicit forms of the first and the second Maxwell's equation can be obtained by separating time and space components of Eq. (B.12), and using the definition of $F_{\mu\nu}$ given below.

We now focus on obtaining the third and the fourth equation. Starting from the following equality[4]

$$\partial_\alpha F_{\beta\gamma} + \partial_\beta F_{\gamma\alpha} + \partial_\gamma F_{\alpha\beta} = 0, \tag{B.13}$$

where the components of $F_{\mu\nu}$ in the free-falling observer's frame, in the conformal-Newtonian gauge,

[2] In flat Minkowski spacetime, $\sqrt{-g} = 1$, which recoveres the standard result.

[3] Note that the covariant derivatives (denoted with ∇_μ) of the metric and the Levi-Civita tensor vanish, which can be used to write this equation only in terms of $F^{\mu\nu}$.

[4] This equality holds for any metric, since $F_{\alpha\beta} = -F_{\beta\alpha}$, by definition.

to first order in Φ and Ψ, read

$$\begin{aligned} F_{00} = F_{11} = F_{22} = F_{33} = 0, \\ F_{01} = -E_x a^2(1 - \Phi + \Psi), \\ F_{02} = -E_y a^2(1 - \Phi + \Psi), \\ F_{03} = -E_z a^2(1 - \Phi + \Psi), \\ F_{12} = B_z a^2(1 - 2\Phi), \\ F_{13} = -B_y a^2(1 - 2\Phi), \\ F_{23} = B_x a^2(1 - 2\Phi), \end{aligned} \tag{B.14}$$

and considering, respectively, the following two cases: $\alpha = 1$, $\beta = 2$, $\gamma = 3$, and $\alpha = 0$, $\beta = 1$, $\gamma = 2$, we arrive at the third and fourth Maxwell's equation including the Chern-Simons term in curved spacetime,

$$\begin{aligned} \vec{\nabla}(\vec{B}a^2(1 - 2\Phi)) = 0, \\ \vec{\nabla} \times (\vec{E}a^2(1 - \Phi + \Psi)) = -\frac{\partial}{\partial \tau}(\vec{B}a^2(1 - 2\Phi)). \end{aligned} \tag{B.15}$$

Bibliography

[1] S. Dodelson, *Modern cosmology*. 2003. I, 1

[2] J. Beringer, *Cosmic Microwave Background*, *Phys.Rev.* **D86** (2012). I, 2, 3.3

[3] M. Kamionkowski, A. Kosowsky and A. Stebbins, *Statistics of cosmic microwave background polarization*, *Phys.Rev.* **D55** (1997) 7368–7388 [astro-ph/9611125]. I, 3.2, 7.2, 7.2, 8.1

[4] V. Gluscevic, M. Kamionkowski and A. Cooray, *Derotation of the cosmic microwave background polarization: Full-sky formalism*, Phys. Rev. D **80** (July, 2009) 023510 [0905.1687]. I, 0, 6.2, 6.2, 6.2, 7.2, 8.2, 8.6, 9.1

[5] V. Gluscevic, D. Hanson, M. Kamionkowski and C. M. Hirata, *First CMB constraints on direction-dependent cosmological birefringence from WMAP-7*, Phys. Rev. D **86** (Nov., 2012) 103529 [1206.5546]. I, 0

[6] R. R. Caldwell, V. Gluscevic and M. Kamionkowski, *Cross-correlation of cosmological birefringence with CMB temperature*, Phys. Rev. D **84** (Aug., 2011) 043504 [1104.1634]. I, 6.8, 1, 8

[7] V. Gluscevic and M. Kamionkowski, *Testing parity-violating mechanisms with cosmic microwave background experiments*, Phys. Rev. D **81** (June, 2010) 123529 [1002.1308]. I, 6.6, 7.2, 1

[8] "http://lambda.gsfc.nasa.gov/." I, 6.1, 6.1, 6.4, 1, 6.7.0.3, 9.2

[9] P. S. Team, *Planck: The Scientific Programme (Blue Book). ESA-SCI (2005)-1. Version 2. European Space Agency.*, 2005. 2, 2, 8.1

[10] B. P. Crill, P. A. R. Ade, E. S. Battistelli, S. Benton, R. Bihary, J. J. Bock, J. R. Bond, J. Brevik, S. Bryan, C. R. Contaldi, O. Doré, M. Farhang, L. Fissel, S. R. Golwala, M. Halpern, G. Hilton, W. Holmes, V. V. Hristov, K. Irwin, W. C. Jones, C. L. Kuo, A. E. Lange, C. Lawrie, C. J. MacTavish, T. G. Martin, P. Mason, T. E. Montroy, C. B. Netterfield, E. Pascale, D. Riley, J. E. Ruhl, M. C. Runyan, A. Trangsrud, C. Tucker, A. Turner, M. Viero and D. Wiebe, *SPIDER: a balloon-borne large-scale CMB polarimeter*,

in *Society of Photo-Optical Instrumentation Engineers (SPIE) Conference Series*, vol. 7010 of *Society of Photo-Optical Instrumentation Engineers (SPIE) Conference Series*, Aug., 2008. 0807.1548. 2, 7.2, 7.2, 8.1

[11] J. Bock, A. Cooray, S. Hanany, B. Keating, A. Lee, T. Matsumura, M. Milligan, N. Ponthieu, T. Renbarger and H. Tran, *The Experimental Probe of Inflationary Cosmology (EPIC): A Mission Concept Study for NASA's Einstein Inflation Probe*, *ArXiv e-prints* (May, 2008) [0805.4207]. 2, 7.2, 8.1

[12] V. Gluscevic and R. Barkana, *Statistics of 21-cm fluctuations in cosmic reionization simulations: PDFs and difference PDFs*, MNRAS **408** (Nov., 2010) 2373–2380 [1005.3814]. I, 0

[13] V. Gluscevic, M. Kamionkowski and D. Hanson, *Patchy Screening of the Cosmic Microwave Background by Inhomogeneous Reionization*, *ArXiv e-prints* (Oct., 2012) [1210.5507]. I, 0

[14] A. A. Penzias and R. W. Wilson, *A Measurement of Excess Antenna Temperature at 4080 Mc/s.*, ApJ **142** (July, 1965) 419–421. II

[15] V. Mukhanov, *Physical Foundations of Cosmology*. Nov., 2005. 1

[16] U. Seljak and M. Zaldarriaga, *A Line-of-Sight Integration Approach to Cosmic Microwave Background Anisotropies*, ApJ **469** (Oct., 1996) 437 [arXiv:astro-ph/9603033]. 1

[17] A. Lewis, A. Challinor and A. Lasenby, *Efficient Computation of Cosmic Microwave Background Anisotropies in Closed Friedmann-Robertson-Walker Models*, ApJ **538** (Aug., 2000) 473–476 [arXiv:astro-ph/9911177]. 1

[18] C. L. Bennett, M. Bay, M. Halpern, G. Hinshaw, C. Jackson, N. Jarosik, A. Kogut, M. Limon, S. S. Meyer, L. Page, D. N. Spergel, G. S. Tucker, D. T. Wilkinson, E. Wollack and E. L. Wright, *The Microwave Anisotropy Probe Mission*, ApJ **583** (Jan., 2003) 1–23 [arXiv:astro-ph/0301158]. 2

[19] C. L. Bennett, D. Larson, J. L. Weiland, N. Jarosik, G. Hinshaw, N. Odegard, K. M. Smith, R. S. Hill, B. Gold, M. Halpern, E. Komatsu, M. R. Nolta, L. Page, D. N. Spergel, E. Wollack, J. Dunkley, A. Kogut, M. Limon, S. S. Meyer, G. S. Tucker and E. L. Wright, *Nine-Year Wilkinson Microwave Anisotropy Probe (WMAP) Observations: Final Maps and Results*, *ArXiv e-prints* (Dec., 2012) [1212.5225]. 2.1, 2.2

[20] "http://pole.uchicago.edu/spt/." 2

[21] J. E. Carlstrom, P. A. R. Ade, K. A. Aird, B. A. Benson, L. E. Bleem, S. Busetti, C. L. Chang, E. Chauvin, H.-M. Cho, T. M. Crawford, A. T. Crites, M. A. Dobbs, N. W.

Halverson, S. Heimsath, W. L. Holzapfel, J. D. Hrubes, M. Joy, R. Keisler, T. M. Lanting, A. T. Lee, E. M. Leitch, J. Leong, W. Lu, M. Lueker, D. Luong-van, J. J. McMahon, J. Mehl, S. S. Meyer, J. J. Mohr, T. E. Montroy, S. Padin, T. Plagge, C. Pryke, J. E. Ruhl, K. K. Schaffer, D. Schwan, E. Shirokoff, H. G. Spieler, Z. Staniszewski, A. A. Stark, C. Tucker, K. Vanderlinde, J. D. Vieira and R. Williamson, *The 10 Meter South Pole Telescope*, PASP **123** (May, 2011) 568–581 [0907.4445]. 2

[22] A. Kosowsky, *The Atacama Cosmology Telescope project: A progress report*, New A Rev. **50** (Dec., 2006) 969–976 [arXiv:astro-ph/0608549]. 2

[23] "http://bolo.berkeley.edu/polarbear/." 2

[24] J. E. Austermann, K. A. Aird, J. A. Beall, D. Becker, A. Bender, B. A. Benson, L. E. Bleem, J. Britton, J. E. Carlstrom, C. L. Chang, H. C. Chiang, H.-M. Cho, T. M. Crawford, A. T. Crites, A. Datesman, T. de Haan, M. A. Dobbs, E. M. George, N. W. Halverson, N. Harrington, J. W. Henning, G. C. Hilton, G. P. Holder, W. L. Holzapfel, S. Hoover, N. Huang, J. Hubmayr, K. D. Irwin, R. Keisler, J. Kennedy, L. Knox, A. T. Lee, E. Leitch, D. Li, M. Lueker, D. P. Marrone, J. J. McMahon, J. Mehl, S. S. Meyer, T. E. Montroy, T. Natoli, J. P. Nibarger, M. D. Niemack, V. Novosad, S. Padin, C. Pryke, C. L. Reichardt, J. E. Ruhl, B. R. Saliwanchik, J. T. Sayre, K. K. Schaffer, E. Shirokoff, A. A. Stark, K. Story, K. Vanderlinde, J. D. Vieira, G. Wang, R. Williamson, V. Yefremenko, K. W. Yoon and O. Zahn, *SPTpol: an instrument for CMB polarization measurements with the South Pole Telescope*, in *Society of Photo-Optical Instrumentation Engineers (SPIE) Conference Series*, vol. 8452 of *Society of Photo-Optical Instrumentation Engineers (SPIE) Conference Series*, Sept., 2012. 1210.4970. 2

[25] G. Hinshaw, D. Larson, E. Komatsu, D. N. Spergel, C. L. Bennett, J. Dunkley, M. R. Nolta, M. Halpern, R. S. Hill, N. Odegard, L. Page, K. M. Smith, J. L. Weiland, B. Gold, N. Jarosik, A. Kogut, M. Limon, S. S. Meyer, G. S. Tucker, E. Wollack and E. L. Wright, *Nine-Year Wilkinson Microwave Anisotropy Probe (WMAP) Observations: Cosmological Parameter Results*, *ArXiv e-prints* (Dec., 2012) [1212.5226]. 3.1, 4

[26] M. Kamionkowski, A. Kosowsky and A. Stebbins, *A Probe of Primordial Gravity Waves and Vorticity*, *Physical Review Letters* **78** (Mar., 1997) 2058–2061 [arXiv:astro-ph/9609132]. 3.2

[27] U. Seljak and M. Zaldarriaga, *Signature of Gravity Waves in the Polarization of the Microwave Background*, *Physical Review Letters* **78** (Mar., 1997) 2054–2057 [arXiv:astro-ph/9609169]. 3.2

[28] M. Zaldarriaga and U. Seljak, *All-sky analysis of polarization in the microwave background*, Phys. Rev. D **55** (Feb., 1997) 1830–1840 [arXiv:astro-ph/9609170]. 3.2, 6.2

[29] J. Chluba and R. A. Sunyaev, *The evolution of CMB spectral distortions in the early Universe*, MNRAS **419** (Jan., 2012) 1294–1314 [1109.6552]. 5

[30] W. Hu, *Weak lensing of the CMB: A harmonic approach*, Phys. Rev. D **62** (Aug., 2000) 043007 [arXiv:astro-ph/0001303]. 3.2, 5.1, 5.2, 5.2, 5.3

[31] S. M. Carroll, *Quintessence and the Rest of the World: Suppressing Long-Range Interactions*, *Physical Review Letters* **81** (Oct., 1998) 3067–3070 [arXiv:astro-ph/9806099]. III, 4, 4, 4, 6.8

[32] A. H. Guth, *Inflationary universe: A possible solution to the horizon and flatness problems*, Phys. Rev. D **23** (Jan., 1981) 347–356. 4, 8

[33] A. G. Riess, A. V. Filippenko, P. Challis, A. Clocchiatti, A. Diercks, P. M. Garnavich, R. L. Gilliland, C. J. Hogan, S. Jha, R. P. Kirshner, B. Leibundgut, M. M. Phillips, D. Reiss, B. P. Schmidt, R. A. Schommer, R. C. Smith, J. Spyromilio, C. Stubbs, N. B. Suntzeff and J. Tonry, *Observational Evidence from Supernovae for an Accelerating Universe and a Cosmological Constant*, AJ **116** (Sept., 1998) 1009–1038 [arXiv:astro-ph/9805201]. 4, 8

[34] S. Perlmutter, G. Aldering, B. J. Boyle, P. G. Castro, W. J. Couch, S. Deustua, S. Fabbro, R. S. Ellis, A. V. Filippenko, A. Fruchter, G. Goldhaber, A. Goobar, D. E. Groom, I. M. Hook, M. Irwin, A. G. Kim, M. Y. Kim, R. A. Knop, J. C. Lee, T. Matheson, R. G. McMahon, H. J. M. Newberg, C. Lidman, P. Nugent, N. J. Nunes, R. Pain, N. Panagia, C. R. Pennypacker, R. Quimby, P. Ruiz-Lapuente, B. Schaefer, N. Walton and Supernova Cosmology Project, *Measurements of Omega and Lambda from 42 High-Redshift Supernovae*, in *19th Texas Symposium on Relativistic Astrophysics and Cosmology* (J. Paul, T. Montmerle and E. Aubourg, eds.), Dec., 1998. 4

[35] M. Hicken, W. M. Wood-Vasey, S. Blondin, P. Challis, S. Jha, P. L. Kelly, A. Rest and R. P. Kirshner, *Improved Dark Energy Constraints from ˜100 New CfA Supernova Type Ia Light Curves*, ApJ **700** (Aug., 2009) 1097–1140 [0901.4804]. 4, 6.8

[36] B. Ratra and P. J. E. Peebles, *Cosmological consequences of a rolling homogeneous scalar field*, Phys. Rev. D **37** (June, 1988) 3406–3427. 4

[37] J. Goldstone, A. Salam and S. Weinberg, *Broken symmetries*, *Phys. Rev.* **127** (Aug, 1962) 965–970. 4

[38] J. A. Frieman, C. T. Hill, A. Stebbins and I. Waga, *Cosmology with Ultralight Pseudo Nambu-Goldstone Bosons*, *Physical Review Letters* **75** (Sept., 1995) 2077–2080 [arXiv:astro-ph/9505060]. 4

[39] S. M. Carroll, G. B. Field and R. Jackiw, *Limits on a Lorentz- and parity-violating modification of electrodynamics*, Phys. Rev. D **41** (Feb., 1990) 1231–1240. 4

[40] R. Rabadan, A. Ringwald and K. Sigurdson, *Photon regeneration from pseudoscalars at X-ray laser facilities*, *Phys.Rev.Lett.* **96** (2006) 110407 [hep-ph/0511103]. 3

[41] S. Gardner, *Possibility of Observing Dark Matter via the Gyromagnetic Faraday Effect*, *Physical Review Letters* **100** (Feb., 2008) 041303 [arXiv:astro-ph/0611684]. 4

[42] S. di Serego Alighieri, F. Finelli and M. Galaverni, *Limits on Cosmological Birefringence from the Ultraviolet Polarization of Distant Radio Galaxies*, ApJ **715** (May, 2010) 33–38 [1003.4823]. 4

[43] M. Kamionkowski, *Nonuniform cosmological birefringence and active galactic nuclei*, Phys. Rev. D **82** (Aug., 2010) 047302 [1004.3544]. 4, 6.6, 6.9, 7.1.1

[44] H. C. Chiang, P. A. R. Ade, D. Barkats, J. O. Battle, E. M. Bierman, J. J. Bock, C. D. Dowell, L. Duband, E. F. Hivon, W. L. Holzapfel, V. V. Hristov, W. C. Jones, B. G. Keating, J. M. Kovac, C. L. Kuo, A. E. Lange, E. M. Leitch, P. V. Mason, T. Matsumura, H. T. Nguyen, N. Ponthieu, C. Pryke, S. Richter, G. Rocha, C. Sheehy, Y. D. Takahashi, J. E. Tolan and K. W. Yoon, *Measurement of Cosmic Microwave Background Polarization Power Spectra from Two Years of BICEP Data*, ApJ **711** (Mar., 2010) 1123–1140 [0906.1181]. 4

[45] E. Y. S. Wu, P. Ade, J. Bock, M. Bowden, M. L. Brown, G. Cahill, P. G. Castro, S. Church, T. Culverhouse, R. B. Friedman, K. Ganga, W. K. Gear, S. Gupta, J. Hinderks, J. Kovac, A. E. Lange, E. Leitch, S. J. Melhuish, Y. Memari, J. A. Murphy, A. Orlando, L. Piccirillo, C. Pryke, N. Rajguru, B. Rusholme, R. Schwarz, C. O'Sullivan, A. N. Taylor, K. L. Thompson, A. H. Turner and M. Zemcov, *Parity Violation Constraints Using Cosmic Microwave Background Polarization Spectra from 2006 and 2007 Observations by the QUaD Polarimeter*, *Physical Review Letters* **102** (Apr., 2009) 161302 [0811.0618]. 4

[46] E. Komatsu, K. M. Smith, J. Dunkley, C. L. Bennett, B. Gold, G. Hinshaw, N. Jarosik, D. Larson, M. R. Nolta, L. Page, D. N. Spergel, M. Halpern, R. S. Hill, A. Kogut, M. Limon, S. S. Meyer, N. Odegard, G. S. Tucker, J. L. Weiland, E. Wollack and E. L. Wright, *Seven-year Wilkinson Microwave Anisotropy Probe (WMAP) Observations: Cosmological Interpretation*, ApJS **192** (Feb., 2011) 18 [1001.4538]. 4, 6.2, 6, 6.6, 6.3, 6.7, 7.2, IV

[47] M. Pospelov, A. Ritz and C. Skordis, *Pseudoscalar Perturbations and Polarization of the Cosmic Microwave Background*, *Physical Review Letters* **103** (July, 2009) 051302 [0808.0673]. 4, 7.1.1, 8.6

[48] A. L. Erickcek, M. Kamionkowski and S. M. Carroll, *A hemispherical power asymmetry from inflation*, Phys. Rev. D **78** (Dec., 2008) 123520 [0806.0377]. 4

[49] A. L. Erickcek, S. M. Carroll and M. Kamionkowski, *Superhorizon perturbations and the cosmic microwave background*, Phys. Rev. D **78** (Oct., 2008) 083012 [0808.1570]. 4

[50] A. R. Pullen and M. Kamionkowski, *Cosmic microwave background statistics for a direction-dependent primordial power spectrum*, Phys. Rev. D **76** (Nov., 2007) 103529 [0709.1144]. 4, 5.2, 4, 5.4, 8.1

[51] M. Kamionkowski, *How to Derotate the Cosmic Microwave Background Polarization*, *Physical Review Letters* **102** (Mar., 2009) 111302 [0810.1286]. 5.1, 2, 5.2, 4, 6.2, 6.2, 8.6

[52] K. M. Górski, E. Hivon, A. J. Banday, B. D. Wandelt, F. K. Hansen, M. Reinecke and M. Bartelmann, *HEALPix: A Framework for High-Resolution Discretization and Fast Analysis of Data Distributed on the Sphere*, ApJ **622** (Apr., 2005) 759–771 [arXiv:astro-ph/0409513]. 5.2

[53] A. Hajian and T. Souradeep, *Measuring the Statistical Isotropy of the Cosmic Microwave Background Anisotropy*, ApJ **597** (Nov., 2003) L5–L8 [arXiv:astro-ph/0308001]. 5.2

[54] A. P. S. Yadav, R. Biswas, M. Su and M. Zaldarriaga, *Constraining a spatially dependent rotation of the cosmic microwave background polarization*, Phys. Rev. D **79** (June, 2009) 123009 [0902.4466]. 5.2, 5.2, 8.2, 8.6

[55] M. Zaldarriaga and U. Seljak, *Gravitational lensing effect on cosmic microwave background polarization*, Phys. Rev. D **58** (July, 1998) 023003 [arXiv:astro-ph/9803150]. 5.3

[56] U. Seljak and M. Zaldarriaga, *Measuring Dark Matter Power Spectrum from Cosmic Microwave Background*, *Physical Review Letters* **82** (Mar., 1999) 2636–2639 [arXiv:astro-ph/9810092]. 5.3

[57] M. Zaldarriaga and U. Seljak, *Reconstructing projected matter density power spectrum from cosmic microwave background*, Phys. Rev. D **59** (June, 1999) 123507 [arXiv:astro-ph/9810257]. 5.3

[58] T. Okamoto and W. Hu, *Cosmic microwave background lensing reconstruction on the full sky*, Phys. Rev. D **67** (Apr., 2003) 083002 [arXiv:astro-ph/0301031]. 5.3, 6.2

[59] W. Hu and T. Okamoto, *Mass Reconstruction with Cosmic Microwave Background Polarization*, ApJ **574** (Aug., 2002) 566–574 [arXiv:astro-ph/0111606]. 5.3

[60] M. Kesden, A. Cooray and M. Kamionkowski, *Separation of Gravitational-Wave and Cosmic-Shear Contributions to Cosmic Microwave Background Polarization*, *Physical Review Letters* **89** (July, 2002) 011304 [arXiv:astro-ph/0202434]. 5.3

[61] L. Knox and Y.-S. Song, *Limit on the Detectability of the Energy Scale of Inflation*, *Physical Review Letters* **89** (July, 2002) 011303 [arXiv:astro-ph/0202286]. 5.3

[62] M. Kesden, A. Cooray and M. Kamionkowski, *Lensing reconstruction with CMB temperature and polarization*, Phys. Rev. D **67** (June, 2003) 123507 [arXiv:astro-ph/0302536]. 5.3

[63] P. Cabella and M. Kamionkowski, *Theory of Cosmic Microwave Background Polarization*, *ArXiv Astrophysics e-prints* (Mar., 2004) [arXiv:astro-ph/0403392]. 5.3

[64] A. Lewis and A. Challinor, *Weak gravitational lensing of the CMB*, Phys. Rep. **429** (June, 2006) 1–65 [arXiv:astro-ph/0601594]. 5.3

[65] E. Komatsu, J. Dunkley, M. R. Nolta, C. L. Bennett, B. Gold, G. Hinshaw, N. Jarosik, D. Larson, M. Limon, L. Page, D. N. Spergel, M. Halpern, R. S. Hill, A. Kogut, S. S. Meyer, G. S. Tucker, J. L. Weiland, E. Wollack and E. L. Wright, *Five-Year Wilkinson Microwave Anisotropy Probe Observations: Cosmological Interpretation*, ApJS **180** (Feb., 2009) 330–376 [0803.0547]. 5.4, 5.4, 8, 8.1

[66] M. Betoule, E. Pierpaoli, J. Delabrouille, M. Le Jeune and J.-F. Cardoso, *Measuring the tensor to scalar ratio from CMB B-modes in the presence of foregrounds*, A&A **503** (Sept., 2009) 691–706 [0901.1056]. 5.4

[67] B. Feng, M. Li, J.-Q. Xia, X. Chen and X. Zhang, *Searching for CPT Violation with Cosmic Microwave Background Data from WMAP and BOOMERANG*, *Physical Review Letters* **96** (June, 2006) 221302 [arXiv:astro-ph/0601095]. 5.4, 8, 8.6

[68] B. Gold, N. Odegard, J. L. Weiland, R. S. Hill, A. Kogut, C. L. Bennett, G. Hinshaw, X. Chen, J. Dunkley, M. Halpern, N. Jarosik, E. Komatsu, D. Larson, M. Limon, S. S. Meyer, M. R. Nolta, L. Page, K. M. Smith, D. N. Spergel, G. S. Tucker, E. Wollack and E. L. Wright, *Seven-year Wilkinson Microwave Anisotropy Probe (WMAP) Observations: Galactic Foreground Emission*, ApJS **192** (Feb., 2011) 15 [1001.4555]. 6.1, 7.1.2

[69] M. Kamionkowski, A. Kosowsky and A. Stebbins, *Statistics of cosmic microwave background polarization*, Phys. Rev. D **55** (June, 1997) 7368–7388 [arXiv:astro-ph/9611125]. 6.2

[70] K. M. Smith, O. Zahn and O. Doré, *Detection of gravitational lensing in the cosmic microwave background*, Phys. Rev. D **76** (Aug., 2007) 043510 [0705.3980]. 6.2, 6.2

[71] C. M. Hirata, N. Padmanabhan, U. Seljak, D. Schlegel and J. Brinkmann, *Cross-correlation of CMB with large-scale structure: Weak gravitational lensing*, Phys. Rev. D **70** (Nov., 2004) 103501 [arXiv:astro-ph/0406004]. 6.2, 9.4

[72] D. Hanson, A. Lewis and A. Challinor, *Asymmetric beams and CMB statistical anisotropy*, Phys. Rev. D **81** (May, 2010) 103003 [1003.0198]. 6.7.0.1

[73] G. De Zotti, M. Massardi, M. Negrello and J. Wall, *Radio and Millimeter Continuum Surveys and their Astrophysical Implications*, *Astron.Astrophys.Rev.* **18** (2010) 1–65 [0908.1896]. 6.7.0.2

[74] R. C. Bolton, G. Cotter, G. Pooley, J. Riley, E. Waldram *et. al.*, *The Radio source population at high frequency. Follow-up of the 15-GHz 9C survey*, *Mon.Not.Roy.Astron.Soc.* **354** (2004) 485 [astro-ph/0407228]. 6.7.0.2

[75] A. Cooray, D. E. Holz and R. Caldwell, *Measuring dark energy spatial inhomogeneity with supernova data*, J. Cosmology Astropart. Phys. **11** (Nov., 2010) 15 [0812.0376]. 6.8

[76] G. D'Amico and E. Sefusatti, *The nonlinear power spectrum in clustering quintessence cosmologies*, *JCAP* **1111** (2011) 013 [1106.0314]. 6.8

[77] M. Kamionkowski and J. March-Russell, *Planck scale physics and the Peccei-Quinn mechanism*, *Phys.Lett.* **B282** (1992) 137–141 [hep-th/9202003]. 1

[78] R. Holman, S. D. Hsu, T. W. Kephart, E. W. Kolb, R. Watkins *et. al.*, *Solutions to the strong CP problem in a world with gravity*, *Phys.Lett.* **B282** (1992) 132–136 [hep-ph/9203206]. 1

[79] C.-P. Ma and E. Bertschinger, *Cosmological Perturbation Theory in the Synchronous and Conformal Newtonian Gauges*, ApJ **455** (Dec., 1995) 7 [arXiv:astro-ph/9506072]. 7.1.2, 7.1.2, 6, 7.1.2

[80] G. Jungman, M. Kamionkowski, A. Kosowsky and D. N. Spergel, *Cosmological-parameter determination with microwave background maps*, Phys. Rev. D **54** (July, 1996) 1332–1344 [arXiv:astro-ph/9512139]. 7.2, 8.1

[81] "http://www.rssd.esa.int/planck." 7.2

[82] L. Pagano, P. de Bernardis, G. de Troia, G. Gubitosi, S. Masi, A. Melchiorri, P. Natoli, F. Piacentini and G. Polenta, *CMB polarization systematics, cosmological birefringence, and the gravitational waves background*, Phys. Rev. D **80** (Aug., 2009) 043522 [0905.1651]. 7.3

[83] A. Lue, L. Wang and M. Kamionkowski, *Cosmological Signature of New Parity-Violating Interactions*, *Physical Review Letters* **83** (Aug., 1999) 1506–1509 [arXiv:astro-ph/9812088]. 8, 8.1, 8.2

[84] C. R. Contaldi, J. Magueijo and L. Smolin, *Anomalous Cosmic-Microwave-Background Polarization and Gravitational Chirality*, *Physical Review Letters* **101** (Oct., 2008) 141101 [0806.3082]. 8, 8.1, 8.4

[85] N. F. Lepora, *Cosmological Birefringence and the Microwave Background*, *ArXiv General Relativity and Quantum Cosmology e-prints* (Dec., 1998) [arXiv:gr-qc/9812077]. 8

[86] S. Saito, K. Ichiki and A. Taruya, *Probing polarization states of primordial gravitational waves with cosmic microwave background anisotropies*, J. Cosmology Astropart. Phys. **9** (Sept., 2007) 2 [0705.3701]. 8, 8.1, 8.1, 8.1, 8.4

[87] T. L. Smith, A. L. Erickcek, R. R. Caldwell and M. Kamionkowski, *Effects of Chern-Simons gravity on bodies orbiting the Earth*, Phys. Rev. D **77** (Jan., 2008) 024015 [0708.0001]. 8.1

[88] T. Takahashi and J. Soda, *Chiral Primordial Gravitational Waves from a Lifshitz Point*, *Physical Review Letters* **102** (June, 2009) 231301 [0904.0554]. 8.1

[89] J. F. C. Wardle, R. A. Perley and M. H. Cohen, *Observational Evidence against Birefringence over Cosmological Distances*, *Physical Review Letters* **79** (Sept., 1997) 1801–1804 [arXiv:astro-ph/9705142]. 8.6

[90] M. Li and X. Zhang, *Cosmological CPT violating effect on CMB polarization*, Phys. Rev. D **78** (Nov., 2008) 103516 [0810.0403]. 8.6

[91] N. Seto and A. Taruya, *Measuring a Parity-Violation Signature in the Early Universe via Ground-Based Laser Interferometers*, *Physical Review Letters* **99** (Sept., 2007) 121101 [0707.0535]. 8.6

[92] N. Seto, *Quest for circular polarization of a gravitational wave background and orbits of laser interferometers in space*, Phys. Rev. D **75** (Mar., 2007) 061302 [arXiv:astro-ph/0609633]. 8.6

[93] N. Seto and A. Taruya, *Polarization analysis of gravitational-wave backgrounds from the correlation signals of ground-based interferometers: Measuring a circular-polarization mode*, Phys. Rev. D **77** (May, 2008) 103001 [0801.4185]. 8.6

[94] N. Seto, *Prospects for Direct Detection of the Circular Polarization of the Gravitational-Wave Background*, *Physical Review Letters* **97** (Oct., 2006) 151101 [arXiv:astro-ph/0609504]. 8.6

[95] S. Alexander and N. Yunes, *Chern-Simons modified general relativity*, Phys. Rep. **480** (Aug., 2009) 1–55 [0907.2562]. 8.6

[96] R. H. Becker, X. Fan, R. L. White, M. A. Strauss, V. K. Narayanan, R. H. Lupton, J. E. Gunn, J. Annis, N. A. Bahcall, J. Brinkmann, A. J. Connolly, I. Csabai, P. C. Czarapata, M. Doi, T. M. Heckman, G. S. Hennessy, Ž. Ivezić, G. R. Knapp, D. Q. Lamb, T. A. McKay, J. A. Munn, T. Nash, R. Nichol, J. R. Pier, G. T. Richards, D. P. Schneider, C. Stoughton, A. S. Szalay, A. R. Thakar and D. G. York, *Evidence for Reionization at z˜6: Detection of a Gunn-Peterson Trough in a z=6.28 Quasar*, AJ **122** (Dec., 2001) 2850–2857 [arXiv:astro-ph/0108097]. IV

[97] S. P. Oh and S. R. Furlanetto, *How Universal is the Gunn-Peterson Trough at z˜6?: A Closer Look at the Quasar SDSS J1148+5251*, ApJ **620** (Feb., 2005) L9–L12 [arXiv:astro-ph/0411152]. IV

[98] M. A. Schenker, D. P. Stark, R. S. Ellis, B. E. Robertson, J. S. Dunlop, R. J. McLure, J.-P. Kneib and J. Richard, *Keck Spectroscopy of Faint 3 ¡ z ¡ 8 Lyman Break Galaxies: Evidence for a Declining Fraction of Emission Line Sources in the Redshift Range 6 ¡ z ¡ 8*, ApJ **744** (Jan., 2012) 179 [1107.1261]. IV

[99] D. Larson, J. Dunkley, G. Hinshaw, E. Komatsu, M. R. Nolta, C. L. Bennett, B. Gold, M. Halpern, R. S. Hill, N. Jarosik, A. Kogut, M. Limon, S. S. Meyer, N. Odegard, L. Page, K. M. Smith, D. N. Spergel, G. S. Tucker, J. L. Weiland, E. Wollack and E. L. Wright, *Seven-year Wilkinson Microwave Anisotropy Probe (WMAP) Observations: Power Spectra and WMAP-derived Parameters*, ApJS **192** (Feb., 2011) 16 [1001.4635]. IV

[100] M. Kamionkowski, D. N. Spergel and N. Sugiyama, *Small-scale cosmic microwave background anisotropies as probe of the geometry of the universe*, ApJ **426** (May, 1994) L57 [arXiv:astro-ph/9401003]. IV

[101] P. R. Shapiro, M. L. Giroux and A. Babul, *Reionization in a cold dark matter universe: The feedback of galaxy formation on the intergalactic medium*, ApJ **427** (May, 1994) 25–50. IV

[102] M. Tegmark, J. Silk and A. Blanchard, *On the inevitability of reionization: Implications for cosmic microwave background fluctuations*, ApJ **420** (Jan., 1994) 484–496 [arXiv:astro-ph/9307017]. IV

[103] M. McQuinn, A. Lidz, O. Zahn, S. Dutta, L. Hernquist and M. Zaldarriaga, *The morphology of HII regions during reionization*, MNRAS **377** (May, 2007) 1043–1063 [arXiv:astro-ph/0610094]. IV, 10, 10.1, 10.1, 10.2, 10.3, 10.3, 10.4

[104] R. Barkana and A. Loeb, *In the beginning: the first sources of light and the reionization of the universe*, Phys. Rep. **349** (July, 2001) 125–238 [arXiv:astro-ph/0010468]. IV

[105] J. D. Bowman and A. E. E. Rogers, *A lower limit of dz ¿ 0.06 for the duration of the reionization epoch*, *ArXiv e-prints* (Sept., 2012) [1209.1117]. IV, 9

[106] O. Zahn, C. L. Reichardt, L. Shaw, A. Lidz, K. A. Aird, B. A. Benson, L. E. Bleem, J. E. Carlstrom, C. L. Chang, H. M. Cho, T. M. Crawford, A. T. Crites, T. de Haan, M. A. Dobbs, O. Doré, J. Dudley, E. M. George, N. W. Halverson, G. P. Holder, W. L. Holzapfel, S. Hoover, Z. Hou, J. D. Hrubes, M. Joy, R. Keisler, L. Knox, A. T. Lee, E. M. Leitch, M. Lueker, D. Luong-Van, J. J. McMahon, J. Mehl, S. S. Meyer, M. Millea, J. J. Mohr, T. E. Montroy, T. Natoli, S. Padin, T. Plagge, C. Pryke, J. E. Ruhl, K. K. Schaffer, E. Shirokoff, H. G. Spieler, Z. Staniszewski, A. A. Stark, K. Story, A. van Engelen, K. Vanderlinde, J. D. Vieira and R. Williamson, *Cosmic Microwave Background Constraints on the Duration and Timing of Reionization from the South Pole Telescope*, ApJ **756** (Sept., 2012) 65 [1111.6386]. IV, 8.8, 9.3

[107] A. Gruzinov and W. Hu, *Secondary Cosmic Microwave Background Anisotropies in a Universe Reionized in Patches*, ApJ **508** (Dec., 1998) 435–439 [arXiv:astro-ph/9803188]. IV, 1, 9.3

[108] C. Dvorkin and K. M. Smith, *Reconstructing patchy reionization from the cosmic microwave background*, Phys. Rev. D **79** (Feb., 2009) 043003 [0812.1566]. 9, 9, 9.1, 9.1

[109] C. Dvorkin, W. Hu and K. M. Smith, *B-mode CMB polarization from patchy screening during reionization*, Phys. Rev. D **79** (May, 2009) 107302 [0902.4413]. 9, 9.1

[110] D. Hanson and A. Lewis, *Estimators for CMB statistical anisotropy*, Phys. Rev. D **80** (Sept., 2009) 063004 [0908.0963]. 9, 9.3

[111] G.-C. Liu, N. Sugiyama, A. J. Benson, C. G. Lacey and A. Nusser, *Polarization of the Cosmic Microwave Background from Nonuniform Reionization*, ApJ **561** (Nov., 2001) 504–516 [arXiv:astro-ph/0101368]. 1

[112] M. J. Mortonson and W. Hu, *The Maximum B-Mode Polarization of the Cosmic Microwave Background from Inhomogeneous Reionization*, ApJ **657** (Mar., 2007) 1–14 [arXiv:astro-ph/0607652]. 1

[113] O. Doré, G. Holder, M. Alvarez, I. T. Iliev, G. Mellema, U.-L. Pen and P. R. Shapiro, *Signature of patchy reionization in the polarization anisotropy of the CMB*, Phys. Rev. D **76** (Aug., 2007) 043002 [arXiv:astro-ph/0701784]. 1

[114] N. Y. Gnedin and A. H. Jaffe, *Secondary Cosmic Microwave Background Anisotropies from Cosmological Reionization*, ApJ **551** (Apr., 2001) 3–14 [arXiv:astro-ph/0008469]. 9.1

[115] O. Zahn, M. Zaldarriaga, L. Hernquist and M. McQuinn, *The Influence of Nonuniform Reionization on the CMB*, ApJ **630** (Sept., 2005) 657–666 [arXiv:astro-ph/0503166]. 9.1

[116] W. Hu, *Reionization Revisited: Secondary Cosmic Microwave Background Anisotropies and Polarization*, ApJ **529** (Jan., 2000) 12–25 [arXiv:astro-ph/9907103]. 9.1

[117] I. T. Iliev, U.-L. Pen, J. R. Bond, G. Mellema and P. R. Shapiro, *The Kinetic Sunyaev-Zel'dovich Effect from Radiative Transfer Simulations of Patchy Reionization*, ApJ **660** (May, 2007) 933–944 [arXiv:astro-ph/0609592]. 9.1

[118] M. McQuinn, S. R. Furlanetto, L. Hernquist, O. Zahn and M. Zaldarriaga, *The Kinetic Sunyaev-Zel'dovich Effect from Reionization*, ApJ **630** (Sept., 2005) 643–656 [arXiv:astro-ph/0504189]. 9.1

[119] M. G. Santos, A. Cooray, Z. Haiman, L. Knox and C.-P. Ma, *Small-Scale Cosmic Microwave Background Temperature and Polarization Anisotropies Due to Patchy Reionization*, ApJ **598** (Dec., 2003) 756–766 [arXiv:astro-ph/0305471]. 9.1

[120] D. Baumann, A. Cooray, S. Dodelson, J. Dunkley, A. A. Fraisse, M. G. Jackson, A. Kogut, L. M. Krauss, K. M. Smith and M. Zaldarriaga, *A Mission to Map our Origins*, in *American Institute of Physics Conference Series* (S. Dodelson, D. Baumann, A. Cooray, J. Dunkley, A. Fraisse, M. G. Jackson, A. Kogut, L. Krauss, M. Zaldarriaga and K. Smith, eds.), vol. 1141 of *American Institute of Physics Conference Series*, pp. 3–9, June, 2009. 0811.3911. 9.3

[121] P. Madau, A. Meiksin and M. J. Rees, *21 Centimeter Tomography of the Intergalactic Medium at High Redshift*, ApJ **475** (Feb., 1997) 429 [arXiv:astro-ph/9608010]. 10

[122] S. R. Furlanetto, S. P. Oh and F. H. Briggs, *Cosmology at low frequencies: The 21 cm transition and the high-redshift Universe*, Phys. Rep. **433** (Oct., 2006) 181–301 [arXiv:astro-ph/0608032]. 10

[123] R. Barkana and A. Loeb, *The difference PDF of 21-cm fluctuations: a powerful statistical tool for probing cosmic reionization*, MNRAS **384** (Mar., 2008) 1069–1079 [0705.3246]. 10, 10.2, 10.3, 10.3, 10.3

[124] I. T. Iliev, G. Mellema, U.-L. Pen, J. R. Bond and P. R. Shapiro, *Current models of the observable consequences of cosmic reionization and their detectability*, MNRAS **384** (Mar., 2008) 863–874 [arXiv:astro-ph/0702099]. 10

[125] M. G. Santos, A. Amblard, J. Pritchard, H. Trac, R. Cen and A. Cooray, *Cosmic Reionization and the 21 cm Signal: Comparison between an Analytical Model and a Simulation*, ApJ **689** (Dec., 2008) 1–16 [0708.2424]. 10

[126] J. D. Bowman, M. F. Morales and J. N. Hewitt, *The Sensitivity of First-Generation Epoch of Reionization Observatories and Their Potential for Differentiating Theoretical Power Spectra*, ApJ **638** (Feb., 2006) 20–26 [arXiv:astro-ph/0507357]. 10

[127] M. McQuinn, O. Zahn, M. Zaldarriaga, L. Hernquist and S. R. Furlanetto, *Cosmological Parameter Estimation Using 21 cm Radiation from the Epoch of Reionization*, ApJ **653** (Dec., 2006) 815–834 [arXiv:astro-ph/0512263]. 10

[128] G. Harker, S. Zaroubi, G. Bernardi, M. A. Brentjens, A. G. de Bruyn, B. Ciardi, V. Jelić, L. V. E. Koopmans, P. Labropoulos, G. Mellema, A. Offringa, V. N. Pandey, A. H. Pawlik, J. Schaye, R. M. Thomas and S. Yatawatta, *Power spectrum extraction for redshifted 21-cm Epoch of Reionization experiments: the LOFAR case*, MNRAS **405** (July, 2010) 2492–2504 [1003.0965]. 10

[129] S. R. Furlanetto, M. Zaldarriaga and L. Hernquist, *The Growth of H II Regions During Reionization*, ApJ **613** (Sept., 2004) 1–15 [arXiv:astro-ph/0403697]. 10, 10.4

[130] S. Saiyad Ali, S. Bharadwaj and S. K. Pandey, *Probing the bispectrum at high redshifts using 21-cm HI observations*, MNRAS **366** (Feb., 2006) 213–218 [arXiv:astro-ph/0510118]. 10

[131] G. J. A. Harker, S. Zaroubi, R. M. Thomas, V. Jelić, P. Labropoulos, G. Mellema, I. T. Iliev, G. Bernardi, M. A. Brentjens, A. G. de Bruyn, B. Ciardi, L. V. E. Koopmans, V. N. Pandey, A. H. Pawlik, J. Schaye and S. Yatawatta, *Detection and extraction of signals from the epoch of reionization using higher-order one-point statistics*, MNRAS **393** (Mar., 2009) 1449–1458 [0809.2428]. 10

[132] K. Ichikawa, R. Barkana, I. T. Iliev, G. Mellema and P. R. Shapiro, *Measuring the history of cosmic reionization using the 21-cm probability distribution function from simulations*, MNRAS **406** (Aug., 2010) 2521–2532 [0907.2932]. 10, 10.2, 10.2, 10.3

[133] R. Barkana and A. Loeb, *Unusually Large Fluctuations in the Statistics of Galaxy Formation at High Redshift*, ApJ **609** (July, 2004) 474–481 [arXiv:astro-ph/0310338]. 10.3, 10.4